

# **Towards Directional Colloidal Interactions**

---

Op weg naar Directionele Colloïdale Interacties

(met een samenvatting in het Nederlands)

## **Proefschrift**

ter verkrijging van de graad van doctor aan de Universiteit Utrecht  
op gezag van de rector magnificus, prof. dr. G. J. van der Zwaan, ingevolge  
het besluit van het college voor promoties in het openbaar te verdedigen op  
maandag 6 juli 2015 des middags te 4.15 uur

door

**Marlous Kamp**

geboren op 22 mei 1986 te Ermelo

**Promotor:** Prof. dr. A. van Blaaderen  
**Copromotor:** Dr. A. Imhof

This research was financially supported by the Netherlands Organisation for Scientific Research (NWO) through an ECHO grant (project number 700.58.025).



Universiteit Utrecht



*Voor mijn ouders.*

PhD thesis, Utrecht University, the Netherlands, July 2015.

ISBN: 978-94-6233-000-9

Printed by Gildeprint.

The work described in this thesis was performed in the Soft Condensed Matter group, part of the Debye Institute for NanoMaterials Science, at Utrecht University.

A digital version of this thesis is available at <http://web.science.uu.nl/SCM/>.

**Cover:**

Digitally colorized SEM micrograph of silica/MPS hetero-dimer particles (chapter 6).

**Overleaf:**

'Academiegebouw' (Nov. 2008), photograph courtesy of B'Rob (Roberto Ruiz).

All rights reserved.

**Chapter pages:**

Artistic impressions of the colloids used in the chapter concerned. Design by M. Kamp.

# Contents

|          |  |            |
|----------|--|------------|
| <b>1</b> | <b>Introduction to patchy particles</b>  | <b>1</b>   |
| 1.1      | Colloids and nanoparticles . . . . .   | 3          |
| 1.2      | Patchy colloids: terminology and classifications . . . . .                     | 4          |
| 1.3      | Experimental studies on patchy particles . . . . .                             | 6          |
| 1.4      | Theoretical studies on patchy particles . . . . .                              | 13         |
| 1.5      | Scope of this thesis . . . . .   | 13         |
| <b>2</b> | <b>Surface freezing transitions of alkane-grafted surfaces</b>                 | <b>15</b>  |
| 2.1      | Introduction . . . . .   | 17         |
| 2.2      | Experimental details . . . . .   | 23         |
| 2.3      | Results & Discussion . . . . .   | 26         |
| 2.4      | Conclusions & Outlook . . . . .  | 39         |
| <b>3</b> | <b>Properties of n-octadecyl-alkane-functionalized silica</b>                  | <b>41</b>  |
| 3.1      | Introduction . . . . .   | 43         |
| 3.2      | Experimental details . . . . .   | 49         |
| 3.3      | Results . . . . .  | 54         |
| 3.4      | Summary & Discussion . . . . .   | 65         |
| <b>4</b> | <b>Synthesis of patchy silica particles with silica or titania protrusions</b> | <b>67</b>  |
| 4.1      | Introduction . . . . .   | 69         |
| 4.2      | Experimental details . . . . .   | 78         |
| 4.3      | Results & Discussion . . . . .   | 83         |
| 4.4      | Conclusions & Outlook . . . . .  | 98         |
| 4.5      | Appendix: Overview of syntheses . . . . .                                      | 99         |
| <b>5</b> | <b>Patch number distributions</b>  | <b>101</b> |
| 5.1      | Introduction . . . . .   | 103        |
| 5.2      | Experimental details . . . . .   | 104        |
| 5.3      | Results & Discussion . . . . .   | 108        |
| 5.4      | Conclusions & Outlook . . . . .  | 115        |

---

|   |            |
|---|------------|
| <b>6 Hetero-dimer particles through site-specific nucleation and growth</b>                   | <b>117</b> |
| 6.1 Introduction . . . . .  | 119        |
| 6.2 Experimental details . . . . .  | 121        |
| 6.3 Results & Discussion . . . . .  | 125        |
| 6.4 Conclusions & Outlook . . . . .   | 135        |
| <b>7 Electric-field-induced directional alignment of hetero-dimer colloids</b>                | <b>137</b> |
| 7.1 Introduction . . . . .  | 139        |
| 7.2 Experimental details . . . . .  | 142        |
| 7.3 Results & Discussion . . . . .  | 146        |
| 7.4 Conclusions & Outlook . . . . .   | 151        |
| <b>8 Selective depletion interactions in mixtures of rough and smooth silica spheres</b>      | <b>153</b> |
| 8.1 Introduction . . . . .  | 155        |
| 8.2 Methods . . . . .   | 157        |
| 8.3 Results & Discussion . . . . .  | 160        |
| 8.4 Conclusions & Outlook . . . . .   | 164        |
| 8.5 Appendix: Supplementary experimental information . . . . .                                | 165        |
| <b>9 Electric-field-induced lock-and-key interactions between colloidal spheres and bowls</b> | <b>167</b> |
| 9.1 Introduction . . . . .  | 169        |
| 9.2 Experimental details . . . . .  | 170        |
| 9.3 Results & Discussion . . . . .  | 175        |
| 9.4 Summary & Outlook . . . . .   | 182        |
| <b>Summary</b>  | <b>182</b> |
| <b>Samenvatting voor een breed publiek</b>  | <b>189</b> |
| <b>References</b>   | <b>195</b> |
| <b>Dankwoord</b>  | <b>210</b> |
| <b>About the author</b>   | <b>215</b> |
| <b>List of Publications</b>   | <b>217</b> |

---



# CHAPTER 1

## Introduction to patchy particles

In this chapter, we introduce colloid science and specifically the field of complex colloids and the concept of patchy particles. A broad overview is given of experimental work which has been carried out on patchy particles in recent years, as well as a short explanation of the practical applications of patchy particles. An introduction to theoretical and numerical studies on systems of patchy particles is also given. Lastly, the scope of this thesis is discussed.

---



## 1.1 Colloids and nanoparticles

Colloids are defined as material particles with a size that is in the range of ~1 nm (molecules) up to several microns in at least one dimension. Such particles are 60-80 times smaller than a human hair, depending on hair type and exact colloid size. These particles cannot be separately distinguished by the naked human eye, but they are still visible by conventional microscopes and other microscopes working with wavelengths in the visual range since they are large enough to scatter light. The term 'colloids' was first coined by Scottish chemist Thomas Graham, who distinguished particles based on whether they were able to pass a permeable membrane [1,2]. Since most of the substances which were unable to pass - such as glue, gelatin and gum arabic - had a glue-like appearance, he named them 'colloids' using the Greek words *κολλα* for glue and *ειδος* for like. Substances which were able to pass the membrane were often of crystalline nature - such as sugar and sodium chloride - hence Graham called these 'crystalloids'. Grahams division into colloids and crystalloids has not survived time, since it was realized that it was merely a difference in size that determined whether the particles could pass the membrane, not related to the crystallinity of the material. However, the difference between solutions (in which the substance dissolves to individual molecules or ions) and dispersions (in which the particles are present as small aggregates of molecules) is closely related to Grahams discoveries.

The upper size limit for colloids is defined by the fact that most particles below this size (depending on weight and dispersion medium) experience Brownian motion. That is, the particles are moved by forces exerted by the molecules of the dispersion medium. Brownian motion was named for Scottish botanist Robert Brown, who studied the motions of grains of pollen suspended in water (published in 1827). The phenomenon was studied earlier by Jan Ingen-housz in charcoal particles suspended in ethanol (published in 1784) and independently by J. Bywater in 1819 [3]. One could even state that the phenomenon was described first by the Greek philosophers: Lucretius (ca. 99 B.C. - ca. 55 B.C.) described the motion of dust in the sunlight in his *On The Nature Of The Universe* (Latin: '*De Rerum Natura*') and even more clearly in his 'Dance of the Atoms', believing it was proof of the existence of atoms [4]. Albert Einstein's famous 1905 paper delivered a theoretical framework for Brownian motion [5], while Marian Smoluchowski published theoretical papers on the matter in the time frame 1904-1907 [3]. A little known fact is that Australian physicist William Sutherland presented theoretical work on Brownian motion - proposing the notion of a diffusion coefficient and deriving the diffusion equation - on a conference in 1904, preceding Einstein, of which the conference proceedings were also published in 1905 [6].

Colloids are present in everyday life, for example in the form of proteins in our blood, soot particles in exhaust and as emulsion droplets in mayonnaise, yoghurt and hand creams. We use colloids in such diverse products as foods, cosmetics, household products, paints and inks.

Thus, colloid science has a very direct link with everyday products. Such dispersed systems consist of a dispersed phase and a continuous phase (medium), and each combination of phases has its own name, such as a foam (gas dispersed in liquid) or an aerosol (solid particles in gas), with the nomenclature first given by Ostwald [7]. Many other terms are used to describe certain types of particles and dispersions - such as 'vesicles', 'micro-emulsions'/'mini-emulsions', 'aerogels'/'hydrogels' - and an elaborate explanation of terms used in Refs. [8,9]. 'Nanoparticles' are sometimes classified as roughly those colloids with sizes (in at least one dimension) below 100 nm. An important reason for distinguishing nanoparticles as a subclass is that quantum effects come into play at this scale. Practical reasons are that nanoparticles fall in the same size range as large molecules and that they need different imaging techniques for observation than larger colloids do.

Soft matter - or soft condensed matter - is the broader field which studies colloids, their phases and interactions, and also granular matter (material of grains larger than the colloid scale, such as sand grains and biological materials). The name of the field refers to the fact that dispersed systems are deformed by little force, even though the individual particles can consist of materials of high hardness. Since physical behaviors of soft matter systems occur on the energy scale of room temperature, many of the systems experience 'self-organization' (organization due to entropy) into structures on the mesoscale, that is, on scales larger than the individual constituents but smaller than the bulk. Soft matter systems can also be subject to out-of-equilibrium mesoscale phenomena, such as turbulence smaller than the system size [10,11].

## 1.2 Patchy colloids: terminology and classifications

Over the last two decades, researchers have been able to create increasingly complex colloids in terms of shape and chemical composition. With this complexity comes a need to group and classify these particles. A very general division of complex colloids was put forward by Yang *et al.* [12]. They divide complex colloids into three classes: shape-anisotropic particles, internally structured particles, and chemically patterned particles.

For a good understanding of the topic of this thesis, 'patchy particles', it is necessary to peruse the notion of *anisotropy*. As its literal translation - 'not uniform in all directions' - indicates, anisotropy implies that some property is directionally dependent. Colloidal particles can obviously be anisotropic in *shape*, such as is the case for rod-like [13] or cube-like particles [14]. On the other hand, anisotropy can also be manifest in the *chemical composition*. A famous division of the various 'anisotropy dimensions' was put forward by Glotzer and Solomon, who distinguished: (A) surface coverage / patchiness, (B) aspect ratio, (C) faceting, (D) pattern quantization, (E) branching, (F) chemical ordering, (G) shape gradient, and (H) roughness [15]. Arguably, one could place properties A-D-F under the header of

chemical anisotropy, while B-C-E-G-H could be considered forms of shape anisotropy. However, particles often exhibit a combination of these anisotropy dimensions. For example, the particles in Ch. 4 have twelve hydrophilic patches on a hydrophobic surface, thus combining properties (A) surface coverage and (E) branching. Notice that the branching property pertains more to chemical composition than to the actual shape of the particle; the particle need not have branches or protrusions. Patchiness amounts to an incomplete surface coverage. Glotzer and Solomon further define a patchy particle as “a patterned particle with at least one well-defined patch through which it can experience a strongly anisotropic, highly directional interaction with other particles or surfaces”. In principle, this definition includes macromolecules with site-specific interactions, such as globular proteins [16]. In this thesis, we adopt Glotzer and Solomon’s definition of patchy particles, but limit it to non-biological, synthetic particles on the nanoparticle or colloid scale.

The topic of patchy particles is very rich and extensive. Many good review papers on these topics have been published in recent years. Already mentioned are the papers by Yang *et al.* on complex colloids in general [12] and by Pawar and Kretzschmar about patchy particle synthesis [16]. A very in-depth review on patchy particles was recently published by Walther and Müller [17], while an earlier review focussing on Janus particles (see below) was published by the same authors in 2008 [18]. A review paper on a more specific topic involving Janus particles is that by Kumar *et al.* [19] about Janus particles at fluid interfaces. Other review papers are those by Perro *et al.* [20], Lee *et al.* [21], Du and O’Reilly [22], Hu *et al.* [23] and Chen *et al.* [24]. A review article on the slightly broader topic of hierarchical organization of colloidal particles was published in 2007 by Edwards, Wang and Möwald [25].

Janus particles are the most elementary type of patchy particles, namely particles consisting of two halves of different chemical or physical properties. The term refers the two-faced Roman god Janus - god of beginnings and endings, guard of the doors of heaven, and namesake of the month January. The term was first coined in a paper by Casagrande and Veyssié [26], but gained popularity after Pierre-Gilles de Gennes’s Nobel Lecture in 1991 [27]. Incidentally, Casagrande and Veyssié mention de Gennes as the person suggesting the study to them. This is not to say that the notion of Janus particles had not been around - in fact, an electronic display with granular Janus particles had already been invented [28] in the 1970’s - but this suitable name helped to gain awareness on the topic. Examples of properties that can differentiate the two hemispheres in a Janus particle are: a hydrophilic/hydrophobic surface, a charged/unchanged or positively/negatively charged surface, a contrasting refractive index or dielectric constant, a rough/smooth surface, or a sticky/non-sticky surface. In the case of one hydrophobic and one hydrophilic hemisphere, Janus particles are the colloidal analogue of a surfactant. An interesting difference between Janus particles and surfactants stressed by Pierre-Gilles de Gennes in his Nobel lecture is that assemblies of (spherical) Janus particles at

an oil/water interface are permeable thanks to the interstices between the particles, whereas membranes of surfactants are rather impermeable [27].

## 1.3 Experimental studies on patchy particles

### 1.3.1 Janus particles: synthesis methods

#### 1.3.1.1 Classic Janus particles

A simple method to produce Janus particles is masking one hemisphere and modifying the other hemisphere with some agent. This course was taken by Casagrande and Veysié. Glass beads were partially masked with cellulose tannish and modified with octadecyltrichlorosilane. They proceeded to show that such Janus beads preferentially reside at the oil/water interface so as to reduce the total interfacial energy. Hong, Jiang and Granick later introduced a masking method for producing Janus particle in higher quantities [29]. In their scheme, colloids are thoroughly mixed with wax and water at elevated temperature, so that a Pickering emulsion forms (consisting of molten wax in water stabilized by colloids). The wax 'colloidosomes' remain stable upon cooling, hence the colloids at the wax surface can then be modified on the exposed side and then released by dissolution of the wax in chloroform. The method has a somewhat lower effective yield since the colloidosomes are prone to losing colloids upon handling. In a later article from the same group, a solvent-free synthesis modification route by means of vapor phase modification is described to alleviate that problem [30]. Similar work was performed by Perro and coworkers, who instead studied particles of smaller size [31]. They also improved the relative quantity of particles that were absorbed at the wax-water interface; that is, the efficiency was increased.

Janus particles can also be obtained by depositing a thin layer of metal onto a monolayer of particles through for instance chemical vapor deposition (CVD). An early study on this method was performed by Takei and Shimizu [32]: gold was deposited onto latex spheres, and the golden hemispheres were selectively modified with thiol-groups. A technique for Janus particle production closely related to CVD is microcontact printing, in which a PDMS stamp with water-insoluble molecules is used to print a layer of those molecules onto a monolayer of colloidal particles. This technique was exploited by Cayre *et al.* [33], showing that the printed side of the Janus particle could be preferentially dyed with fluorescent molecules. They made the first steps towards self-assembly of Janus particles by creating dimers and raspberry particles. Finally, capillary fluid flow techniques such as microfluidics [34] and electrohydrodynamic co-jetting [35] are excellent for making Janus particles of two immiscible monomers, which can then polymerize and form the two halves of a Janus particle. The particles created by microfluidics [36] or co-jetting are often in the granular regime (40-100  $\mu\text{m}$ , [16]), or in the colloidal regime but are then more polydisperse [37].

### 1.3.1.2 Extended versions of Janus particles

The concept of a standard Janus particle can be extended to more complex Janus particles by changing the particle shape or the amount of surface coverage. Casagrande and Veyssié already speculated about the adsorption behavior of asymmetric Janus particles - i.e. those with a patch that does not cover the entire hemisphere - in their 1989 article [26]. Such particles could easily be realized in their masking method by changing the height of the tarnish masking layer, and Veyssié published about it in the following year [38]. Jiang and Granick, moreover, could simply change the 'Janus balance' of their Janus particles by adding various concentrations of surfactant to the emulsions: the colloids sink deeper into the wax with more surfactant added [39]. Liu *et al.* have utilized the wax emulsion method on amine-functionalized particles in combination with etching, resulting in mushroom-shaped particles with an amine-functionalized head [40]. When Janus particles are produced by CVD or rather glancing-angle deposition (GLAD), one can readily vary the opening angle of the hydrophobic patch by changing the angle of incidence [41], or vary the shape of the patch by rotating the substrate [42]. The Granick group also produced triblock Janus particles (with patches on both sides) by GLAD [43], but since this particle is in fact a patchy particle it will be discussed in paragraph 1.3.3.

Another generalization of the Janus particle is the Janus dumbbell: a particle consisting of two attached spheres with different properties. A beautiful example was published by Kraft *et al.*: Janus dumbbells with a rough and a smooth sphere. Under the addition of a depletant smaller than the size of the roughness, these particles self-assembled into colloidal micelles, since the depletion attraction experienced between the rough sides is much smaller than between the smooth sides [44]. Incidentally, Badaire *et al.* already employed roughness on the round side of SU-8 cylinders to create preferential stacking along the cylinder axis; such particles are essentially two-patch particles [45]. Another nice example of a Janus dumbbell and its behavior was described by Nagao *et al.* [46]. They synthesized polymer dumbbells with a silica or titania core incorporated in one of the lobes. Silica and titania have a much higher dielectric constant than polymer, causing interesting behavior of the particles when brought in an alternating electric field. For example, the Janus dumbbells with an amorphous titania core oriented perpendicular to the field at low (kHz) frequencies but parallel to the field at high (MHz) frequencies. Janus dumbbells with spheres of different chemical properties at the surfaces can also be obtained by swelling surface-functionalized polymer particles with a monomer until they overload and form a (polymerizable) second, non-functionalized lobe. This approach was for instance taken by Kim and coworkers [47] (who produced dumbbells with a polystyrene side and a PEI-modified side) and by van Ravensteijn *et al.* [48] (who produced polystyrene dumbbells with a chlorinated lobe which can be further modified using click chemistry). Sacanna and coworkers developed a method in which an oil droplet (of a

polymerizable silane) nucleates onto a pre-existing particle and is hardened with the help of an initiator. Most notably, they embedded single hematite cubes into an organosilica sphere [49]. Since hematite is weakly ferromagnetic at room temperature, the particles can self-assemble through directional magnetic bonds in an aqueous salt solution. Magnetic fields can be used to disassemble the structures.

Another example of Janus particles with non-spherical shape are Janus rod-like particles. Janus rods consisting of two different consecutive pieces were prepared by He *et al.* [50]. These rods were prepared using the method for growing silica rods introduced by Kuijk *et al.* [13]. These Janus rods also formed colloidal micelles with the hydrophobic tails inwards or outwards depending on the solvent. Janus rods with a very short hydrophobic tip - dubbed colloidal matchsticks - were produced by Chaudhary *et al.* by the CVD method [51]. These matchsticks self-assembled into bipods, tripods and tetrapods in an aqueous salt solution. Janus particles with the Janus property along the direction parallel to the rod were studied in a paper by Yan *et al.* [52]. The particles were prepared by sputtering nickel onto one half, thus making the rods magnetic on one side. These dipolar Janus rods form interesting ribbon structures, which in turn form rings in a weak magnetic field. Janus particles with the dividing planes along the long axes of the rods have already been produced by the Solomon group through an entirely different method. Ellipsoidal rods are prepared from polystyrene which are embedded in a PVA polymer and the layer is stretched out, and finally gold deposited on a monolayer of rods [53]. They found that the Janus rods form bundles with preferential bonds between of the gold patches at low (2.5 mM) salt concentrations. What is more, by reversing the order of gold deposition and film stretching, they also obtain Janus 'kayak' particles with a very small gold patch in the middle. These particles still have a strong patch-to-patch bonding but lower directional order due to the patch shape.

Finally, several synthesis routes have been presented for the preparation of Janus cap-like particles. Tang *et al.* prepared Janus caps with an amino- or octadecyl-modified convex side *via* the synthesis of patchy particles [54]. After synthesis of hollow polystyrene spheres, a silane was added, and forms bulges by phase separation from the polystyrene. The number and the size of these bulges could be adjusted by the ratio of polystyrene monomer and silane agent. The organosilica cap-shaped bulges can be released by dissolution of the polystyrene. A preceding modification step of the composite patchy particles with a silane would result in caps with a Janus property.

### 1.3.2 Particles with multiple patches: synthesis methods

Several authors have tried to categorize the various synthesis techniques for particles with at least two patches [16, 17]. The following division is loosely based on Pawar and Kretzschmar's work [16].

Firstly, templating/masking techniques such as (a) modification of wax Pickering emulsions and (b) CVD on particle monolayers have already been mentioned. The former technique is difficult to extend to making particles with two patches, but double emulsions might offer a possibility [16]. The CVD technique can form triblock particles when it is combined with a technique to inverse the particle monolayer after the first metal deposition. For instance, the particle monolayer can be inverted using a PDMS stamp. This technique has been widely employed in the Granick group, see section 1.3.3. A second interesting variation of particles they prepared is an asymmetric triblock particle, with one patch larger than the other [55,56]. As a result of the patches' size difference, one patch has a valency of 1 and the other a valency of 2. The particles form Y-shaped bonds, leading to self-assembled two-dimensional layers with room to shift rows of particles (floppiness). Möhwald *et al.* obtained particles with two to five ordered small gold patches by evaporation of gold onto thin crystalline layers of polystyrene microspheres [57]. The upper two layers of particles were then stripped off with tape, and in that way the patches on top of the third layer could be imaged by electron microscopy. By stripping this layer off as well, the patches on the bottom of the particle layer were also investigated.

An entirely different technique for patchy particle synthesis utilizes colloidal clusters. A recent study by Demirörs *et al.* employed attractions between oppositely charged colloids combined with long-ranged repulsions to form clusters with different charges on the core particle and the patches [58]. Other techniques are based on emulsions: clusters are formed by first emulsifying a mixture of water, oil and colloids. The colloids reside in the emulsions droplets, so subsequent evaporation of that dispersed phase will yield small colloid clusters. These clusters are not in and of themselves patchy. However, when the colloids themselves are of different materials, the clusters will have lobes of dissimilar chemical and physical properties. This course was taken by Cho *et al.* [59], who combined silica and polystyrene spheres. Alternatively, small particles are introduced in the emulsion droplets to form a layer of contrasting surface properties around the clusters. For instance, Cho and coworkers also combined sulfonated polystyrene microspheres inside the emulsion droplets with silica nanoparticles, gold nanoparticles or polystyrene homopolymer [60]. After evaporation of the emulsion droplets, the clusters of polystyrene spheres became partially enveloped by the smaller species, thus yielding hydrophilic particles with hydrophobic patches. Y. Wang *et al.* likewise used colloidal clusters, but the starting material consisted of amidated polystyrene particles. They covered the major parts with non-amidated polystyrene with the help of a swelling agent [61]. The amidated patches could be modified with biotin and eventually with DNA. Conveniently, DNA attaches only to complementary DNA strands, so the researchers achieved preferential bonding between particles with different DNA marking. Therefore the particles have a 'valency' and can form the colloidal analogue of molecules,

such as ethylene, *cis/trans* molecules and copolymers. Sacanna *et al.* allowed a hydrolyzed silane (3-methacryloxypropyltrimethoxysilane, MPS) to nucleate onto polystyrene colloidal clusters [62]. After condensation of the MPS, patchy particles with positively or negatively charged polystyrene hydrophilic patches on a hydrophobic body were obtained. This nucleation procedure is very versatile, as the seed particles can be varied in shape, size and chemical composition.

In contrast to the above researchers, Kraft and coworkers [63] took a bottom-up approach: they created cross-linked polymer particles with a liquid protrusion, which were then allowed to coalesce. The central liquid droplet of the particles could then be polymerized as well using an initiator. Typically, 10% of dimers and 1% of higher multimers were formed in 24 hours. Later, Kraft also established that the bond angle between the seed particles - which form the patches - can be adjusted reliably by adjusting the size of the liquid protrusions which will form the central sphere [64]. An advantage of all methods mentioned in this and the previous paragraph is that synthesis can be done in bulk rather than on a (semi) two-dimensional substrate as in masking/templating techniques. They also share a disadvantage: there is little control over the number of patches, because it depends on either the number of colloids that end up in each droplet (Cho, Sacanna, Wang) or the number of particles that coalesce (Kraft). Hence, centrifugation techniques are needed to separate particles of a specific number of patches.

Methods based on particle lithography give more control over the number of patches. Particle lithography methods are those which employ as a mask the contact region of a particle with a surface or with other particles. The size of the patch may be controlled by the particle size, and the size of the modifying agent (as this size determines how close the agent can approach the contact point). An early one-patch example was published by Snyder *et al.*, who adsorbed positively-charged polystyrene spheres on a negatively charged glass surface, and decorated the exposed particle surface with a negatively-charged polyelectrolyte [65]. Similarly, Chastek *et al.* coated monolayers of polystyrene spheres with polyelectrolyte [66]. The presence of patches on the spheres could be proven: small particles with a charge of a sign opposite to that of the polystyrene core particles would selectively stick to the patches. Particle lithography can also be applied to entire colloidal crystals. This not only allows for multiple patches, but more importantly constitutes one of the few bulk methods for patchy particle synthesis which do not require a density gradient centrifugation step. The prime example is the one first published by L. Wang *et al.* [67]. They demonstrated that the contact areas in the colloidal crystal were not modified by (a) growing silica onto the non-modified patches in the case of silica particles and (b) by growing polystyrene onto the modified (sulfonated) regions outside the contact areas in the case of polystyrene particles. Their method (a) is amply explored in this thesis. Braun *et al.* employed this method to

create PEG-silane patterned particles. Silver particles were fixed to the non-modified patches, and a patch-patch attraction was brought about by introducing dithiols to the system, as dithiols link the silver particles together [68]. Kamalasanan *et al.* recently published on templating a 2D array of colloidal polystyrene particles, resulting in patchy particles with six protein labeled patches [69].

Finally, microfluidics has been used as a tool to create patchy particles, for example particles with 3 to 6 compartments in a beach ball configuration [70], but with a size in the granular regime these are beyond the scope of this thesis.

### 1.3.3 Applications of patchy particles

#### 1.3.3.1 Applications in industry

Janus particles have found their way towards industrial application, thanks to fabrication processes which allow for larger scale production. In fact, the first electronic paper called *Gyricon* was based on granular Janus particles [71]. It was patented already in 1978, before the term Janus particle became popular [28]. Other purposes for Janus particles that are currently being explored experimentally are water-repellent textile [72] and chemical sensors and oriental probes [73] [16]. Janus particles can potentially attach selectively to a drug destination site. Experimental [74,75] and theoretical [76] studies on medical applications are ongoing. Patchy particles with multiple patches are currently used in fundamental research only, due to their more involved synthesis and characterization. Possible applications include those for Janus particles, targeted drug delivery and electronics, and also selective membranes [43].

#### 1.3.3.2 Applications of Janus particles in fundamental research

Janus particles have already generated immediate fundamental results in the form of new structures and new behavior. Park *et al.* studied the behavior of Janus particles (produced by CVD) at the oil/water interface [77]. They showed that the undulation of the contact line about the Janus border introduces quadrupolar capillary forces, which cause attraction between the particle that result in open aggregated networks. Chen *et al.* demonstrated that Janus particles can self-assemble into chiral clusters and triple helices [78].

Janus particles also offer the opportunity to study the orientation of individual colloids; they can display 'lunar phases' with respect to the viewing angle. In collaboration with the Granick group, Anthony and Kim presented experimental methods (differential interference contrast microscopy, DIC) and image analysis methods to measure the orientation of metal-coated Janus colloids in situ [79].

Janus particles exhibit interesting behavior in electric fields as well. Takei and Shimizu demonstrated that gold-coated Janus spheres can undergo electrophoretic motion in a DC

electric field, with the positively charged gold surface reorienting towards the negative electrode. Perhaps more unexpected is the effect that in an AC field, Janus particles will propel in the direction perpendicular to the field [80–82]. In an alternating field (with a frequency below the Maxwell-Wagner limit, see Ch. 7), the Janus particles have no time to orient towards a pole. Instead, an effect called induced-charge electro-osmotic flow (ICEO) around the most polarizable hemisphere causes the Janus particles to orient with their equator along the field [83]. Subsequently, the faster ICEO fluid flow at the conducting side causes the particle to move in the direction perpendicular to the field [83]. Boymelgreen and coworkers showed that fixated Janus gold/polystyrene doublets can also be oriented perpendicular to the field direction in an AC field.

Logsdail and Johnston performed a theoretical study of the optical properties of bimetallic Au-Ag Janus nanoparticles, employing the discrete-dipole approximation [84]. They predicted that the extinction coefficient of light at 350 nm is significantly higher (namely by a factor 2.5 at this wavelength) for Au-Ag Janus particles than for Au@Ag or Ag@Au core-shell particles. The effect was attributed to the larger division between the materials of higher and lower dielectric constant. The electric field strength in the gold hemisphere was dependent not only on wavelength but also on the orientation of the Janus particle in the field. For example, the Au hemisphere could dampen resonances created on the Ag side.

Janus particles with a patch with catalytic properties can be made to self-propel, since the catalytic reaction at the patch will induce diffusiophoresis. Such self-propelling particles are often called swimmers. A typical catalytic reaction is the degradation of hydrogen peroxide by catalysts such as titania [85], platinum [86], or hematite [87]. The organosilica particles with a hematite patch by Sacanna and coworkers have been used as colloidal *surfers* [87]. The particles surf on the osmotic flow created at the silica substrate above which they reside. Due to imperfections in the particles, they do not stay stationary on this flow, but turn and move parallel to the surface. The particles exhibited crystal formation due to the attraction between particles attributed to their phoretic motion.

### 1.3.3.3 Applications of patchy particles in fundamental research

Patchy particles allow the study of directional interactions. As a result, they can act as model systems for other systems with directional interactions. For instance, many researchers conduct (experimental and computational) studies on patchy particles as models for protein globules and polyoxymetalates, which also have specific attractive sites [88–91]. Understanding the aggregation of proteins is even very relevant for food products [92]. The study of patchy particles has also helped in understanding the phase behavior at low volume fractions of a particular kind of industrial clay particles called Laponite [93, 94].

As mentioned previously, the Granick group demonstrated that triblock Janus particles

self-assembled into open network structures called ‘kagome’ lattices via the hydrophobic interaction between the patches [43]. The kagome lattice is a non-close-packed structure with large holes and small holes. Kagome lattices had been observed almost a decade before, namely in binary colloidal crystal grown via layer-by-layer deposition [95], however not yet by self-assembly. Conveniently, the large patches on the triblock Janus particles fitted the patches of two other triblock Janus particles. Effectively, the triblock particles acted as particles with four diagonally aligned patches, which would take longer to align by self-assembly. Directly after salt addition, the system started forming doublets, triplets and strings. The kagome lattice formed slowly over the course of two days from metastable intermediates; chunks with ordering close to the kagome lattice. The hydrophobic attraction of  $10k_B T$  per contact allows for correction of defects in the final structure. The researchers even observed stacking of kagome sheets. Sciortino and coworkers performed numerical simulations of two-patch Kern-Frenkel model particles to investigate the phase diagram of such triblock Janus particles, and indeed the phase diagram contained a kagome phase [96–98]. With an eye on possible applications, it is interesting that the kagome lattice has two pore sizes, with the smaller pores surrounded by hydrophobic patches and the larger pores bordered by the hydrophilic charged parts of the triblock Janus particles. These kagome lattice might be applicable as size-selective filters.

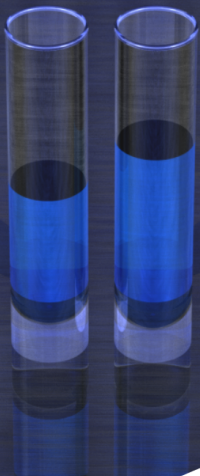
## 1.4 Theoretical studies on patchy particles

In the field of patchy particles, theoretical and numerical results have been ahead of experimental realizations, due to the difficult synthesis methods for patchy particles. Such work is especially important in order to better understand self-assembly pathways. The body of theoretical and numerical work is too large to discuss in adequate detail here, but review papers on the topic are for example Refs. 15, 16, 99–103.

## 1.5 Scope of this thesis

In this thesis, the synthesis and characterization of various new types of patchy particles are presented, as well as investigations on often-used interactions to self-assemble such patchy colloids. The present chapter contains an overview of the current state of experimental and theoretical research on patchy particles. Chapters 2 and 3 contain investigations on surface-grafted silica with the aim of understanding the properties of these silica surfaces for use in systems of patchy-particles; the chapters treat measurements of the surface freezing transition via capillary rise experiments, and by measurements of the pair potential via 2D radial distribution functions, respectively. In Chapters 4 and 5, we discuss the synthesis, characterization, and self-assembly of a system of patchy particles consisting of a silica core

particle and up to twelve hemispherical silica or titania protrusions, prepared by surface-grafting close-packed colloidal crystals of silica colloids. Chapters 6 and 7 present a new system of silica/MPS hetero-dimer particles of acorn-, dumbbell- and lollipop-shape, as well as the self-assembly of these particles in an electric field. Chapter 8 is dedicated to studying the influence of surface roughness on depletion attractions between spherical particles, since suppression of depletion attraction by surface roughness is an often exploited self-assembly method for patchy particles. Finally, in Chapter 9 we discuss a new synthesis route to create silica/siloxane or PS/siloxane composite particles by electric-field-induced lock-and-key interactions.



## CHAPTER 2

# Surface freezing transitions of alkane-grafted surfaces

A surface freezing transition is the freezing of a layer of (possibly grafted) molecules on a surface or interface. In surface-grafted colloids, such a freezing transition leads to a gelation transition from a dispersion to a gel phase because of the increase in van der Waals forces. An example of such a system are octadecanol-grafted silica colloids in hexadecane, but other alkane-grafted silica surfaces are expected to possess a similar surface-freezing transition and change of contact angle, which is caused by the leap in density of the alkane layer and thus a jump of surface tension. This gelation transition offers a potential mechanism to obtain a temperature-switchable attraction between the patches on patchy particles. However, in such a system not only the patches need a grafting layer (for reversible sticking) but also the rest of the particle surface (for steric stabilization). For instance, alkane chains of different length could be used on the patch and on the rest of the particle surface. In this chapter, we measured transition temperatures of alkane solvents on borosilicate surfaces grafted with silane coupling agents of varying chain lengths. These transition temperatures were measured as a change in contact angle through the capillary rise method, which exploits the fact that the height of the fluid column in a capillary is directly proportional to the cosine of the contact angle. The onset of the freezing transition in OTMOS-grafted capillaries was found to increase from 20 °C to 30 °C as the solvent chain length increased from 14 carbon atoms (tetradecane) to 18 carbon atoms (octadecane). Likewise, the gelation transition for colloidal particles can be tuned with the choice of grafted chain length, which was also confirmed experimentally. We conclude that there exists a window for which the patches will stick but the rest of the surface will remain repulsive.

---



## 2.1 Introduction

Octadecanol-grafted silica particles (also called: 'stearyl-silica', since stearyl alcohol is an alternative name for octadecanol) undergo a temperature-dependent transition from a gel phase to a dispersed phase in solvents such as hexadecane and toluene [104–106]. While the nature of the transition in toluene is rather poorly understood, the transition in hexadecane is known to be induced by solvent molecules, which can interdigitate with the grafted molecules on the silica surface and induce crystallization of only one layer of solvent molecules in/onto the grafted layer [105–107]. This surface freezing transition happens a few degrees above the bulk freezing point, since the surface-grafted molecules have a lower degree of freedom than molecules in the bulk. In this crystalline limit, the stabilizing effect of the grafted layer vanishes (as the density increases, so do the effective van der Waals forces) and particles form a gel. Such a grafting with a freezing transition is interesting for patchy particles, with an eye on temperature-dependent patchy interactions. The surface freezing can be detected on grafted macroscopic surfaces by a change in contact angle. In this chapter, we study the change in contact angle of solvents on grafted surfaces as a function of temperature, for various surface graftings and various alkane solvents. Most graftings were found to exhibit a surface-freezing transition. Alkane-grafted silica particles were used to verify that this surface freezing transition also results in a gelation transition in colloids.

### 2.1.1 Surface freezing of stearyl-silica

Silica functionalized with stearyl alcohol can be dispersed in apolar solvents such as hexane. Good solvents for such silicas are those that solvate the alkyl chains, while in bad solvents the alkyl chains will prefer contacts with each other over contact with the solvent molecules, hence steric stabilization disappears [108]. A reversible coagulation has been observed for such dispersions upon cooling. For example, Rouw *et al.* mention a reversible coagulation at a transition temperature of  $-18^{\circ}\text{C}$  for stearyl-silica in n-dodecane [109]. For stearyl-silica in hexadecane, studies by Roke *et al.* [105, 106] evidenced that the primary cause of this coagulation is the freezing of the monolayer of alkyl chains at the particles' surface below a certain transition temperature. Steric stabilization thus vanishes and the particles coagulate mainly due to van der Waals attraction. The flocculation can be reversed by lifting the temperature above the transition temperature. Some bridging of solvent molecules between the grafting layers colloidal particles may occur, but not as a primary source of flocculation.

Among the first authors to make mention of the molecular origin of this behavior were Riedo *et al.* [110], who measured contact angles for silica modified with R-alkyl-dimethylsilanes. They remarked for the range of silanes with tetradecyl to docosyl chains that: "There seems to be a transition temperature below which the surface is less wettable". Ocko *et al.* investigated surface freezing films of alkanes (of several angströms thickness) and measured the temperature range above the bulk freezing point over which a frozen surface layer exists [111]. For stearyl alcohol they measured a bulk freezing point of  $29.33^{\circ}\text{C}$ , and a surface freezing up to  $2.05^{\circ}\text{C}$  above the bulk freezing point. Hence, an educated guess for the transition temperature of stearyl-grafted silica in an alkane solvent could be approximately  $31^{\circ}\text{C}$ . Roke *et al.* reported a transition range between

24.7 °C and 34.0 °C for dispersions of stearyl-grafted silica in n-hexadecane of various volume fraction (although no monotonous relationship between the volume fraction and the transition temperature was established) [105]. In accordance with these results, Eberle *et al.* [112] have reported transition temperatures in tetradecane of 28–32 °C for stearyl-grafted silicon wafers and of 27–31 °C for silica particles, with the latter volume fraction dependent.

Roke and coworkers performed extensive studies to link the macroscopic properties of stearyl-grafted silica dispersions to microscopic changes in the surface molecular layer of the silica [105, 106]. They employed turbidity and calorimetry measurements to probe the macroscopic dispersion properties and the surface-specific vibrational technique of sum-frequency generation (SFG) scattering for studying the microscopic properties of the alkyl chain layer. SFG yields information on the microscopic properties due to the following. In gel state, the SFG spectra are dominated by the symmetric and asymmetric methyl (CH<sub>3</sub>) stretching modes, as the methylene (CH<sub>2</sub>) vibration is restricted in the crystalline layer of alkyl chains. On the other hand, in the fluid state the CH<sub>3</sub> modes are below the detection limit due to the isotropic orientational distribution of the methyl groups but there is a faint signal of the methylene (CH<sub>2</sub>) groups as a result of their anchoring to the surface. Turbidity measurements give insight into the microscopic structure; the cloud point of a dispersion is the temperature below which a dispersion is turbid, and as such marks the transition from the gel to the fluid state upon temperature rise. Turbidity measurements revealed a cloud point of 310K (37 °C) for stearyl-grafted silica in hexadecane. The integrated SFG intensity already decreased by an order of magnitude from 293K (20 °C) onwards. Thus, the transition on the microscopic scale (from a crystalline to a disordered alkyl chain layer starting at 20 °C) coincides with the transition on the macroscopic scale (from an aggregated gel via aggregates the size of the wavelength of light at 37 °C to a dispersion). Moreover, calorimetry revealed a peak in the heat uptake in the same temperature range. This heat uptake scaled with the particle size and, secondly, did not occur in a solvent in which stearyl-grafted silica does not exhibit gelation, hence Roke *et al.* were able to conclude that this heat uptake is solely due to the configurational change of the surface alkyl layer and not to the colloidal gelation itself. The freezing of surface alkyl chains from a disordered state to a crystalline state is accompanied by release of heat. The surface grafting density reported by Roke *et al.* for their stearyl-silica was ~1 group/nm<sup>2</sup> [106]. The grafting density is filled up to the crystalline monolayer density by interpenetrating solvent molecules during the surface freezing transition [106]. Roke and coworkers found that grafted molecules comprised about one third of the total amount of molecules at the surface (32 ± 5 %) [105].

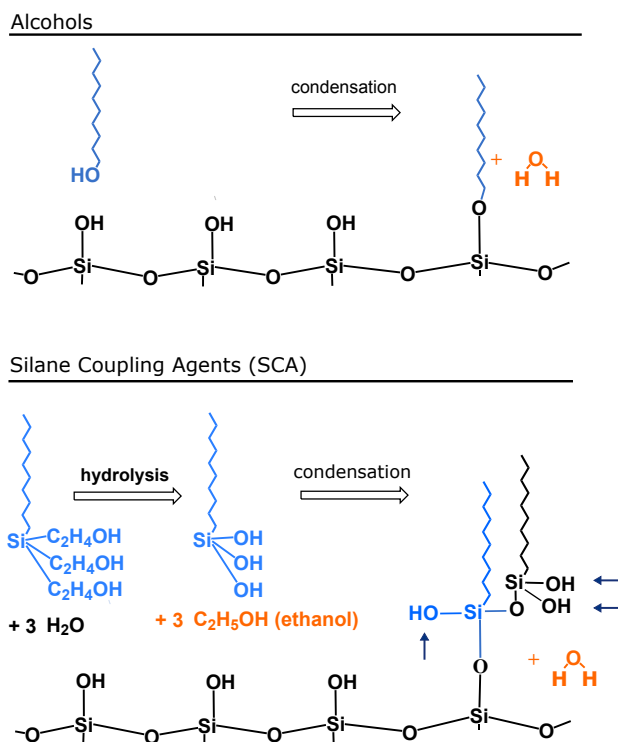


**Figure 2.1:** Schematic representation of the reactions involved in the grafting of alcohols and silane coupling agents (with multiple (m)ethoxy groups) to the silica surface. Notice that silane coupling agents (with multiple (m)ethoxy groups) can undergo further 'branching': the blue arrows indicate groups which can undergo a condensation reaction. Thus, for SCAs the packing density of alkane chains may be larger than the grafting density of SCA molecules to the surface. Molecules indicated in purple denote reaction products expelled in the hydrolysis and condensation steps.

Studies on the wetting behavior (around the surface freezing transition temperature) have not only been carried out for grafted alkanes, but also on silanized surfaces. Silanized surfaces are silica surfaces treated with silane coupling agents (SCAs), which are molecules with a central silicon atom, one or more organic chains, and one or more (m)ethoxy groups that can bond with the OH groups of the silica surface (see Fig. 2.1). Riedo *et al.* were already mentioned before in this regard. Montgomery and Wirth investigated the wetting of silica plates grafted with an SCA with protruding methyl groups (chlorodimethyl octadecyl silane) by alcohols of various chain lengths. The study revealed through infrared spectroscopy that long-chain alcohols form a submonolayer with the alcohols' chains interpenetrating in the frozen  $C_{18}$  monolayer [107]. Apparently, these silanized surfaces allow interdigitation of solvent molecules similarly to stearyl-grafted silica wetted by *n*-hexadecane. Montgomery and Wirth moreover employed fluorescence anisotropy of a hydrophobic probe molecule *p*-bis(o-methyl)-styrylbenzene to measure the angle of the grafted chains with the

surface normal in various solvents. This average tilt angle gradually diminished with alcohol chain length, from  $54.8^\circ \pm 0.2^\circ$  in heptanol to  $52.9^\circ \pm 0.2^\circ$  in decanol ( $79.6^\circ \pm 0.4^\circ$  in water). Roke *et al.* found a comparable tilt angle for stearyl-grafted silica wetted by n-hexadecane:  $52.5^\circ \pm 5^\circ$ . On a similar note, Eberle *et al.* found that the surface monolayer in frozen state (at  $25^\circ\text{C}$ , when the grafting molecules are straight) was  $1.3 \text{ \AA}$  thicker than in liquid state (at  $40^\circ\text{C}$ , when the grafting molecules can bend and explore more configurations) [112]. Chain length is very important for the wetting angle as well. Fadeev and McCarthy [113] showed for n-alkyldimethylsilanes modified surfaces that the water wetting angle is  $\sim 105^\circ$  independent of chain length, indicating that water does not penetrate the alkyl chain layer, yet the hexadecane contact angle at room temperature decreases steadily with chain length  $n$  until complete wetting ( $\theta = 0$ ) is reached for  $n = 12$ . They also studied contact angles for a wide range of (short) branched alkylchlorosilanes and hysteresis of the contact angles. Generally, the water contact angles are much lower for these branched alkylchlorosilanes, because of the denser packing of end groups. Finally, Fadeev and McCarthy mention an anomalous temperature-dependent change of the contact angle of hexadecane on surfaces modified with alkyldimethylsilanes for carbon numbers  $n = 18$  and higher, that is, they suggest that a surface freezing transition not only exists for alcohol-modified surfaces but also for silane-modified surfaces.

Finally, an interesting question is what transition temperatures and contact angles arise for surfaces of mixed grafted alkyl chains. The Israelachvili equation (Eqn. 2.1) can be employed to predict contact angles for mixed surface-grafted layers, which is more accurate than the Cassie equation (Eqn. 2.2) whenever the sizes of the domains of different chemical composition approach the size of the molecules. For example, Fadeev and MCarthy predicted a contact angle  $\theta_1 = 104^\circ$  for methylsiloxy groups ( $\theta_1 = 110^\circ$ ) and dimethylsiloxy groups ( $\theta_2 = 101^\circ$ ) in a 1:1 ratio; this predicted contact angle was close to the experimentally determined value of  $102\text{-}105^\circ$  for trimethylchlorosilane treated surfaces [113].

$$[1 + \cos(\theta)]^2 = f_1[1 + \cos(\theta_1)]^2 + f_2[1 + \cos(\theta_2)]^2 \text{ with } f_1 + f_2 = 1 \quad (2.1)$$

$$\cos(\theta) = f_1 \cos(\theta_1) + f_2 \cos(\theta_2) \text{ with } f_1 + f_2 = 1 \quad (2.2)$$

Stearyl-grafted silica not only gel below a transition temperature when dispersed in alkanes, but also in benzene, toluene or carbon tetrachloride. For example, Jansen *et al.* observed strongly increased turbidities in 5%w/w stearyl-silica dispersions in benzene below  $40^\circ\text{C}$ , in toluene below  $10^\circ\text{C}$ , and in xylene below  $-10^\circ\text{C}$  [108]. Gelation in such solvents is weaker than in alkanes, for it only appears at higher particle volume fractions [105], and also occurs over a much broader transition temperature range than in alkanes [105, 109]. Rouw *et al.* mention that the interaction in benzene and toluene must be due to local interactions between the stabilizing chains and the solvent molecules [109], since these solvents cannot interdigitate with the surface layer. In other words, it is a result of bad solvation of the grafting layer, rather than a surface freezing effect.

## 2.1.2 Contact angle measurements

A contact angle is the angle under which a fluid droplet contacts a surface, as measured through the fluid. The contact angle  $\theta$  satisfies a force balance: it depends on the three surface tensions between liquid-air  $\gamma_{LA}$ , solid-air  $\gamma_{SA}$ , and liquid-solid  $\gamma_{LS}$ , according to Young's equation:

$$\gamma_{SA} + \gamma_{LS} = \gamma_{LA} \cos(\theta) \quad (2.3)$$

In practice, when placing a droplet on a surface, the contact line will be pinned, and there will be a range of contact angles as the volume of the droplet is increased or decreased. The maximum contact angle is called the 'advancing contact angle'  $\theta_A$  and the minimum contact angle is called the 'receding contact angle'  $\theta_R$ . When the maximum contact angle is reached but more liquid is added to the droplet, the contact line will shift but the contact angle will remain stable at  $\theta_A$ . The difference  $\theta_A - \theta_R$  is called the contact angle hysteresis.

The simplest way to measure a contact angle is by placing a droplet on a surface, photographing the droplet's profile, and measuring the angle on the picture. Measurement methods based on this principle are called 'sessile drop methods'. Similarly, the surface tension  $\gamma$  can be calculated from a drop hanging from a surface - these are called 'pendant drop methods'. A pendant droplet of diameter  $d_e$  and neck width  $d_s$  and density  $\rho$  satisfies the relation  $\gamma = \rho g d^2 / H$ , with  $H$  a correction factor determined from  $d_s$  and  $d_e$ . An alternative method for measuring contact angles is the Wilhelmy plate method. In this method, a plate is suspended vertically in a liquid. A force  $F$  is applied to the plate to pull it upwards. The liquid will stand up to the plate under a contact angle  $\theta$  and along its perimeter  $2L$ . When  $\gamma$  is known, the contact angle is calculated from the force using the formula

$$\gamma = \frac{F}{2L \cos(\theta)} \quad (2.4)$$

Review articles of measurement techniques for contact angles and surface tensions are for example Refs. [114–116]. A previous study on the contact angle of water and hexadecane on silanized surfaces was performed by Fadeev and McCarthy [113]. An extensive study on contact angles of surfaces grafted with R-alkyldimethylsilanes has been carried out by Riedo and coworkers [110].

In this chapter, we investigate the contact angle of alkanes on octadecanol-grafted and R-alkyltri(m)ethoxy-grafted silica surfaces as a function of temperature, including the influence of surface-freezing transitions on this contact angle. Previous researchers performed studies on R-alkyldimethylsilylated surfaces [110] (but not on R-alkyltri(m)ethoxysilylated silica) or on stearyl-grafted silica surfaces while indicating a transition temperature as a single value (i.e. the transition was not studied as a function of temperature) [105, 106]. In principle, the freezing transition as a function of temperature can be studied by closely observing the gelation transition (aggregation and redispersion under the influence of temperature changes) of alkane-grafted silica particles in alkane solvents. However, theoretical studies showed that the phase diagram of hard-sphere particles with a short-range attraction is dependent on the total volume fraction when the particles are polydisperse [108, 117]. Since, in practice, spherical particles always carry some polydispersity and patchy particles with protrusions even more, it is difficult to study the influence of temperature by observing

gelation. Verduin and Dhont, using both theoretical and experimental measurements, also showed that the position of the gel line varies with volume fraction and mention that the gel line (static percolation line) is measured while the dynamic percolation line is calculated in their experiments [118]. In this chapter, we therefore study the freezing transitions not by observing gelation transition in systems of particles but by another method to measure contact angles: the capillary rise method. When capillaries are placed vertically in a liquid, the fluid meniscus in the capillaries travels up or down to a certain height due to capillary action (Fig. 2.2). For a liquid that wets the surface of the capillaries ( $\theta < 90^\circ$ ), the fluid meniscus in the capillary will be higher than the surrounding liquid. For a poorly wetting liquid ( $\theta > 90^\circ$ ), the fluid meniscus in the capillary will be below that of the surrounding liquid. The height  $h$  of the liquid column can be calculated from the forces acting on the contact line inside the capillary of diameter  $R$ . The gravitational pull  $F_g$  of the weight of the column on the contact line is:  $F = -\rho g h \pi R^2$ . The surface tension pulls the fluid column up along the contact line with a force  $F = \gamma \cos(\theta) 2\pi R$ . Combining the two equations, we see that in equilibrium:

$$h = \frac{2\gamma \cos(\theta)}{\rho g R} \quad (2.5)$$

Alternatively, one can obtain information about the contact angle by measuring the height of the fluid column, assuming the capillary width  $R$  and the liquid-air surface tension are known. In this way, the freezing transition is effectively studied in the limit of an infinitely dilute system; dependence on the total volume fraction, particle polydispersity, and possibly particle size are eliminated.

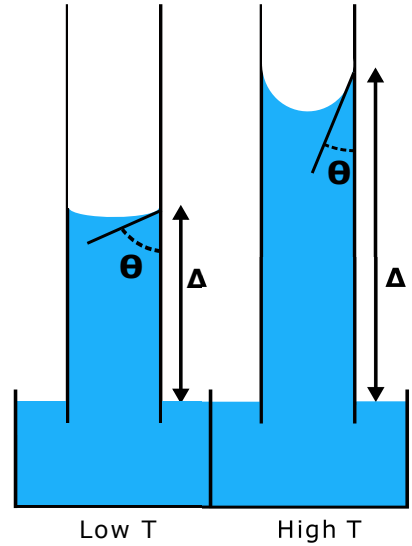


**Figure 2.2:** Schematic representation of the influence of the contact angle on the fluid column height in a capillary rise experiment.

## 2.2 Experimental details

### 2.2.1 Materials

The following alkanes were used: dodecane, tetradecane, hexadecane and octadecane. All alkanes were purchased from *Sigma Aldrich* and of purity  $\geq 99\%$  and olefine free. Silane coupling agents used were the following: n-dodecyltrimethoxysilane ( $C_{12}TMS$ , 95%, Fluorochem), n-hexadecyl-trimethoxysilane ( $C_{16}TMS$ , 95%, Fluorochem), n-octadecyl-trimethoxysilane (OTMOS, 95% (85% n-isomer), Gelest Inc.) and docosyltriethoxysilane ( $C_{20}TES$ , blend, Gelest Inc.).

### 2.2.2 Methods

Silica particles with a fluorescent core were modified with the silane coupling agent OTMOS or  $C_{20}TES$ . Silica particles (RITC-labeled core, 580 nm in size, stored in ethanol) were transferred to toluene by centrifugation, removal of the supernatant ethanol, and brief drying under nitrogen. A total mass of 200 mg silica was transferred to a freshly prepared mixture of 8 mL toluene, 0.8 mL butylamine and 0.8 mL OTMOS or  $C_{20}TES$ . The reaction mixture was sonicated for three hours and stirred overnight at room temperature. The particles were washed three times with toluene by centrifugation and redispersion.

Surface freezing transitions in colloidal particles were studied with a Nikon C1 confocal microscope equipped with a 63x (NA=1.4) oil immersion lens. The dispersions were heated using a *Linkam FTIR600* Hot Stage, by fixating a borosilicate glass capillary (*VitroCom* no.5012, 0.1 mm x 2.0 mm and wall thickness 0.1 mm) filled with dispersion to the heating element. The heating stage was connected to a TP94 controller. The temperature stability of the heating stage is 0.1 °C according to the manufacturer. The oil immersion lens was placed against the glass capillary for imaging; a small influence of the oil on the temperature conductivity is assumed. Particles grafted with OTMOS via the recipe described above were transferred to hexadecane by centrifugation and redispersion. The final volume fraction was  $\phi=0.04$ . The dispersion was sonicated at 50 °C for 1h before use, to break up any aggregates which may form due to the forces exerted on the particles during centrifugation; in the high-temperature sol state particles are more likely to be released if trapped in a van der Waals minimum.

Capillary rise experiments were performed in an *Incufridge* (*Revolutionary Science*, model *RS-IF-203*), which is an incubator oven and a refrigerator combined into one device. The temperature range reachable under proper conditions is 5 °C - 65 °C according to the supplier. The *Incufridge* has a precision of  $\pm 0.7$  °C and a uniformity  $\pm 1.0$  °C over its interior of volume 23.5 L.

Several tens of capillaries were modified with octadecanol in the following way based on Ref. 119. These capillaries had a Stöber silica coating of about 30 nm created by placing the capillaries in a dispersion of silica particles (0.44 g) in a Stöber mixture (6.6 mL ethanol, 0.71 mL ammonia (26.5 wt.%) with TEOS (26  $\mu$ L in 65  $\mu$ L ethanol) for 24h and subsequently washing 8 times with ethanol. The size difference of the silica particles before and after this treatment was estimated as the thickness of the silica layer on the capillaries [120]. The capillaries were then placed carefully upright in a Schlenk flask containing octadecanol molten at 70 °C. The flask was placed under a

nitrogen blanket and heated in an oil bath to 190 °C. The reaction mixture was stirred with a magnet during this reaction in order to maintain a uniform temperature; the stirring bar pushed the capillaries around, but did not break them. The reaction was allowed to proceed for 16 hours, after which the oil bath was allowed to cool to 70 °C. While the octadecanol was still liquid, the capillaries were retrieved using tweezers. They were placed in a vessel containing acetone (to a quarter of the volume). The vessel was placed in an oven at 50 °C for several days, as we found that the solid octadecanol in the narrow capillaries needed a long time to dissolve.

Borosilicate capillaries (*VitroCom* no. CV2033 and no. CV3040, of circular cross section with inner diameters of 0.2 mm and 0.3 mm) were treated with silane coupling agents in toluene according to the following recipe. First, 10 mL toluene, 1 mL butylamine and 1 mL silane coupling agent were mixed in a vial. About 40 capillaries were slowly placed in this vial such that the reaction mixture filled the capillaries without trapped bubbles. The capillaries were left in the reaction mixture for a day at room temperature. Afterwards they were washed with toluene three times to remove residual silane and stored dry. The reason for choosing not to apply a Stöber silica coating in this case, was that we often found the capillary rise to be poorly reversible in the presence of such a coating (i.e. the rise in solvent level was not accompanied by a decrease of the same magnitude upon temperature decrease). Possibly, coating with Stöber silica introduces roughness to the surface, which affects the capillary action. The difference in silica surface between the octadecanol-grafted and silane-treated capillaries unfortunately renders the results of the silane-treated capillaries somewhat less comparable to those of the octadecanol-grafted capillaries.

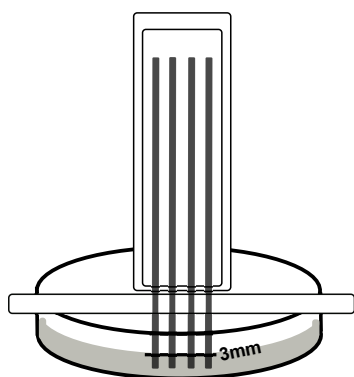


**Figure 2.3:** Schematic representation of the experimental set-up.

For a capillary rise measurement, ten capillaries were stuck to millimeter scale graphing paper which had itself been taped to the outside of a glass vial (Fig. 2.3). The capillaries were aligned along the lines of the scale. The capillaries protruded from below the bottom of the vial by a few centimeters. The vial was placed on top of a plastic petri dish with on a horizontally placed glass cover slide. The side of the petri dish was marked at a height of 3 mm from the bottom. With the glass vial placed on top of the petri dish, the distance from the 3 mm mark to the zero on the scale paper was measured using a ruler with a millimeter scale. In a capillary rise experiment, this distance must be added to the capillary rise indicated on the scale paper to find the total capillary rise. The content in the petri dish (with a diameter of 5.6 cm and fluid interface at 3 mm) is approximately 7 mL, whereas ten capillaries of inner diameter 0.3 mm can maximally contain 7  $\mu$ L. Hence, the petri dish may be seen as a large sink for the alkane, and the height of the alkane/air interface is not significantly affected by any capillary rise of the fluid into the capillaries.

The petri dish, glass vial with the capillaries, and a vial with alkane were placed in the Incufridge oven which had been preheated to the desired starting temperature of a capillary rise experiment. After at least 30 minutes (to allow all objects to adopt the oven's temperature), the glass vial with

capillaries was quickly placed on the petri dish and the petri dish filled to the 3 mm mark. This part of the preparation had to be done with the door of the Incufridge open and was done as quickly as possible, since the temperature dropped with the door open. After the petri dish was filled, the alkane rose in the capillaries. After at least 30 minutes of equilibration the temperature the capillary rise experiment was started. The temperature of the Incufridge was raised manually in steps of 1 °C - 2 °C with a rate equal to or lower than 2 °C/h. For each temperature step, and after an equilibration time of at least 30 minutes, the height of the fluid columns as indicated on the millimeter paper was measured for each of the ten capillaries. With these data, a plot of the capillary height as a function of temperature was obtained.

## 2.3 Results & Discussion

### 2.3.1 Surface freezing transition of octadecanol-grafted surfaces

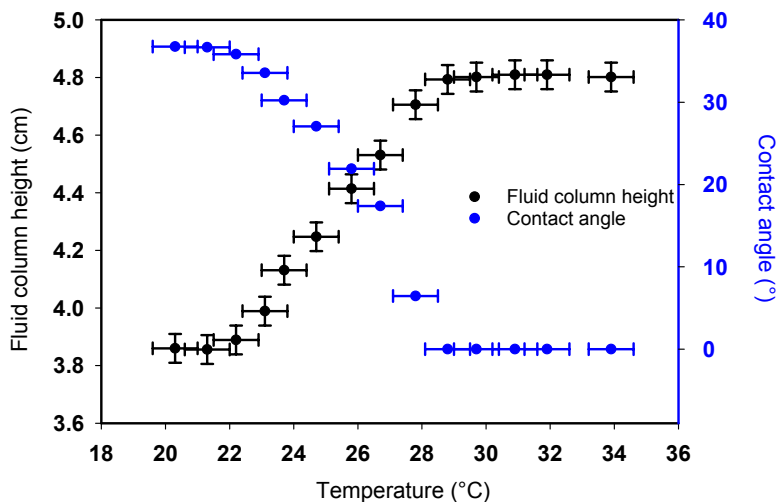


**Figure 2.4:** Capillary rise experiment of hexadecane in octadecanol-grafted capillaries. I.D.=0.3 mm.

In literature, octadecanol-grafted silica particles in hexadecane are the commonest system with a surface freezing transition. Fig. 2.4 shows the result of a capillary rise experiment for hexadecane in octadecanol-grafted capillaries. The fluid column experiences a steep rise in the range 22 °C-29 °C. The rise is not so steep as to define a single transition temperature, however one could define it in the middle of the range:  $25.5\text{ °C} \pm 0.5\text{ °C}$ . Temperature-dependence of the height of the fluid column not only stems from the contact angle, but also from a temperature-dependence in the density and the surface tension of hexadecane, yet such a decrease was only visible on larger temperature scales than those in Fig. 2.4.

Contact angles corresponding to the height of this fluid column (blue symbols in Fig. 2.4) were calculated using equation 2.5. Temperature-dependent values for the density of hexadecane were found by fitting a linear relation through 12 experimental values from Refs. [121–127]. Temperature-dependent surface tension values were obtained by fitting a linear relation (in accordance with the first assumption of the Eötvös rule, which states that the surface tension is a linear function of the temperature) through four experimental values from Ref. 128. In this freezing transition, the contact angle decreases from 37° until full wetting is achieved at 29 °C.

## 2.3.2 Surface freezing transition of silanized surfaces

### 2.3.2.1 Gelation transition in colloidal dispersions

As elaborated upon in the previous section, a freezing transition occurs for octadecanol-grafted particles, which results in a gel below the transition temperature and a sol above the transition temperature. Such a transition is also expected for OTMOS-grafted silica particles, since octadecanol and OTMOS have identical  $C_{18}$ -chains at the surface. Fig. 2.5 shows confocal images from an experiment in which a dispersion of OTMOS-grafted particles in hexadecane ( $\phi=0.04$ ) was heated at a heating rate of  $2^\circ\text{C}/\text{min}$ . The temperature indicated in the figures is that of the heating stage at the time of imaging. The images show that the dispersion transitions from a gel in Fig. 2.5a to a dispersion in Fig. 2.5f, proving that a freezing transition can occur not only for linear alcohol modified silica but also for silanized silica. To our knowledge, such a transition has not been shown in literature for silanized particles. The gelation transition occurs over a broad temperature range; structural changes with respect to the previous image can be seen in each frame of Fig. 2.5. Hence, it is difficult to determine an onset temperature for the gelation transition. The first break-up of the gel was observed at  $29.5 \pm 0.2^\circ\text{C}$ . A second experiment was performed with a slower heating rate ( $0.2^\circ\text{C}/\text{min}$ ), to ensure sufficient time for the capillary to absorb heat from the heating element. The first gel break-up occurred at a slightly higher temperature in this experiment:  $32.1^\circ\text{C}$ . It was helpful to study the surface freezing transition with the capillary rise method, because this gelation transition may have been influenced by the particle size and concentration, as well as the fact that heating rate gel break-up may not be a good indicator for the onset of the surface freezing transition.

Similar transitions were observed for  $C_{20}$ -silanized particles. Fig. 2.6 shows frames of a movie from an experiment in which such particles in hexadecane ( $\phi=0.04$ ) were heated at  $10^\circ\text{C}/\text{min}$ . Again, the gelation transition occurs over a broad temperature range and it is difficult to pinpoint an exact transition temperature. Loose particles are visible in frame 2.6d. However, larger pieces of gelated particles already sink into the field of view in frames 2.6b and 2.6c, indicating gel break-up at a lower temperature.

A general observation was that a large fraction of the particles remained aggregated or clustered even above the freezing transition temperature, even though redispersion was observed in particular areas of the capillary. Apparently, the heated sonication treatment is not effective to liberate all particles from clusters. A plausible reason for the observed clusters is that the R-alkyl-tri(m)ethoxysilanes used introduced extra OH-groups at the surface, which then condensed and formed siloxane bridges between particles the reaction. A decreased hydrophobicity of the particles due to these extra OH-groups is also possible. The clusters formed an impediment to using the observed gelation transition as a reliable way to create reversible patch-patch interactions. Future research should seek to avoid the introduction of extra OH groups at the surface, for example by using R-alkyl-dimethyl silanes.

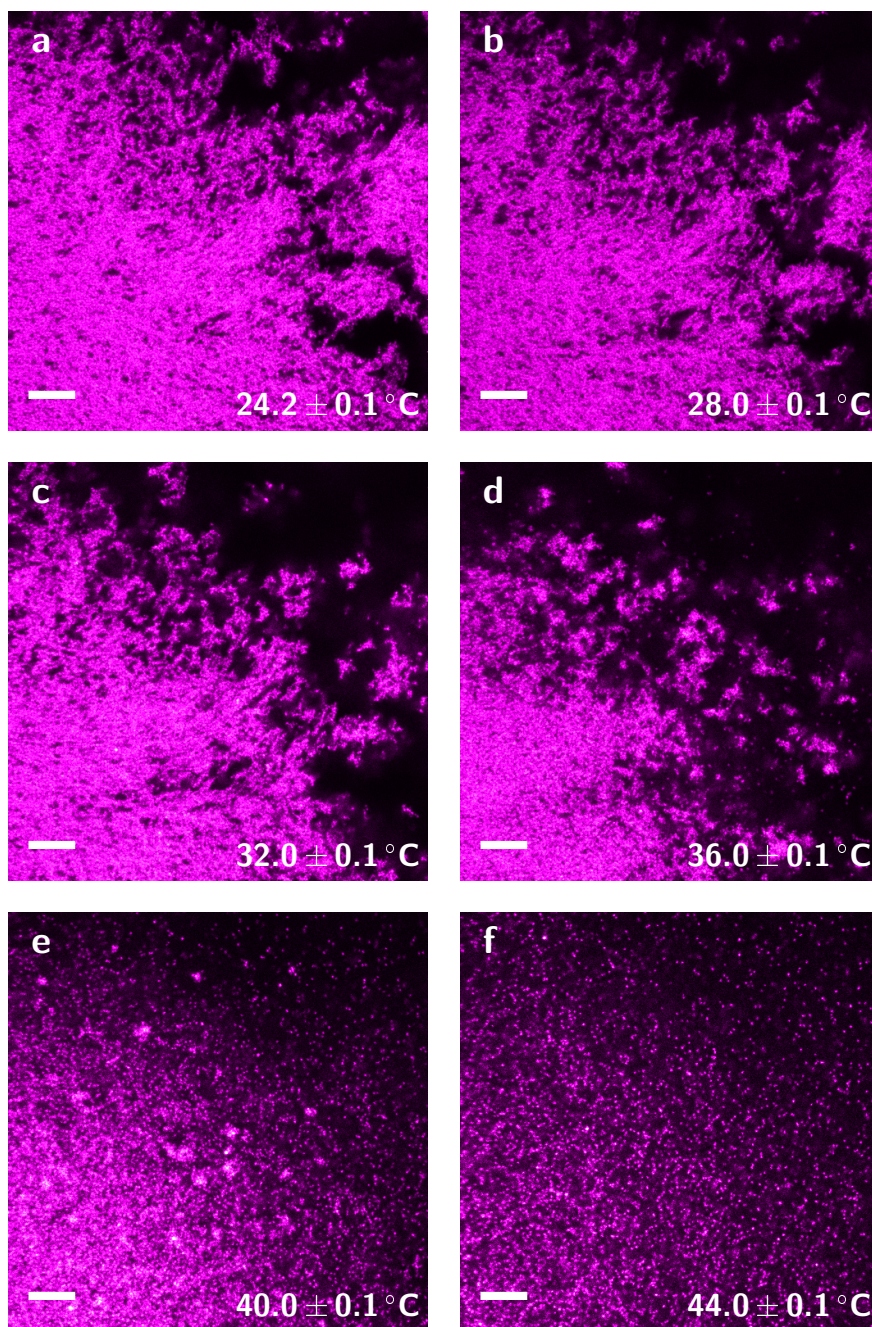


**Figure 2.5:** A dispersion of OTMOS-grafted silica particles in hexadecane is heated on a *Linkam FTIR600* heating stage. Temperatures indicated are that of the heating plate at the time of imaging. The heating rate was  $2 \text{ }^\circ\text{C}/\text{min}$  and the time between frames 5s. Scale bars denote  $10 \mu\text{m}$ .

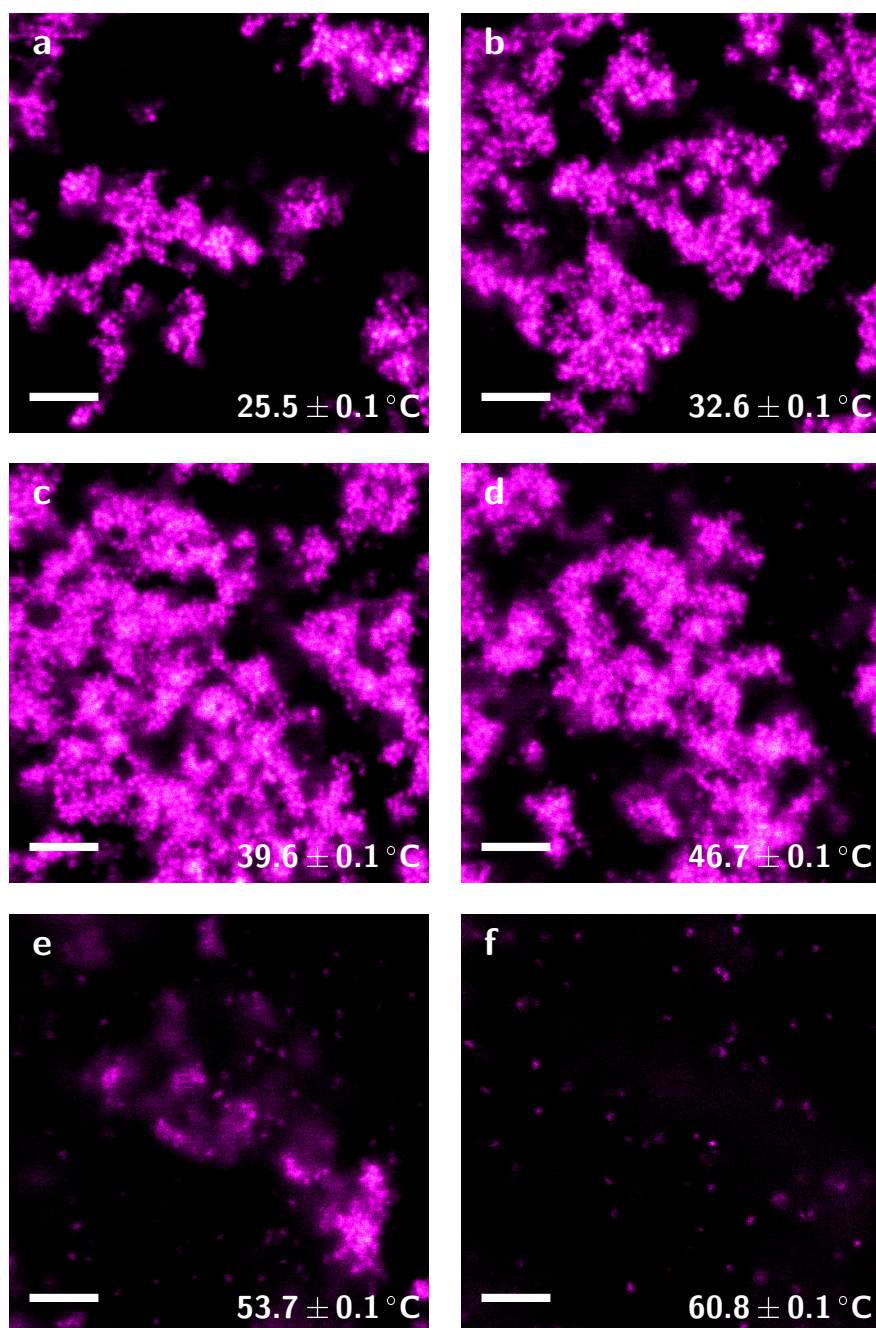


**Figure 2.6:** A dispersion of C<sub>20</sub>TES-grafted silica particles in hexadecane was heated on a *Linkam FTIR600* heating stage. Temperatures indicated are that of the heating plate at the time of imaging. The heating rate was 10 °C/min and time between frames 1s. Scale bars denote 5 μm. The aggregates appear to become larger in the second and third frame; as the gel structure breaks up larger pieces sediment to the bottom.

### 2.3.2.2 Surface freezing transition measured by the capillary rise method: OTMOS-functionalized surfaces

The freezing transition of alkanes on OTMOS-grafted surfaces (rather than octadecanol-grafted surfaces) was also studied using the capillary rise method. Figs. 2.7-2.8 show the results of a capillary rise experiment of hexadecane in OTMOS-grafted capillaries of inner diameter 0.3 mm. The starting temperature was 18.5 °C, which is close to the melting point of hexadecane, 18 °C. Upon temperature increase, the fluid level starts to rise at approximately 22 °C, until it levels at 32 °C. The contact angle decreases from 43° (at 24 °C) to 20° (at 33 °C) in this temperature range. All contact angles are below 90°, so hexadecane wets the OTMOS-grafted surface at room temperature. The decrease in contact angle upon heating implies that hexadecane wets the OTMOS-grafted surface better after heating. The dotted line represents the expected contact angle based solely on the starting height of the meniscus and temperature-dependence of the density and surface tension of hexadecane: the contact angle changes gradually by 3°. The measured contact angle behaves in an anomalous fashion with respect to this predicted contact angle. Thus, this experiment indicates that a freezing transition exists for OTMOS-grafted silica in hexadecane, and it is located slightly above room temperature. Riedo *et al.* provide tables for the contact angle of alkanes on octadecyldimethylsilylated acid-leached glass [110]. In their experiment, the contact angle change for hexadecane lies above 30 °C. Assuming that the acid-leached glass in that study is similar to the borosilicate glass used here, the methyl groups on octadecyldimethylchlorosilane shift the freezing transition temperature. In Fig. 2.7, the red graph denotes the height of the meniscus upon decreasing the temperature. In spite of the slow cooling rate, the graph shows hysteresis with respect to the heating experiment. This hysteresis could be due to the existence of an advancing and a receding contact angle. A high hysteresis angle was also observed by Fadeev and McCarthy on silanized surfaces, although hysteresis decreases with chain length.

Assuming the silica type is not of great influence to these results, two observations can be made. Firstly, the surface freezing transition on OTMOS-grafted capillaries starts and ends approximately 2 °C higher. Secondly, hexadecane completely wets the stearyl-grafted capillaries at temperatures above the freezing transition, while for OTMOS-grafted capillaries the contact angle levels at 20° at temperatures above the freezing transition. A possible explanation for the first point is that the packing of grafted molecules is slightly higher on OTMOS-grafted surfaces than for stearyl-grafted silica (c.f. Ch. 3), since the OTMOS molecules allow for branched structures at the surface (Fig.2.1). The non-complete wetting of the OTMOS-grafted silica by hexadecane remains unexplained.

Surface freezing transitions on OTMOS-grafted surfaces were studied for other alkane solvents as well. Fig. 2.9 shows the results of two capillary rise experiments of tetradecane in OTMOS-grafted capillaries, under heating. The two graphs nicely overlap, showing the reproducibility of the experiment. Furthermore, the freezing transition starts at an 8 °C lower temperature than for hexadecane, as the capillary rise steeply increases already below 20 °C. Contact angles were calculated based on temperature-dependent densities from Refs. [127] and surface tension values from Ref. 128. The contact angle for one of the measurements is displayed in Fig. 2.10. It falls roughly from 38°

(at 12 °C) to 24° (at 25 °C), so the wetting of tetradecane is comparable to that of hexadecane.

The capillary rise results for four alkanes on OTMOS-coated capillaries (I.D. = 0.3 mm) are shown in Fig. 2.11. We observe a transition temperature which increases with the alkane length. For octadecane, the solvent's bulk freezing point (28-30 °C) has caught up with the onset of the surface freezing transition temperature. As a result, it is not possible to measure the entire transition curve for octadecane. Fig. 2.12 shows the contact angles calculated from the capillary rise experiments. For octadecane, the temperature-dependent densities were obtained from Ref. 129 and temperature-dependent surface tension from Ref. 128. It is striking that the contact angles reaches similar values after the freezing transition.

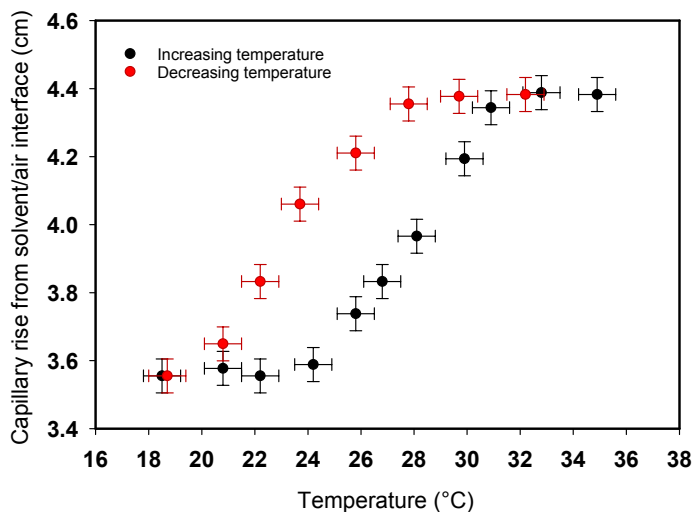


**Figure 2.7:** Heating and cooling capillary rise experiments of hexadecane in OTMOS grafted capillaries, showing hysteresis. I.D.=0.3 mm. Heating and cooling rates were 2 °C/h.

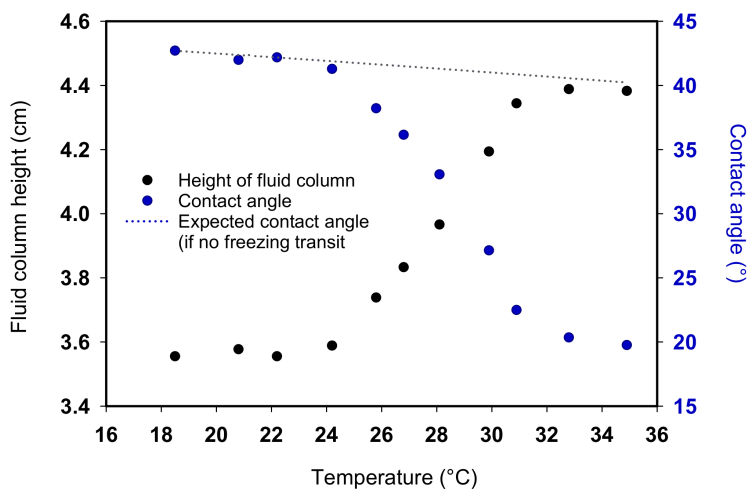


**Figure 2.8:** Capillary rise experiment of hexadecane in OTMOS grafted capillaries, with fluid column height on the left and contact angle on the right vertical axis. I.D.=0.3 mm.

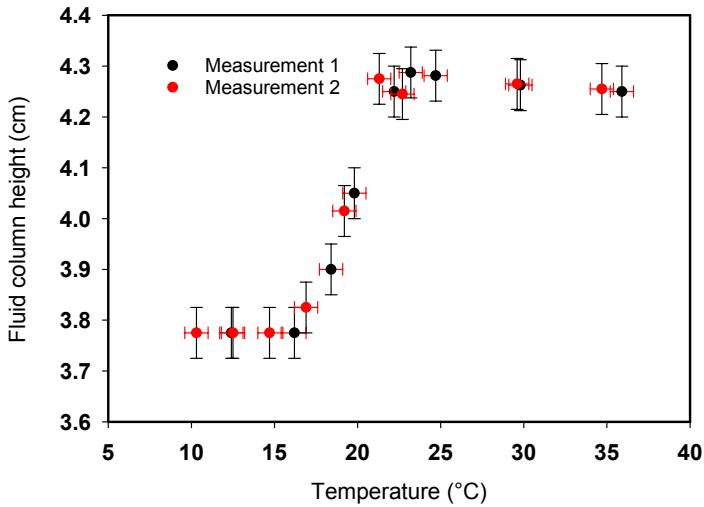


**Figure 2.9:** Two capillary rise experiments of tetradecane in OTMOS grafted capillaries, showing reproducibility. I.D.=0.3 mm.

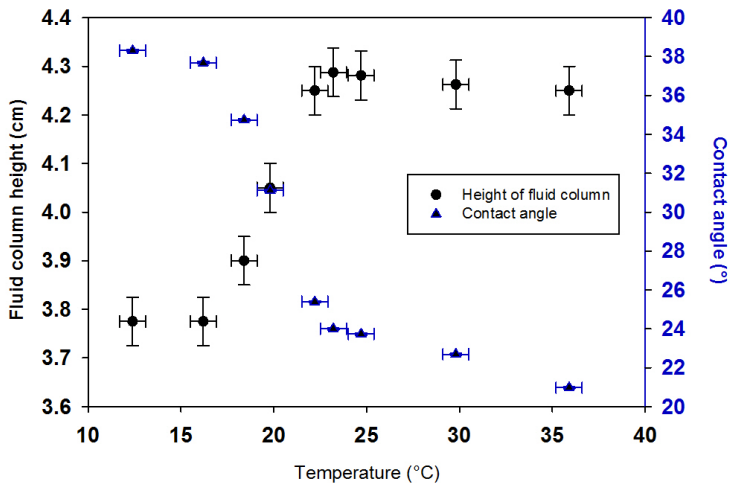


**Figure 2.10:** Capillary rise experiment of tetradecane in OTMOS grafted capillaries, with fluid column height on the left and contact angle on the right vertical axis. I.D.=0.3 mm. The dotted line represents the calculated fluid column height if there were no freezing transition (but only change in viscosity and density).

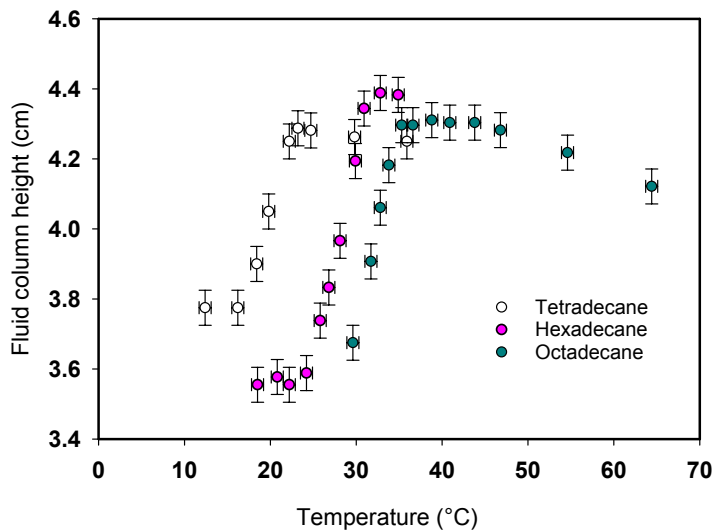


Figure 2.11: Capillary rise experiments for various alkanes in OTMOS grafted capillaries. I.D.=0.3 mm.

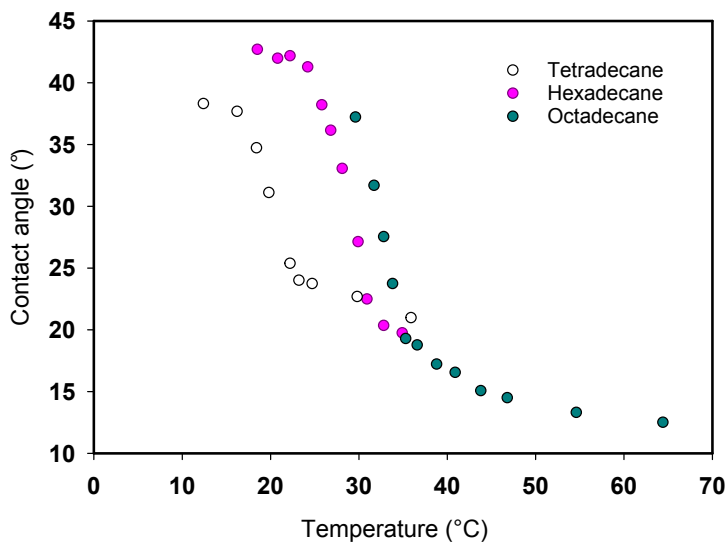


Figure 2.12: Contact angles calculated from capillary rise experiments for various alkanes in OTMOS grafted capillaries. I.D.=0.3 mm.

### 2.3.2.3 Surface freezing transition measured by the capillary rise method: C<sub>16</sub>- and C<sub>20</sub>-functionalized surfaces

We first discuss C<sub>16</sub>TMS-grafted capillaries (Fig. 2.13). As shown in the figure, the freezing transition of hexadecane on this surface appeared to be lower than for OTMOS-grafted capillaries, pushing the transition region partly below the melting point of hexadecane. The freezing transition of tetradecane was also shifted to lower temperatures compared to the temperatures observed for OTMOS-grafted capillaries. It suggests that capillaries grafted with shorter alkane chains have freezing transitions at lower temperatures for equal solvent chain lengths. The contact angles corresponding to these fluid column heights vanished at the end of the surface freezing transition; the solvents become completely wetting (Fig. 2.14).

For C<sub>20</sub>TES-grafted capillaries, we performed the experiments with capillaries of two different diameters (I.D. = 0.3 mm (7 capillaries) and I.D. = 0.2 mm (3 capillaries)). The ratio of the inner diameters is 1.5, so in accordance with equation 2.5 the fluid columns in the thinner capillaries are expected to be 1.5 times as high as in the wider capillaries. The fluid column heights are displayed in Fig. 2.15: we find that the fluid height in the thinner capillaries is between 94% and 98% of the expected height based on the fluid column height in the wider capillaries. This small discrepancy could be due to a small difference in the actual inner capillary diameters from the values 0.3 mm and 0.2 mm indicated by the manufacturer. The discrepancy also influences the contact angles calculated from these capillary rise measurements (shown in Fig. 2.16) such that there is a slight discrepancy between the two series of contact angles, yet they are within each other's error margins.

When comparing the capillary rise experiments for hexadecane in capillaries grafted with various chain lengths (Fig. 2.17), we see that the freezing transition does not shift monotonously with grafting chain length. Rather, the freezing transition occurs at the lowest values for C<sub>16</sub>TMS-grafted capillaries and at the highest temperatures for C<sub>20</sub>TES-grafted capillaries. Possibly, the freezing transition occurs at higher temperatures for OTMOS-grafted surfaces because the hexadecane molecules fit well among the C<sub>18</sub>-chains, but a larger chain length difference induces melting of the frozen surface layer. The contact angles Fig. 2.18 show that complete wetting is attained for hexadecane (C<sub>16</sub>-chains) on C<sub>16</sub>TMS-grafted surfaces. The contact angles for the other silane coupling agents level off near 20°; we conclude that surfaces of non-identical carbon chain lengths do not completely wet.

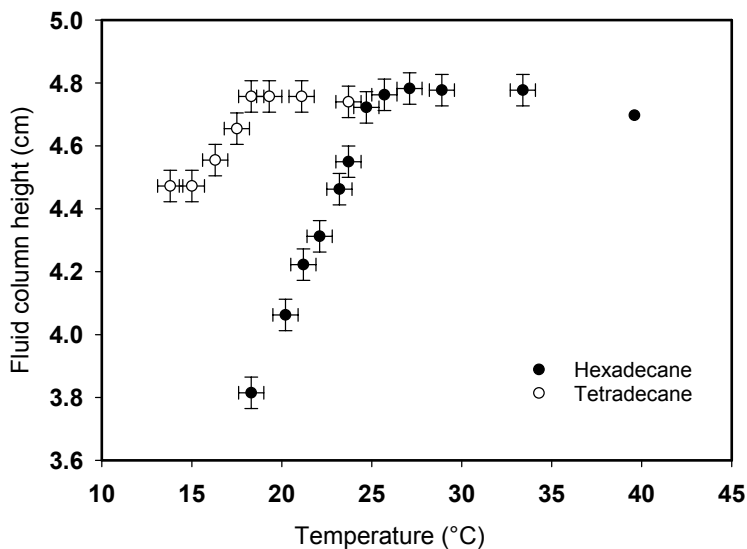


**Figure 2.13:** Fluid column height for capillary rise experiments of hexadecane and tetradecane in  $C_{16}$ TMS-grafted capillaries. I.D.=0.3 mm.

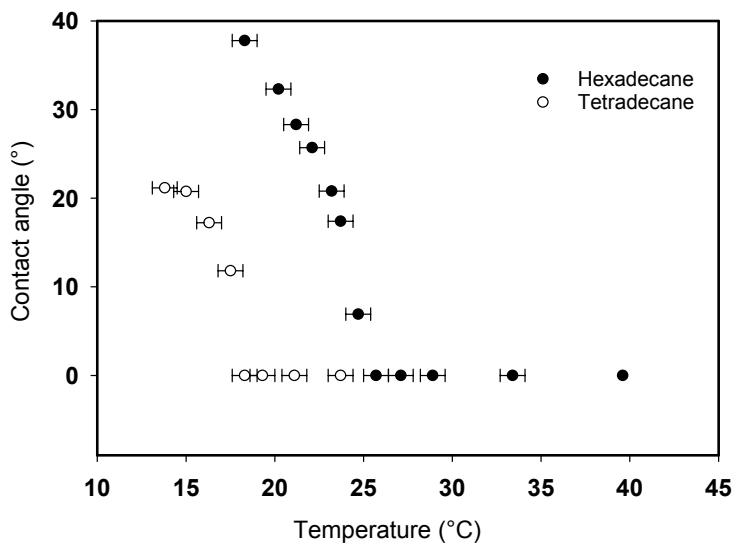


**Figure 2.14:** Contact angles for capillary rise experiments of hexadecane and tetradecane in  $C_{16}$ TMS-grafted capillaries. I.D.=0.3 mm.

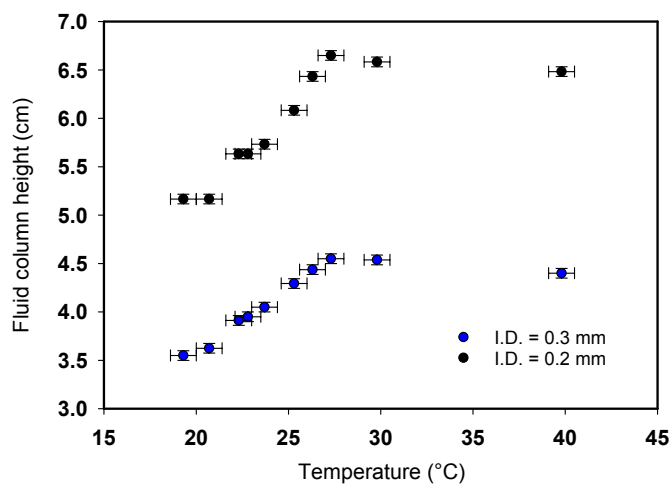


**Figure 2.15:** Fluid column height for capillary rise experiments of hexadecane in C<sub>20</sub>TES-grafted capillaries of two inner diameters: I.D. = 0.3 mm and I.D. = 0.2 mm.

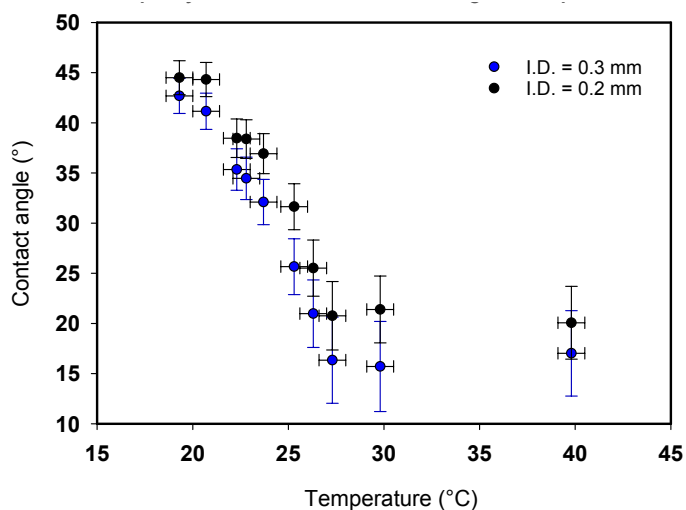


**Figure 2.16:** Contact angles for capillary rise experiments of hexadecane in C<sub>20</sub>TES-grafted capillaries of two inner diameters: I.D. = 0.3 mm and I.D. = 0.2 mm.

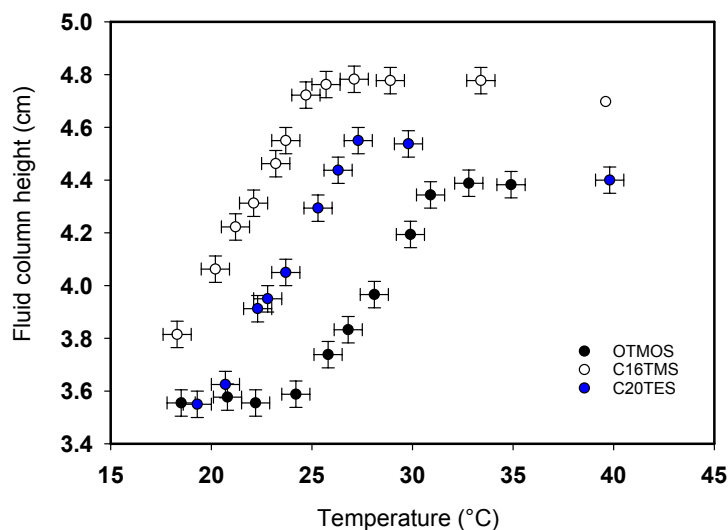


**Figure 2.17:** Fluid column height for capillary rise experiments of hexadecane on C<sub>16</sub>TMS, C<sub>18</sub>TMS (OTMOS) and C<sub>20</sub>TES-grafted capillaries. I.D.=0.3 mm.

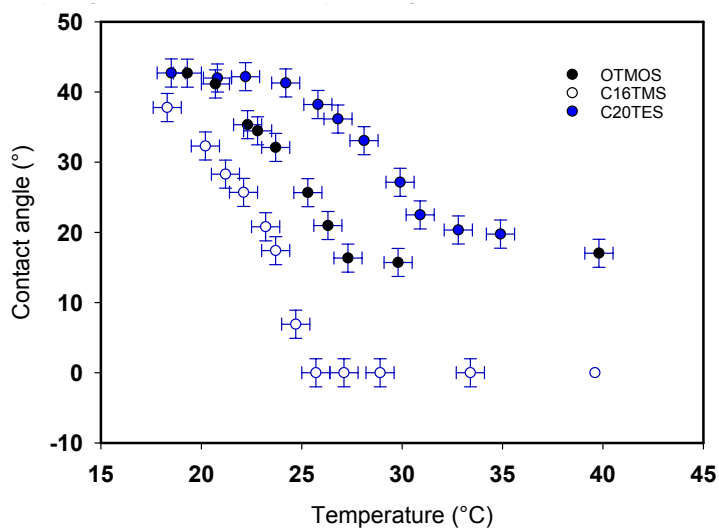


**Figure 2.18:** Contact angles for capillary rise experiments of hexadecane on C<sub>16</sub>TMS, C<sub>18</sub>TMS (OTMOS) and C<sub>20</sub>TES-grafted capillaries. I.D.=0.3 mm.

## 2.4 Conclusions & Outlook

Octadecanol-grafted silica particles in hexadecane undergo a transition from a gel phase to a dispersed phase under temperature variation. We observed a similar transition for OTMOS-grafted and C<sub>20</sub>TES-grafted silica particles in hexadecane in confocal microscopy studies, confirming for colloidal dispersions the suggestion by Fadeev and McCarthy [113] that a surface freezing transition not only exists for alcohol-modified surfaces but also for silane-modified surfaces.

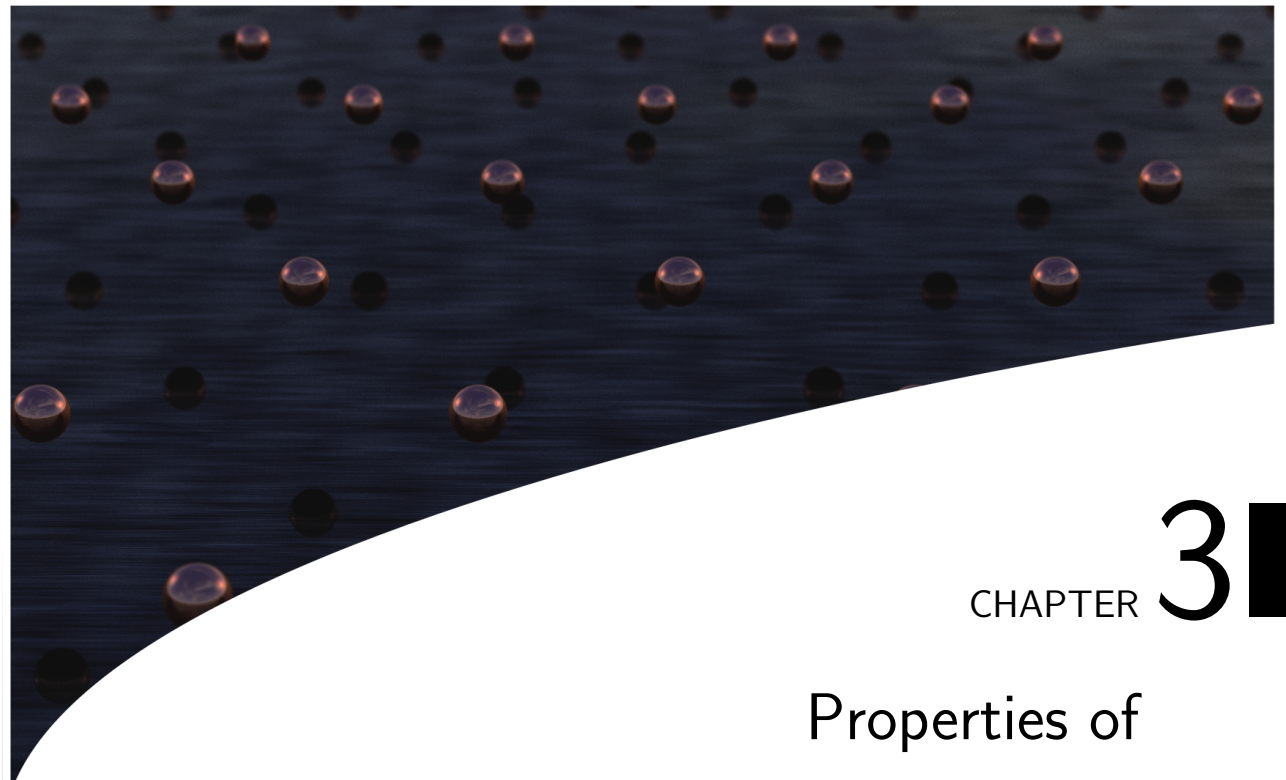
Such a transition is also expected to exist for other alkane chain lengths of the grafting agent and of the solvent. The transition temperatures for several combinations of graftings and solvents were studied via the capillary rise method. The fluid column height of a solvent in a surface-grafted capillary is proportional to the cosine of the contact angle, which changes during the surface freezing transition. This measurement method has advantages over studying a gel-sol transition of a dispersion of grafted silica, since the transition temperature may be size- and volume fraction-dependent in silica dispersions, and since the amount of clustering as a function of temperature is difficult to quantify.

The freezing transition for octadecanol-grafted capillaries with hexadecane (C<sub>16</sub>H<sub>34</sub>) as a solvent started at 22 °C and was completed at 30 °C, which is consistent with the transition temperature range found by Roke *et al.* for dispersions of octadecanol-grafted silica in hexadecane (24.7 °C to 34.0 °C, [105]). The freezing transition for OTMOS-grafted capillaries with hexadecane as a solvent was completed at 33 °C, i.e. the temperature range for which both transitions take place were found to be very similar. Riedo *et al.* observed a freezing transition above 30 °C for octadecyl*dimethyl*silane-grafted capillaries with hexadecane as a solvent. Based on the protruding methyl groups, one would expect a lower surface freezing transition temperature: the difference could lay in the types of glass used (Stöber and borosilicate). Contact angles for hexadecane at OTMOS-grafted surfaces changed during the transition from roughly 40° to 20°, while complete wetting was achieved for octadecanol-grafted surfaces.

In the present work, the onset of the freezing transition in OTMOS-grafted capillaries increased from 20 °C to 30 °C as the *solvent* chain length increased from 14 carbon atoms (tetradecane) to 18 carbon atoms (octadecane). Apparently, alkanes of higher chain length facilitate the freezing of the grafted layer. With a heating/cooling rate of 2 °C/h, considerable hysteresis was observed for the capillary rise of hexadecane on OTMOS-grafted surfaces. The freezing transition temperature of silane-grafted surfaces in hexadecane did not increase with the *grafted chain length*. Instead, the freezing transition temperature was lower for C<sub>16</sub>- and C<sub>20</sub>-grafted surfaces than for C<sub>18</sub>-grafted surfaces. Possibly, the slightly shorter hexadecane molecules are more easily incorporated in the C<sub>18</sub>-grafted layer. Consequently, the contact angle for hexadecane did not decrease with the grafting chain length either.

The transition temperatures found for silanes of different chain length in hexadecane in Fig. 2.17 can be employed to prepare patchy particles with reversibly sticking protrusions. Particles grafted with C<sub>16</sub>TMS are stable in hexadecane at temperatures above approximately 25 °C. Protrusions grafted with OTMOS, however, would stick together as the transition temperature range of OTMOS-grafted silica lies above 25 °C. Alternating the temperature of the system between 25 °C and ~35 °C could then yield a structure of patchy particles sticking at the protrusions. A difficulty to be overcome are

the irreversibly aggregated clusters encountered in the dispersions of silane coupling agent modified silica particles in hexadecane, for which we propose using R-alkyldimethyl silanes. Moreover, the strength of the attraction should be reduced to obtain equilibrium structures of these patchy particles, since fully grafted particles formed (out-of-equilibrium) gel phases. Such a reduction in the attraction strength might be accomplished by using mixtures of alkanes - grafted on the surface or in the solvent - to reduce van der Waals attractions.



## CHAPTER 3

# Properties of n-octadecyl-alkane-functionalized silica

n-Octadecyl-alkane-functionalized silicas are well-studied: for example the surface-freezing transitions of grafted alkane chains [105, 106], contact angles of liquids on silica-functionalized silicas [110] and crystal phases of surface-grafted colloids [130]. It is also known that n-octadecyl-alkane-grafted particles are especially well dispersible in cyclohexyl chloride (CHC) and other low-polar solvents ( $\epsilon \sim 4-15$ ) [131]. However, information on the charging mechanism as well as the differences in surface charge and potential of different n-octadecyl-alkane-functionalized silicas are somewhat limited. Grafting with n-octadecyl-alkane chains is employed to create patchy particles, in this thesis. A thorough understanding of the pair potential of n-octadecyl-alkane-grafted silica in low-polar solvents is necessary for possible self-assembly of those patchy colloids in low-polar solvents. In this chapter, TGA measurements are used to determine the grafting density of both n-octadecyltrimethoxysilane (OTMOS)-functionalized and octadecanol-functionalized silica. Moreover, radial distribution function measurements and (micro-)electrophoresis experiments are performed to determine the pair potential in the low-polar solvent CHC.

---



## 3.1 Introduction

### 3.1.1 Theory on radial distribution functions

In this chapter, the interaction potentials between colloidal particles in a low-polar (i.e.  $4 < \epsilon < 15$ ) solvent are studied. For a well-index-matched dispersion, the van der Waals attraction can be neglected (as a result of dependency on the refractive index mismatch between colloids and solvent). The pair potential  $U(r)$  of a pair of spheres at separation  $r$  then takes the form of a Yukawa (screened Coulomb) repulsion, i.e. a potential decaying at a rate of  $1/r$  (Coulomb) which is 'screened' by an exponential [132, 133], as is found by solving the linearized Poisson-Boltzmann equation for a sphere and calculating the repulsion that results from weak overlap of the double layers of two spheres [134]:

$$\frac{U(r)}{k_B T} = \frac{(Z^*)^2}{(1 + \kappa\sigma/2)^2} \left( \frac{e^2}{4\pi\epsilon_0\epsilon_r k_B T} \right) \frac{\exp[-\kappa r + \kappa\sigma]}{r} \equiv U_0 \frac{\sigma}{r} \exp[-\kappa(r - \sigma)] \quad (3.1)$$

Here, the spheres have a diameter  $\sigma$  and an effective charge number  $Z^*$  ( $e$  is the elementary charge), are dispersed in a medium of dielectric constant  $\epsilon$ , and have Debye screening length  $\kappa^{-1}$ . The quantity  $U_0$  is (defined to be) the potential at contact. The quantity in brackets is also called the Bjerrum length  $\lambda_B$  (with  $k_B$  the Boltzmann constant,  $T$  the absolute temperature,  $\epsilon_0$  the permittivity of vacuum, and  $\epsilon_r$  the relative permittivity of the medium), and is the separation at which the electrostatic interaction between two elementary charges equals  $k_B T$ , i.e. it is indicative of interaction strength between the charges in the electrolyte. It is interesting to measure the pair potential experimentally, so that it can be compared with this theoretical expression, either to derive values such as the Debye length or to check for anomalous behavior in the expected Yukawa decay. Two important methods are:

- Directly: by analyzing the relaxation of particles released from an optical trap using optical tweezers [135].
- Indirectly: by analyzing the liquid structure of a dispersion in equilibrium.

The latter is employed in this chapter.

Radial distribution functions (RDFs) - also called "pair correlation functions"  $g(r)$  - describe how the particle density in a system falls off as a function of distance from a reference particle. The RDF can be written as an ensemble average of a summation of distances over all particles  $j$  relative to a reference particle  $i$ :

$$g(r) = \frac{2V}{N} \left\langle \sum_{i < j} \delta(r - r_{ij}) \right\rangle \quad (3.2)$$

in which  $V$  is the total volume that is analyzed,  $N$  is the total number of particles in the volume, and  $r_{ij}$  is the center-to-center distance of particles  $i$  and  $j$ . In practice, RDFs can be obtained by measuring the distances between all particles in an image of the system, binning the distances into a histogram and finally normalizing by the density.

One important source of error in measuring an RDF is truncation by the limited field of view [132], i.e. only a part of an equilibrium state can be sampled. Moreover, the smaller the field of view, the more dominant edge effects are. This field of view cannot be increased arbitrarily as the particles must still be resolved, hence multiple images of the dispersion are necessary. A second source of error, then, is the fact that the configuration in an image is only uncorrelated to that in the previous image when the particles have had sufficient time to redistribute (i.e. diffuse over at least one inter-particle distance). When two images of the system are taken closer together in time, one particular state is sampled more than other states, and one fails to measure the sample's equilibrium properties. The two afore-mentioned errors are related in the sense that a larger field of view decreases the statistical under-sampling of the equilibrium state. A practical source of error is that the experimental conditions may vary during long measurements; most notably the ion concentration may increase.

Behrens and Grier set out to find an optimum measurement time given a certain areal density  $n$  and a desired accuracy. Suppose we find  $N(r)$  particle pairs with inter-particle separation  $r$  in a snapshot of area  $A$  (with  $A$  is assumed large enough to ignore edge effects). Then in a ring of radius  $r$  about any particle we will find on average  $2N(r)/(nA)$  other particles. Suppose also that we require bin width  $\delta$  for the histogram (so each bin contains the average number of particles between  $r - \delta/2$  and  $r + \delta/2$ ). For a homogeneous dispersion we then expect to find  $2\pi r\delta n$  other particles in this ring. The pair correlation function  $g(r)$  is found by normalizing the counted number  $N(r)/(nA)$  by the expected number for a homogeneous system:

$$g(r) = N(r)/(n^2\pi r\delta A) \quad (3.3)$$

If we now want to measure  $g(r)$  to an accuracy  $\Delta$  in  $M$  snapshots, we can rewrite  $g(r) = 2N(r)M\Delta$  with  $M = (\pi n^2\sigma\delta A\Delta)^{-1}$ . Since  $N(r)$  and  $g(r)$  are of the order 1, we have an estimate for the number of uncorrelated snapshots  $M$  required:  $M \sim 1/(2\Delta)$ . Snapshots are uncorrelated when the particles have been able to diffuse over the mean particle distance  $\sqrt{n}$ . Thus, using the Brownian diffusion theorem which states that in 2D  $\langle x^2 \rangle = 4Dt$ , the time between successive snapshots should be at least  $\tau = (4Dn)^{-1}$  for the snapshots to be uncorrelated. The total time needed for the experiment scales as  $M\tau \propto n^{-3}$ , i.e. it sharply increases at lower particle densities. More snapshots within this total time will not improve the shape of the radial distribution function, although they may reduce experimental noise. Notice that the measurement time quickly increases for dilute samples. Since it is difficult to keep experimental details such as ion concentration constant for long times, the competition between accuracy and measurement time calls for a compromise between statistical and experimental accuracy [132].

Once  $g(r)$  is calculated from an experiment, it can be used to derive the pair potential  $U(r)$  between two particles. In the limit of infinite dilution, this would be an easy feat. Namely,  $U(r)$  is related to  $g(r)$  as [132]:

$$\lim_{n \rightarrow 0} g(r) = \exp[-U(r)/k_B T] \quad (3.4)$$

At finite concentration such a simple inversion relation does not hold, for  $g(r)$  then contains the effect of many-body correlations. The potential in the above relation is then called the 'potential of mean force' [132]

$$w(r) = -k_B T \ln[g(r)] \quad \text{and its inverse} \quad g(r) = e^{[-w(r)/k_B T]} \quad (3.5)$$

Approximations for  $U(r)$  from  $w(r)$  are usually derived using the Ornstein-Zernike (OZ) equation and an appropriate closure relation [136]. The OZ equation relates the *total correlation function* (defined as  $h[r_{12}] = g(r_{12}) - 1$  for two particles at separation  $r_{12}$ ) to the *direct correlation functions*  $c(r_{13})$  and  $c(r_{23})$  of the particles with any other particle 3. Using vectors  $\vec{r}_{ij}$  ( $i,j=1,2,3$ ) for the inter-particle distances, the OZ equation states that:

$$h(\vec{r}_{12}) = c(\vec{r}_{12}) + \rho \int d\vec{r}_{23} c(\vec{r}_{12} - \vec{r}_{23}) h(\vec{r}_{32}) \quad (3.6)$$

or using a mathematical *convolution* (denoted with the symbol  $*$ ):  $h(\vec{r}_{12}) = c(\vec{r}_{12}) + \rho(c * h)(\vec{r}_{12})$ . A closure relation is a relation or operation that results in a member of a group when 'fed' one or multiple members of the group (it is a term stemming from group theory; the group is closed under these operations). For the OZ equation, several closure relations have been proposed in the form of approximations. For example, the Percus-Yevick (PY) closure relation introduces the approximation [137]:  $c(r) = e^{-\beta w(r)} - e^{-\beta[w(r)-u(r)]}$ , yielding as a closed form of the OZ equation:

$$e^{-U(r_{12}/k_B T)} = 1 + \rho \int [e^{-U(r_{13})/k_B T} - 1] e^{-U(r_{13}/k_B T)} h(r_{23}) dr_{23}. \quad (3.7)$$

For purely hard-sphere potentials, the PY approximation has an analytical solution [138]. The Hypernetted Chain approximation is similar to the PY approximation, but employs expansion of the indirect term of  $c(r)$  to first order. Many other closure relations exist, such as the mean spherical approximation (MSA) [139] and the thermodynamically consistent Rogers-Young (RY) closure [140].

For systems with close to hard-sphere interactions, the PY closure relation gives good results [141], while for soft spheres, the HNC approximation is more adequate.  $U(r)$  is then [132]:

$$U(r) = w(r) + \begin{cases} nk_B T I(r), & \text{for the HNC closure relation.} \\ k_B T \ln[1 + nI(r)], & \text{for the PY closure relation.} \end{cases} \quad (3.8)$$

Here  $I(r)$  is a convolution integral that must be calculated from  $g(r)$  as well:

$$I(r) = \int [g(s) - 1 + nI(s)][g(|\vec{s} - \vec{r}|) - 1] 2\pi s ds \quad (3.9)$$

This integral is transcendental, therefore it must be calculated iteratively until it is constant, starting with  $I(s) = 0$  in the first iteration step [142]. The calculation is rather heavy, and is only accurate for low areal densities  $n$  [143].

Most studies are devoted to finding a two-dimensional RDF, due to the experimental difficulty of (nearly) simultaneously measuring all particles in a three-dimensional environment. Therefore, particles are oftentimes confined to a 2D plane and the 2D RDF is studied (note that this 2D RDF can differ from the 3D RDF [140]). The first 3D  $g(r)$  measured by confocal microscopy of a colloidal liquid was that of Ref. 144, but there are some relevant other publications on long-ranged repulsive charged colloidal systems already published as well, see for instance Refs. [145,146]. Confinement of particles to a 2D plane can be done simply by gravity, as in Ref. [132] in which particles were allowed to sediment onto a glass capillary wall. In such a set-up, the particles will nevertheless move in and out of the 2D plane due to Brownian motion. Such a system is not purely 2D, and some error in the apparent 2D RDF as compared to the 'real' 2D RDF is to be expected. For this reason, some studies have been dedicated to measuring  $g(r)$  in confinement between two plates, e.g. Ref. 143. The charge of the glass plates of a sample cell is exploited to confine the particles midway between the plates. Some out-of-plane motion still remains in such a set-up, but in Ref. 143 the estimated error in the separation distance was only 14 nm.

Kepler and Fraden [143] carried out an in-depth study of pair potentials of polystyrene particles in deionized water. They found that the particles experienced a weak attraction ( $-0.2k_B T$ ). This potential minimum could not be explained as a van der Waals attraction, because when the potentials were fitted to a DLVO-potential, the calculated Hamaker constants were an order of magnitude higher than known from previous experiments and theoretical calculations. Kepler and Fraden therefore speculate that the particles experience an as yet unknown attractive force that is a result of the electrostatic influence of the glass plates. Crocker and Grier later confirmed the existence of a long-ranged attractive component in an optical tweezers study on polystyrene sulfate spheres of various diameters in water [147]. However, in experiments with silica particles in deionized water near a charged wall (confined to a height of  $\sim 0.9\mu\text{m}$  above the bottom wall by gravity, with the top glass wall positioned at a height of  $200\mu\text{m}$ ), a purely repulsive interaction potential was reported [132]. Later it was found that for a wall spacing of only  $9.0\mu\text{m}$ , an attractive component in the pair potential was found for these silica particles in deionized water as well. Grier and Han proposed that the distribution of counter-ions extending from the wall is modulated by the presence of the silica particles (which carry the same charge as the glass wall) [148]. This modulation was modeled as a charge  $q$  positioned between two particles. When this charge was incorporated into Eqn. 3.1, the expected pair potentials agreed very well with the experimentally found potentials.

Royall *et al.* studied pair potentials in dispersions of polymethylmethacrylate (PMMA) spheres in a low-polar medium (cyclohexyl bromide, CHB), in 3D and for various densities [144]. The interactions in the system were consistent with a (pairwise) Yukawa potential that did not depend on density. The authors found no anomalous behavior, except relatively short after preparation, e.g. extremely large Debye lengths, but no anomalous attractions. Anomalous behavior was found however in case gradients in the concentration of background ions were created artificially [144] and it was also reported by Royall *et al.* that a reduction in the surface potential for sterically stabilized PMMA particle in the same CHB was responsible for reentrant crystallization and melting at different volume fractions [149]. We are well aware that the presence of attractions in charged colloidal sphere systems

interacting with long-ranged repulsive potentials has literally created hundreds of papers about their experimental description and theoretical explanation, including several controversies. Here is not the place to review this extensive set of literature and we will simply refer to a selection of review papers on the subject, Refs. [150–152] and Refs. [153–158].

### 3.1.2 Thermogravimetric analysis (TGA)

One of the properties defining surface-modified silica is the grafting density, which is the number of grafting molecules per surface area (usually expressed in groups/nm<sup>2</sup>). One method that can be employed to gain information on the grafting density is thermogravimetric analysis (TGA). In TGA measurements, a sample is placed on a balance in a heating chamber filled with an inert gas. The sample is heated, and the mass of the sample is monitored as a function of temperature. This method yields information on the temperatures at which certain combustion processes of the sample occur. In the case of surface-modified silica, it is important that the surface to volume ratio of the silica particles be high, for otherwise mass loss contributions from the grafting layer will be negligible in comparison with the mass loss from the silica. Consequently, the silica colloids used in TGA measurements must be small. As a crude estimate: if the grafting layer were 1 nm thick and of similar density to the silica, the particle size must be below 67 nm for the surface layer to comprise of more than 0.5% of the total mass.

### 3.1.3 Micro-electrophoresis

Here, we briefly discuss electrophoresis; for a discussion on other effects of colloids in electric fields, see section 7.1. Charged colloids in a medium are surrounded by a layer of ions called the *electrical double layer* (EDL, referring to the co- and counterions surrounding the colloids, where the former are repelled and the latter attracted to the colloid). Several models have been proposed for the internal structure of this layer since the nineteenth century, most notably the Helmholtz model in 1853 [159], the Gouy-Chapman diffuse layer point-charge model in 1913 [160,161], the Stern model in 1924 [162], and the Grahame model in 1940 [163]). In the Stern model, the layer closest to the colloid consists of ions adsorbed on the surface (the *Stern layer*). The second layer is a diffuse layer of ions co-moving with the colloid, which is separated by the *slipping plane* from co- and counter-ions that do not move with the colloid. The potential at the slipping plane is called the  $\zeta$ -potential and is generally assumed to be measured in electrophoresis [164–168].

*Electrophoresis* is the motion of a colloid in an electric field  $E$  as a result of the charge  $Q$  on the colloid. The charged colloids experience a force  $F$  pulling them towards the oppositely charged electrode:

$$\vec{F} = Q\vec{E} \quad (3.10)$$

The mobility  $\mu_e$  of the particle obtained in this process, which is affected by for example the viscosity

of the solvent and drag forces due to the particle shape, is defined as:

$$\mu_e = \frac{v}{E} \quad (3.11)$$

with  $v$  the speed obtained by the particle. The total charge  $Q$  of the particle is of course influenced by the ions in the electric double layer. Von Smoluchowski proposed in his 1903 paper [169, 170] that in the limit of a thin double layer:

$$\mu_e = \frac{\epsilon_m \epsilon_0 \zeta}{\eta} \quad (3.12)$$

with  $\eta$  the dynamic viscosity of the medium and  $\zeta$  the *zeta potential*. The Smulochowski equation is only valid in the limit of a thin double layer, i.e.  $\frac{\sigma}{\lambda_D} \ll 1$ . In the limit of a large double layer, a better approximation was given by Hückel [171]:

$$\mu_e = \frac{2}{3} \frac{\epsilon_m \epsilon_0 \zeta}{\eta} \quad (3.13)$$

Typically, the Smoluchowski limit is a good model when  $\frac{\sigma}{\lambda_D} > 10$  and the Hückel limit when  $\frac{\sigma}{\lambda_D} < \frac{1}{10}$ . Henry proposed that for intermediate  $\kappa\sigma$  [172]:

$$\mu_e = \frac{2}{3} \frac{\epsilon_m \epsilon_0 \zeta}{\eta} \cdot f_1(\kappa\sigma) \quad (3.14)$$

in which  $f_1(\kappa\sigma)$  is a function which depends on the particle shape.

The above limiting cases presume dilute dispersions. Many theoretical approaches have been proposed to account for more concentrated dispersions, where interactions between particles affect the electrophoretic mobility [173–176]. The field is too broad to discuss all theories and models here. Carrique *et al.* proposed a theory to predict electrophoretic mobilities for arbitrary zeta potential, particle concentration and double layer thickness, even allowing double layer overlap [177]. Their work, based on the Kuwabara cell model to account for particle-particle interactions, yielded a set of differential equations that can be numerically solved to obtain the mobility for a given volume fraction, double layer thickness and zeta potential.

### 3.1.4 Aim of this chapter

Many of the patchy particles in this thesis possess a partially or entirely n-alkyl-grafted silica surface. The word 'grafted' signifies here that a monolayer of linear alkane molecules is chemically attached to the (Stöber silica) surface to make them more easily dispersible in less polar liquids. This chapter contains experiments with the goal of understanding the properties of such silica surfaces, in particular the grafting density, surface charge or  $\zeta$ -potential, and electrical double layer in the low-polar solvent CHC. We specifically aim to compare silica particles grafted with octadecanol and OTMOS, since these molecules have identical carbon chain length ( $C_{18}$ ) but have different functional groups and synthesis protocols. Any differences found between the two types of particles must be related to the synthesis process or the functional groups.

## 3.2 Experimental details

### 3.2.1 Chemicals

Solvents used were ethanol (absolute, *Merck*), toluene ( $\geq 99.5\%$ , *Sigma Aldrich*), cyclohexane ( $\geq 99.8\%$ , C100307, *Sigma Aldrich*) and cyclohexyl chloride (CHC, for synthesis, *Merck*). Water was deionized with a MilliQ system (Millipore Corporation) and had a resistivity of at least  $18.2 \text{ M}\Omega \cdot \text{cm}$ . Catalysts aqueous ammonia (25 wt.%) and butylamine (99.5%) were purchased from *Sigma Aldrich*. The non-ionic liquid surfactant Igepal CO-520 was obtained from *Sigma Aldrich* (number average molar mass  $M_n$ : 441 g/mol). Modifying agents were octadecyltrimethoxysilane (OTMOS, 95% (85% n-isomer), ABCR GmbH & Co via Gelest, Inc.) and octadecanol (95%, *Aldrich*). Tetraethyl orthosilicate (TEOS, 98%) was obtained from *Aldrich*. All chemicals were used as received without further purification, except for CHC, which was deionized by adding activated alumina ( $\text{AlO}_2$ , activated/neutral/Brockmann I, *Sigma Aldrich*) for several hours and dried over molecular sieves (*Acros Organics*, 4Å, 10-18 mesh) for at least a day. The conductivity of the CHC was measured with a *Scientifica model 627* conductometer connected to a probe which fitted  $\sim 3.8 \text{ mL}$  of liquid.

### 3.2.2 Particle synthesis and thermogravimetric analysis (TGA)

Silica particles of 35 nm (TEM, polydispersity 6%) were synthesized by micro-emulsion synthesis according to the following recipe [178]: 500 mL cyclohexane was mixed with 26.6 mL Igepal and 3.0 mL aqueous ammonia (25%), to which 3.1 mL TEOS was added under stirring. The mixture was left undisturbed for nine days. Afterwards, the particles were washed with ethanol by ultracentrifugation.

The batch of particles was divided into three portions. One portion was not modified and served as a blank sample. The second portion was modified with OTMOS [131] by the anhydrous method introduced in Ch. 2: 60 mg of dried silica was placed in a mixture of 5 mL toluene, 0.25 mL butylamine and 0.5 mL OTMOS. The mixture was sonicated for 1.5h. Then, another 0.25 mL of OTMOS was added and the mixture was sonicated for 1.5h again. The particles were washed several times with fresh toluene. The last portion was modified by octadecanol via the method of van Helden [119]. An amount of 13.8 g octadecanol was dissolved in 32.2 mL ethanol in a round-bottom flask at  $75^\circ\text{C}$ . The silica nanoparticles in ethanol ( $\sim 200 \text{ mg}$ ) were added under stirring, and the ethanol was removed by distillation at  $95\text{--}115^\circ\text{C}$ . An amount of 20 mL 1-propanol was added to ensure that the mixture was above the azeotrope of ethanol and water. The propanol was distilled away at  $125^\circ\text{C}$ . The mixture was placed under a nitrogen atmosphere and heated to  $190^\circ\text{C}$  for 16 hours. The mixture was allowed to cool to  $70^\circ\text{C}$  and mixed with n-hexane. The particles were washed an additional four times with hexane to remove octadecanol remnants.

The silica samples were dehydrated in an oven at  $150^\circ\text{C}$  for two days before TGA measurements were carried out, in order to remove physisorbed water. TGA measurements were performed on a *Pyris*<sup>TM</sup> 1 TGA of *PerkinElmer*.

### 3.2.3 Radial distribution function measurements and simulations

Fluorescent core-shell silica particles of diameter  $1.4\ \mu\text{m}$  ( $1.404\ \mu\text{m}$  by SLS,  $1.384\ \mu\text{m}$  by TEM) were grown by the method of van Blaaderen & Vrij [179]. The synthesis conditions for these colloids is described in detail in Ref. [180,181]. In short, on fluorescently (fluoresceine isothiocyanate, FITC)-labeled organosilica particles ( $386\ \text{nm}$ , large enough to resolve by confocal microscopy) as seeds, silica was precipitated by the Giesche method [182] until the final particle diameter of  $1.4\ \mu\text{m}$  was reached. The particles were either grafted with octadecanol by the method of van Helden *et al.* [119] or grafted with OTMOS by the anhydrous method, both as described in the previous section (sec. 3.2.2). The particles were dispersed in CHC by adding CHC to a known amount of dried silica. The dispersion was mixed using an *IKA RH Basic* lab mixer until few (at highest 1 in 20) dimers and clusters were observed in the dispersion by confocal microscopy. The resulting stock dispersion was diluted with CHC to obtain lower particle densities. The CHC was deionized before use as described in Section 3.2.1. The conductivity of the solvent amounted to  $10\text{-}20\ \text{pS/cm}$  before solvent preparation and cell filling, except for one sample which was prepared with CHC of conductivity of  $200\ \text{pS/cm}$ .

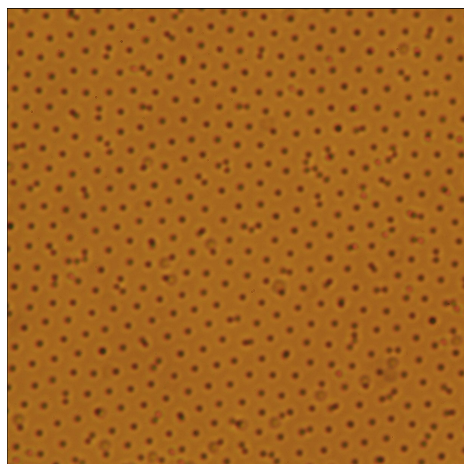


**Figure 3.1:** Optical microscope image (HPX Fluotar 63x/NA=0.70 air lens) of a long-range crystal of octadecanol-grafted colloids in CHC.

Dispersions of silica particles in CHC of various volume fractions were prepared. Dispersions with a silica content of  $10\ \text{g/L}$  in CHC resulted in the formation of long-range crystals in the sample cell, as displayed in Fig. 3.1; other dispersions were obtained by diluting this dispersion with more CHC.

RDF measurements were performed in confined geometry, in order to reduce Brownian displacements out of the plane, and thus be able to study nearly two-dimensional systems. To this end, two-dimensional glass cells were prepared. Glass cover slips (Menzel-Gläser no.0 or no.1) were cleaned with ethanol and grafted with OTMOS by placing the cover slips in a mixture of  $10\ \text{mL}$  toluene,  $1\ \text{mL}$  butylamine and  $1\ \text{mL}$  OTMOS for 24h. Two glass cover slips were glued together by two thin lines of glue (Pattex, Uni-rapide), creating a thin channel in the middle of the cell. The cell was glued to a cover slide (Menzel Gläser, Thermo Fisher Scientific), then filled with the desired dispersion, and sealed with UV-curable glue (Norland Optical Adhesive No.68). The cell was used on the day of preparation.

The dispersions were investigated by CLSM using a Leica SP8 confocal microscope equipped with a  $100\times$  confocal oil immersion objective (Leica HCX Plan Apo STED Orange,  $\text{NA} = 1.4$ ) and LAS-AF imaging software. Images were recorded with a at a scanning speed of  $600\ \text{Hz}$ , and with a line averaging of two. Typical image sizes were  $60\times 60\ \mu\text{m}^2$  to  $150\times 150\ \mu\text{m}^2$  at a resolution of  $1024\times 1024$  pixels, i.e. the pixel size was typically  $60\times 60\ \text{nm}^2$  to  $150\times 150\ \text{nm}^2$ . Time between

images was 3 s - 5 s, and recording a single image took 1.15 s. The number of images per time series varied from 870 to 4000 depending on the areal density of the sample. Areal densities were determined by counting the number of particles in a single frame of the time series and dividing by the image size in  $\mu\text{m}^2$ . The cell height at the recording position was determined by making a z-stack in reflection mode: the position of the glass cover slips is revealed by a peak in scattering intensity. Areal densities for these samples were determined by counting the particles in a single frame and dividing by the frame size.

For a 2D system, the Stokes-Einstein relation for the diffusion of the spherical particles in a dispersion is  $\langle r^2 \rangle = 4D\tau_B$  (with  $\langle r^2 \rangle$  the average distance over which the particles diffuse from their initial positions, and  $D = \frac{k_B T}{6\pi\eta R}$  the diffusion constant for  $k_B$  the Boltzmann constant,  $T$  the absolute temperature,  $\eta$  the solvent's dynamic viscosity and  $R$  the particle radius). The Brownian diffusion time  $\tau_B$  is defined as the time it takes for a particle to diffuse over its own radius  $a$ , so in the 2D case  $\tau_B = \langle a^2 \rangle / 4D$ . For particles of size  $1.4 \mu\text{m}$  in the solvent CHC ( $\eta = 1.5675 \text{ mPa}\cdot\text{s}$  at  $25^\circ\text{C}$  [183]),  $\tau_B$  equals 0.6 s. Possibly, the diffusion constant was slightly reduced (up to 10%) due to coupling between the charged particles and the counter-ions, since the Debye length can be on the order of the particle size [184]. The time between movie frames (3 s-5 s) in these experiments was long enough that the frames are uncorrelated.

Images were converted to gray scale using the image analysis program *ImageJ*. The particles positions were tracked with *Interactive Data Language* (IDL) software. The 2D RDF was extracted with the help of the IDL routine '*ericgr2d*', developed and released by Eric Weeks, John Crocker and David Grier [184]. Peaks in the RDF resulting from dumbbells diffusing into the time series were removed manually from the graphs. For iterative solution of Eqn. 3.9 to calculate the pair potential, we employed a program written in *Mathematica*. Fits to  $w(r)$  were obtained using the 'NonlinearModelFit' function in *Mathematica*.

RDFs were also predicted on the basis of the experimentally obtained  $w(r)$  by means of Monte Carlo simulations, performed by S. Dussi at the Soft Condensed Matter Group at Utrecht University. A hard-core Yukawa potential was fitted to the experimental  $w(r)$ , to obtain estimates for the contact potential. Then, MC simulations were performed in the NVT ensemble for 2D hard-core Yukawa discs with these values for the contact potentials, at the packing fractions measured in the experiments (as well as variations on this packing fraction). Each simulation comprised a total number of  $N = 1000$  particles. After 10,000 MC steps of equilibration, 50,000 MC steps were performed in which the radial distribution function was averaged over 100 independent configurations.

### 3.2.4 Micro-electrophoresis and electrophoresis experiments)

Dispersions were prepared by drying octadecanol-grafted or OTMOS-grafted silica particles (synthesis described in the previous section, sec. 3.2.3) under nitrogen flow, weighing the particles, and dispersing the particles in CHC (deionized as in sec. 3.2.1) at a volume fraction of  $\phi = 0.02$ . These dispersions were then shaken on a lab mixer *IKA RH Basic* until few dimers were visible in the dispersion by light and confocal microscopy. The dispersions acted as stock dispersions to be diluted with deionized CHC. The volume fraction used in micro-electrophoresis was  $\phi = 0.002$ . At the volume

fraction of the stock solution ( $\phi = 0.02$ ) no micro-electrophoresis could be carried out due to strong flows in the capillary. In the dilute dispersion ( $\phi = 0.02$ ) such distorting flows were nearly absent and micro-electrophoresis was possible (also as a result of the strong repulsion and large Debye length of the particles in this solvent, which prevented sedimentation).

Micro-electrophoresis experiments were carried out exactly as described by van der Linden and coworkers in Ref. 185. Electric cells consisted of a 0.1 mm x 2.0 mm x 5 cm borosilicate capillary (*VitroCom* no.5012) taped to a cover slide. Two U-shaped wire electrodes (T2 thermocouple alloy wire, composition 95% Ni, 5% Al/Mn/Si, diameter 50  $\mu\text{m}$ , *Goodfellow*) were inserted from through the ends and fixed at a separation distance of ~2 cm (see Fig. 3.2). The capillaries were treated with OTMOS beforehand to make them hydrophobic, by placing them in a mixture of 10 mL toluene, 1 mL OTMOS and 1 mL n-butylamine for 24 hours and rinsing with toluene. Capillaries were filled with dispersions of silica particles in CHC and sealed with UV-curable glue (*Norland Optical Adhesive No. 68*). We checked that no air bubbles were trapped between the electrodes, as these could disrupt the measurement. The sample cells were equilibrated in a rotating stage (rotating along the long axis) for several hours prior to measurements. Measurements were carried out by applying a DC electric field on the dispersion between the electrodes. A *Krohn-Hite 7602M* wideband amplifier was used to generate the voltages. To record the motion of the colloids in the electric field, we used a *Nikon C1* confocal microscope equipped with a 63x (NA=1.32, *Leica Achromat*) immersion oil objective. This microscope had a vertical stage, and the electric cells were placed with the capillary (and electric field) parallel to the direction of gravity. We recorded movies of the electrophoretic motion along the capillary depth  $z$ , at intervals of 6-8  $\mu\text{m}$ . Each movie consisted of 50 frames (slice thickness 0.16  $\mu\text{m}$ , resolution 512x256 pixels and size: 63.7  $\mu\text{m}$  x 31.9  $\mu\text{m}$  for octadecanol-grafted silica and 70  $\mu\text{m}$  x 35  $\mu\text{m}$  for OTMOS-grafted silica) at an average recording rate of 1.9 frames per second (519 ms per frame).

Particle charges were determined from these data by M.N. van der Linden of the Soft Condensed Matter group at Utrecht University. In short, apparent mobilities were obtained from trajectories of particles using a particle tracking algorithm by Vissers *et al.* (Ref. [186]), with the criterium that the trajectory was followed for at least five consecutive frames. In this way, the mean particle mobility  $\mu_e = v(z)/E$  was obtained as a function of depth  $z$  in the capillary. From a parabolic fit to the mobility profile we then found the mobility at the stationary level  $z_{stat}$  [185], i.e. the depth at which the electro-osmotic flow was assumed to be zero (Eqn. 3.15). Since particles did not stick to the capillary wall and since the system was nearly index-matched, we assumed the walls were located at +50  $\mu\text{m}$  and -50  $\mu\text{m}$  from the center of the parabolic fit (although it would have been more accurate to determine the walls by reflection mode, but in view of the index-matching solvent CHC this was difficult). Since the capillary depth usually varies between 90  $\mu\text{m}$  and 110  $\mu\text{m}$ , this is a source of uncertainty in our experiments. The mobility at the stationary level was converted to a

dimensionless surface potential  $e\Psi/k_B T$  and charge number  $Z$  using theory by Carrique *et al.* [177].

**Stationary plane :**

$$\frac{z_{stat}}{h} = \pm \sqrt{\frac{1}{3} + 4 \frac{2^5}{\pi} \frac{1}{k}}$$

with  $h$  the half depth of the capillary and  $k$  the ratio of width and depth of the channel

(3.15)

Two important points to be mentioned are the following. First, to cancel out the effect of gravity, the mean particle mobility was measured at each depth for a positive and a negative (but equally large) voltage, and these two mean mobilities were averaged. Secondly, for both octadecanol-grafted and OTMOS-grafted particles, we measured mobility profiles at voltages of 30 V and 50 V between the electrodes (field strengths of 1.5 V/mm and 2.5 V/mm).

We also compared micro-electrophoresis results to laser Doppler micro-electrophoresis measurements performed on a *Malvern ZetaSizer Nano ZS* machine, which measures mobilities by means of laser Doppler micro-electrophoresis. We used a *Malvern 'dip'* cell and fused glass cuvette as a probe. All mobility measurements consisted of 50-100 runs carried out in five fold and averaged. The measurement temperature was 25°C and the voltage 40 V. For data acquisition we used *Malvern Zeta Sizer software* version 5.1.

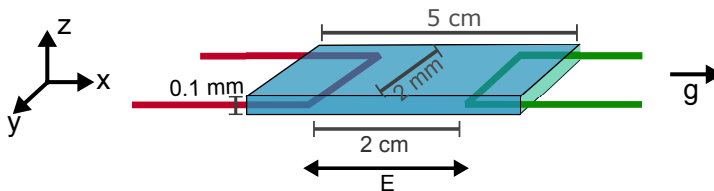


**Figure 3.2:** Schematic drawing of an electric cell used for micro-electrophoresis, indicating the dimensions of the cell, directions of the electric field and gravity, and the labels by which the axes are indicated in this chapter.

## 3.3 Results

### 3.3.1 Thermogravimetric analysis (TGA)

A batch of silica particles of 35 nm, prepared by micro-emulsion synthesis, was divided into three parts. One portion was kept as a non-modified 'blank' sample; one portion was grafted with octadecanol (octadecyl alcohol); and one portion was grafted with OTMOS (octadecyl trimethoxysilane). Samples of ~20 mg of each batch were subjected to thermogravimetric analysis. Fig. 3.3 shows the relative mass loss for each sample. The mass of the blank sample stabilized at 85.9% of its original mass, whereas the octadecanol-grafted sample and the OTMOS-grafted sample reached 81.3% and 80.0%, respectively. The mass of all samples slowly decreased upon heating to 200 °C. This relative mass loss is due to desorption of physisorbed water, as mentioned by Zhuravlev [187]. The silica had been heated for two days at 150 °C before TGA measurements were carried out, which explains why the relative mass loss in this temperature regime was moderate. The mass loss at higher temperatures is due to condensation of surface silanol groups and internal silanol groups [188, 189].

The additional mass loss of the *grafted* silica compared to the pristine silica sample in the temperature range above 200 °C is a result of the combustion of the carbon chains attached to the silica surface. There is also a small difference in mass loss between the octadecanol-grafted sample and the OTMOS-grafted sample, which is most likely related to the different molecular structure of octadecanol and OTMOS. Octadecanol has one OH-group with which it can attach to the silica surface. OTMOS molecules have three silanol groups (after hydrolysis), which can on the one hand cause steric hindrance (when not all of these groups attach to the silica), but on the other hand can also react with other silanol groups of the silane coupling agent without directly reacting with the silica silanol groups. The latter makes it hard to predict beforehand whether the OTMOS coating density would be higher or lower than that of the alcohol. The higher mass loss of the OTMOS-grafted silica compared to the octadecanol-grafted silica implies that the OTMOS-silica had a slightly higher *packing density* of C<sub>18</sub> chains at the silica surface. (Notice here that the *grafting densities* of octadecanol and OTMOS molecules to the surface is not necessarily different.)

The TGA data can be used to estimate the grafting densities on the octadecanol-grafted silica and the OTMOS-grafted silica. For every 100 g of octadecanol-grafted silica, 14.1 g of the mass loss upon heating was due to loss of water, as follows from the mass loss of the blank sample: thus, 4.6 g (19.6 mmol) of mass loss stemmed from the combustion of alkane chains. The assumption here that seems reasonable, given that all samples were heated at 150 °C for a long time, is that the water content was not changed by the octadecanol coating. The surface area corresponding to the original 95.4 g of pure silica was  $7.4 \cdot 10^{21}$  nm<sup>2</sup> (assuming a silica density of 2.2 g/mL), hence the measured mass loss implies a packing density (which is for octadecanol equal to the grafting density) of 1.6 chains/nm<sup>2</sup>. This grafting density agrees well with the one mentioned by Roke *et al.* for their octadecanol-silica (1 group/nm<sup>2</sup> [106]). According to the Zhuravlev model, the maximum density of silanols is 4.6-4.9 nm<sup>-1</sup> [187]. Thus, this grafting density corresponds to 33% of the silanol population.

Similarly, we found a packing density of 2.1 chains/nm<sup>2</sup> for the OTMOS-grafted silica. Castellano and coworkers grafted Zeosil silica (Rhodia Company) with various silanes by immersion in the silane,

solvent evaporation and heating the particles to 120 °C. They reported slightly lower grafting densities, ranging from 0.55 - 1.3 chains/nm<sup>2</sup>. Possibly, the presence of the catalyst in the present modification method increased the grafting density. According to Zhuravlev, the maximum silanol density on silica is 4.6-4.9 nm<sup>-2</sup>. Under the hypothesis of full condensation of OTMOS onto the silica surface, a packing density of 2.1 chains/nm would require 6.3 silanols/nm<sup>2</sup> since each OTMOS molecule has three silanol groups (after hydrolysis). From the previous two remarks follows that not all silanol groups (of the hydrolyzed OTMOS molecules) were attached to the silica surface. Some OTMOS molecules must have condensed with the silanol groups of hydrolyzed OTMOS molecules, resulting in a branching of the OTMOS molecules and a higher OTMOS packing density than the surface grafting density.

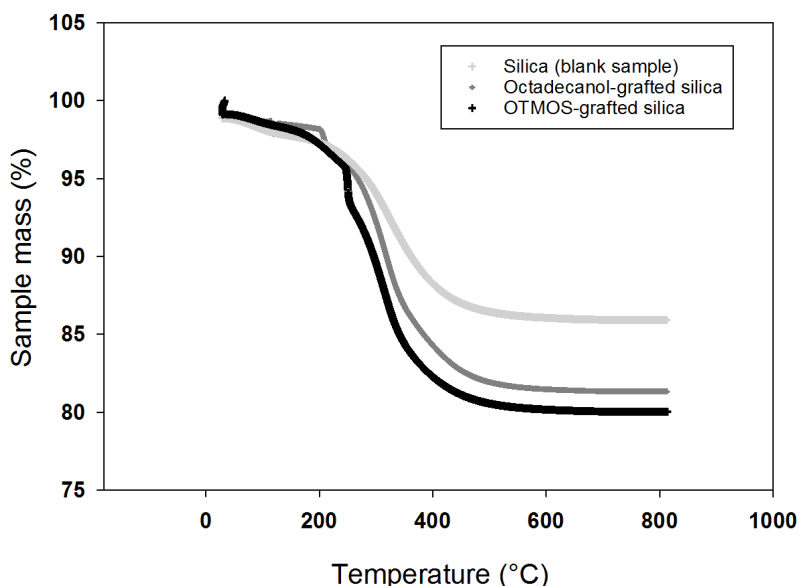
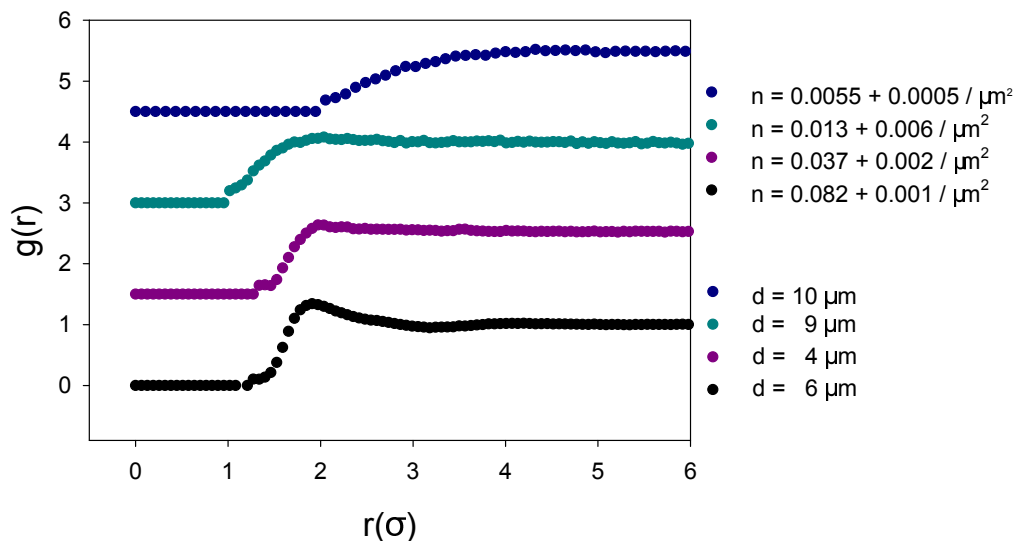


Figure 3.3: TGA results for three samples of surface-modified silica and a blank sample.



**Figure 3.4:** Radial distribution functions measured for octadecanol-grafted silica particles ( $1.4 \mu\text{m}$  in diameter) in CHC at various areal densities. The graphs are offset vertically for clarity. Distance (horizontal axis) is indicated in particle diameters. The cell heights were sufficiently small to confine the particles in the middle of each cell. The sample represented by the cyan graph was prepared with CHC of conductivity  $200 \text{ pS/cm}$ , while the other samples were prepared with CHC of conductivity  $20 \text{ pS/cm}$ .

### 3.3.2 Radial distribution functions

Radial distribution functions were measured to gain information on the pair potential in systems of various areal densities, see Fig. 3.4. The RDFs for areal densities  $n = 0.082 \mu\text{m}^{-2}$ ,  $n = 0.037 \mu\text{m}^{-2}$  and  $n = 0.006 \mu\text{m}^{-2}$  (for which the system is a fluid) have first peaks at respectively  $(1.91 \pm 0.06) \sigma$ ,  $(1.97 \pm 0.06) \sigma$  and  $(2.04 \pm 0.06) \sigma$ . As also found by Carbajal-Tinoco *et al.* for polystyrene particles in deionized water, the position of these peaks is nearly independent of areal particle concentration in this areal density regime [136]. The cyan graph corresponds to a sample prepared with CHC of higher conductivity ( $200 \text{ pS/cm}$ ) than the other samples ( $20 \text{ pS/cm}$ ). The higher conductivity is not apparent in the position of the first peak ( $2.04 \pm 0.06 \sigma$ ), but rather in the range of the attraction; in Fig. 3.5a the potential of mean force of the sample of higher conductivity (cyan curve) has a slower decay than the potentials of samples of lower conductivity. We attempted to obtain pair potentials from the potentials of mean force by iterative solution of Eqn. 3.9, but the resulting potentials deviated appreciably from zero at large separations; we are investigating the cause of this.

The radial distribution function for  $n = 0.0055 \text{ nm}^{-2}$  (blue graph in Fig. 3.4) was smooth enough to fit a Yukawa potential  $U(r)$ . Computer simulations were used to check whether this radial distribution function was affected to a large extent by many-body interactions or attractions. The pair potential in Fig. 3.5b is a fit to the potential of mean force obtained for the sample of areal density  $n = 0.0055 \mu\text{m}^{-2}$ . The RDF calculated by Monte Carlo simulations for areal density  $n = 0.0055 \mu\text{m}^{-2}$

(green graph) from this fitted pair potential is shown in Fig. 3.5c. The experimentally obtained RDF (black graph) nearly coincides with the simulated RDF. The slight variation between the two graphs could imply a weak attractive interaction between the particles, but most likely it is a result of the uncertainty in the particle density. The RDFs for two other areal densities (red:  $n = 0.0039 \mu\text{m}^{-2}$  and blue:  $n = 0.0039 \mu\text{m}^{-2}$ ) are also shown in Fig. 3.5c. An areal density of  $n = 0.0039 \mu\text{m}^{-2}$  (which is within the error bar of the experimentally determined areal density) yields a calculated RDF that fits the experimental RDF even better. Thus, we conclude that there is no evidence for anomalous attractions in the system. Fig. 3.5d shows that the calculated RDF is comparatively insensitive to variations in the Debye length as a fitting parameter. On the other hand, Fig. 3.5e shows that  $U_0$  should be  $17.5k_B T - 25k_B T$  to obtain a good agreement between the calculated RDF and the experimental RDF, so we feel the fitted contact potential is a good estimate to the true contact potential.

Figure 3.6a displays the RDF (inset) and potential of mean force for a system of OTMOS-grafted particles in CHC ( $n = 1.21 \pm 0.17 \times 10^{-3} \mu\text{m}^{-2}$ ). The first peak in the RDF is located at  $(11.5 \pm 0.2)\sigma$ , far beyond the first peaks in the RDFs of the octadecanol-grafted particles at similar solvent conductivities ( $(2.0 \pm 0.1)\sigma$ ). The simulated RDF (Fig. 3.6c) for a hard-core Yukawa potential again shows good agreement with the RDF obtained from experiments. Although it is difficult to exclude a weak attraction or some many-body interactions in this way, these results do not give reason to believe anomalous attractions are at play. Panels Fig. 3.6c-e show that the simulated RDF is not strongly sensitive to variations in the areal density and the fitting parameters  $U_0$  and  $\lambda_D$ . On the one hand, this implies that it is meaningful to compare the experimental and simulated RDF. On the other hand, it also means that the contact potential is difficult to judge by fitting a Yukawa potential.

The Debye length can additionally be estimated from the measured conductivity of the dispersion medium. Walden's rule states that the product of the limiting equivalent conductance  $\Lambda$  and the viscosity  $\eta$  is constant for different media 1 and 2:  $\Lambda_1 \eta_1 = \Lambda_2 \eta_2$  [185,190]. For water, the equivalent molar conductances of  $\text{Cl}^-$  and  $\text{H}^+$  at 25 °C are  $76.3 \text{ S cm}^2/\text{mol}$  [144] and  $349 \text{ S cm}^2/\text{mol}$  [191] respectively, so the equivalent molar conductance in water is  $\Lambda_0 = 425 \text{ S cm}^2/\text{mol}$  (consistent with Ref. [192]) and in CHC  $273 \text{ S cm}^2/\text{mol}$  ( $\eta_{\text{CHC}} = 1.56 \text{ mPas}$  [183]). This way, we find ionic strengths  $c_i = C/\Lambda$  (with  $C$  the measured conductivity) of 70 pM (for 20 pS/cm) and 700 pM (for 200 pS/cm). With these values, Debye lengths of 11  $\mu\text{m}$  (for 20 pS/cm) and 3.5  $\mu\text{m}$  (for 200 pS/cm) are expected. The latter is on the order of the Debye lengths found, but we conclude that the ionic strength was probably higher than the stated values of 20 pS/cm and 200 pS/cm. The conductivity of the CHC was measured before dispersing particles in it, and ions stemming from the colloids were not included in the conductivity value, which explains the smaller observed Debye length.

It is interesting to compare estimates for the charge per particle for octadecanol-grafted silica and OTMOS-silica in CHC. By averaging five different fits of a Yukawa potential to the experimental  $w(r)$ , we obtained fitting parameters with uncertainties: for octadecanol-grafted silica  $U_0 = (20 \pm 2)k_B T$  and  $\lambda_D = 0.89 \pm 0.03 \mu\text{m}$ , and for OTMOS-grafted silica  $U_0 = (630 \pm 160)k_B T$  and  $\lambda_D = 2.7 \pm 0.6 \mu\text{m}$ . From these fitting parameters and Eqn. 3.1, one finds  $|Z| = (109 \pm 5)$  electrons

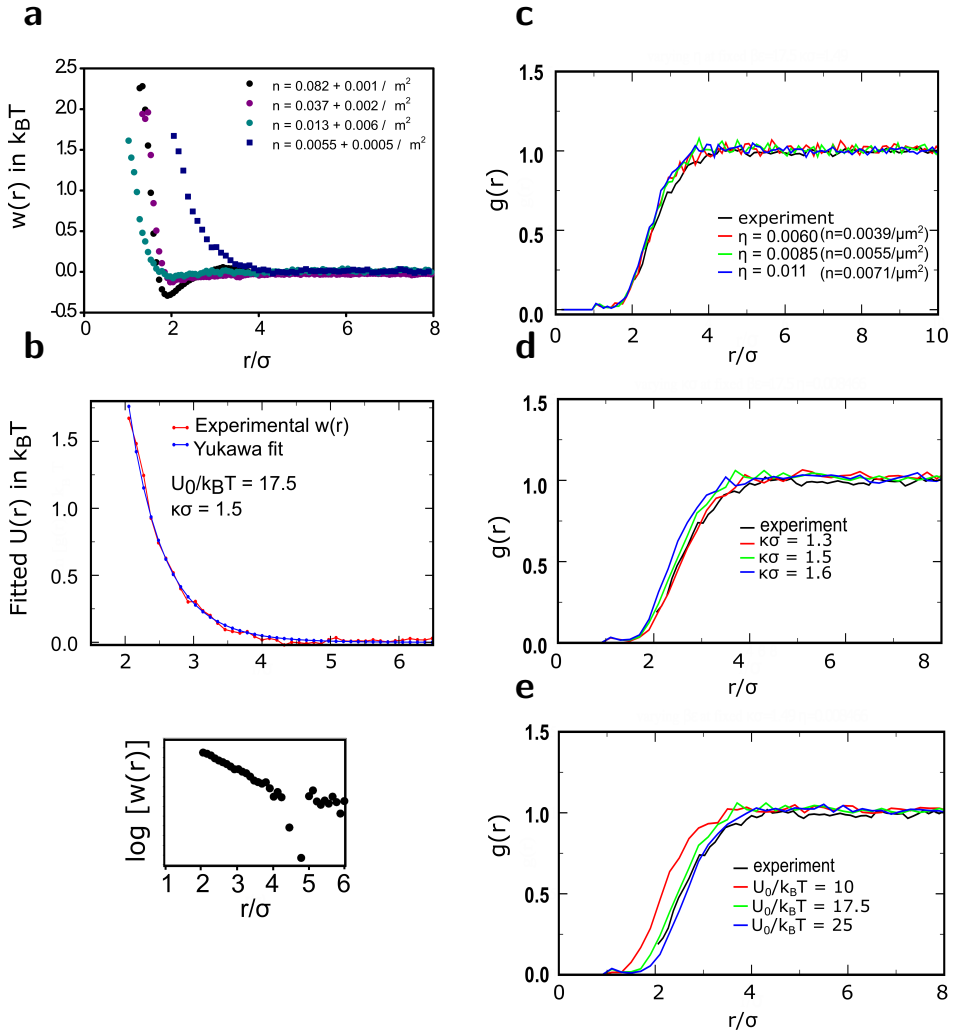


**Figure 3.5: Pair potential for octadecanol-grafted silica** (a) Potentials of mean force  $w(r)$  for samples of octadecanol-grafted silica particles ( $\sigma = 1.4 \mu m$ ) in CHC at various areal densities, calculated with Eqn. 3.5. (b) The pair potential  $U(r)$  fitted to the experimentally obtained  $w(r)$  for the sample of areal density  $n = 0.0055 \mu m^{-2}$ . The contact potential and Debye length obtained from the fit are indicated:  $U_0 = 17.5$  and  $\lambda_D = 0.67 \sigma = 0.93 \mu m$ . The inset shows  $w(r)$  on a semi log (Ln) plot: the fact that the data are linear up to  $4\sigma$  shows that the Yukawa potential (Eqn. 3.1) is a good approximation in this regime (after which the noise becomes larger than the value of the exponential). (c) RDFs simulated from the fitted pair potential of panel (b), for the measured 2D packing fraction ( $\eta = 0.0085$ , corresponding to areal density  $n = 0.0055 \mu m^{-2}$ ) and two other packing fractions  $\eta = 0.0060$ , and  $\eta = 0.011$  (corresponding to  $n = 0.0039 \mu m^{-2}$  and  $n = 0.0071 \mu m^{-2}$ ). (d) RDFs simulated from the fitted pair potential ( $U_0 = 17.5$  and  $\kappa\sigma = 1.5$ ) and for two other values of the Debye length (varying  $\kappa\sigma$ ). (e) RDFs simulated from the fitted pair potential ( $U_0 = 17.5$  and  $\kappa\sigma = 1.5$ ) and for two other values of the contact potential (varying  $U_0$ ).

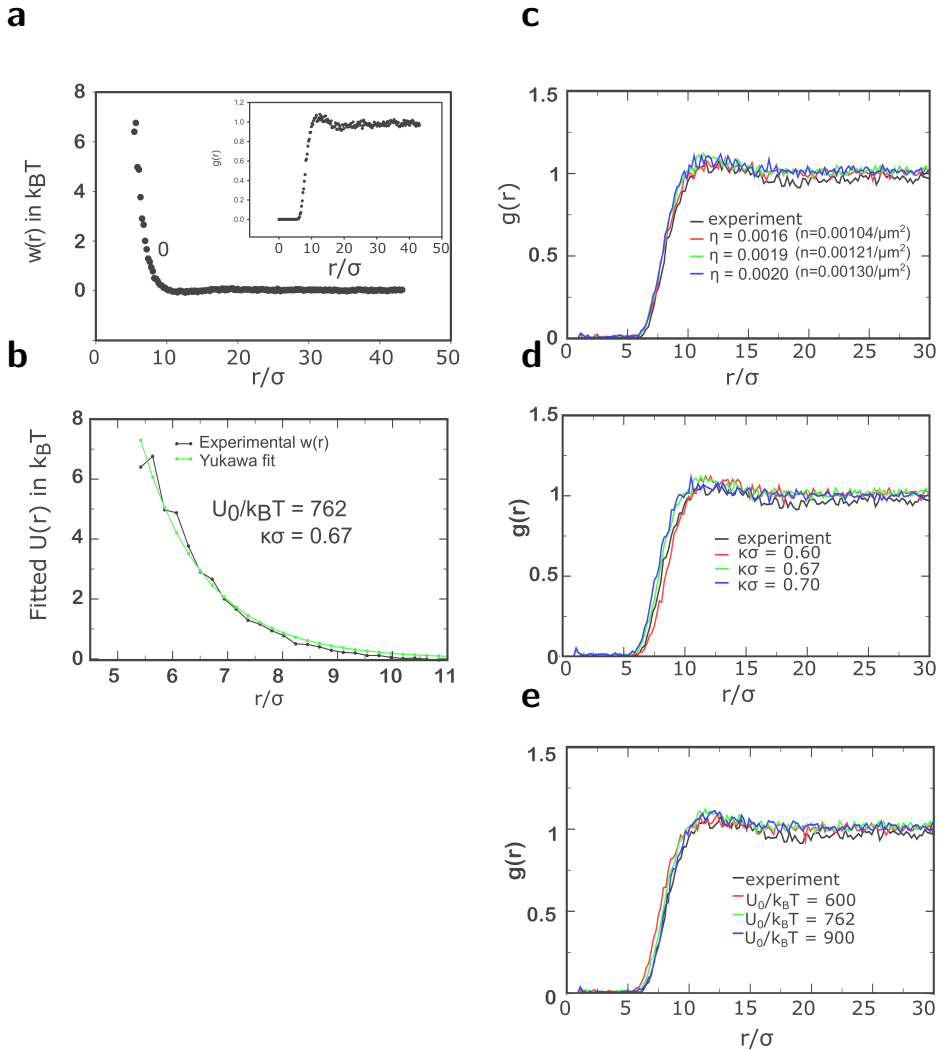


**Figure 3.6: Pair potential for OTMOS-grafted silica** (a) The RDF (inset) and potential of mean force for a sample of OTMOS-grafted silica particles ( $1.4\ \mu\text{m}$  in diameter) in CHC, areal density  $n = 1.21(\pm 0.17) \times 10^{-3}\ \mu\text{m}^{-2}$ . (b) The pair potential  $U(r)$  fitted to the experimentally obtained  $w(r)$  for the sample of OTMOS-grafted silica particles in CHC which was used for simulations. The contact potential and Debye length obtained from the fit are indicated:  $U_0 = 762$  and  $\lambda_D = 1.5\sigma = 2.1\ \mu\text{m}$ . (c) RDFs simulated from the fitted pair potential of panel (b), for the measured 2D packing fraction ( $\eta = 0.0019$ , corresponding to areal density  $n = 0.00121\ \mu\text{m}^{-2}$ ) and two other packing fractions  $\eta = 0.0016$ , and  $\eta = 0.020$  (corresponding to  $n = 0.00104\ \mu\text{m}^{-2}$  and  $n = 0.00130\ \mu\text{m}^{-2}$ ). (d) RDFs simulated from the fitted pair potential ( $U_0 = 762$  and  $\kappa\sigma = 0.67$ ) and for two other values of the Debye length (varying  $\kappa\sigma$ ). (e) RDFs simulated from the fitted pair potential ( $U_0 = 762$  and  $\kappa\sigma = 0.67$ ) and for two other values of the contact potential (varying  $U_0$ ).

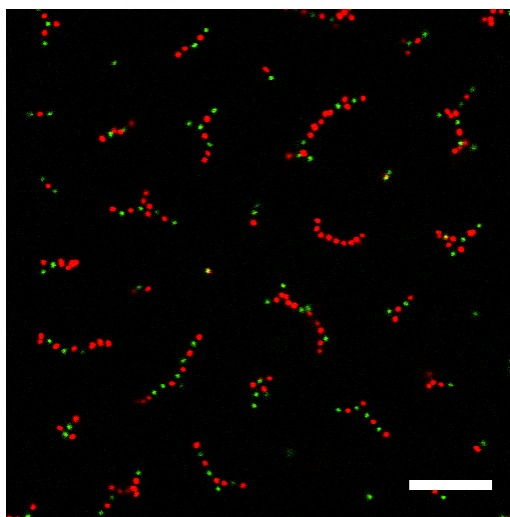


**Figure 3.7:** Strings of alternating particle type formed by mixing dispersions of OTMOS-grafted silica particles (rhodamine-labeled, red) and a sample of octadecanol-grafted silica particles (fluoresceine, green) of equal volume fractions in CHC in a one-to-one ratio. The scale bar denotes 10  $\mu\text{m}$ .

for octadecanol-grafted silica in CHC and  $|Z| = (610 \pm 70)e$  for OTMOS-grafted silica in CHC (note that the sign of the charge can only follow from electrophoresis experiments, see section 3.3.3). Thus, the charge on the OTMOS-grafted particles is significantly higher than on the octadecanol-grafted silica particles according to these results. An explanation is that the silane OTMOS introduces extra chargeable groups to the surface when compared to (grafting with) octadecanol.

Finally, we mixed a dispersion of octadecanol-grafted silica colloids (with an FITC-labeled core) in CHC and a dispersion of OTMOS-grafted silica colloids (with an RITC-labeled core) in CHC in the following way: a capillary was first filled halfway with the dispersion of octadecanol-grafted particles, and then filled up with the OTMOS-silica dispersion. After several minutes, strings of particles were encountered in the region where the two types of particles had mixed (see Fig. 3.7). These strings prevalently consisted of alternating octadecanol-grafted particles (imaged in green) and OTMOS-grafted particles (imaged in red). In view of the above results on the particle charges, we think the strings are caused by (local) recharging of the less charged octadecanol-grafted surfaces by the higher charged OTMOS-grafted particles. Such string formation was observed and reported previously by Van der Linden [193] in binary dispersions of poly(methyl methacrylate) (PMMA) particles in cyclohexyl bromide (CHB). The two particle types in those dispersions were both positive charged but had a different absolute charge due the fact that one species was chemically locked.

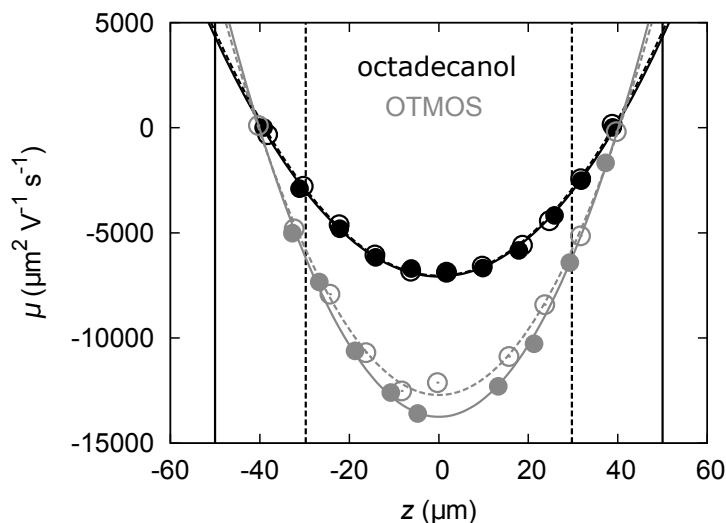
### 3.3.3 Electrophoresis and micro-electrophoresis

Micro-electrophoresis was performed on both OTMOS-grafted and octadecanol-grafted silica in CHC at volume fractions of  $\phi = 0.02$ . Both octadecanol-grafted and OTMOS-grafted particles were

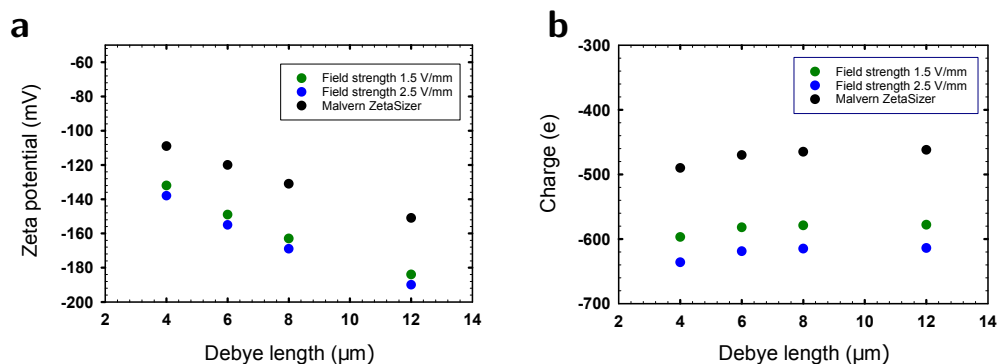
prepared from the same batch of silica particles ( $\sigma = 1.4 \mu\text{m}$ ), so that any differences in mobility observed must be due to the grafting and not the silica. Fig. 3.8 displays the mobility profiles measured for both species at two field strengths, 1.5 V/mm and 2.5 V/mm. The data are fitted well by parabolas, indicating that no disruptive flows were present in the electric cells. Since no particles were stuck to the walls in these capillaries, we assumed a capillary depth of 100  $\mu\text{m}$ , which yields stationary planes at  $z_{stat} = \pm 29.8 \mu\text{m}$  from the center. Placing the center of the parabolic fits at  $z_{stat} = 0$ , we found mobilities of  $(-3.0 \pm 0.1) \cdot 10^3 \mu\text{m}^2\text{V/s}$  for octadecanol-grafted silica and  $(-6.0 \pm 0.2) \cdot 10^3 \mu\text{m}^2\text{V/s}$  for OTMOS-grafted silica. Clearly, OTMOS-grafted silica particles had a higher mobility than octadecanol-grafted particles, which is in accordance with the results obtained from RDF measurements.

Fig. 3.9 displays the calculated zeta potential and electric charge for octadecanol-grafted silica based on the mobility profiles for various assumptions of the Debye length. The graphs show that the calculated zeta potential increases with the assumed Debye length, but the particle charge is comparatively insensitive to the screening length (averaging over the two field strengths:  $Q = (617 \pm 20)e$  at  $\lambda_D = 4 \mu\text{m}$ ). The values from micro-electrophoresis were calculated using the theory of Carrique *et al.*, i.e. by solving the full Poisson-Boltzmann equations. Therefore, the results are expected to be higher than the 'renormalised' charge and surface potential that are found by fitting a Yukawa potential (which is a solution to the linearized Poisson-Boltzmann equation) to the  $e$  potential of mean force. Indeed, the charge estimated by fitting a Yukawa potential to the potential of mean force (derived from  $g(r)$ ) was significantly lower for octadecanol-silica: only  $109 \pm 5 e$ . Unfortunately, we were not able to calculate the zeta potential and charge from the mobility profile of the OTMOS-grafted silica, since the model by Carrique *et al.* had no solutions for the measured values of the mobility.

Zeta potential measurements were also performed by means of electrophoresis using a *Malvern ZetaSizer Nano ZS* machine on the dispersions used for micro-electrophoresis of (1) octadecanol-grafted and (2) OTMOS-grafted colloids in deionized CHC (20 pS/cm) at the volume fraction used in the experiments. The measurement for OTMOS-grafted silica was performed immediately after the microelectrophoresis experiment (on the stock dispersion, not the used dispersion), while the measurement on octadecanol-grafted silica was performed a day after the microelectrophoresis. Fig. 3.10 shows the zeta potentials obtained for several acceleration voltages in the range 8 V - 20 V. These zeta potentials were calculated from the mobilities assuming that the systems satisfy the Hückel limit, but this assumption is not very reliable since there is double layer overlap, hence we have also calculated the zeta potentials of octadecanol-grafted silica from the mobilities using the model by Carrique and coworkers for various assumptions of the Debye length (included in Fig. 3.9). For octadecanol-grafted silica particles, we measured a zeta potential of  $-91 \pm 7 \text{ mV}$ . The OTMOS-grafted particles had a zeta potential peak near the limit of the operating range of the machine,  $\sim -200 \text{ mV}$  (hence this result is not very accurate). We can conclude that the net charge on the OTMOS-grafted silica particles was higher than on the octadecanol-grafted silica. The higher zeta potential of OTMOS-grafted silica compared to octadecanol-grafted silica indicates that OTMOS introduces extra hydrolyzable functional groups to the surface. In other words, some of the (hydrolyzed) methoxy-groups do not attach or link to other OTMOS molecules, and most likely provide the particles with an extra source



**Figure 3.8: Mobility profiles for octadecanol-grafted and OTMOS-grafted silica in CHC ( $\phi = 0.002$ )** Mobility profiles for octadecanol-grafted (black) resp. OTMOS-grafted (red) silica in CHC for two field strengths, 1.5 V/mm (filled symbols) and 2.5 V/mm (open symbols). The lines through the data are parabolic fits to the mobility profiles. The theoretical stationary planes (assuming a capillary width of 100  $\mu\text{m}$ ) are indicated with vertical dotted lines for clarity.



**Figure 3.9: Zeta potential and charge for octadecanol-grafted in CHC ( $\phi = 0.002$ ).** (a) Zeta potential calculated from the electrophoretic mobilities (in Fig. 3.8) measured by micro-electrophoresis using the theory of Carrique *et al.* [177], under various assumptions for the Debye length. (b) Particle charge calculated from the electrophoretic mobilities (in Fig. 3.8) measured by micro-electrophoresis using the theory of Carrique and coworkers [177], under various assumptions for the Debye length. In both (a) and (b), we also included the zeta potentials calculated using the model of Carrique *et al.* from measurements using a *Malvern ZetaSizer Nano* on the same dispersions as those used for micro-electrophoresis.

of charge in addition to the remaining surface silanol groups.

It is also interesting to study the zeta potential as a function of volume fractions, since pair potentials can be volume fraction dependent. Measurements were performed by laser Doppler microelectrophoresis (on a Malvern ZetaSizer Nano) for octadecanol-grafted and OTMOS-grafted colloids ( $\sigma = 1.4 \mu\text{m}$ ) in non-deionized CHC, at volume fractions 0.0002, 0.0005, 0.0008, 0.001, 0.005, 0.008 and 0.01. Fig. 3.11 shows the measured zeta potentials for both particle species (assuming the Hückel limit). A clear general trend is observed: the zeta potential of both particle species decreases (becomes less negative) with volume fraction. The zeta potential of OTMOS-grafted silica was more negative than that of octadecanol-grafted silica in the three most dilute samples, indicating that the net charge on these particles was higher. The higher mobility is consistent with the conclusion in Section 3.3.1 that some of the silanol groups of the OTMOS molecules have not attached to silanol groups of the silica surface, and provide the particles with a source of charge. At higher volume fractions, however, the zeta potential of octadecanol-grafted silica was more negative. The conspicuous jump in the zeta potential for octadecanol-grafted silica is somewhat suspicious and may be due to the dilution of the volume fractions with fresh CHC (possibly of different ionic strength) to obtain the lower volume fractions. That means that the solvent has a considerable influence on the particle charge. In future research, the ionic strength of the dispersions should be controlled more carefully.

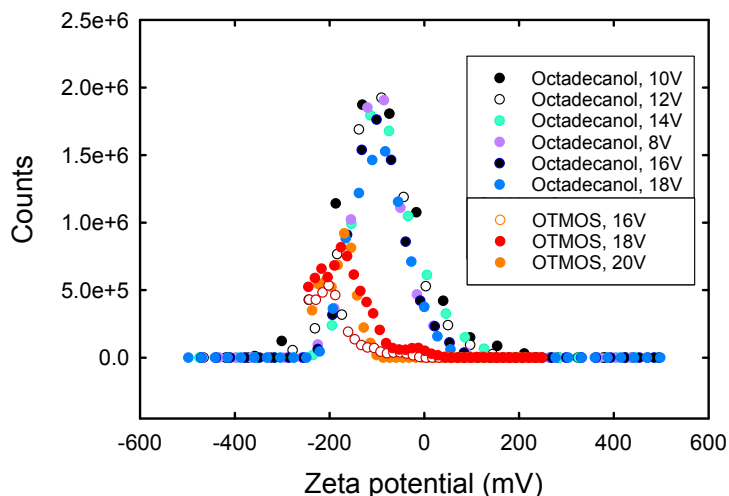


**Figure 3.10:** Zeta potentials measured for octadecanol-grafted silica particles and OTMOS-grafted silica particles in deionized CHC ( $\phi = 0.002$ ). Silica particles stemmed from the the same batch ( $\sigma = 1.4 \mu\text{m}$ ). Zeta potentials were calculated from the electrophoretic mobility under the assumption that the Hückel limit applies.

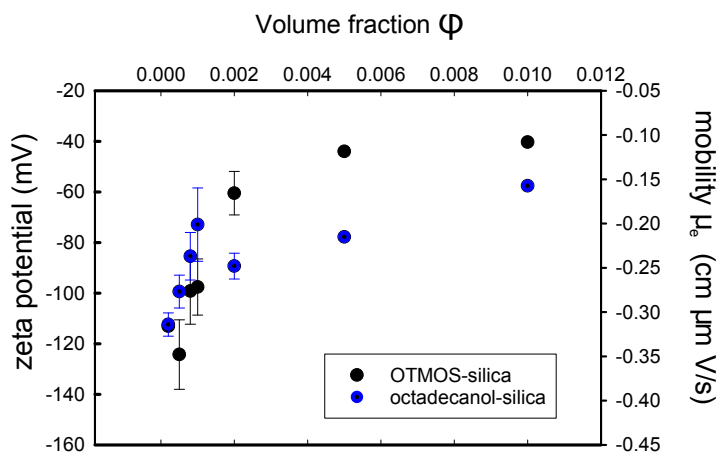


**Figure 3.11:** Results of laser Doppler microelectrophoresis measurements for dispersions of octadecanol-grafted silica particles and OTMOS-grafted silica particles of the same silica batch ( $\sigma = 1.4 \mu\text{m}$ ), at various volume fractions in CHC. Mobilities (in  $\mu\text{m cm V/s}$ ) are indicated on the right vertical axis and corresponding zeta potentials (in mV) are indicated on the left vertical axis. Electrophoretic mobilities were converted to zeta potential under assumption of the Hückel limit here; in Fig. 3.9 the mobilities were converted using the theory of Carrique *et al.* [177].

### 3.4 Summary & Discussion

In this chapter, we investigated the properties of surface-functionalized silica. The grafting density of OTMOS-grafted silica particles and octadecanol-grafted silica particles (35 nm) was determined by thermogravimetric analysis (TGA). The grafting density of OTMOS-grafted silica (2.1 chains/nm<sup>2</sup>) was slightly higher than for octadecanol-grafted silica (1.6 chains/nm<sup>2</sup>). This packing density of OTMOS chains on the surface is higher than would be possible if all the silanol groups of the OTMOS molecules were to condense with surface silanol groups, hence we conclude that OTMOS-molecules link to other OTMOS-molecules through some of their silanol groups. This branching of OTMOS molecules allows for a slightly higher packing density of C<sub>18</sub> chains on OTMOS-grafted silica than on octadecanol-grafted particles. However, this assumes the silane coupling agent coated surface is as smooth/flat as that of the octadecanol coated surface which is as stated unlikely. Electrophoresis measurements (using a Malvern ZetaSizer nano) indicated that the zeta potential of OTMOS-grafted particles in CHC was about -200 mV (near the limit of the instrument) while the zeta potential of octadecanol-grafted particles was -100 mV. Thus, the OTMOS molecules also impart extra charge to the particles by way of non-condensed hydrolyzed methoxy groups.

We derived 2D radial distribution functions for n-octadecyl-alkane-grafted silica particles in CHC by confining the particles between similarly-grafted cover slips via electrostatic repulsion and recording the configurations over time. The RDFs displayed first peaks at  $2.0\sigma$  for octadecanol-grafted silica and at  $11.5\sigma$  for OTMOS-grafted silica. Since the ionic strengths (and also fitted Debye lengths) were comparable in the dispersions, these peak locations were a first indication that the OTMOS-grafted silica particles had a higher surface charge than the octadecanol-grafted silica particles in CHC. Yukawa potentials were fitted to the experimental potential of mean force to obtain estimates for the contact potential. Simulations of the expected 2D  $g(r)$  (for discs with a Yukawa potential of the fitted contact potential) were in good agreement with the measured  $g(r)$ , i.e. we find no evidence for unusual attractions. The potentials of mean force were best approximated by Yukawa potentials with a contact potential  $U_0 = 20k_B T$  and  $\lambda_D = 0.9\mu\text{m}$  (for octadecanol-grafted silica in CHC), and  $U_0 = 20k_B T$ ,  $\lambda_D = 2.7\mu\text{m}$  (for OTMOS-grafted silica in CHC). These fitted contact potentials correspond to charges of  $Z_{\text{octadecanol-silica}} = 109 \pm 5 e$  and  $Z_{\text{OTMOS-silica}} = 630 \pm 160 e$ . Thus, the OTMOS-grafted particles carry a higher charge than the octadecanol-grafted silica particles in CHC.

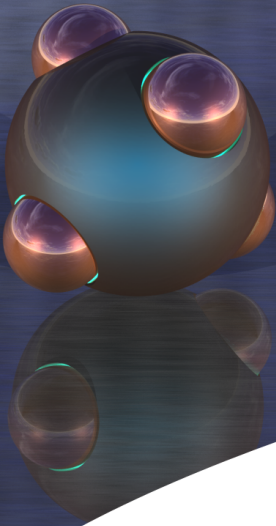
The particle charges were also investigated by capillary micro-electrophoresis. That is, the electrophoretic mobility profile was determined along the depth of a channel of rectangular cross-section, and the mobility was extracted from the stationary plane of a parabolic fit to the profile. The mobility of octadecanol-grafted silica was  $-3000\mu^2\text{V/s}$  and that of OTMOS-grafted silica  $-6000\mu^2\text{V/s}$ , yet again indicating that the charge of OTMOS-grafted silica in CHC is higher than the charge of octadecanol-grafted silica in CHC. Using the theory of Carrique and coworkers, we find that the mobility of octadecanol-grafted silica corresponds to a charge of circa  $600e$ . This charge (of octadecanol-grafted silica in CHC) found from micro-electrophoresis is higher than the charge obtained by fitting of a Yukawa potential to a measured  $w(r)$  (a 'renormalized' charge), as is expected for solutions of the full Poisson-Boltzmann equation.

Electrophoresis measurements by laser Doppler micro-electrophoresis at various particle volume

fractions indicated a strongly decreasing (less negative) zeta potential with increasing volume fraction. Future research should focus on carefully controlling the ionic strength in the dispersion - also while diluting dispersions to the desired volume fraction - to obtain more accurate values for the zeta potential as a function of volume fraction.

## Acknowledgements

TGA experiments were performed together with Bing Liu, as part of a collaboration on surface-grafted silica. Marjolein van der Linden is gratefully acknowledged for her hard work calculating the surface charges from micro-electrophoresis data. All computer simulations of the  $g(r)$  were performed by Simone Dussi, for which he is gratefully thanked. We also thank Weikai Qi for discussions and initial simulations. We thank Arjen van der Glind and Marjan Versluijs-Helder for carrying out the TGA measurements. Jacob Hoogenboom is thanked for providing the 1.4  $\mu\text{m}$  core-shell silica particles.



## CHAPTER 4

# Synthesis of patchy silica particles with silica or titania protrusions

We report methods to synthesize patchy silica particles with a hydrophobic grafting on the seed particle and with silica or amorphous titania protrusions on the patches, based upon and extended from Ref. [67]. The size (width and height) of the patches was measured and compared to a simple model. Silica protrusions were also grown along the length of rod-like particles. The titania protrusions were successfully dyed with a fluorescent dye and were imaged by confocal laser scanning microscopy (CLSM). The amorphous titania protrusions were converted to crystalline titania by sintering the patchy particles. By electron diffraction (ED), it was shown that the protrusions are of the anatase form and that the crystal size (with respect to the size of the selected area) increases with sintering time (2h or 8h at 500°C) and sintering temperature (500°C, 900°C or 1100°C).

---

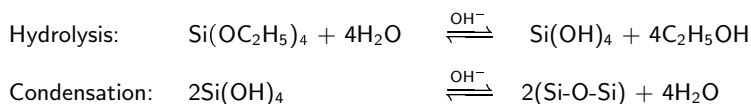


## 4.1 Introduction

In this chapter, we describe the development of a system of patchy particles with silica and titania protrusions. The synthesis method is modified and extended from earlier results by Wang *et al.* [67]. The aim was to develop a system with protrusions which are visible by confocal microscopy, i.e. which have a fluorescent dye incorporated. The latter was achieved for titania protrusions infiltrating the porous titania with a conjugate of dye and silane coupling agent. This dye infiltration step also rendered the particles stable against annealing, and the (amorphous) titania was converted to anatase titania, which may be important for applications in catalysis. In addition, the size of the protrusions - which is also important when using confocal microscopy to image the particles - was compared for various particle radii and synthesis routes.

### 4.1.1 Synthesis of silica colloids

Silica colloids are one of the most intensely studied model systems in colloid science. Spherical silica particles of well-controlled size and monodispersity were first synthesized by Stöber and coworkers [194]. In this scheme, a silica precursor (tetraethyl orthosilicate - TEOS) is added under stirring to a mixture of ethanol, water and ammonia (called a Stöber mixture). The ammonia is a catalyst for the hydrolysis and condensation of TEOS to silica. Water is added because it is required for the reaction. In practice, hydrolysis and condensation do not occur sequentially, but the balanced equations for complete hydrolysis and condensation are as follows (see Ref. [195] for equations that detail the action of the basic or acidic catalyst):



The Stöber method typically yields seed particles with a diameter up to 1.5 microns [194]. Variations in particle size can be achieved by changing such factors as the ammonia content, the water content, the solvent and the reaction temperature. The particle size can be increased beyond that of the seed particle by seeded growth: extra precursor is added in steps after the seed particles have been formed. This method was introduced by Philipse and Vrij [196] and independently by Bogush and coworkers [197], and later modified by Giesche *et al.* by using a continuous feed [182].

For laser confocal microscopy studies, it is required that particles contain a fluorescent dye. Van Blaaderen and Vrij incorporated a fluorescent dye into silica seeds by covalently coupling the dye to a silane coupling agent, (3-aminopropyl)triethoxysilane (APTES) [179]. This silane coupling agent is a molecule similar to TEOS and is incorporated into the silica matrix. APTES contains organic groups, hence the final particles are organo-silica colloids.

Stöber silica has pores smaller than 2 nm, i.e. it is microporous [119, 179], but the pore size can be increased by incorporating silane coupling agents such as also APTES [179]. Inside the core of the particle, most TEOS molecules exist as fully reacted 'Q4' species. During particle growth, Q2 and Q3 oligomers attach to the particle surface [198]. Acid-catalyzed hydrolysis is slower than

base-catalyzed hydrolysis, yielding particles with a lower cross-linking density, so particles prepared via acid-catalyzed syntheses contain more Q2 and Q3 oligomers in the interior [195].

### 4.1.2 Colloidal stability: DLVO theory

Classical DLVO theory [199–201] predicts that the total potential  $U(r)$  between two particles separated by a distance  $r$  is a sum of a repulsion  $u_R(r)$  and an attractive potential  $u_A(r)$  due to Van der Waals forces. In short:

$$U(r) = u_R(r) + u_A(r) \quad (4.1)$$

The simplest choice for the repulsive term is a hard-sphere repulsion. Hard-sphere potentials describe particles which cannot overlap in space, assuming other interactions between the particles are absent:

$$\frac{u_R(r)}{k_B T} = \begin{cases} 0, & r \geq \sigma \\ \infty, & r < \sigma \end{cases} \quad (4.2)$$

Such a repulsive term is often associated with sterically stabilized colloids in apolar solvents when the length of the grafted molecules is small compared to the particle size, such as stearyl-grafted silica colloids in cyclohexane. However, in many solvents with  $\epsilon > 2$ , some degree of charge-stabilization is present even in surface-grafted colloids, resulting in a combined 'electrosteric' stabilization [202]. As an aside, surface charge can also be generated on particles in apolar solvents with the help of surfactants, such as Aerosol-OT [203–205].

For colloidal particles with surface charge, the repulsive term in the Van der Waals potential includes an electrostatic repulsion in addition to their hard-sphere repulsion. Electrostatic repulsion is described well by a screened Coulomb (also known as "Yukawa") interaction. That is, the repulsive potential  $u(r)$  between two charged particles in vacuum is described by Coulomb's law ( $u(r) \propto -1/r$ ), but screening of the surface charge by the ions in a dispersion introduces a factor  $e^{-r/\lambda_D}$  (with  $\lambda_D$  the Debye screening length). For example, for particles with a hard core at an inter-particle separation  $r$ , the repulsive term is [190]:

$$\frac{u_R(r)}{k_B T} = \begin{cases} \epsilon_c \frac{\exp[-(r - \sigma)]/\lambda_D}{r/\sigma}, & r \geq \sigma \\ \infty, & r < \sigma \end{cases} \quad (4.3)$$

with  $k_B$  the Boltzmann constant and  $\sigma$  the diameter of the hard core.  $\epsilon_c$  is the potential at contact:  $\epsilon_c = \frac{z^2}{(1+\sigma/2\lambda)^2} \frac{\lambda_B}{\sigma}$  with  $\lambda_B$  the Bjerrum length of the medium.

The attractive term is a Van der Waals potential  $u(r) = -\frac{C}{r^6}$  with  $C$  a constant. For two spherical particles at center-to-center separation  $r$ , the Derjaguin approximation can be invoked to derive (by volume integration) that the attractive term is proportional to the Hamaker constant  $A$ :

$$\frac{u_A(r)}{k_B T} = -\frac{A}{6r} \frac{R_1}{R_2}, \quad \text{with } A = \pi^2 C \rho_1 \rho_2 \quad (4.4)$$

(with  $R_1$  and  $R_2$  the radii of the two colloidal particles and  $\rho_1$  and  $\rho_2$  their respective number of atoms per unit volume). For other particle shapes, integration of the Van der Waals potential yields similar expressions. Typical values of  $A$  are  $10^{-19} \text{ J} - 10^{-20} \text{ J}$ .

The Hamaker constant  $A$  can also be expressed in terms of the refractive index mismatch and dielectric constant mismatch between particles and medium, through estimation by the Lifshitz theory of macroscopic Van der Waals interactions. For colloids of equal material (dielectric constant  $\epsilon_p$  and refractive index  $n_p$ ) in a medium (dielectric constant  $\epsilon_m$  and refractive index  $n_m$ ):

$$A = -\frac{3}{4}k_B T \left( \frac{\epsilon_p - \epsilon_m}{\epsilon_p + \epsilon_m} \right)^2 + \frac{3h\nu_e}{16\sqrt{2}} \frac{(n_p^2 - n_m^2)^2}{(n_p^2 + n_m^2)^{3/2}} \quad (4.5)$$

An important corollary is that for a well index-matched dispersion ( $n_p \approx n_m$ ) the Van der Waals attraction will be negligible; in the first term  $\epsilon_p - \epsilon_m$  vanishes (because for any material  $n = \sqrt{\epsilon\mu}$ ), and in the second term  $n_p^2 - n_m^2$  vanishes.

The combined DLVO potential for charged spherical particles of diameter  $\sigma$  at a separation distance  $r$  is:

$$\frac{U(r)}{k_B T} = \frac{u_R(r)}{k_B T} + \frac{u_A(r)}{k_B T} = \begin{cases} \epsilon_c \frac{\exp[-(r-\sigma)/\lambda_D]}{r/\sigma} - \frac{A}{6r}, & r \geq \sigma \\ \infty, & r < \sigma \end{cases} \quad (4.6)$$

This potential has a barrier which prevents the particles from aggregating irreversibly. When the Debye layer is decreased by (for example) the addition of salt, a secondary minimum can develop which does not have a potential barrier. The salt concentration at the onset of the formation of a secondary minimum is called the critical coagulation concentration [199].

### 4.1.3 Colloidal stability of silica particles

In experiments, silica particles were found to be stable when weakly charged (i.e. at low pH) and at high ionic strength (i.e. at high salt concentrations) [206–209], both conditions under which DLVO theory predicts aggregation. However, other researchers measured aggregation rates in line with DLVO theory and only an increased stability at low pH, which was ascribed to the formation of a sterically stabilizing layer of polysilicic acid chains [210]. Colloidal stability is influenced by many factors regarding surface morphology, and that is possibly responsible for the variation in results. Stöber-type silica, for example, has a porous surface, and the concomitant apparent diminution of the Hamaker constant is a plausible reason for the remarkable stability of silica particles. Additionally, surface porosity implies that the surface charge is dependent on the size of the counter-ions in the dispersion: small metal alkali ions can enter the pores and reverse or enhance surface charge, whereas large tetra-alkyl ammonium ions cannot penetrate the pores and only screen the surface charge [210]. Another factor that influences surface charge is aging in water: it may promote the growth of the hairy polysilicic acid layer and enhance the anomalous stability at low pH [210].

### 4.1.4 Origin of the surface charge

The surface of silica is terminated with silanol (SiOH) groups. Several types of surface silanol groups can be distinguished (Fig. 4.1) [211]:

- single silanols
- vicinal (bridged) silanol groups, where the hydrogen atom of one silanol forms a hydrogen bond with the oxygen atom of the silanol next to it
- free geminal silanol groups, with two hydroxyl groups bonded to the same silicon atom
- hydrogen-bonded geminal groups, where the hydrogen atom of one hydroxyl on a geminal silanol forms a hydrogen bond with the oxygen atom of the other hydroxyl group of the geminal silanol group.

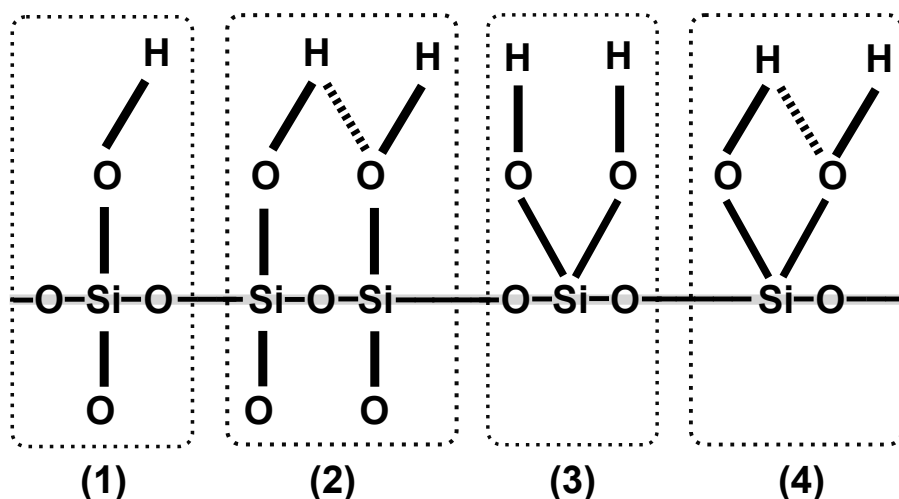


**Figure 4.1:** Schematic representation of the various silanol group configurations that can exist at the silica surface. Solid lines represent covalent bonds, while dashed lines indicate hydrogen bonds. The grey line denotes the silica surface.

The origin of the surface charge is debated, but could stem from the deprotonation of the surface silanol groups in polar solvents [210]:



Protonation occurs at low pH, i.e. at high  $H^+$  concentration. The pH value at which silica is not charged (neither protonated nor deprotonated) is called the isoelectric point (IEP). The IEP varies for different materials, but for silica lies around pH2. This value can be altered by the type of ion species - for example, chloride ions shift the IEP to higher pH - or, when dispersed in organic solvents, by trace amounts of water in the dispersion medium or in the colloids' pores [212]. Thus, the porosity of the silica plays an important role in shifting of the IEP. Stöber-type silica is known to

be porous, with pore sizes of 0.3 nm [213]. As a result, silica displays sieving properties like zeolites: small ions such as protons, hydroxyl groups, and sodium ions can enter the pores whereas large ions cannot. When the anions are small and the cations are large, the amount of negative charge on the colloids can thus be increased.

### 4.1.5 Surface modification of silica

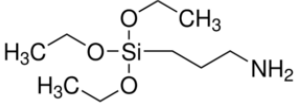
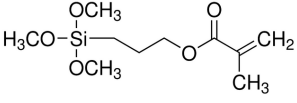
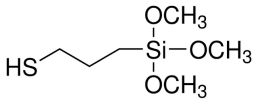
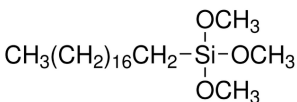
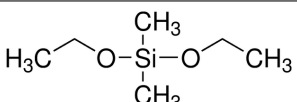
Charges do not readily dissociate in apolar solvents, hence charge stabilization is not usually feasible in these solvents (although some surfactants such as aerosol-OT are known to impart charge on particles in such dispersions [134]). To suspend silica particles in more apolar solvents, alkyl chains are often attached to the surface. These alkyl chains serve a double purpose: they make the surface more hydrophobic and they provide steric stabilization. It is important that the alkyl chains be long enough to prevent the colloids from entering the Van der Waals minimum in the inter-particle potential. For example, methylated silica particles may be hydrophobic but not sterically stabilized.

When most of the surface silanols have been replaced by alkyl chains, particles are fully sterically stabilized in apolar solvents ( $\epsilon \sim 2$ ) such as cyclohexane. Partial alkylation can render the particles hydrophobic enough for suspension in low-polar media such as cyclohexylchloride ( $\epsilon = 7.6$ ), yet not hydrophobic enough for apolar solvents. Alternatively, the number of grafted chains may not be enough to sterically stabilize the particles in apolar solvents, but in the low-polar solvent this problem may be overcome by charge stabilization. The degree of surface modification obviously depends on whether the grafting reaction has been carried out adequately, but the spacing between the alkyl chains also reflects the chemical heterogeneity of the silanols on the surface [214]. The silanol density may depend on the synthesis technique and history of the sample, such as heating.

Alkylation can be effected in three ways [104]:

1. by covalent bonding of silane coupling agents to the surface: silanization.
2. by covalent bonding of alcohols or carboxylic acids to the silica surface: etherification or esterification.
3. by adsorption of cetyl triammonium bromide (CTAB) surfactant ions or similar ions to the silica surface.

Considering silanization: silane coupling agents are molecules with a silicon atom at the center, one or more linker groups attached to the silicon atom which can react with silanols (such as methoxy and ethoxy groups or chloro groups), and one or more alkyl chains attached to the silicon atom. Some examples are given in Table 4.1. The type of alkyl chain used is essential for the surface properties of the surface modified silica. For example, the amino group of (3-aminopropyl)triethoxysilane can be protonated in water and can therefore alter the particle's surface charge. Likewise, the length of the alkyl chain is important to the hydrophobicity of the silica. On the other hand, the number of linker groups is important for the grafting density. We can differentiate between silanes based on the number of linker groups, into monomeric, difunctional and trifunctional silane coupling agents. The latter two can polymerize in the presence of water and form oligomers before reacting with the silica; a process called *solution polymerization*. Monomeric silane coupling agents and alcohols are more likely to first adsorb to the silica surface and then react; a process called *surface polymerization* [214]. Surface

| Chemical name:                            | Structure formula:  |
|---|---|
| Aminopropyl-triethoxysilane (APTES)       |  |
| Methacryloxypropyl-trimethoxysilane (MPS) |  |
| Mercaptopropyl-trimethoxysilane (MPTMS)   |  |
| Octadecyl-trimethoxysilane (OTMOS)        |  |
| Dimethyl-diethoxysilane (DMDES)           |  |

**Table 4.1:** Table of some examples of silane coupling agents.

polymerization yields a higher grafting density (up to the crystalline monolayer limit of  $8 \mu\text{mol}/\text{m}^2$ , or  $4.8 \text{ groups}/\text{nm}^2$ ) than solution polymerization ( $5 \mu\text{mol}/\text{m}^2$ , or  $3 \text{ groups}/\text{nm}^2$ ) [214]. Nonetheless, monomeric silanes with protruding non-reactive groups usually yield low grafting densities ( $2.5\text{--}3.3 \mu\text{mol}/\text{m}^2$ , or  $1.5\text{--}2 \text{ groups}/\text{nm}^2$ ) [214], conceivably due to steric hindrance at the surface.

Silanization can be carried out in polar and apolar solvents, and in this thesis we will refer to the two different methods as the *Stöber-like method* (polar) and the *anhydrous method* (apolar). The main difference between these routes is: in the Stöber-like route silica particles are stable in the solvent at the start of the reaction yet unstable at its completion, whereas in the anhydrous route the stability in the reaction solvent is reversed. Silanization by the Stöber-like route is similar to Stöber silica growth: in ethanol with aqueous ammonia as a catalyst, the silane coupling agent hydrolyzes and condenses on the surface. In the anhydrous method, silica particles are suspended in an apolar solvent with a silane coupling agent and optionally a catalyst. Hydrolysis of the silane coupling agent occurs thanks to trace amounts of water in the apolar solvent or water adsorbed to the silica surface; i.e. this method is not strictly anhydrous. Historically, the anhydrous method was applied in the area of chromatography (cf. [215–217]). Finally, silanization need not be carried out in solution, but can also happen directly from the gas phase. This route is often selected for chlorosilanes, which are highly reactive.

An entirely different method of alkylation is surface grafting with alcohols and acids. The chemical bonds formed between their respective groups and the silanol groups at the surface are ethers and esters, hence these reactions are called *etherification* and *esterification*. Like monomeric silanes, alcohols have a hydroxyl group which can condense with the silanol groups of silica, but they lack the protruding non-reactive groups that monomeric silanes have. This potentially allows for high grafting densities, hence many systems that require dispersibility in highly apolar solvents are based on etherification. Nevertheless, such dispersibility has also been reported for some silicas modified with silanes, for example by Cho *et al.* [60].

### 4.1.6 Colloidal titania

Most syntheses of colloidal titania yield amorphous titania, but this material can transform into crystalline structures under high temperature treatment. Two such polymorphs are anatase and rutile titania (an in-depth review paper on these polymorphs is in Ref. [218]). A third high-temperature polymorph, brookite (see Ref. [219]), can be formed in some recipes by controlling the pH during synthesis [220, 221]. Rutile has a lower Gibbs free energy than anatase and brookite at atmospheric pressure for all temperatures, so both anatase and brookite are metastable [218, 220, 222]. The conversion rate is low at room temperature, but can be increased by heating. For example, conversion of anatase to rutile has been observed by heating under the electron beam in an electron microscope [223]. Transition temperatures are influenced by many factors such as particle size and shape; sample volume and container; presence of impurities; heating rate; atmosphere [218]. Broad estimates are that anatase forms at 200°C - 600°C, while most studies report rapid transition of anatase to rutile titania at 600°C [218].

Titania has properties which are interesting for applications. Firstly, titania polymorphs have much higher refractive indices (between  $n = 2.3$  for anatase [224, 225] and  $n = 2.9$  for rutile [218], with various degrees of birefringence), densities ( $\rho \sim 4 \text{ g/cm}^3$  [226]) and dielectric constants (e.g.  $\epsilon = 180/90$  for rutile (along the a-axis and c-axis) [227, 228]) than amorphous silica ( $n = 1.45$ ,  $\rho = 2.0\text{--}2.2 \text{ g/cm}^3$ ,  $\epsilon = 3.8$ ). The high refractive index makes titania useful as a whitener in paints, and also for creating photonic band gaps in photonic crystals. Secondly, titania is a 'photocatalyst'. That is, titania polymorphs have an electronic band gap (respectively:  $\sim 3.2 \text{ eV}$  for anatase titania,  $\sim 3.0 \text{ eV}$  for rutile titania [218],  $3.0 \text{ eV}$  for amorphous titania [229, 230] and  $3.1\text{--}3.4 \text{ eV}$  for brookite [219]), such that illumination with (UV) light can generate excitons. The free electrons and holes can for example react with adsorbed molecules like water and oxygen to create radicals [218], which are able to undergo secondary reactions in view of their high reactivity. Therefore, titania is used for all kinds of purification processes. The electronic band gap is also the reason why titania is used in Grätzel type solar cells (dye-sensitized solar cells, DSC's). The energy of sunlight (at its maximum emission wavelength) is not high enough to excite electrons in titania directly, but in DSC's a dye is used to convert the energy of photons from sunlight into excited electrons, which flow into the titania and then towards the electrodes. Colloidal titania is also used to produce active particles [231]: titania creates ion gradients in a hydrogen peroxide solution as it catalyzes the break-down of hydrogen peroxide into hydrogen ( $\text{H}_2$ ) and oxygen ( $\text{O}_2$ ). When a colloid has titania covering its surface with a

broken symmetry, the particle will move.

#### 4.1.7 Synthesis of patchy silica particles

The synthesis route for patchy particles employed in this thesis is based upon that published by Wang *et al.* [67], although various modifications were made. In short, the synthesis procedure is as follows (see Fig. 4.2): silica particles with short ranged repulsive interactions are self-assembled into a colloidal crystal by sedimentation. The crystal is dried and sintered, then grafted with silane coupling agents, after which the crystal is disassembled into single individual particles by sonication. (Sintering entails heating the particles to such a temperature that they fuse together at the contact points. During this sintering step, contact points broaden and start to chemically link [232, 233]). During the grafting step, the silane coupling agent is size-excluded from the contact areas between the particles, in view of the finite size of the silane molecules and the fact that most spheres touch. The silica particles thus attain non-functionalized patches at the contact areas after they are forcefully broken loose. Such particles will hereafter be called “surface-patterned particles”, even though they already satisfy the definition of a patchy particle (see Ch.1) in view of their non-uniform surface properties. Finally, material is grown specifically onto the patches in order to prove their existence and to increase their surface area. The resulting particles will often be called ‘patchy particles’ in this thesis. Sintering increases the contact areas between the particles as they start to deform (visco-

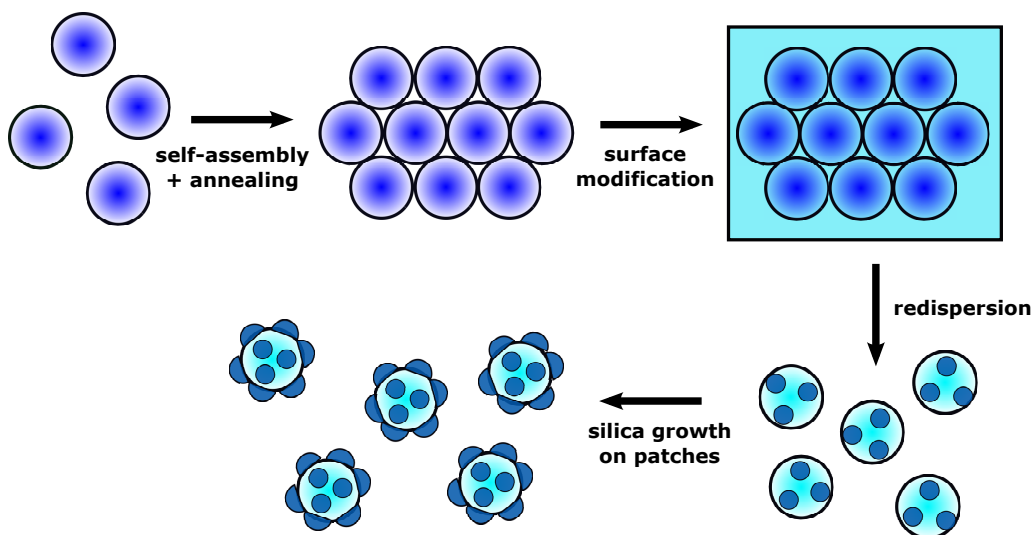


**Figure 4.2:** Schematic drawing of the synthesis route for surface-patterned particles.

)elastically [189, 234, 235]. Indeed, Wang and coworkers [67] state that they were able to tune the patch size between  $95 \pm 13$  nm and  $115 \pm 17$  nm by prolonging the sintering time from five to eight hours at a temperature of  $750^\circ\text{C}$ . They grafted the silane coupling agent 3-(methacryloxy)propyltrimethoxysilane onto the silica surface in ethanol under Stöber conditions (i.e. with ammonia and water present in

the reaction mixture). This method requires prior sintering of the particles, since many of the silica colloids in a dried colloidal crystal will disperse spontaneously when placed in ethanol.

This control over the patch size is an advantage of sintering, but there are disadvantages as well. First, sintering requires drying the crystal, and drying causes cracks due to strong capillary forces [236–244]. Cracks disrupt the order in the crystal. Sintering also results in shrinking of colloids [235,245]. Lastly, sintering degrades fluorescent dyes, while we would like to retain the dyed core for imaging purposes. In this chapter we discuss how surface modification by an anhydrous method can eliminate the need for a sintering step.

## 4.2 Experimental details

### 4.2.1 Materials & Instruments

Solvents used were ethanol (absolute, *Merck*), ethylene glycol ( $\geq 99.5$  wt%, *Fluka*), acetone (pro analysis, *Merck*) and toluene ( $\geq 99.5$  wt%, *Sigma Aldrich*). Water was deionized with a MilliQ system (Millipore Corporation) and had a resistivity of at least  $18.2 \text{ M}\Omega\text{cm}$ . The catalysts aqueous ammonia ( $\sim 25$  wt%) and butylamine (99.5 wt%) were purchased from *Sigma Aldrich*. Silane coupling agents used were: (3-aminopropyl)triethoxysilane (APTES,  $\geq 98\%$ , *Sigma Aldrich*), 3-methacryloxypropyltrimethoxysilane (MPS,  $\geq 98$  wt%, *Sigma Aldrich*, also known as 'TPM': 3-(trimethoxysilyl)propyl methacrylate) and octadecyl-trimethoxysilane (OTMOS, 95% (85% n-isomer), ABCR GmbH & Co via Gelest, Inc.). Precursors tetraethylorthosilicate (TEOS, 98 wt.%) and titanium (IV) butoxide (TBT, 97 wt%) were obtained from *Aldrich*. The dyes fluoresceine isothiocyanate (FITC,  $\geq 90$  wt% (HPLC)) and rhodamine B iso-thiocyanate (RITC, mixed isomers) were also ordered from *Sigma Aldrich*. All chemicals were used as received without further purification.

For centrifugation, a *Hettich Rotina 46S* or a smaller *Heraeus Sepatech Labofuge Ae* were used. Calcination for synthesis of silica particles with silica protrusions was carried out in a *Carbolite AAF Ashing furnace*, whereas a similar *Carbolite* oven with type 301 controller was employed for sintering of patchy particles with titania protrusions. Samples were sonicated in a *Branson 8510* or *2510* sonication bath. For high power sonication (to break up and redisperse sintered colloidal crystals) we employed a *Vibra-Cell* ultrasonic processor (750 W) from *Sonics & Materials, Inc*. Syringe pumps applied in the growth step were from *KD Scientific*, models *KDS-410* (single syringe pump) and *KDS-200-CE* (double syringe pump). *IKA RH Basic* stirrers were used for magnetic stirring during silica growth.

### 4.2.2 Synthesis methods

#### 4.2.2.1 Patchy silica particles with silica protrusions

Silica seed particles were fluorescently labeled by incorporating an APTES-dye conjugate during silica growth as introduced by Van Blaaderen and Vrij [130,179]). A non-fluorescent silica shell was grown onto the seed particles according to the continuous growth method by Giesche [182], which is a modification of the method by Bogush *et al.* [197]. The various particles used can be found in the table in App. 4.5.

Colloidal crystals were prepared from the silica colloids as follows. Particles in the size range of 200 nm to  $1 \mu\text{m}$  and of polydispersity  $\leq 6\%$  were dispersed in ethanol at volume fractions 1-5%. They were allowed to sediment in 20 mL vial with a flat bottom and form a flat, random hexagonal close-packed (RHCP) crystal [246–248]. After crystal formation, the vial was opened and the ethanol was left to evaporate at room temperature.

Some syntheses were aimed at reproducing Wang and coworkers' results [67]. In that case, pieces of crystal were placed in a ceramic cup and placed in a calcination furnace. The particles were sintered at  $750^\circ\text{C}$  for five hours with one hour heat-up time. For the grafting step, 50 mg of

colloidal crystal were placed in a mixture of 40 mL ethanol, 1.5 g H<sub>2</sub>O, 0.5 mL silane coupling agent MPS and 1 mL aqueous ammonia. The reaction mixture with the dried crystal in it was left for 24 hours, without stirring. The colloidal crystal was then washed five times with ethanol to remove non-reacted silane coupling agent. The crystal was broken up into individual particles in ethanol with an ultrasonic processor (sonication time: 30 mins. Pulses: 5 s at 1 s intervals).

Wang and coworkers grew silica protrusions onto the patches in the following way. A dispersion of 0.5 mg/mL MPS-patterned particles in ethanol was prepared. To 40 mL of dispersion, they added 5 g water and 1 mL aqueous ammonia. A TEOS solution (40  $\mu$ L TEOS in 40 mL ethanol) was added under stirring at a rate of 3.6 mL/h. After all TEOS solution were added, the reaction mixture was stirred for two more hours and finally the particles were collected by centrifugation. We used the same recipe for silica protrusions, however, all volumes were five times smaller: to 8 mL of dispersion were added 1 g water and 0.2 mL aqueous ammonia. A TEOS solution (8  $\mu$ L TEOS in 8 mL ethanol) was added under magnetic stirring at a rate of 0.72 mL/h, using a syringe pump. The silica content was not adjusted for particle size. For micron-size particles, the total amount of TEOS solution added was increased to 16 mL, still at the rate of 0.72 mL/h.

In one experiment, the influence of extended protrusion growth was studied. In this study, MPS-patterned particles were prepared as in the previous paragraph (the template particles for sample B from App. 4.5). As above, a dispersion of 0.5 mg/mL of these particles in 8 mL ethanol, 1 g water and 0.2 mL aqueous ammonia was prepared. At the same constant rate as above - 0.72 mL/h - a mixture of 24  $\mu$ L TEOS in 24 mL ethanol was added under magnetic stirring. After 17.3 mL of precursor solution had been added, 0.3 mL of aqueous ammonia was added to ensure continued growth. Four samples of 1 mL were taken from the reaction mixture during this time, washed with ethanol by centrifugation, and analyzed by TEM.

The sintering step can be circumvented by carrying out the grafting step in an apolar solvent; we call this type of grafting the 'anhydrous' route. A dried colloidal crystal was not found to redisperse when placed in such a solvent, probably as a result of the hydrophilicity of the particle surface and the limited surface charge in such a solvent. We typically placed  $\sim$ 20 mg silica crystal in a mixture [249, 250] of toluene (10 mL), butylamine (1 mL) and silane coupling agent (1 mL). The silane coupling agent was either MPS or OTMOS. The butylamine acts as a catalyst, analogously to ammonia in the Stöber-like method. The colloidal crystal was left in the reaction mixture for 24 hours, after which the supernatant was removed. The crystal was washed once with toluene, and placed in an oven at 100°C for one hour to ensure complete condensation of the silane coupling agent with the silica surface. Two additional washing steps with toluene and three with ethanol followed. Finally, the crystal was placed in ethanol and broken up by sonication with an ultrasonic processor (30 mins. at an amplitude of 25% and with pulses of 5 s at 1 s intervals). Crystals larger than a few millimeters in diameter were broken up into smaller pieces with a spatula prior to sonication, as we found that such large crystals did not break up through sonication within a reasonable time span (2h).

In one experiment, we aimed to grow silica protrusions using Stöber synthesis, i.e. by adding all TEOS at once. OTMOS-patterned silica particles ( $280 \pm 10$  nm, prepared via the anhydrous method

as in the above paragraph) were dispersed in ethanol (0.5 mg/mL silica). To 8 mL of dispersion, we added 1 mL water and 0.2 mL ammonia (25 wt%). Under magnetic stirring, a mixture of 8  $\mu\text{L}$  TEOS in 8 mL ethanol was added at once. After stirring for five hours, the particles were washed twice with ethanol.

We attempted to incorporate dye into these silica protrusions in the following way. Particles (packed in a colloidal crystal, sintered at 750°C for 5h) were surface-patterned by grafting the crystal with MPS via the Stöber-like method overnight. After washing 4 times with ethanol, the particles were dried and placed in an MPS reaction mixture again (for 24h). After washing with ethanol (4 times) and drying, the colloidal crystal was placed in an oven at 100°C for two days. The crystal was broken up into single particles by sonication with the high-power ultrasonic processor. A dispersion of 0.5 mg/mL surface-patterned particles in ethanol was prepared from these particles. To 1.5 mL dispersion we slowly added two solutions, both at a rate of 67.5  $\mu\text{L}/\text{min}$ : 1.5 mL of a solution of TEOS and 1.5 mL of a solution of dye. The TEOS solution consisted of 2  $\mu\text{L}/\text{mL}$  TEOS in ethanol. The dye solution was prepared using a recipe based on Refs. [130,179]), by first letting 5 mg APTES and 5 mg FITC react in 312  $\mu\text{L}$  ethanol in the dark for 8 hours, and then diluting 15  $\mu\text{L}$  of this solution in 10 mL ethanol. These two solutions were added to the reaction mixture with a syringe pump from separate syringes, and under magnetic stirring. After all TEOS solution and dye solution had been mixed in, the reaction mixture was left to stir for five more hours, and the particles were washed with ethanol until no coloring of the supernatant was observed.

### 4.2.2.2 Fluted rod-like particles

The procedure for growing silica patches onto silica core particles was extended to rod-like bullet-shaped particles. Spherocylinders of high aspect ratio ( $L/D > 3.7$ ) can form smectic phases [251,252]. Such phases have been found experimentally for bullet-shaped particles as well [13]. For low enough polydispersity in diameter, the rods are packed hexagonally within the smectic layers. This offers the possibility to pattern colloidal rods at the particle surface, creating elongated patches parallel to the rods' axes.

Rod-like particles were prepared according to a modified method based on Kuijk *et al.* [13] as described in Ref. [253]. The rods were left to grow for 36 hours to achieve a high aspect ratio, as needed for smectic phases and for long patches. The rods' final dimensions were: a length  $L = 2.07 \mu\text{m}$  and a diameter  $D = 0.22 \mu\text{m}$  with respective polydispersities of  $\delta_L = 8.9\%$  and  $\delta_D = 20\%$  (aspect ratio  $L/D = 9.6$ ). These silica rods were allowed to sediment in ethanol and the solvent was left to evaporate. A piece of the sediment was sintered for five hours at 600°C. The sintered crystal was grafted with MPS as described previously for silica spheres: a total of 50 mg sintered rods was placed in a mixture of 8 mL ethanol, 0.3 mL water, 0.2 mL ammonia (aqueous, 25%) and 0.1 mL MPS and left in the mixture without stirring for 24 h. The colloids in the crystal were redispersed in ethanol by sonication with the ultrasonic processor. Silica was grown onto the patches through slow addition of TEOS to a dispersion of 0.5 mg/mL of surface-patterned rod-like particles in ethanol in the following way. First, 1 mL of water and 0.1 mL of ammonia (aqueous, 25%) were added to 8 mL of the sol of rods in ethanol. Subsequently, a mixture of 16  $\mu\text{L}$  TEOS in 16 mL ethanol was

added with a syringe pump at a rate of 0.72 mL/hr. This addition rate was equal to that in Section 4.2.2.1, but the total amount of added TEOS solution was doubled. Since water is consumed in the condensation of TEOS, an extra 1 mL of water was added to the reaction mixture at the time when 8 mL precursor solution had been added by the syringe pump. After all the TEOS solution had been added, the reaction mixture was left stirring for two more hours and subsequently washed three times with ethanol.

#### 4.2.2.3 Patchy silica particles with titania protrusions

Titania protrusions were grown according to a recipe by Bae *et al.* [254]. We prepared a solution of 200  $\mu\text{L}$  TBT in 30 mL of ethylene glycol and stirred it for 12 h-24 h. Dry OTMOS-patterned particles ( $1.12 \pm 0.01 \mu\text{m}$ ) were dispersed in acetone at a concentration of 2 mg/mL. To 40 mL of this dispersion, we added 100  $\mu\text{L}$  water (needed for hydrolysis of the TBT). Under magnetic stirring, we then added 0.5 mL of the TBT solution. The reaction mixture was left stirring overnight and the patchy particles were collected by centrifugation and washing with ethanol.

The titania protrusions were dyed successfully with a fluorescent dye. The dye molecules can penetrate the porous titania, as already shown before by Demirörs *et al.* [225]. A solution of RITC coupled to APTES was first prepared as follows: to 20 mg RITC we added 1 g (1.27 mL) ethanol and 20  $\mu\text{L}$  APTES, after which the solution was left on rollers for a night. Since the RITC forms a conjugate molecule with the APTES, the dye could be covalently coupled to the titania protrusions. To 10 mL of a dispersion of the silica particles with titania protrusions, we added 100  $\mu\text{L}$  aqueous ammonia and 40  $\mu\text{L}$  dye solution. The dispersion was left for two hours on rollers. We washed the residual dye away by centrifuging and replacing the supernatant with fresh ethanol. The washing step was repeated until the supernatant was not visibly colored with dye anymore, which usually took three washing steps.

Some of the final particles were sintered with the objective of converting the amorphous titania protrusions into crystalline titania. Particles were dried in a ceramic cup and placed in a calcination furnace under ambient conditions. The furnace was heated to the desired temperature (500°C, 900°C or 1100°C) at a heating rate of 9°C/min. After sintering for 2 h (and one time 8 h at 500°C), the furnace was left to cool by itself. The ceramic cup was placed in a beaker with 40 mL of ethanol. The beaker was placed in a sonication bath to collect the sintered particles with titania protrusions in the form of a colloidal dispersion in ethanol.

### 4.2.3 Characterization

The shape of patchy particles was examined by transmission electron microscopy (TEM) with a *Tecnai 10* or *Tecnai 12* microscope from *FEI* company, at acceleration voltages of 100 kV and 120 kV respectively. HR-TEM imaging was performed on a *Tecnai 20 FEG* (*FEI* company) at an acceleration voltage of 200 kV. As sample holders, we used home-made TEM grids (preparation: cf. [255], on G200-Cu grids *Electron Microscopy Sciences*), onto which the particles were dropcast and dried from ethanol. Scanning electron microscopy (SEM) images were obtained utilizing a table-top *Phenom*

or a *Nova Nanolab 600 (FEI)*. Selected area electron diffraction (SAED) was also performed on the *Tecnai 20FEG* electron microscope.

Particle and patch sizes were obtained from TEM images via the software program *iTEM* (version 5.0). Particle sizes were measured as follows. A threshold was indicated for the grey value of pixels which were considered to be inside the particle cross section. Then, the image was binarized (i.e. a black-and-white image was created) and several erosion steps were performed until nearly all particles were non-touching. *iTEM* was then asked to create a 'skeleton dark' picture, which displays the Voronoi cells associated with the particle centers. Using a logical addition of the binarized image and the 'skeleton dark' image, *iTEM* can detect the (touching) particles separately. *iTEM* was asked to calculate particle perimeters from the resulting picture, and the particle diameters were calculated from these perimeters. The standard deviation of ten diameter measurements of a single particle was taken as the uncertainty in the diameter. Patch widths and heights were estimated by drawing line segments tangentially and orthogonally (respectively) to the core particle through the patch silhouette. Each measurement was averaged over at least twenty counts of different patches. The standard deviation of these measurements was used as a 'polydispersity' of the patch size.

For some particles we determined the 3D shape by electron tomography (see Ref. 256). Electron tomography is a technique for deriving the surface morphology of an object by TEM imaging. Images of the object are recorded under various angles. All images are Fourier transformed and combined. The Projection Theorem states that the 2D Fourier transform of a 2D image is equal to a 2D slice through a 3D Fourier transform of a 3D image [256–259]. A 3D inverse Fourier transform of the combined slices therefore yields a 3D image of the particle surface. The quality of the reconstruction depends on the total range of tilt angles over which the 2D images were acquired. Here, the tilt angle ranged between  $-60^\circ$  and  $+60^\circ$  and we recorded at intervals of  $1^\circ$ - $2^\circ$ .

Confocal images were recorded on a *Leica SP8* confocal microscope with a 100x oil immersion objective (*Leica HCX Plan Apo STED Orange*, designed for the purpose of STED microscopy, NA = 1.4). This confocal microscope was fitted with a white light fiber laser; we selected the wavelengths 495 nm and 543 nm to excite FITC and RITC dye, respectively. This confocal microscope is equipped with two types of detectors: photomultiplier tubes (PMT) and hybrid detectors (HyD) developed by *Leica*. HyD detectors combine a traditional PMT with an avalanche photo diode (APD), resulting in a higher sensitivity and signal-to-noise ratio's for these detectors. Fluorescent signals from the FITC and RITC dyes were recorded on such HyD detectors. Samples were usually prepared in borosilicate capillaries (*VitroCom* no.5010 or no.5012,  $n = 1.474$  at 589.3 nm). The capillaries were sealed with *Norland Optical Adhesive no.68* that was cured under UV light ( $\sim 350$  nm). For clearer imaging, cover slips are preferable over glass capillaries, since capillaries have a rougher inner surface which can scatter incoming light [260]. Sample cells were built from a borosilicate square cover slip glued to a microscope slide. Immersion oil (*Leica, Type F*,  $n = 1.52$ ) was used between the sample and the confocal lens in all confocal imaging.

## 4.3 Results & Discussion

### 4.3.1 Patchy silica particles with silica protrusions

Typical images of patchy particles grown according to the method published by Wang *et al.* are shown in Fig. 4.3. These images show that well-defined protrusions were grown onto chemically created patches, with little to no silica deposition elsewhere on the particle. Such protrusions did not appear when all TEOS was added at once; rather, the particles were then covered with a thin layer of silica. Apparently, slow addition of silica precursor is a requirement for successful protrusion growth; a possible explanation is that the formation of silica oligomers must be avoided, since these can cover the surface beyond the borders of the patches. Using electron tomography all protrusions on a particle could be visualized and their patch number determined (Fig. 4.3c,d). Often the number of patches was lower than twelve. Simulations were performed to establish how many contacts can be expected within colloidal crystals depending on polydispersity; these results are described in Ch. 5.

To quantify the patch growth, patch widths and heights were measured. Fig. 4.4 displays average patch sizes (widths and heights) measured for patchy particles of various diameters. The patchy particles indicated with green markers were prepared by the procedure of Wang *et al.* with five hours of sintering (at 750°C, except for the micron-sized particles, which were sintered at 500°C). The patchy particles indicated with red markers were prepared by the anhydrous method, i.e. without sintering. The patch width for particles of 411 nm (which is  $99 \pm 11$  nm) prepared via the method of Wang *et al.* [67] agrees well with the patch size mentioned by Wang and coworkers for their 415 nm particles (which is  $95 \pm 13$  nm). Patch sizes are larger for sintered particles than for non-sintered particles, which is as expected since sintering broadens the contact areas. Patch heights and widths follow different trends as a function of particle diameter: the average patch widths increase with particle diameter for both Wang's method and the anhydrous method, while the average patch height remains nearly constant.

Protrusion growth was studied in time by continuing TEOS addition at a constant rate after the usual reaction time (i.e. the time described in Ref. [67]: 11.11 h). Fig. 4.5a is a graph showing patch widths and heights for particles at various times during the patch growth. The surfaces of the particles with patches grown for more than 36 h were rough, because some silica had grown onto the entire surface (Fig. 4.5b). This silica deposition is probably the result of the silane coupling agent dissociating from the particle over time in the basic environment of the Stöber mixture. The patch height increased (significantly) by 15 nm between the first and the last aliquot. The increase in protrusion height can be used to influence the shape of the protrusions, but the occurrence of surface roughness after 36 h of protrusion growth limits the total growth time and amount of TEOS that can be added. Protrusions were also grown onto silica particles larger than a micron [67] (see Fig. 4.6b). The protrusions on the smaller particles were usually hemispherical, while the protrusions on these larger particles appeared flatter with the same amount of TEOS added, since the ratio between patch height and patch width decreases (see graph 4.4). As the total amount of TEOS added is the same for all particle diameters, one might expect the height to decrease with particle diameter. However, since the total silica content was kept constant for all particle diameters, the total number of particles in the reaction mixture also decreased with size, and the two effects nearly

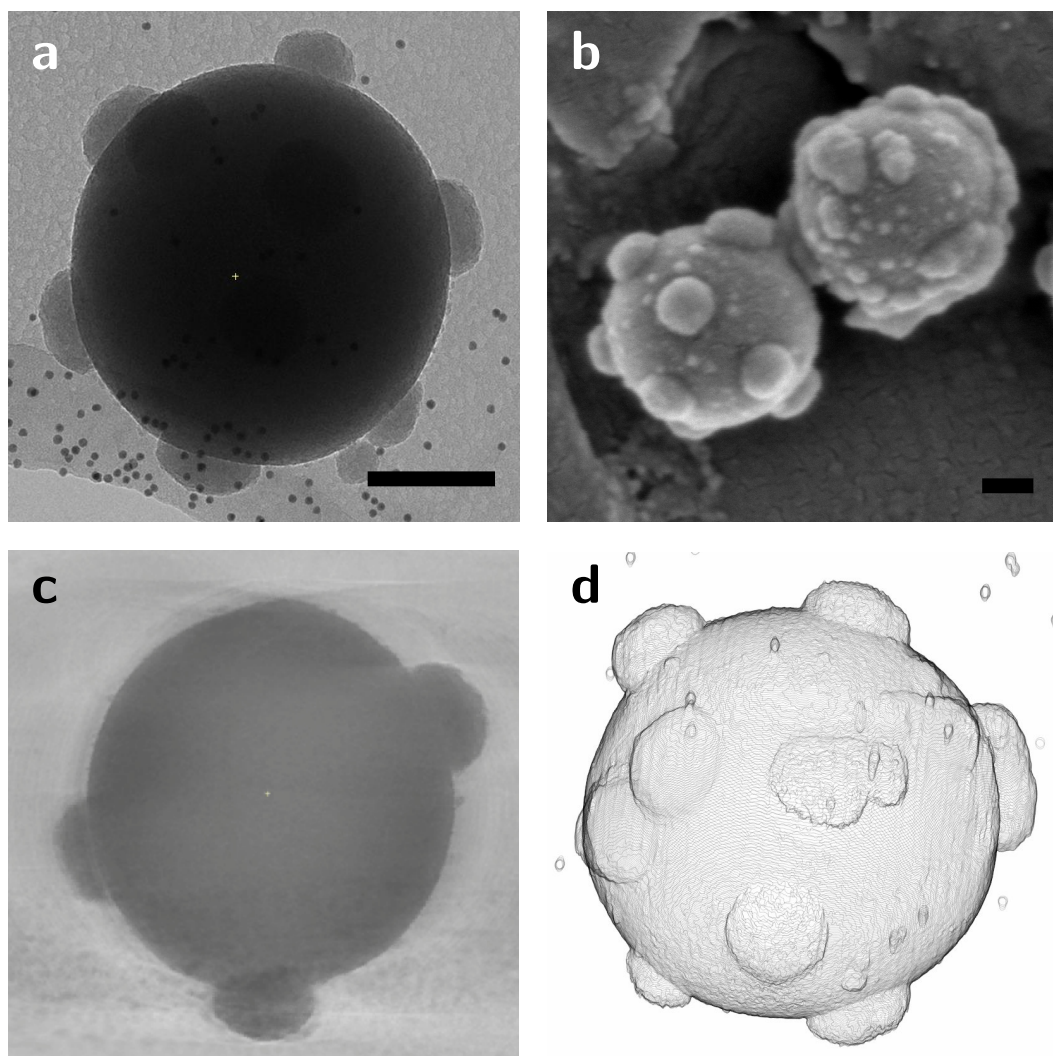


**Figure 4.3: Typical images of silica particles with silica protrusions grown by the method of Wang et al. [67], i.e. annealed at 750°C and with an MPS patterning (from sample *D* in App.4.5). (a) TEM micrograph (with gold markers). (b) SEM micrograph. (c) Slice and (d) surface rendering of a tomographic reconstruction of a patchy particle obtained via electron tomography. All scale bars denote 100 nm.**

canceled each other<sup>1</sup>. More hemispherical shapes were obtained in titania protrusions for any core

<sup>1</sup>A rough calculation is the following. Suppose  $R$  is the average particle diameter,  $r$  the average patch diameter and  $H$  the average patch height. We may model a patch as a cylinder of volume  $\pi r^2 H$ . For a total silica content  $M$  of seed particles in the reaction mixture, the number of silica particles  $N$  in the reaction mixture is  $N = M / (\frac{4}{3} \pi R^3 \rho)$ , with  $\rho$  the density of silica. Given the total volume  $V$  of silica that can be formed from the added amount of TEOS, the volume  $v$  of a protrusion is then  $v = \frac{V}{12N} = \frac{\pi R^3 \rho V}{9M}$ . Equating

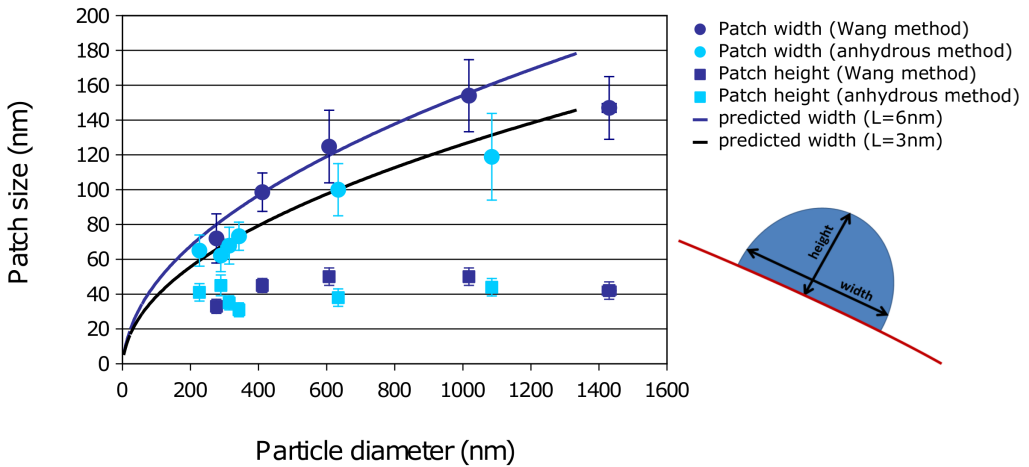


**Figure 4.4:** Graph of the average patch sizes as a function of particle diameter for patchy particles grown according to the method by Wang *et al.* [67] (dark blue) and by the anhydrous method (light blue). Circles indicate patch widths, and squares indicate patch heights. The patch sizes of the green series are plotted against the particle diameter as measured after sintering, which is responsible for the slight offset with the diameters of the patchy particles made via the anhydrous method. Error bars for the particle diameter are smaller than the symbol size, hence this difference is significant. Error bars in the y-direction are standard deviations of the patch size measurements, i.e. a 'polydispersity' in the patch size. The black lines are fits to equation 4.8. Samples are (dark blue) A, D, E, F, G and (light blue) A2, B2, C2, D2, J, H from App. 4.5. Samples B and C were ignored because some damage to the particles from sintering and crystal break-up was observed, which influences the protrusion size.

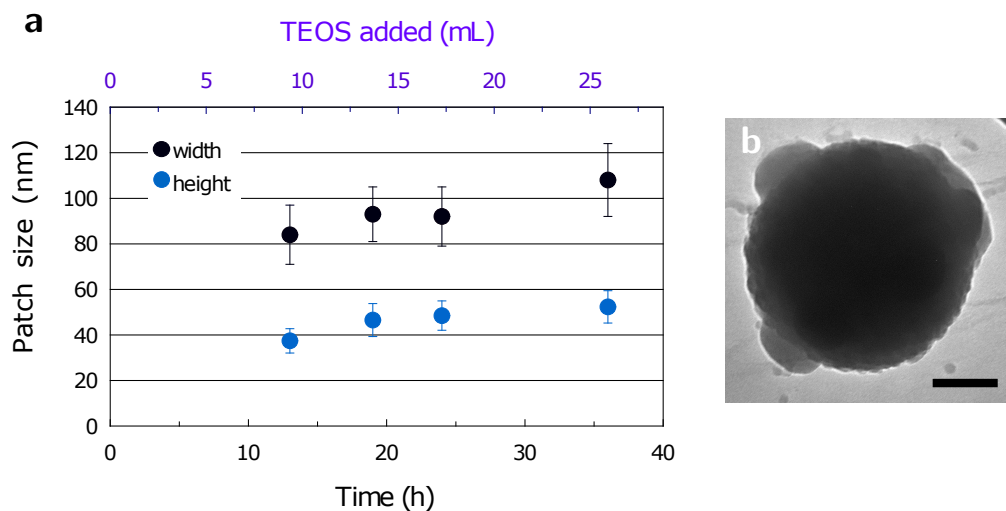


**Figure 4.5:** (a) Patchy particles grown according to a method similar to that of Wang *et al.*, by continuing TEOS addition for 36 h. (b) Patchy particle with protrusion growth continued for 36 h. Silica has precipitated onto the entire surface due to the erosion of the protective alkane chains in the basic environment. The scale bar represents 100 nm.

particle size (see section 4.3.3).

A simple model was used to obtain more insight into expected patch sizes (Fig. 4.6a). Assuming that patches are formed thanks to size-exclusion of the silane coupling agent from the contact points of the particles in the crystal (without taking sintering into account), the molecule cannot reach the particles' surface from a position where the distance to the surface is longer than its stretched length  $L$ . The volume containing such positions can be drawn around a particle of radius  $R$  as a shell of radius  $R+L$ . The patch was modeled as the intersection of the shells (patch radius  $A/2$  indicated in green). The opening angle of the patch then equals  $\arccos\left(\frac{R}{R+L}\right)$ , and since arc length equals angle times radius, the patch size  $A$  is:

$$A = 2R \cos^{-1} \left( \frac{R}{R+L} \right) \quad (4.8)$$

Based on carbon bond lengths with hydrogen, oxygen, silicon and other carbon atoms [261], the maximum length of a stretched MPS molecule is 1.9 nm. The predicted patch sizes for hypothetical molecular sizes of 3 nm and 6 nm are indicated in Fig. 4.4. The experimental values for the patch widths are described well by the curves of predicted patch sizes for these values of  $L$ . The patch widths

---

the volume of the cylinder to  $v$ , we arrive at  $H = \frac{\rho V}{9M} \frac{R^3}{r^2}$ . From figure 4.4, we see that as the particle radius triples from  $\sim 350$  nm to 1050 nm ( $R \rightarrow 3R$ ), the patch width (anhydrous method) approximately doubles from 60 nm to 120 nm ( $r \rightarrow 2r$ ). Thus,  $\frac{R^3}{r^2} \rightarrow \frac{(3R)^3}{(2r)^2} = \frac{9}{4} \frac{R^3}{r^2}$ , and the patch height is actually expected to increase rather than decrease. The model is not completely accurate, since at small heights the volume of the protrusion is closer to a hemisphere of volume  $v = \frac{4}{3}\pi r^3$

are larger than predicted for  $L = 1.9$  nm; a plausible reason is that the silane coupling agent molecules may have formed oligomers before attaching to the surface, resulting in a larger effective size  $L$ . In addition, surface roughness was not taken into account in this model. As already mentioned, sintering also adds to the patch width for particles prepared via the method of Wang and coworkers [67] as was confirmed by the experimental data in Fig. 4.4.

We first attempted to incorporate a dye into the silica protrusions of particles prepared via the route of Wang *et al.* in combination with the silane coupling agent method by Van Blaaderen and Vrij [179], as described in detail in Section 4.2.2.1. In short, dye-APTES conjugate was added to the reaction mixture during protrusion growth. Fig. 4.7a shows the resulting particles; the protrusions are well-defined. In spite of the acceptable patch shape, such particles were too small for imaging by confocal microscopy. Micron-sized particles were prepared in the same manner, but a monolayer of dye was bound to the entire particle surface (visible as a fluorescent ring, see Fig. 4.7b). Fig. 4.7c shows silica particles grafted with MPS via the anhydrous method and subsequently treated overnight with APTES-RITC in a Stöber mixture. After two washing steps with ethanol, the particles still appeared as fluorescent rings under the confocal microscope. In conclusion, MPS molecules are not long enough to prevent APTES-RITC from binding to the silica surface. As we learned from the particles with titania patches (see section 4.2.2.3), a layer of OTMOS molecules grafted by the anhydrous method does prevent such binding of APS-RITC conjugate to the grafted silica surface. OTMOS molecules are long enough to shield the silica surface from dye conjugates. Surface-patterned particles with an OTMOS grafting have the additional advantage of a larger difference in hydrophobicity between the patch and the core particle.

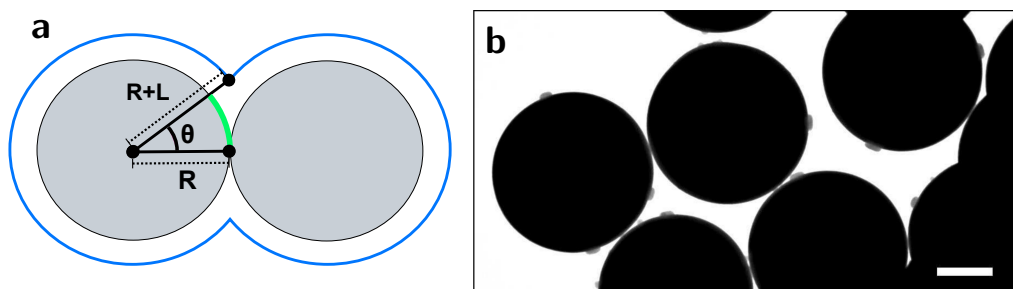


**Figure 4.6:** (a) A schematic drawing indicating the parameters used to predict patch sizes for non-sintered particles.  $R$  is the particle radius,  $L$  is the size of the grafting molecule, and  $\theta$  is opening angle of the patch. (b) Patchy particle of micron size with an MPS grafting on the silica core and with silica protrusions. These particles were prepared according to the method by Wang *et al.*, however the sintering temperature was  $500^{\circ}\text{C}$  (10h) (Sample G, Appendix 4.5). Scale bar denotes 500 nm.

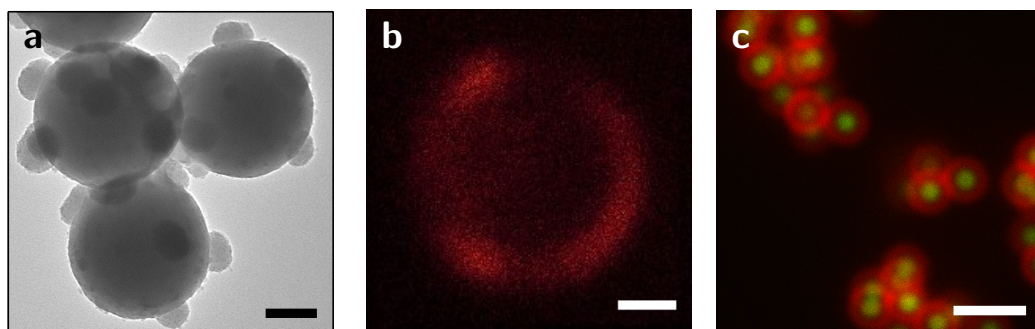


**Figure 4.7:** Dyeing silica patches. (a) TEM image of patchy particles with silica protrusions with APTES-FITC incorporated. MPS grafted twice (Stöber-like conditions). (b) Confocal micrograph of silica particles with silica protrusions with APTES-FITC incorporated. The dye is imaged with a 'glow color' table. (c) MPS-grafted (anhydrous method) non-patchy silica particles reacted overnight with APTES-RITC conjugate and washed twice with ethanol, in CHC. RITC dye displayed in red, FITC-dyed core displayed in green. The scale bars denote 100 nm, 400 nm and  $2\mu\text{m}$ , respectively.

### 4.3.2 Fluted rod-like particles

Rod-like particles were successfully surface-patterned by extending the method of Wang *et al.* to a smectic liquid crystal of rod-like particles. In this procedure, particles packed in a colloidal crystal were sintered at 750°C before the grafting step. Rod-like particles sintered for 5 hours at 750°C did not redisperse within two hours by sonication with the ultrasonic processor. A possible explanation is that the contact areas between rod-like particles are larger than between spherical particles, although it is also true that the rod diameter is smaller than the sphere diameters used, and thus the forces exerted by sonication are smaller as well. When sintered for 5h at 600°C, the rods could be dispersed fully by sonication. Additionally, SEM images revealed that the smectic order in the crystal was retained after this sintering step (Fig. 4.8).

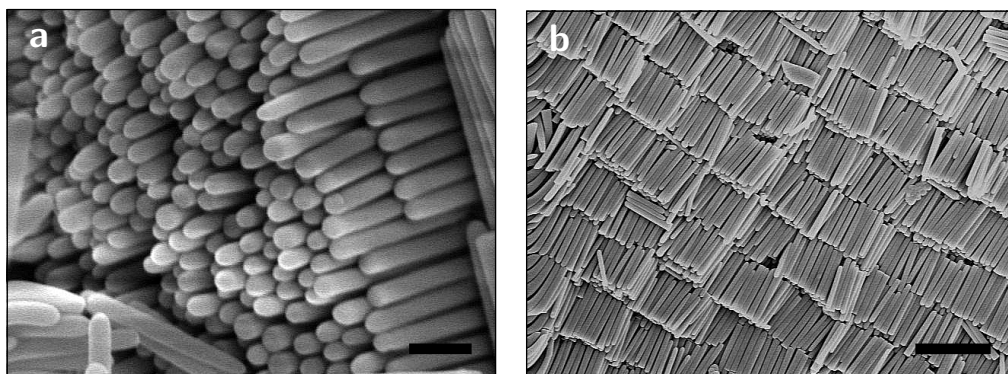


**Figure 4.8:** Smectic crystal of rod-like particles ( $L = 2.07\ \mu\text{m}$ ,  $D = 0.22\ \mu\text{m}$ ) before (left) and after (right) sintering (5 h at 600°C, sample I in Appendix 4.5). Scale bars denote 0.5  $\mu\text{m}$  and 3  $\mu\text{m}$ .

The surface of the particles was patterned with MPS and silica protrusions were grown as described in Section 4.2.2.2. Figures 4.9(a)-(c) display a patchy rod under three different angles; the protrusions are of a lighter grey shade than the core as they are thinner. They run along the length of the rods like a wing. The angle dependence (of visible protrusions upon turning the sample by 30°) shows that the protrusions are not a matter of incorrect focussing. A tomographic reconstruction of one patchy rod is shown in Fig. 4.9d, providing further evidence for the fluted shape.

The protrusions have a width of  $56 \pm 3\ \text{nm}$ , which is similar to the height measured for silica protrusions on spherical patchy particles. The protrusions do not all run along the full lengths of the rods, presumably because the rod-like particles are slightly tapered. This tapering is a result of shrinking of the emulsion droplet from which the rod grows during synthesis, since the rod consumes precursor and water from the droplet. In addition, many rods had fewer than six protrusions. Liquid crystals of the type smectic A do not necessarily have hexagonal ordering within layers, but these rods do often have local ordering (see Fig. 4.8 and Ref. [262]). The missing protrusions are probably not due to lack of local order, but due to the relatively high polydispersity in diameter.

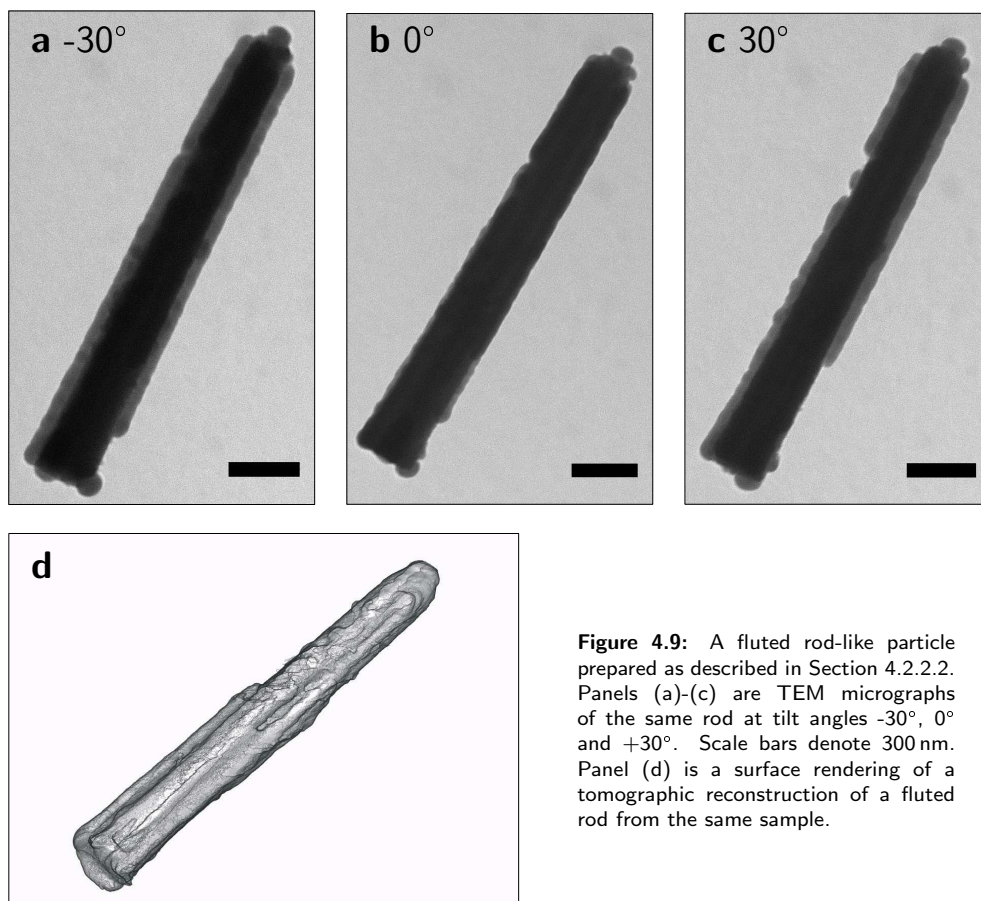


**Figure 4.9:** A fluted rod-like particle prepared as described in Section 4.2.2.2. Panels (a)-(c) are TEM micrographs of the same rod at tilt angles  $-30^\circ$ ,  $0^\circ$  and  $+30^\circ$ . Scale bars denote 300 nm. Panel (d) is a surface rendering of a tomographic reconstruction of a fluted rod from the same sample.

### 4.3.3 Patchy silica particles with amorphous, dyed titania patches

Titania protrusions were larger than silica protrusions in both patch width and patch height (cf. graphs 4.4 and 4.12). The standard deviation of the patch widths increased with particle size, as indicated by the larger vertical bars. In theory, the patch width can be influenced by the grafting molecules used: OTMOS (stretched molecule length 3.3 nm) is a larger molecule than MPS (stretched length: 1.9 nm), hence a larger area about the contact points is excluded for this molecule. However, Fig. 4.12 shows that the standard deviations of the patch widths of both OTMOS-patterned particles and MPS-patterned particles is too large to draw a conclusion on the influence of grafting moiety. When compared to silica protrusions, the width of titania protrusions for equal grafting moiety - MPS- was larger at all particle sizes. This indicates that some titania grew beyond the edges of the patches, in spite of the shape of the patches that arches back (Fig. 4.10a). The height of titania protrusions was larger in an absolute sense, reaching 106 nm for titania patches instead of 50 nm for silica patches in micron-size particles. The titania protrusions reached a more hemispherical shape

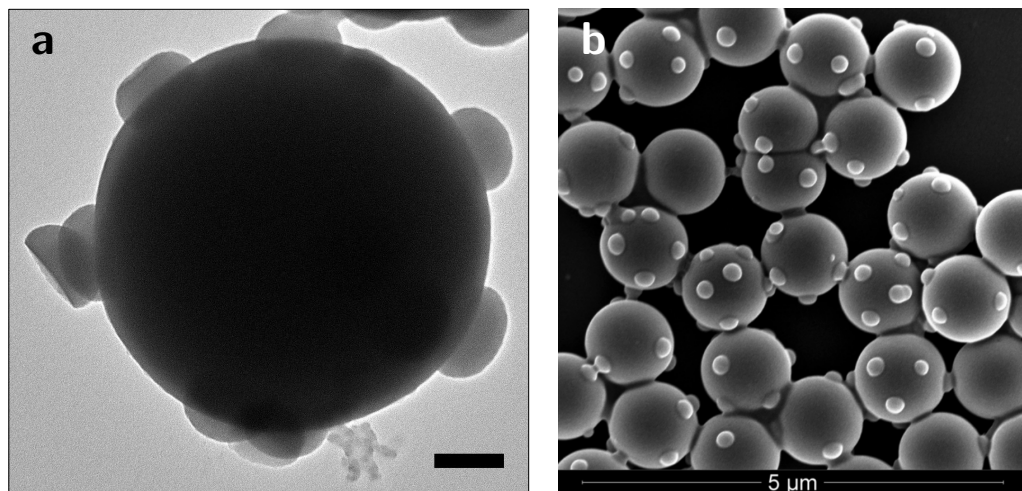


**Figure 4.10: Silica particles with amorphous titania protrusions.** Samples grown from silica particles with an OTMOS-patterning, as described in Section 4.2.2.3. (a) TEM micrograph of synthesis *J2* (scale bar: 200 nm) and (b) SEM image of synthesis *P* in Appendix 4.5.

than silica protrusions in micron-size particles. It is noteworthy that in the respective recipes, we added  $9\ \mu\text{mol}$  ( $2\ \mu\text{L}$ ) TEOS versus only  $0.3\ \mu\text{mol}$  ( $0.11\ \mu\text{L}$ ) TBT per milligram silica particles. It is known that TEOS hydrolysis in base-catalyzed solutions continues beyond two hours of reaction time [263–265], so it is unlikely that all TEOS condenses on the patches, yet on account of the long addition time we can assume that at most TEOS has reacted. The flatter shape of the silica patches can not be attributed to this.

In TEM images of patchy particles with titania protrusions, some loose hemispheres were encountered, which we think are dislodged protrusions (see the attached hemisphere in Fig. 4.10a). Heating by the electron beam in the electron microscope may be responsible for the dislodging: if the titania and the silica shrink to a different degree, stresses inside the particle can cause this detachment. This was also observed in silica-titania core-shell particles [224]. It is also consistent with the fact that titania protrusions remained intact upon sintering only when infiltrated with silica (see section 4.3.4).

Dyed titania protrusions were bright and separate protrusions on one particle were clearly distinguishable (Fig. 4.11). By eye, patchy particles with RITC-dyed protrusions always appeared bright pink after dyeing, in spite of their yellow FITC-dyed cores, while patchy particles with FITC-dyed protrusions and an RITC-dyed core appeared yellow/orange. An explanation for the brightness is the high microporosity of titania [224], which allows the dye complex to fully penetrate the protrusions, and which also allows for a larger total amount of dye conjugate to be attached to the inner surface of the protrusion. The surface grafting on the particles must consist of OTMOS to ensure that no APTES-RITC conjugate attaches to the core particle. Particles patterned with MPS showed dyed patches under confocal microscopy, but oftentimes dye conjugates were attached to the seed particle as well.

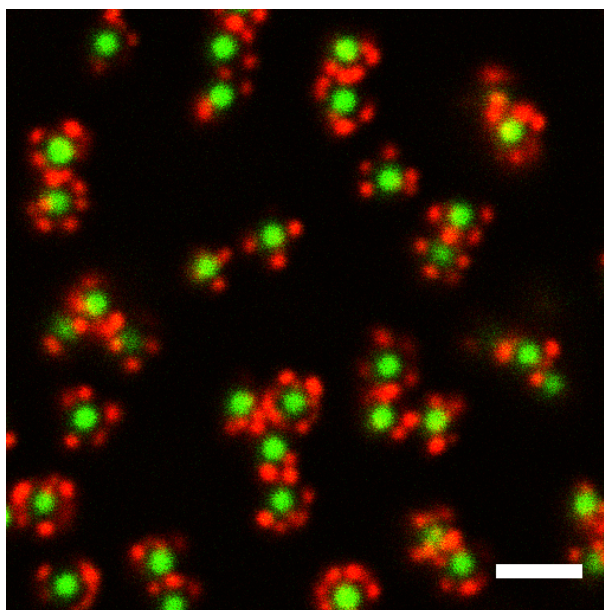


**Figure 4.11:** Confocal image of OTMOS-patterned patchy particles with an FITC-dyed core and RITC-dyed titania protrusions in cyclohexyl chloride (CHC) (Sample K, Appendix 4.5). The particles were synthesized as described in Section 4.2.2.3. The silica core particles have a diameter of  $1085 \pm 5$  nm in ethanol (SLS). The scale bar denotes 2  $\mu$ m.

#### 4.3.4 Patchy silica particles with crystalline titania patches

In order to convert the amorphous titania patches to anatase or rutile titania, we initially sintered patchy particles with non-dyed titania patches at 400°C (Fig. 4.13a). The resulting particles had deformed protrusions. However, particles with titania protrusions that had been dyed with APTES-RITC could be sintered for 2 hours at 500°C (Fig. 4.13(b)) without distortion or loss of the protrusions. A plausible explanation for this difference in resistivity against heating is the following. Titania is known to shrink significantly (as much as 40% at 650°C) under sintering due to the collapse of its porous structure (see e.g. [224]). However, Demirörs *et al.* found that titania spheres infiltrated with silica shrunk considerably less under the same conditions [266, ch.2]. The silica helps to prevent strong shrinkage of the titania and reduces stress within the particle. The authors did find that the anatase titania formed in these spherical particles was more polycrystalline than anatase particles formed from titania that had not been infiltrated with silica [266]. Apparently, the silica had not intervened chemically at these temperatures and remained dispersed independently in between the anatase crystallites. In the present work, the silica formed inside the titania from the silane coupling agent APTES prevented shrinkage of the titania protrusions under heating.

Electron diffraction studies were performed on both sintered and non-sintered patchy particles with titania protrusions. The electron diffraction was focused on a spot of diameter 274 nm (selected area) on a patchy particle using a pinhole. The area selected was a protrusion, but it included a

small portion of the silica core particles due to the round shape of the beam (as in Fig. 4.14c). Figures 4.14f and 4.14g show the patterns recorded for a pristine (dyed) patch and a (dyed) patch sintered at 500°C for two hours. The non-sintered patch does not yield diffraction rings, indicating that this titania is indeed not amorphous. The sintered patches, however, do diffract the electron beam into diffraction rings, proving the presence of a form of polycrystalline titania. The patches of the particles sintered at 900°C have diffraction spots rather than rings, indicating that this titania contains fewer crystalline domains with respect to the 274 nm area used to obtain the diffraction. The patches sintered at 1100°C exclusively display diffraction spots; this titania is predominantly monocrystalline. One batch of silica particles with titania protrusions was sintered at 500°C for eight hours instead of two hours. ED patterns from the protrusions showed rings of disconnected spots, so increasing the sintering time from two to eight hours slightly reduced the number of crystal domains (and so increased the crystal size).

Diffraction patterns satisfy the Bragg's law [ $2d\sin(\theta) = m\lambda$ , with  $m$  an integer] for small angles, i.e. assuming  $R \ll L$ :

$$d \cdot R = \lambda \cdot L \quad (4.9)$$

with  $d$  the lattice spacing in the crystal,  $R$  the radius of the diffraction ring,  $\lambda$  the wavelength of the electrons and  $L$  the distance between sample and detector. Once the "camera constant"  $\lambda L$  is known, the lattice spacings can be derived by measuring the radii of the diffraction rings  $R$  in a diffraction pattern. An electron diffraction pattern of gold was used as a calibration to determine the camera constant for the instrument (electron microscope and detector) used. By measuring the radius of the diffraction rings in Fig. 4.14, we arrived at the lattice spacings  $d$  in table 4.2. The spacings agree with those of the anatase phase to within the error bars. The rutile phase has a first diffraction ring at 3.247Å: this value lies outside the error margin of the observed first ring. The brookite phase diffraction rings which are rather similar to those of anatase, yet brookite has a strong diffraction ring at 2.9Å, which is absent in the present spectrum. Therefore, we believe that the titania patches of the patchy particles have converted to anatase titania by sintering two hours at 500°C. The lattice spacings calculated from diffraction rings for particles sintered for 8h at 500°C and 2h at 900°C are close to anatase as well, but the fact that the diffraction patterns consist of spots rather than rings affects the measurement uncertainty.

| Ring number | $d(\text{\AA})$<br>(2h, 500°C) | $d(\text{\AA})$<br>(8h, 500°C) | $d(\text{\AA})$<br>(2h, 900°C) | $d(\text{\AA})$ (anatase, Ref. [261])                                  | hkl  |
|-------------|--------------------------------|--------------------------------|--------------------------------|--|--|
| 1           | $3.59 \pm 0.03$                | $3.60 \pm 0.02$                | $3.55 \pm 0.05$                | 3.520  | 101  |
| 2           | $2.44 \pm 0.04$                | $2.45 \pm 0.03$                | $2.44 \pm 0.04$                | $\left\{ \begin{array}{l} 2.431 \\ 2.378 \\ 2.332 \end{array} \right.$ | $\left\{ \begin{array}{l} 103 \\ 004 \\ 112 \end{array} \right.$ |
| 3           | $1.94 \pm 0.02$                | $1.97 \pm 0.01$                | $1.95 \pm 0.03$                | 1.892  | 200  |
| 4/5         | $1.70 \pm 0.01$                | $1.73 \pm 0.01$                | $1.74 \pm 0.1$                 | $\left\{ \begin{array}{l} 1.700 \\ 1.667 \end{array} \right.$          | $\left\{ \begin{array}{l} 205 \\ 211 \end{array} \right.$        |
| 6           | $1.51 \pm 0.02$                | $1.53 \pm 0.01$                | too faint                      | $\left\{ \begin{array}{l} 1.493 \\ 1.480 \end{array} \right.$          | $\left\{ \begin{array}{l} 213 \\ 204 \end{array} \right.$        |
| 7           | $1.38 \pm 0.02$                | $1.39 \pm 0.02$                | too faint                      | 1.364  | 116  |
| 8           | too faint                      | $1.30 \pm 0.01$                | too faint                      | 1.338  | 220  |

**Table 4.2:** Table of the lattice spacings found from the diffraction rings of patchy particles with titania protrusions sintered at 500°C for 2h, and comparative data from JCPDS card 21-1272 [267]. The second ring is a composite ring due to three very similar lattice spacings. 'Too faint' indicates that individual spots could still be seen, but it was unclear which formed a ring together.

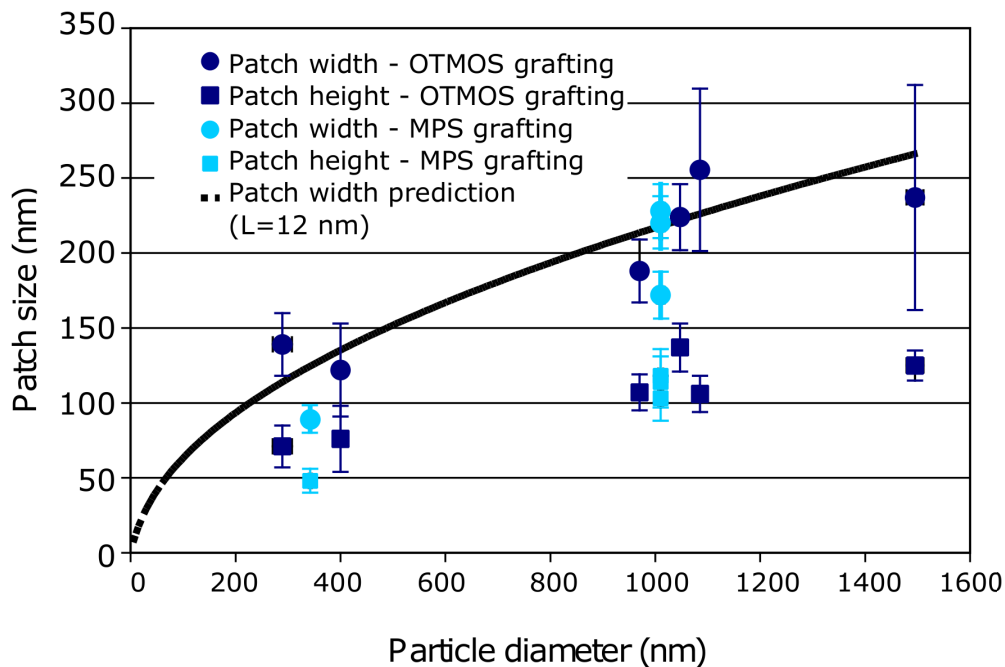


**Figure 4.12:** Graph showing the average patch size of titania protrusion grown by the recipe described in Section 4.2.2.3. Patch widths are labeled by circles and patch heights by squares. Green symbols indicate an MPS patterning are labeled with green symbols and purple symbols indicate particles with an OTMOS patterning. The dashed line is a fit to equation 4.8 for  $L=12$  nm. (Samples *C4*, *J2*, *K*, *L*, *C5*, *J3*, *M*, *N* from Appendix 4.5.)

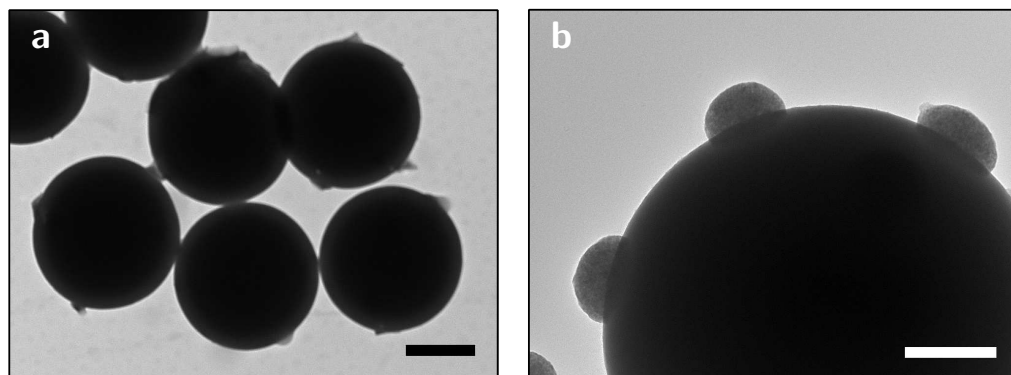


**Figure 4.13:** Patchy particles with titania protrusions of the same batch (a) sintered for 2h at 400°C, and (b) infiltrated with APTES-RITC and sintered for 2h at 500°C. Scale bars: 500 nm and 200 nm.

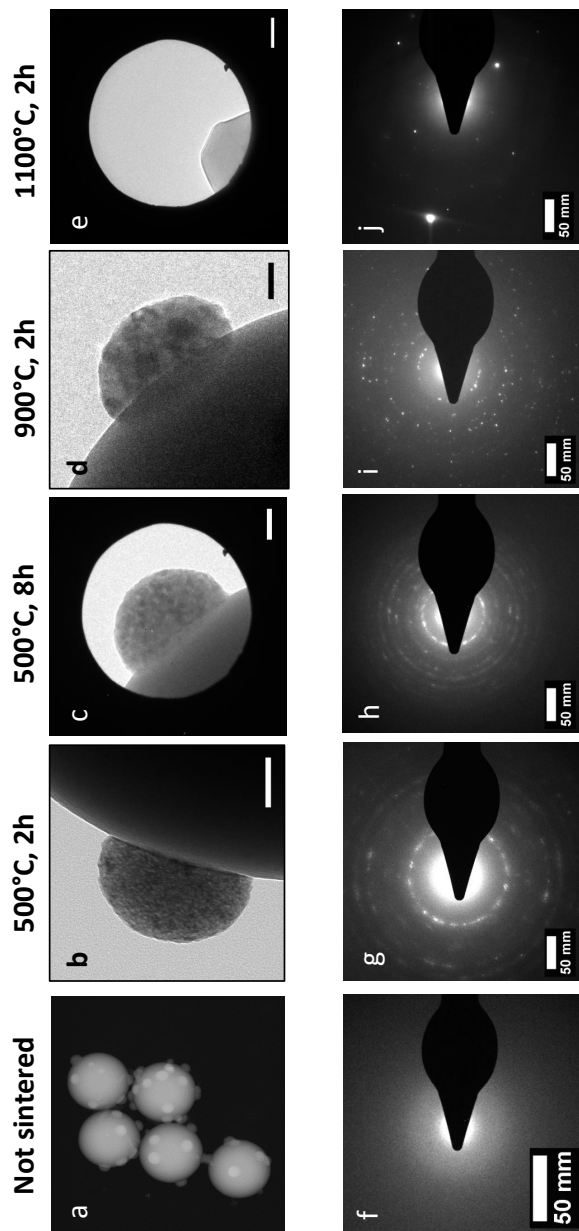


**Figure 4.14:** Close-ups (top row) and electron diffraction patterns (bottom row) of patchy particles with titania protrusions sintered at various temperatures and sintering times: (a)/(f) no sintering; (b)/(g) 2h at 500°C; (c)/(h) 8h at 500°C; (d)/(i) 2h at 900°C; (e)/(j) 2h at 1100°C. Scale bars in the top panels denote 50 nm.

The monocrystallinity of the titania protrusions sintered at 1100°C showed in various other ways besides the discrete spots in the diffraction pattern. The protrusions changed shape under the intense sintering conditions, and their shapes often showed faceting (Fig. 4.14(e)). Secondly, during TEM imaging, the patches were accompanied by a white 'shadow' resulting from electrons scattered in one direction by the crystal planes. Finally, dark field TEM images show clear signs of monocrystallinity as well. Under various azimuthal angles of the incident beam, varying protrusions light up in bright white (Fig. 4.15). This happens when the incident beam is under an angle with respect to the detector and the crystalline planes in the monocrystalline protrusions that satisfies Bragg's law.

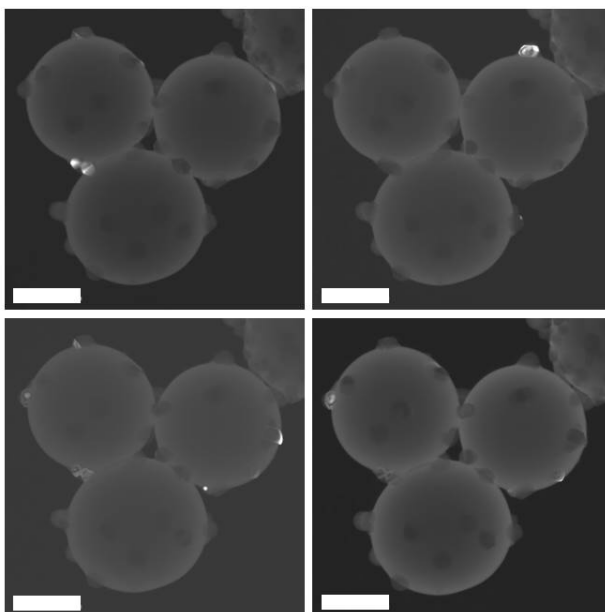


**Figure 4.15:** Dark field TEM images of silica particles with titania patches sintered at 1100°C under various angles. The scale bars denote 0.5  $\mu\text{m}$ .

## 4.4 Conclusions & Outlook

We prepared patchy particles with silica protrusions according to the method by Wang *et al.* [67]. The diameter of the patches was dependent on particle diameter in a way consistent with size-exclusion of (oligomers of) a grafting molecule from the contact areas. We successfully extended the synthesis method to silica rods, which resulted in fluted rods with up to six wing-shaped protrusions along the length of the rods. Through an anhydrous grafting method, we were able to eliminate the need for a sintering step in the synthesis route. Moreover, we successfully synthesized silica particles with titania protrusions. The protrusions were also dyed with a covalently-bound fluorescent molecule by infiltration of the porous titania with dye-APTES conjugate, making the particles suitable for confocal microscopy. Patchy particles with titania protrusions infiltrated with a silane coupling agent were sintered up to 900°C with excellent preservation of their shapes. Via selected area electron diffraction (SAED), we obtained strong indications that the patches on particles sintered at 500°C, 900°C and 1100°C had converted to anatase titania. The domain size of the anatase crystallites increased with sintering time and temperature. The protrusions sintered at 1100°C had converted to monocrystalline anatase titania. This finding is potentially useful for catalytic processes and self-propelling particles.

## Acknowledgements

We thank Bart de Nijs for calculating the tomographic reconstructions from tilt series of patchy particles, Bo Peng for suggesting the titania patch growth and for supplying the smectic crystal of rod-like particles, Bing Liu for sharing his knowledge on graftings in apolar solvents, and Thijs Besseling for sharing his knowledge on imaging with the confocal microscope. Merel Lefferts is acknowledged for helping to extend the patchy particle method to micron-size particles and studying dye incorporation on patchy particles with silica patches. Fig. 4.10b was made by Jasper Hooijmans, Faranaaz Rogier and Zhan Shu as part of an EM course. Hans Meeldijk and Chris Schneijdenberg are gratefully thanked for their skilled and knowledgeable help with the electron diffraction studies in particular and EM studies in general.

## 4.5 Appendix: Overview of syntheses

In the overview of syntheses below, patchy particles made from similar seed particles are coded with the same letter and varying number.

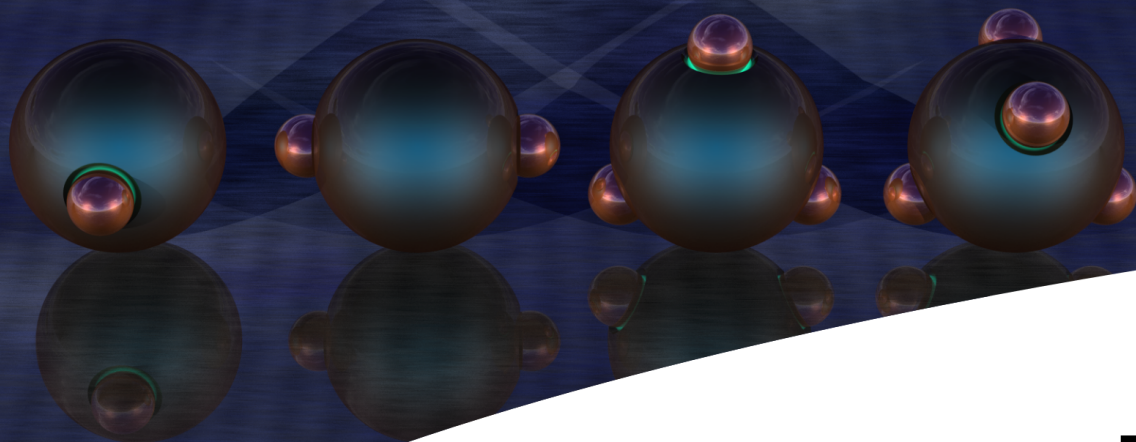
Surface modifications:

- $\alpha$  = Sintering at 750°C, tens of milligrams placed in a mixture of 8 mL ethanol; 0.3 mL water; 0.2 mL NH<sub>3</sub> (25%); 0.1 mL MPS for 24h.
  - $\alpha$ 500 = Idem to  $\alpha$ , but sintering at 500°C for 10h.
  - $\alpha$ 600 = Idem to  $\alpha$ , but sintering at 600°C for 5h.
  - $\beta$  = MPS grafting by anhydrous method: several tens of milligrams placed in a mixture of 5 mL toluene; 0.5 mL n-butylamine; 0.5 mL MPS for 24h.
  - $\gamma$  = OTMOS grafting by anhydrous method: several tens of milligrams placed in a mixture of 5 mL toluene; 0.5 mL n-butylamine; 0.5 mL MPS for 24h.
- Silica grown according to Wang's recipe: to 8 mL of silica in ethanol (silica content: 0.5 mg/mL), added 1 mL water and 0.2 mL ammonia (25%). At a rate of 720  $\mu$ L/hr, added a mixture of 8  $\mu$ L TEOS in 8 mL ethanol. After all precursor solution had been added, the dispersion was stirred for two hours before washing with ethanol.
  - $\omega$ = Silica grown via seeded Stöber growth: to a silica dispersion of OTMOS-patterned particles (0.5 mg/mL) in ethanol were added 1 mL water and 0.2 mL ammonia (25%). Then, a mixture of 8  $\mu$ L TEOS in 8 mL ethanol was added at once. The reaction proceeded under magnetic stirring for 5h and was stopped by washing twice with ethanol.
  - Titania grown according to the recipe by Bae et al.: to 20 mL of acetone with 2-4 mg/mL silica content, added to 25  $\mu$ L water and 0.5 mL precursor solution (200  $\mu$ L TBT in 30 mL ethylene glycol). Solution was stirred overnight before washing with ethanol. The number in brackets is the silica content in the acetone in mg/mL, since the silica content influences the final protrusion size.

| Code | Seed diameter (counts) (nm)                                  | P.d.  | Dye label core          | Patch width    | Patch height   | Mod. <sup>†</sup> | Patches       |
|------|--|---|-------------------------|----------------|----------------|-------------------|---------------|
| A    | 276 ± 3 (498) (TEM, after sintering)                         | 5%  | FITC (before sintering) | 72 ± 14 (43)   | 33 ± 4 (40)    | α                 | Silica        |
| B    | 331 ± 7 (65) (TEM, after sintering)                          | 4%  | -                       | 106 ± 5 (139)  | 49 ± 7 (28)    | α                 | Silica        |
| C    | 284 ± 8 (88) (TEM, after sintering)                          | 7%  | FITC (before sintering) | 104 ± 10 (65)  | 46 ± 7 (28)    | α                 | Silica        |
| D    | 411 ± 4 (17) (TEM, after sintering)                          | 4%  | -                       | 99 ± 11 (23)   | 44 ± 6 (25)    | α                 | Silica        |
| E    | 607 ± 6 (284) (TEM, after sintering)                         | 7%  | -                       | 125 ± 21 (123) | 50 ± 5 (42)    | α                 | Silica        |
| F    | 1018 ± 5 (74) (TEM, after sintering)                         | 1.8%  | FITC (before sintering) | 154 ± 21 (36)  | 50 ± 8 (24)    | α                 | Silica        |
| G    | 1430 ± 20 (16) (TEM, after sintering)                        | 1.8%  | FITC (before sintering) | 147 ± 18 (17)  | 42 ± 5 (16)    | α500              | Silica        |
| I    | rod-like particles: (L/D = 9.6)<br>L = 2.07 μm & D = 0.22 μm | δ <sub>L</sub> = 8.9%<br>δ <sub>D</sub> = 20% | -                       | -              | -              | α600              | Silica        |
| H    | 226 ± 11 (17) (TEM, after sintering)                         | 1.6%  | FITC (before sintering) | 65 ± 9 (34)    | 38 ± 4 (25)    | β                 | Silica        |
| C2   | 286 ± 6 (23) (TEM, after sintering)                          | 5%  | FITC (before sintering) | 62 ± 9         | 45 ± 6         | β                 | Silica        |
| C3   | 286 ± 6 (23) (TEM, after sintering)                          | 5%  | FITC (before sintering) | 89 ± 9 (31)    | 35 ± 4 (23)    | β                 | Silica *      |
| A2   | 314 ± 3 (42) (TEM, no sintering)                             | 4%  | FITC                    | 68 ± 11 (50)   | 35 ± 4 (39)    | β                 | Silica        |
| B2   | 343 ± 3 (25) (TEM, no sintering)                             | 4%  | -                       | 139 ± 21 (16)  | 71 ± 14 (12)   | β                 | Silica        |
| D2   | 652 ± 10 (51) (TEM, no sintering)                            | 4%  | -                       | 100 ± 15 (37)  | 8 ± 5 (27)     | β                 | Silica        |
| J    | 1124 ± 7 (47) (TEM, no sintering)                            | 2%  | FITC                    | 119 ± 25 (49)  | 44 ± 5 (29)    | β                 | Silica        |
| X    | 280nm  |   | FITC                    | -              | -              | γ                 | Silica ω      |
| C4   | 289 ± 20 (18) (TEM, no sintering)                            | 2%  | FITC                    | 139 ± 21 (16)  | 71 ± 14 (12)   | β                 | Titania       |
| K    | 1010 ± 5 (SLS, ethanol)                                      | 2%  | FITC                    | 172 ± 27(35)   | 103± 15 (28)   | β                 | Titania (2.8) |
| Q    | 1010 ± 5 (SLS, ethanol)                                      | 2%  | FITC                    | 228 ± 28 (75)  | 118 ± 8 (56)   | β                 | Titania (2.8) |
| J2   | 1085 ± 5 (SLS, ethanol)                                      | 1%  | FITC                    | 255 ± 54 (22)  | 106 ± 12 (27)  | β                 | Titania       |
| L    | 1495 ± 16 (9) (TEM, no sintering)                            | 1%  | FITC                    | 237 ± 75 (25)  | 125 ± 10 (16)  | β                 | Titania       |
| C4   | 289 ± 20 (18) (TEM, no sintering)                            | 2%  | FITC                    | 139 ± 21 (17)  | 71 ± 14 (12)   | γ                 | Titania       |
| N    | 400 ± 3 (SLS, ethanol)                                       | 3.5%  | FITC                    | 122 ± 31 (99)  | 76 ± 22 (83)   | γ                 | Titania (3.0) |
| O    | 970 ± 5 (SLS, ethanol)                                       | 2%  | FITC                    | 188 ± 21 (108) | 107 ± 12 (105) | γ                 | Titania (3.0) |
| P    | 1047 ± 5 (SLS, ethanol)                                      | 8%  | RITC                    | 224 ± 22 (81)  | 137 ± 16 (71)  | γ                 | Titania (2.9) |
| J3   | 1085 ± 5 (SLS, ethanol)                                      | 1%  | FITC                    | 255 ± 54 (22)  | 106 ± 12 (27)  | γ                 | Titania       |
| M    | 1495 ± 16 (TEM, no sintering)                                |   | FITC                    | 237 ± 75       | 125 ± 10       | γ                 | Titania       |

\* For silica growth, the total amount of TEOS added was increased by a factor 1.5 (at constant addition speed).

† Mod. = Surface modification of the core particle.



# CHAPTER 5

## Patch number distributions

The particles in Ch. 4 were expected to have twelve patches each based on the close-packed crystal structure they were part of, yet TEM and CSLM imaging revealed that most particles possessed fewer patches. The discrepancy is mainly caused by the fact that colloidal particles are not perfectly monodisperse, which reduces the number of contact points of the particles in a colloidal crystal, although polydispersity can increase the number of contact points in a colloidal glass. In this chapter, the numbers of protrusions per patchy particle were determined by acquiring 3D confocal microscopy data, tracking the positions of particle cores and protrusions, and using two algorithms to count the number of protrusions per particle. These patch number distributions were compared to simulations which investigated the effect of two factors on the distributions: polydispersity of the particle size, and the maximum allowed separation between the particle surfaces for patch formation.

---



## 5.1 Introduction

The patchy colloids examined in Ch. 4 were synthesized by surface-grafting the particles while packed in a random hexagonal close-packed (RHCP) colloidal crystal. RHCP stacking is a combination of the two types of close-packed structures that exist for spherical particles: face-centered cubic (FCC) and hexagonal close-packing (HCP). Both FCC and HCP have the same near-neighbor shells, i.e. particles in HCP and FCC structures have the same number of neighbors (twelve). However, TEM and CSLM imaging revealed that most particles possessed fewer than twelve patches. Possible causes for the discrepancy are defects such as point defects [268], and the fact that colloidal particles are not perfectly monodisperse (which reduces the number of contact points of the particles in a colloidal crystal, although in a colloidal glass the number of contacts can be increased by polydispersity). The low number of patches per particle as compared to the 'ideal' number of twelve patches per particle is not due to size fractionation, since size fractionation is usually observed for colloids of polydispersity (p.d.) below 6% [269].

Here, experimental patch number distributions were obtained using particle tracking on data stacks from confocal microscopy (CLSM). The cores and the protrusions of the patchy particles were tracked separately, which was possible since different dyes were used to label these parts of the particles during synthesis. Two different programs were used to extract the patch number distributions from the coordinate files: one based on the analysis of clusters of oppositely colored particles, and one based on counting the number of neighbors within a certain cut-off distance. Simulations were employed to predict distributions of the number of patches per particle. The influence of two factors on the distributions were included in the simulations: polydispersity of the particle size, and the maximum 'allowed' separation between the particle surfaces that still results in patch formation. The experimentally obtained distributions of the number of patches per particle were then compared with these simulations. The experimental results for the patch number distributions showed qualitative agreement with the simulation data.

## 5.2 Experimental details

### 5.2.1 Chemicals

Reaction solvents used were ethanol (absolute, *Merck*), ethylene glycol ( $\geq 99.5$  wt%, *Fluka*), acetone (pro analysis, *Merck*) and toluene ( $\geq 99.5$  wt%, *Sigma Aldrich*). Water was deionized with a MilliQ system (Millipore Corporation) and had a resistivity of at least  $18.2 \text{ M}\Omega\text{cm}$ . The catalyst aqueous ammonia ( $\sim 25$  wt%), the fluorescent dye rhodamine B isothiocyanate (RITC, mixed isomers) and the silane coupling agents (3-aminopropyl)triethoxysilane (APTES,  $\geq 98\%$ ) and octadecyltrimethoxysilane (OTMOS, 95% (85% n-isomer) were purchased from *Sigma Aldrich*. Titanium (IV) butoxide (TBT, 97 wt%, *Aldrich*) was used after storage in a glovebox. These chemicals were used as received without further purification.

Low-polar solvents cyclohexyl chloride (CHC, 99%) and 1,2-dichloro-ethane (DCE,  $>99\%$ ) were obtained from *Aldrich*. CHC was deionized by adding alumina ( $\text{AlO}_2$ , activated / neutral / Brockmann I, *Sigma Aldrich*). After several hours, the CHC was placed over molecular sieves (*Acros Organics*,  $4\text{\AA}$ , 10-18 mesh) for at least a day. The conductivity of the CHC was measured with a *Scientifica model 627* conductometer connected to a probe which fitted  $\sim 3.8$  mL. The CHC had a conductivity of  $20 \pm 10$  pS/cm. DCE was used as received and had a conductivity of  $7.4 \cdot 10^3$  pS/cm.

### 5.2.2 Particle synthesis and dispersion preparation

Titania particles were synthesized as follows and in analogy to the synthesis of the titania protrusions on OTMOS-patterned silica colloids (Ch. 4). A solution of  $200 \mu\text{L}$  TBT in 30 mL of ethylene glycol was prepared and stirred for 12 h-24 h. To 40 mL of acetone, we added  $100 \mu\text{L}$  deionized water (needed for hydrolysis of the TBT). Under magnetic stirring, we then added 0.5 mL of the TBT solution. The reaction mixture was left stirring overnight and the titania particles were collected by centrifugation and washing with ethanol.

The titania particles were dyed for confocal microscopy in the following way. A solution of RITC coupled to APTES was first prepared: to 20 mg RITC we added 1 g (1.27 mL) ethanol and  $20 \mu\text{L}$  APTES, after which the solution was left on rollers for a night. Since the RITC forms a conjugate molecule with the APTES, the dye could be covalently coupled to the titania protrusions. To 10 mL of a dispersion of titania particles, we added  $100 \mu\text{L}$  aqueous ammonia and  $40 \mu\text{L}$  dye solution. The dispersion was left for two hours on rollers. We washed the residual RITC and RITC-APTES away by centrifuging and replacing the supernatant with fresh ethanol. The washing step was repeated until the supernatant was not visibly colored with dye anymore. The titania particles were used the same day as prepared.

Spherical silica particles grafted with OTMOS were prepared from 1.4 textmum organosilica-Stöber core-shell silica particles by drying 60 mg silica particles, redispersing in a mixture of 10 mL toluene, 1 mL n-butylamine and 1 mL OTMOS, and sonicating for several hours. The OTMOS-silica particles were then washed with toluene and ethanol.

Patchy particles with an OTMOS-grafted silica core particle and dyed titania patches were prepared as described in Ch. 4 (Samples *J3* and *P*, App. 4.5). The patchy particles were dispersed

in low-polar solvents to attempt to induce patch-patch interactions. Dispersions of these patchy particles (or dyed titania particles) in CHC or DCE were prepared by drying particles under nitrogen flow, weighing the sediment, adding the desired amount of solvent CHC or DCE, and shaking the dispersion on a lab mixer (*IKA RH Basic*). Dispersions of spherical OTMOS-grafted particles without titania protrusions prepared in the same way resulted in sols without aggregated particles.

### 5.2.3 Sample preparation and characterization

Samples for confocal microscopy were prepared by filling a borosilicate capillary of rectangular cross section (*VitroCom* no.5010,  $0.1 \times 1$  mm) with dispersion and sealing the capillary with UV-curable glue (*Norland Optical adhesive no. 68*). The glue was cured using a UV-lamp with an emission peak at 352 nm. The glue simultaneously served the purpose of attaching the capillary to a borosilicate cover slip (*Menzel Gläser*, Thermo-Scientific, 26 mm  $\times$  76 mm). Capillaries were grafted with OTMOS according to the recipe in Section 2.2 prior to use.

Patchy particles typically had an fluoresceine isothiocyanate (FITC)-labeled core and rhodamine isothiocyanate (RITC)-labeled patches, or vice versa. CLSM images were recorded on a *Leica SP8* confocal microscope. The microscope was equipped with a *Leica HCX Plan Apo STED Orange 100x* oil immersion confocal objective (NA = 1.4), which is optimized for use in STED mode. Excitation wavelengths of 495 nm and 543 nm were selected from the spectrum of a white light laser by means of an acousto-optical beam splitter (AOBS) to excite the fluoresceine and rhodamine dye, respectively. Two detectors recorded the fluorescent signals in different wavelength ranges: 510-540 nm (for the fluoresceine) and a 565-700 nm (for the rhodamine). The two channels were displayed in different 8-bit color look-up tables: green (fluoresceine) and red (rhodamine). The final images were acquired by overlaying these two channels. Typical images consisted of  $512 \times 512$  pixels and  $12 \times 12 \mu\text{m}^2$ . For 3D imaging, no fast imaging was employed, since the gels were stationary on the timescale of imaging. A 3D stack typically had a height of 30-40  $\mu\text{m}$  and images were recorded with a step size of 80 nm.

Measurements of the electrophoretic mobility and zeta potential were performed on a *Malvern ZetaSizer Nano* by *Malvern Instruments*.

### 5.2.4 Analysis routines

Confocal z-stacks were obtained of dilute dispersions of patchy particles in the index-matching solvent CHC with the aim of counting the number of protrusions per particle. Particle cores were FITC-labeled and titania protrusions were RITC-dyed or vice versa, so that is possible to track cores and protrusions separately in the confocal images. The resulting coordinate files were combined to create computer-generated images of the patchy particles (Fig. 5.1a). The particle tracking algorithm delivered the number of cores and the number of patches, hence the average number of patches per particle followed immediately from particle tracking.

To obtain information on the patch number distribution around this average number, two methods were employed. The first method will be referred to as the 'tracking' method. For this method, particles were assigned a 'patch parameter': cores were assigned the number '0' and patches the number '1'. The particle tracking program (by M. Hermes and T.H. Besseling, developed at the

Soft Condensed Matter Group at Utrecht University) was asked to additionally deliver the number of 'bonds' per particle for each core and for a certain bond length. Due to the fact that the program was written for particles of a single size, it automatically chooses the average diameter  $0.5(\sigma_{core} + \sigma_{patch})$  as bond length 1. The bond lengths were therefore scaled post analysis by a factor  $2\sigma_{core}/(\sigma_{core} + \sigma_{patch})$ . One source of error in this method is the choice of bond length, which should be large enough to include the patches but not so large as to include neighboring particles. A dilute dispersion thus yields more accurate results, but has the drawback of low statistical accuracy.

In order to double check the accuracy of the findings, a second routine was used, which will be referred to as the 'cluster method'. The code (by J.C.P. Stiefelhagen, developed at the Soft Condensed Matter Group at Utrecht University) was originally written for clusters of oppositely charged particles. This code checks for connections between particles of dissimilar color (but not for connections between particles of identical color). That is, it detects clusters of alternating particles. For each particle (diameter  $d1$ ), the program searches for particles (diameter  $d2$ ) of a different color. Two particles are marked as belonging to the same cluster when their inter-particle distance is smaller than  $(d1 + d2) \cdot 0.5 \cdot factor$  (with *factor* set by the user, which we choose 1.05) but larger than  $(d1 - d2) \cdot 0.5$ . The code then returns the number of particles in each cluster. For patch number distribution, we considered only 'clusters' with a single core, meaning patchy particles of which a patch is in contact with a second core particle were ignored. Notice that the program does not check for touching particles of the same color, so patchy particles of which only the cores are in contact are counted as separate clusters. This effect could slightly change the distribution about the average patch number, but we do not expect many cores to touch due to the protecting layer of protrusions. Fig. 5.1b displays these clusters of equal (total) number of patches and cores in equal colors.

## 5.2.5 Simulations

NpT "Monte Carlo" simulations were performed by M.N. van der Linden of the Soft Condensed Matter group at Utrecht University to investigate whether the obtained patch number distributions can be explained by polydispersity and maximum inter-particle separation (that still allows for size exclusion of the grafting molecules). Briefly, the initial configuration for each simulation was an FCC lattice with a volume fraction slightly above 0.5 and a log-normal distribution for a specific size polydispersity. The total system size was  $N = 2048$ . The configuration was then compressed until the volume fraction remained constant. Each simulation consisted of  $10^5$  cycles, and per cycle on average one attempt was carried out to change the volume by  $N-1$  attempts to move a randomly chosen particle (with  $N = 2048$ ). The particles are hard spheres (approximated by assigning  $\kappa\sigma \approx 1000$ ) with a Yukawa potential and a contact energy of  $k_B T = 81$ . Simulations were carried out for particle p.d. 0%, 1%, 2%, 3%, 4% and 5%, with five independent simulations per polydispersity. A particle (of radius  $R_1$ ) was assumed to have a patch when the distance to its neighbor (of radius  $R_2$ ) was smaller than  $R_1 + R_2 + d$ , in which  $d$  is a cut-off distance that depends on the grafting molecule size (i.e. the maximum distance between the surfaces of the particles which still excludes the grafting molecules due to their finite size). Simulations were performed for three values for  $d$ : 0.1%, 1% and 10% of the average particle diameter. The simulations returned the coordinates of the particles in the

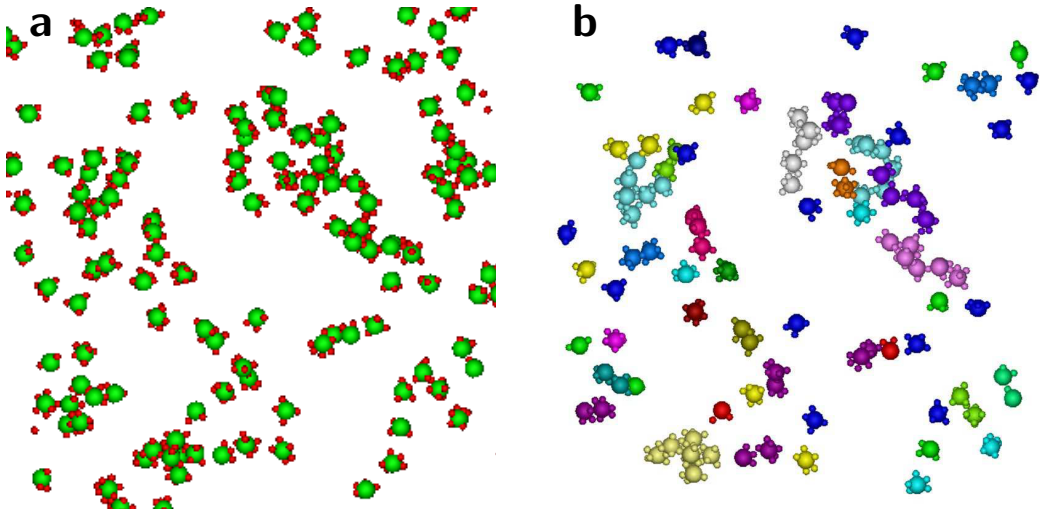


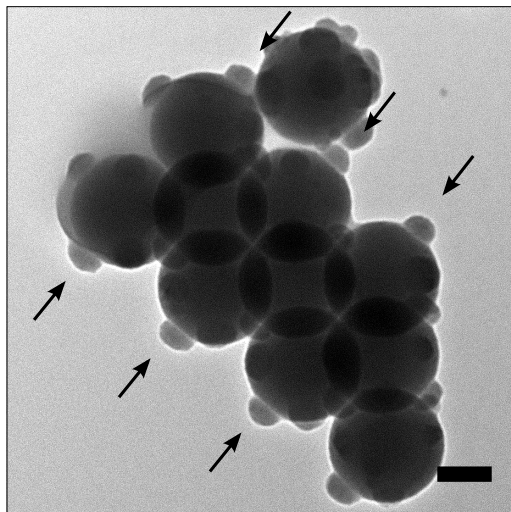
**Figure 5.1:** For sample  $J3$  in App.4.5 (1085 nm core, FITC-labeled core, RITC-labeled titania patches): (a) Computer-generated image of a dilute dispersion of the patchy particles, obtained by particle-tracking confocal z-stacks of a dilute dispersion in CHC. A total of 143 core particles and 570 protrusions was counted (not all particles are displayed). (b) The same system analyzed with a code that tracks clusters. Units of equal color have equal numbers of cores and patches in total. Notice that this routine neglects some clusters close to the rim of the image.

final configuration and, more importantly, histograms of the number of patches per particle (patch number distributions).

## 5.3 Results & Discussion

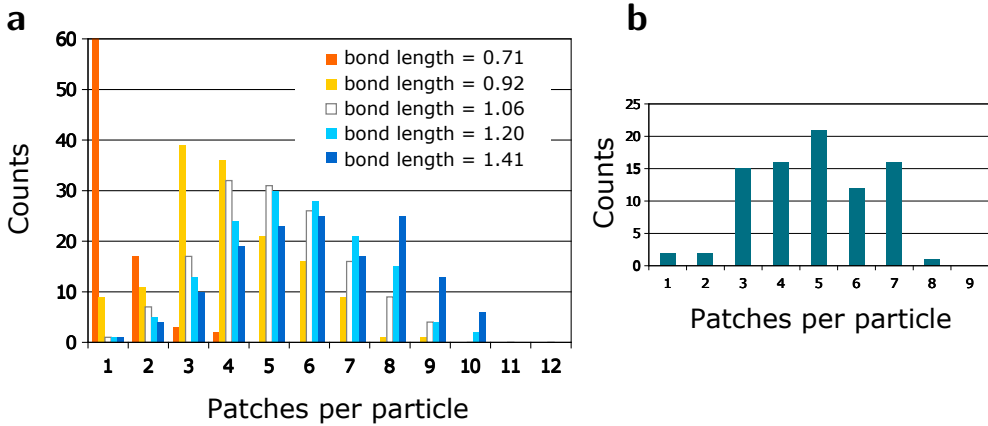
### 5.3.1 Experimental

Fig. 5.2 shows protrusions grown onto a small crystallite that had failed to completely redisperse into single particles before protrusion growth. The positions of the protrusions - indicated by black arrows - nicely illustrate that protrusions grow onto the areas which were contact areas of two particles in the colloidal crystal. Some protrusions, however, are missing. From SEM and TEM images, it was clear that most patchy particles had fewer than twelve patches. Particles packed in a close-packed lattice have twelve neighbors. Thus, some of the patches are 'missing'. Causes could be: polydispersity of the particles, defects in the structure (with extra defects created during solvent evaporation), and shrinking and crack formation in the sintering step. The sintering step was absent in the anhydrous route (see Ch. 4), but the patch number was still significantly lower than twelve in those patchy particles. Plausibly, polydispersity has an especially large influence on the number of protrusions. Patches are formed when the silane is excluded from the contact area during the grafting step. However, silane coupling agents are small molecules ( $\sim 1$  nm) that can easily enter the cavity between two spheres when they are not precisely touching. Thus, even small polydispersity and asphericity have a large influence on the number of patches.



**Figure 5.2:** Silica protrusions grown onto a crystallite, which had not been broken up during sonication. The regular spacing between the protrusions - as pointed out by the black arrows - shows that they grew at the contact areas of the silica particles in the crystal.

Figure 5.3 displays patch number distributions obtained from the dilute sample of Fig. 5.1. The cluster routine yielded a distribution centered around five patches per particle for this sample, although the dilute sample contained too few particles in total for a smooth distribution. The 'tracking' routine yielded a similar distribution for a cut-off bond length of  $1.2\sigma_{core}$ . For a bond length of  $1.4\sigma_{core}$ , a second peak in the distribution appears. This second peak indicates that the protrusions of neighboring patchy particles were included for this choice of bond length, as also confirmed by the fact that two particles with more than twelve patches were found in this case. Since the distribution found for a bond length of  $1.2\sigma_{core}$  is the least skewed and closest to a Gaussian, a bond length of  $1.1\sigma_{core}$  to  $1.2\sigma_{core}$  was judged as appropriate for further analyses with this routine.



**Figure 5.3:** Histograms of the patch number distribution of a the dilute dispersion of sample  $J_2$  (polydispersity 1%) of which zoomed-in renderings are displayed in Fig. 5.1. Histograms were obtained (a) via the particle tracking program (for various bond length between 1.3 - 2.0 times the core diameter), and (b) via the cluster routine, by including only clusters containing one core particle - such as the yellow and green particles in Fig. 5.1(b). A total of 143 core particles was counted, and 37 were single clusters (26%).

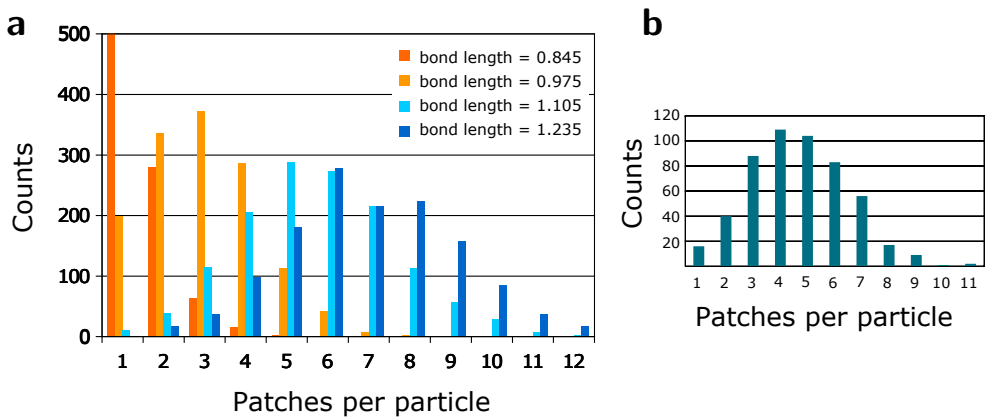


**Figure 5.4:** Histograms of the patch number distribution of sample  $J_2$  (polydispersity 1%) from App. 4.5 obtained (a) via the particle tracking program (for a bond length of 1.3 times the core diameter), and (b) via the cluster routine, by including only clusters containing one core particle - such as the yellow and green particles in Fig. 5.1b - which amounted to 525 particles out of a total of 1361 (39%).

Figs. 5.4 and 5.5 contain histograms obtained from two samples of different polydispersities: sample  $J_2$  (polydispersity 1%) and sample  $P$  (polydispersity 5%) in App. 4.5. The patch number distributions of sample  $J_2$  were centered around 4-5 patches per particle for the cluster routine (for  $factor$  1.05) and 5-6 patches per particle for the tracking routine with bond length  $1.1\sigma_{core}$  (Fig. 5.4). The slight difference is most likely due to our choice of cut-off distance  $d_1 \cdot d_2 \cdot 0.5 \cdot 1.05$  in the cluster routine.

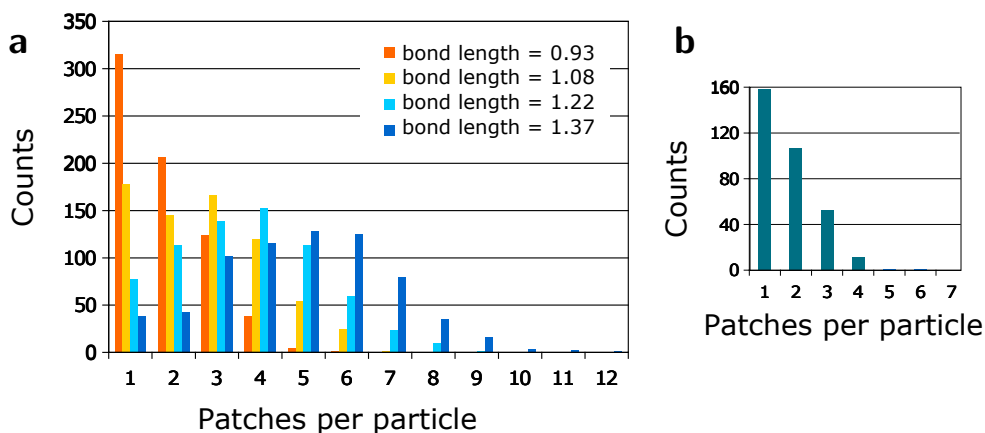


**Figure 5.5:** Histograms of the patch number distribution of sample  $P$  (polydispersity 5%) from App.4.5 obtained (a) via the particle tracking program (for a bond length of 1.3 times the core diameter), and (b) via the cluster routine, by including only clusters containing one core particle - such as the yellow and green particles in Fig. 5.1b - which amounted to 328 particles out of a total of 689 (48%).

The simulation results (see Section 5.3.2, Figs. 5.6a-b), predicted a patch number distribution centered around six patches per particle for this sample  $J2$  assuming  $d$  on the order of  $0.001\sigma_{core}$ , and 8-9 assuming  $d$  on the order of  $0.01\sigma_{core}$ . (Although the molecule size of OTMOS equals at most (stretched) 3.3 nm, titania protrusion widths correlated well with  $d = 12$  nm in Ch. 4, most likely due to kinetic effects preventing the OTMOS molecules from diffusing into the crevices between the particles. Thus, an appropriate estimate for the cut-off distance is (with  $d=3$  nm - 12 nm and  $\sigma_{core} = 1085$  nm) between  $d = 0.003\sigma_{core}$  and  $d = 0.011\sigma_{core}$ .) One explanation for the discrepancy is that domain walls, point defects and cracks were not taken into account in the simulation. Also, small patches (such as patches with a cross section smaller than one pixel) may not be recorded or not counted in the tracking algorithm, whereas small patches are still counted in the simulation results. For sample  $P$  with 5% polydispersity, the 'tracking' routine showed a distribution centered about 5 for a bondlength of  $1.2\sigma_{core}$ . The 'cluster' routine displayed a steeply decreasing distribution of 1-3 patches (Fig. 5.5) for the chosen (somewhat low) cut-off factor of 1.05. The simulations predicted 5-6 patches on average for this sample (see Section 5.3.2, Fig. 5.6a for p.d. 5%), which is in good agreement with the experimental result with the former experimental result.

### 5.3.2 Simulations

Fig. 5.6a shows simulated patch number distributions for a cut-off distance of 0.1% of the average core particle diameter and for various polydispersity values (of the particle core diameter). For a purely monodisperse system, all particles possess twelve patches (black graph), as expected. For higher polydispersity, the patch number distribution quickly drops to lower average patch numbers, illustrating the strong effect of polydispersity on the average patch number. Thus, the experimental

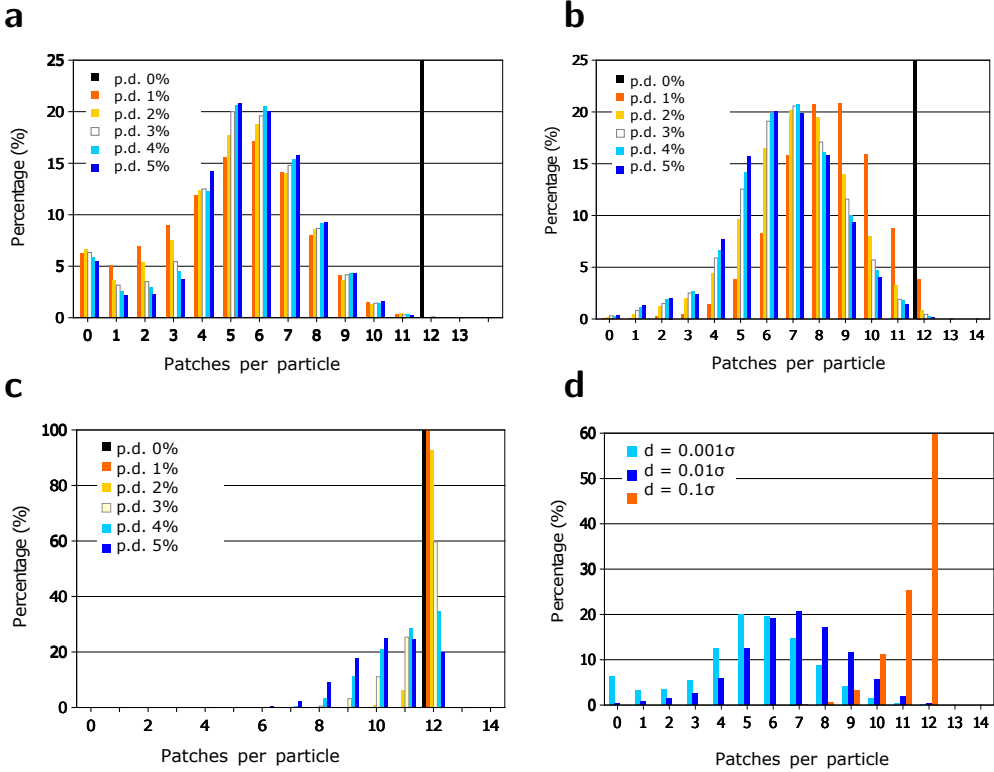


**Figure 5.6:** Patch number distributions as calculated by NpT simulations for particles of polydispersity 0%-5% and cut-off distance (a)  $d = 0.001\bar{\sigma}$ , (b)  $d = 0.01\bar{\sigma}$  and (c)  $d = 0.01\bar{\sigma}$ . The vertical axis is discontinued at 25% for clarity in panels (a) and (b). (d) Patch number distributions as calculated by NpT simulations for particles of 3% polydispersity, comparing the distributions for three different cut-off distances.

patch number distributions and the simulation results are in agreement that higher polydispersity of the core particles shifts the number of patches per particle to a lower value.

Figs. 5.6a-c show that this is a general trend for different cut-off distances  $d$ , but that the effect is smaller for very short cut-off distances: in Fig. 5.6b (for  $d=0.01\sigma$ ) the median of the number of patches per particle shifts from 9 (for 1% polydispersity, red) to 6 (for 5% polydispersity, yellow), while for  $d=0.001\sigma$  (Fig. 5.6a) the median of the number of patches per particle shifts from 6 (for 1% polydispersity, red) to 5 (for 5% polydispersity, yellow).

In Fig. 5.6d the patch number distributions are displayed at a single polydispersity (3%) but for varying cut-off distances  $d$ . The average number of patches per particle shifts to higher values for increasing cut-off distance  $d$ . This effect was naively expected, since a larger  $d$  implies that particles with a larger inter-particle separation can still form patches.

### 5.3.3 Gels of patchy particles in low-polar solvents

The fact that the patchy silica particles with titania protrusions presented in Ch. 4 do not possess a narrow distribution of the number of patches per particle implies that these particles are more likely to form gels than crystalline structures, even with suitable patch-patch interactions. We indeed encountered gel structures by dispersing these particles in low-polar solvents; this section describes our investigation into the nature of the inter-particle interactions.

Patchy particles with an OTMOS-grafted silica core particle and dyed titania patches were prepared as described in Ch. 4 (Sample J3, App. 4.5). The particles were dispersed in low-polar solvents to attempt to induce patch-patch interactions. Such interactions are expected, since the titania protrusions do not possess a hydrophobic grafting and can stick due to solvophobic and van der Waals interactions. The solvents opted for were low-polar solvents, since the grafted silica can be charge-stabilized in these solvents: cyclohexyl chloride (CHC, static  $\epsilon = 7.6$  [270],  $n_D^{20} = 1.46$  [271] and  $\rho = 0.993$  at 25 °C [183]) and 1,2-dichloroethane (DCE, static  $\epsilon = 10.7$ ,  $n_D = 1.44$  and  $\rho = 0.862$  g/cm<sup>3</sup> at 25 °C [272]). The conductivity of the CHC was 20 pS/cm, corresponding to a Debye length of 11  $\mu$ m (see Ch.3). The patchy particles formed gels in both solvents within the time needed (~10 minutes) to cure the glue (Fig. 5.8a-b). The gel in CHC was easily broken up into a fluid of clusters upon turning the capillary upside down for confocal microscopy (Fig. 5.8a), while the gels in DCE did not break up under the same conditions.

These patchy particle gels were too dense to accurately determine whether titania patches stuck to other patches or rather to the particle cores. Therefore, OTMOS-grafted silica particles and RITC-infiltrated titania particles in CHC were mixed to discover whether the two species are mutually attractive in specific solvents. In CHC, the (non-patchy) OTMOS-grafted silica particles formed a hexagonal long-ranged crystal indicating a strong electrostatic repulsion, while the dyed titania particles aggregated (most likely due to the absence of a hydrophobic grafting layer). When mixed, the OTMOS-particles stuck to the titania clusters, as shown in Fig. 5.8c. This indicates that in CHC titania protrusions stick to the particle cores (and most likely also to other titania protrusions).

In DCE, the behavior of the individual species was similar to that in CHC: OTMOS-grafted silica particles repelled each other, while dyed titania formed aggregates since the titania is hydrophilic. However, when mixed in DCE, the two species of particles did not stick to each other, unlike they did in CHC (Fig. 5.8d). Thus, in gels of patchy particles with OTMOS-grafted cores and titania protrusions, it is probable that the protrusions stick to one another. Such a patch-patch attraction could have a partially solvophobic character although van der Waals attraction will certainly also contribute given the dielectric constant mismatch: the patches have no hydrophobic grafting and the surface area exposed to the apolar solvent is reduced by sticking together.

To gain further insight into the interactions in the gel formation, we measured the electrophoretic mobility of titania particles and OTMOS-grafted silica particles in DCE and CHC. Unfortunately, RITC-labeled titania particles did not yield clear results, most likely since the fluorescent dye disturbs the laser (633 nm) Doppler electrophoresis. Fig. 5.7 shows the zeta potentials measured for non-dyed titania particles in CHC and DCE as well as for OTMOS-grafted silica particles in the same solvents, assuming the Hückel limit applies. While the titania particles were positively charged in

both DCE and CHC, the OTMOS-silica particles were negatively charged in CHC and positively charged in DCE. Therefore, it is likely that in CHC the (positively charged) titania protrusions stick to the (negatively charged) OTMOS-silica cores. In contrast, in DCE all constituents are positively charged. Since OTMOS-silica did not aggregate in DCE, most likely the titania protrusions stick to other protrusions through solvophobic and/or van der Waals interactions. Thus, these zeta potential results confirm the conclusions drawn above from confocal imaging of mixtures of OTMOS-silica and titania in CHC and DCE. The inclusion of APTES-RITC into the titania is likely to make the titania even more positively charged (since RITC has a positive amine group) and does not alter this conclusion.

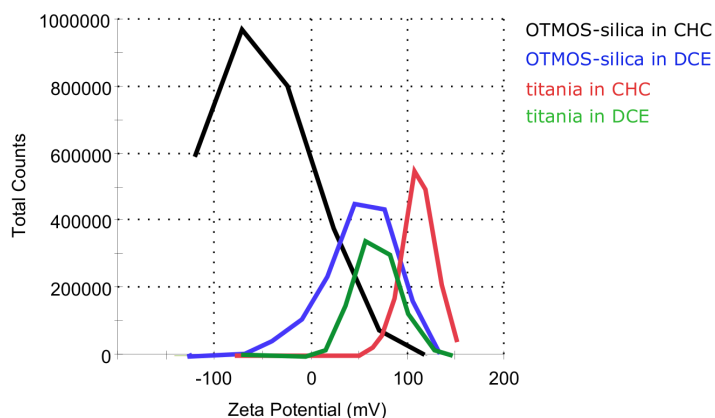


**Figure 5.7:** Zeta potentials measured for OTMOS-silica particles and (non-dyed) titania particles in CHC and DCE. The voltages used were 10-20V as higher voltages resulted in multiple peaks. Titania concentration 1.1 mg/mL. The OTMOS-silica concentration was adjusted by dilution until a slight scattering was observed by eye.

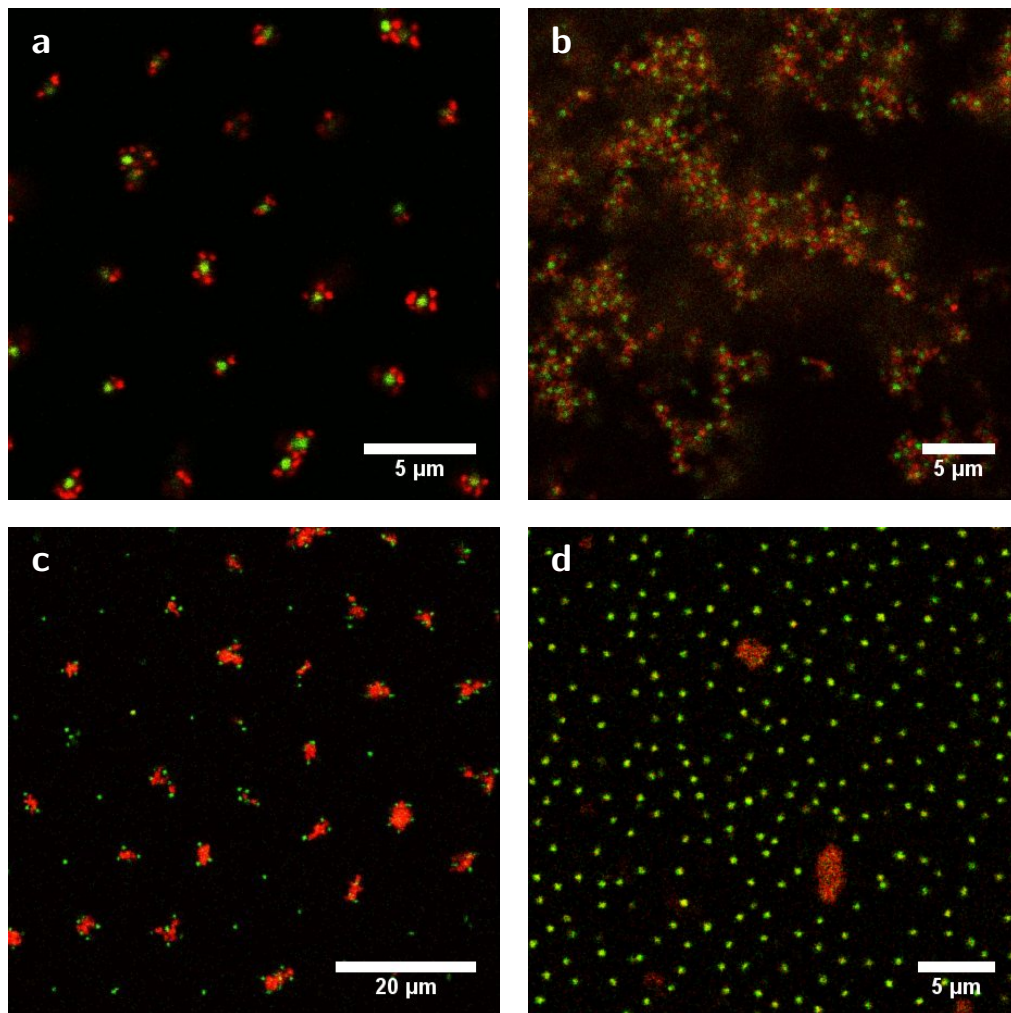


**Figure 5.8:** Patchy particles and component species in CHC and DCE: (a) Patchy particles dispersed in CHC, after turning the sample upside down for confocal imaging. (b) Patchy particles dispersed in DCE, after turning the sample upside down for confocal imaging. (c) OTMOS-grafted silica and RITC-dyed titania in CHC. (d) OTMOS-grafted silica and RITC-dyed titania in DCE.

## 5.4 Conclusions & Outlook

In this chapter, experimental values of the patch number distributions for the particles presented in Ch. 4 were obtained by analyzing 3D confocal z-stacks. Two routines were used to extract the distributions from the data coordinate files. A 'tracking routine' checked for particles within a certain bond length around designated as 'core' particles. A 'cluster routine' checked for clusters of alternating particles, and only clusters with a single 'core' particle were considered for the patch number distributions. The patch number distributions obtained with the tracking routine were in agreement with the simulations for a bond length of  $1.1\sigma_{core}-1.2\sigma_{core}$ , which is a reasonable choice, since the centers of the patches reside at  $1\sigma_{core}$ . The patch number distributions obtained via the cluster routine generally yielded slightly lower average patch numbers due to our choice of cut-off factor. The dilute dispersion (Fig. 5.3b) was intended to yield the most accurate results by reducing the risk of double counting of protrusions, yet the absolute number of particles was low, which affected the shape of the distribution. In future research, the 'cluster' routine should be used with multiple cut-off factors.

The distributions of the number of patches per particle were simulated using the compression of randomly distributed polydisperse particles on a crystal lattice and taking size polydispersity and maximum particle-to-particle separation (representing the grafting molecule size, but also kinetic factors such as the probability to diffuse into small crevices) into account. A small polydispersity (1%) already had a large influence on the average number of patches per particle: for this polydispersity a maximum separation  $d$  of  $d=0.001\bar{\sigma}$  shifted the median patch number to 6 (compared to 12 in a crystal of monodisperse particles). The simulations did not take rattlers - i.e. encaged particles - into account, which should be done in future studies. Another factor not taken into account are defects and cracks due to drying the colloidal crystal. Thus, the agreement between the simulations and experimental results is qualitative at this point.

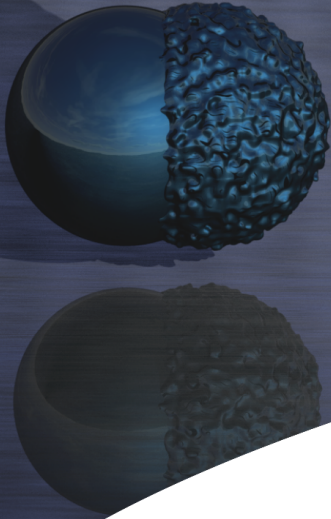
We can conclude from the simulated distributions that to obtain patchy particles with (a distribution close to) twelve patches per particle with the synthesis method presented in Ch. 4 it is necessary that the polydispersity of the particles be below 0.5%. By micro-emulsion synthesis, colloidal particles with polydispersities below 0.1% can be prepared (D. 't Hart, personal communication), and such particles could be used in future research. Incidentally, poly(methyl methacrylate) (PMMA) particles with twelve flat sides (colloidal rhombic dodecahedrons) have recently been prepared [273] by thermal annealing; that synthesis route can most likely also be extended to silica [189]. Centrifugation techniques such as in Refs. 44, 59, 274 may be applied in future research to separate particles of different patch numbers. In a glassy system, the volume fraction and number of contacts between colloids may even be slightly higher than in a colloidal crystal [275], so colloidal glasses could be used to increase the patch number and/or to obtain patchy particles with more than twelve patches.

Finally, we showed that patchy silica particles with titania protrusions form gel structures in the low-polar solvents CHC and DCE. The nature of the the inter-particle interactions was investigated by mixing silica particles and dyed titania particles in CHC and in DCE. We find that the titania protrusions stick to the silica cores (in CHC) or to other protrusions (in DCE) due to the absence of a hydrophobic grafting. In DCE, OTMOS-silica and dyed titania had a charge of the same sign,

whereas in CHC the sign of the charges as opposite. Also, in DCE, OTMOS-silica and dyed titania did not coagulate. These observations lead to the conclusion that in DCE the patchy particles gel via solvophobic patch-patch interactions.

## Acknowledgements

All patch number distribution simulations were performed by Marjolein van der Linden, and she is sincerely thanked for this hard work. We thank Zdenek Preisler for useful discussions and also initial simulations. Johan Stiefelhagen and Frank Smalenburg are thanked for kindly sharing their code on binary clusters, and Thijs Besseling and Michiel Hermes for sharing and discussing their particle tracking routine. Without these codes the experimental work would not have been possible.



# CHAPTER 6

## Hetero-dimer particles through site-specific nucleation and growth

We describe a synthesis method for hetero-dimer particles with a lollipop shape by combining a templating method described in Ref. 276 with recent findings that surface heterogeneity and particle geometry are of influence to liquid adsorption on a particle [253]. Specifically, 3-methacryloxypropyltrimethoxysilane (MPS) was condensed and grown onto silica particles of various shapes. We confirmed that the surface geometry is of considerable influence to the final particle geometry, since the synthesis method yielded lollipop-shaped colloids for nail-shaped seed particles, yet not for bullet-shaped seed particles. The particles also offer interesting possibilities for future research, such as surface modification of the MPS side.

---



## 6.1 Introduction

### 6.1.1 Geometry dependent polymer condensation and growth on bullet-shaped particles

Investigations by Peng *et al.* have shown that poly(methylmethacrylate) (PMMA) and styrene can condense and grow specifically onto the flat end of 3-methacryloxypropyltrimethoxy silane (MPS)-grafted bullet-shaped silica particles. In their system, Peng *et al.* found that the site-specificity in their work is most likely a combined effect of surface heterogeneity and particle geometry [253].

First, let us briefly consider how particle geometry can influence the contact angle. The surface tension between a liquid and a solid surface is set not only by the contact angle for the liquid on the flat solid surface, but also by curvature of the surface. Namely, a curved surface creates a larger interface on a droplet of equal volume than a flat surface does. Thus, surface curvature was a potential explanation as to why PMMA attached to the flat end of bullet-shaped particles in Ref. 253.

A difference in intrinsic contact angle (surface tension) was, however, also necessary to explain the experiments. How could the intrinsic contact angle differ for the edge and the end of the bullet-shaped particle? During the growth of the bullet-shaped silica particles used by Peng *et al.* from emulsion droplets of water in pentanol [13, 253, 277], the flat end stays attached to a PVP-loaded water droplet, hence the flat end conceivably contained more PVP than the rest of the particle surface. In a clever set of experiments, such a compositional difference was confirmed. Bullet-shaped particles were sintered for two hours to burn away all PVP. For those particles PMMA polymerized on the edge of the bullets rather than the end. This observation led to the conclusion that not only the shape of the silica rod determined the preferred site of polymerization but that the end of the bullets most likely also had a different surface tension. In other experiments, the surface tension was made uniform (on edge and end) by coating the bullets with a layer of silica. For a thick (150 nm) silica shell, all PMMA indeed polymerized at the edge of the bullets, confirming calculations also presented in the paper on the influence of the particle shape in combination with the surface tension. However, for a thin (15 nm) silica shell, most PMMA still polymerized specifically at the bullets' flat end, implying that geometry affected the locus of condensation as well.

Detailed calculations on the free energy of adsorption for bullet-shaped particles (adsorbed to a flat interface which was also considered not be deformed) were performed in Refs. 253, 278–280. Peng and coworkers showed that the adsorption free energy has a global minimum for edge-on adsorption when the intrinsic contact angle is the same on all parts of the bullet [253]. When the edge and the end of the bullet had unequal surface tensions for the nucleating liquid in the reaction medium, a local minimum for end-on adsorption of the bullet appeared when the flat end was either sufficiently wettable or sufficiently non-wettable (namely when  $|\cos\theta| > 0.3$ ). Thus, assuming polymer nucleation is an equilibrium process, adsorption occurred preferentially at the flat end of the bullet shaped particles for certain combinations of the surface tensions between the colloid, the medium and the nucleating liquid.

In principle, the expression for the free adsorption energy described the case of a macroscopic, flat interface and a microscopic particle, so the calculations should be regarded as a first step towards

disentangling the influence of shape and local surface tension on site-specific adsorption. More realistic calculations have to take a finitely-sized droplet of liquid into account and probe its free energy as it is adsorbed at different locations on the solid particle.

## 6.1.2 Overview of this chapter

This chapter concerns the synthesis and investigation of various types of hetero-dimer particles, i.e. particles with two patches of different chemical composition. First, hetero-dimer particles with an acorn shape or a dumbbell shape were prepared by hydrolysis and condensation of 3-methacryloxypropyltrimethoxysilane (MPS) droplets onto octadecyltrimethoxysilane (OTMOS)-grafted silica spheres following Ref. 276. Then, the same synthesis route was applied to rod-like particles with a nail-like shape, and it was found that the MPS droplets adsorbed site-specifically to the head of the nail, resulting in “MPS-lollipop particles”. We investigated the effect of the particle shape and size on the MPS nucleation and growth by control experiments.

## 6.2 Experimental details

### 6.2.1 Chemicals

The following chemicals were used. Silane coupling agents: (3-methacryloxypropyl)trimethoxysilane (MPS,  $\geq 98\%$ , *Sigma Aldrich*), octadecyltrimethoxysilane (OTMOS, 90%, technical grade, *Aldrich*), n-octadecyltriethoxysilane (OTEOS, *Sigma Aldrich*) and (3-aminopropyl)triethoxysilane (APTES,  $\geq 98\%$ , *Sigma Aldrich*). Surfactants: Pluronic F108 block copolymer surfactant (average mol.wt.: 14600 g/mole, BASF), Triton X-100 (*Sigma Aldrich*) and Igepal CO-520 (average mol.wt.: 441 g/mole, *Aldrich*). Water was deionized with a *Millipore Direct-Q UV3* reverse osmosis filter apparatus (*Millipore Corporation*) and had a resistivity of at least 18.2 M $\Omega$ cm. Ethanol (absolute) was obtained from *Merck* and 1-pentanol (*ReagentPlus*,  $\geq 99\%$ ) from *Sigma Aldrich*. The catalysts aqueous ammonia (26.6wt.%), butylamine (99.5 wt.%) and sodium citrate dihydrate (p.a.  $\geq 99.0\%$ , anhydrous) were purchased from *Sigma Aldrich*. 2,2'-Azobis(2-methylpropionitrile) (AIBN) initiator from *Janssen Chimica* was recrystallized from ethanol. RAS (rhodamine isothiocyanate-aminostyrene) dye conjugate was prepared as described in Ref. 281 and dissolved in acetone (99%, *Merck*). Fluorescein isothiocyanate (FITC,  $\geq 90$  wt.% (HPLC)) was purchased from *Sigma Aldrich*, as was polyvinyl-pyrrolidone (PVP, K-30, 40.000 g/mol). All chemicals were used as received.

### 6.2.2 Synthesis of acorn/dumbbell-shaped silica/MPS particles

Acorn-shaped silica/MPS particles (with an OTMOS-grafted silica side and an MPS bulge) were prepared according to a procedure given in Ref. 276. Silica particles (size:  $970 \pm 5$  nm, 2% p.d.) with a non-fluorescent shell grown by the method of Giesche *et al.* [182] around fluorescein isothiocyanate (FITC)-labeled silica seed particles of  $\sim 300$  nm in diameter served as template particles. The particles were grafted with OTMOS using the anhydrous recipe described in Ch. 4.

MPS was then hydrolyzed in water by a base-catalyzed reaction, in which a surfactant is added to influence the contact angle of the hydrolyzed MPS with the grafted surface. The liquid MPS droplets attach to the OTMOS-silica surface. In a typical synthesis, 18 mg of OTMOS-grafted silica particles - dried from ethanol - were redispersed in a mixture of 2.875 mL water and 1.14 mL 0.35 wt.% Pluronic F108 in water by sonication in an ultrasonic bath (*Branson 2510* or *8510*) in a 20 mL glass vial. Under magnetic stirring, 4  $\mu$ L aqueous ammonia and subsequently 70  $\mu$ L MPS were added. MPS droplets attached to the OTMOS-silica were noticeable within 15-20 minutes.

To fluorescently label the MPS droplets, the following procedure was used. Rhodamine isothiocyanate (RITC) was coupled to aminostyrene according to a recipe by Bosma *et al.* [281]. The reaction product (RAS, (rhodamine isothiocyanate)-aminostyrene) was dissolved in acetone to a final concentration of  $\sim 0.2$  mg/mL. After the MPS had reacted for 1h under magnetic stirring, 20  $\mu$ L of the solution of RAS in acetone was added to the reaction mixture. The RAS in acetone is taken up by the MPS droplets, making the MPS droplets suitable for CSLM studies.

While the MPS droplets hydrolyze to form liquid droplets and then polymerize through the formation of siloxane bonds from the hydrolyzed methoxy groups, the MPS gel can also be cross-

linked through its organic functional groups by a free radical polymerization reaction using the initiator AIBN and heating the reaction mixture. After 1 h stirring with the dye solution, the methacrylate groups of the MPS were cross-linked by adding 6 mg of AIBN, stirring for 10 minutes, and heating overnight at 70 °C in an oil bath. The shape of the MPS bulge with this recipe was cap-like.

The shape of the hetero-dimer particles was successfully varied by using a different surfactant. Adding a 0.35 wt.% Igepal CO-520 or a 0.35 wt.% Triton X-100 in water solution instead of the Pluronic F108 solution yielded a more pronounced dumbbell shape. Successful cross-linking was not achieved in the case of these dumbbell-shaped particles as described in Section 6.3.

The above procedure was also performed on supraparticles [256]. Cobalt iron oxide core-shell ( $\text{FeO@CoFe}_2\text{O}_4$ ) nanoparticles were prepared as in Ref. 282; these nanoparticles had a monolayer of oleic acid as a capping agent. Supraparticles were prepared by B. de Nijs (Utrecht University) from these nanoparticles as described in Ref. 283, but with toluene as the anhydrous phase. In brief, a dispersion of nanoparticles in toluene was emulsified in water containing sodium dodecyl sulfate (SDS) by shearing at a rate of  $1.56 \cdot 10^{-5} \text{ s}^{-1}$ . The toluene was then slowly evaporated by heating at 68 °C for four hours, yielding clusters of nanoparticles in water (called supraparticles). To prepare hetero-dimers, the supraparticles were dispersed in water by sedimentation in gravity, exchanging the supernatant for deionized water, and sonicating for a few seconds. No further washing steps were carried out since the supraparticles may disintegrate when the SDS is washed away. The supraparticles were not dried prior to use, and the final supraparticle concentration was 45 g/L. To 2.86 mL of the dispersion of supraparticles in water, we added 1.14 mL F108 solution (0.35 wt.% in water), 4  $\mu\text{L}$  aqueous ammonia and subsequently 70  $\mu\text{L}$  MPS. The addition was carried out under shaking using a VV3 vortex mixer (VWR), since the particles have a tendency to stick to magnetic stir bars due to their paramagnetism. After shaking the reaction mixture for 1.5 h, 20  $\mu\text{L}$  of RAS-saturated acetone were added. The MPS side was cross-linked through the methacrylate groups as described in the previous paragraph, by adding 6 mg of AIBN, shaking for 10 minutes, and heating overnight in an oil bath at 70 °C. The reaction mixture was not stirred or shaken during the heating step. The final particles were collected by washing twice with deionized water and once with ethanol.

### 6.2.3 Hetero-dimer particles in CHC

To make the silica/MPS acorn-shaped particles dispersible in low-polar solvents, the particles were treated with the silane coupling agent docosyltriethoxysilane ( $\text{C}_{20}\text{TES}$ ) in the following way. After cross-linking in water, the particles were washed with ethanol three times. Then, an amount corresponding to ~75 mg silica was sonicated in a mixture of 10 mL toluene, 1 mL *n*-butylamine and 1 mL  $\text{C}_{20}\text{TES}$  for 2 h. The reaction was allowed to proceed for two days without stirring. The particles were washed twice with ethanol and once with cyclohexyl chloride (CHC) by sedimentation in gravity and exchange of the supernatant.

Crystals and glasses of silica/MPS acorn-shaped particles with long-range interactions were prepared from  $\text{C}_{20}\text{TES}$  treated acorn-shaped particles. These particles were dispersed in CHC and diluted to the desired volume fraction with more CHC. The initial volume fraction contained an equivalent of 150 g/L silica particles while the final volume fractions were 30 g/L (5x diluted) and 10 g/L (15x

diluted). The CHC was deionized before use by placing it over molecular sieves for several days (conductivity at the time of use: 1-2 pS/cm). Samples were prepared by filling a 0.1 × 1.0 mm borosilicate capillary (*VitroCom* no.5010).

### 6.2.4 Synthesis of lollipop-shaped silica/MPS particles

Nail-shaped particles were prepared using regulation of the growth temperature, as recently published in Ref. 284 based on the original work of Kuijk *et al.* [13]. In this case, 1 g of PVP (40.000 g/mol) was dissolved in 10 mL pentanol by sonication in a 20 mL glass vial (*Wheaton*). To this solution, 1 mL of ethanol, 0.28 mL of water and 67  $\mu$ L of sodium citrate (0.18 M in water) were added. After shaking the vial by hand, 0.225 mL of ammonia was added. Again, the vial was shaken by hand. Finally, 100  $\mu$ L TEOS was added and the vial was shaken once more. (In the nail-shaped particles used in this chapter, a mixture of 98  $\mu$ L TEOS and 2  $\mu$ L OTEOS was used instead, but we checked that the OTEOS was not necessary for the particle shape). The reaction mixture was immediately placed in an oven thermostated at 50 °C. As described in Ref. 284, performing the reaction at elevated temperature reduces the rod diameter. After two hours in the oven, the bottle was placed in a fridge at 4 °C in order to grow the nails' wider "head". After 6-18 h, ethanol was added to quench the reaction and the nail-shaped particles were collected by centrifugation and redispersion in ethanol. This synthesis method was also successfully repeated at a larger scale (150 mL PVP/pentanol mixture, in a 250 mL round-bottom flask) by F. Hagemans (Utrecht University).

These nail-shaped particles were dyed with FITC dye [13] and then grafted with OTMOS before the MPS condensation step. For the dyeing step, a mixture of 4 mg FITC, 4  $\mu$ L APTES and 250  $\mu$ L ethanol was allowed to form APTES-dye conjugates for two hours under stirring. To 8.5 mg of dried nail-shaped particles we added 1 mL of ethanol, 10  $\mu$ L ammonia and 40  $\mu$ L dye solution. After 2 h reaction time, the dyed particles were centrifuged and washed two times with water. For the OTMOS-grafting step, the nail-shaped particles were dried once more, and a mixture of 1 mL of toluene, 0.1 mL of butylamine and 0.1 mL OTMOS were added. After two days with intermittent sonication, the dyed and OTMOS-grafted nail-shaped particles were washed twice with ethanol.

Particles consisting of a silica rod with a cross-linked MPS sphere at one end of the rod (called 'MPS-lollipop particles' hereafter) were synthesized by combining these nail-shaped particles with the recipe for MPS nucleation and growth outlined in Section 6.2.2. Nail-shaped particles ( $\sim$ 8.5 mg) were dried and redispersed in a mixture of 890  $\mu$ L water and 355  $\mu$ L F108 in water (0.35 wt.%). To this dispersion, 1.25  $\mu$ L ammonia and 18  $\mu$ L MPS were added. The dispersion was stirred for 30 minutes, during which an MPS protrusion grew onto the nail-shaped particles. Subsequently, 10  $\mu$ L of acetone saturated with RAS-dye were added to the reaction mixture. After an additional 10 minutes of stirring, the final MPS-lollipop particles were collected by centrifuging twice with water and then stored in ethanol.

To test the nucleation and condensation of MPS onto rod-like particles with a flat end (bullet-shaped particles), the exact same synthesis route was performed on two batches of bullet-shaped particles (of different size and aspect ratio:  $L/D = 6 \pm 1$  and  $D = 0.31 \pm 0.06 \mu\text{m}$  versus  $L/D = 2.1 \pm 0.4$  and  $D = 0.47 \pm 0.18 \mu\text{m}$ ). These rod-like particles were prepared as described in Ref. 253 after the

original method of Kuijk *et al.* [13].

To test whether MPS-lollipops could be polymerized through the methacrylate groups, 2.8 mg OTMOS-grafted nail-shaped particles were dispersed in 0.88 mL deionized water and 0.34 mL of Pluronic F108 solution (0.35 wt.%) by sonicating for 2 h. Then, 1  $\mu$ L of ammonia (26.6 wt.%) and 18.75  $\mu$ L MPS were added. After stirring this reaction mixture for 1 h, 7 mg AIBN was added. The mixture was heated at 70 °C for 24 h and subsequently washed with absolute ethanol (100%) several times until no scattering from secondary nucleation was visible.

### 6.2.5 Imaging silica/MPS hetero-dimer particles

CLSM images were recorded on a Leica SP8 confocal microscope. The microscope was equipped with a *Leica HCX Plan Apo STED Orange* 100x oil immersion lens (NA = 1.4), which is optimized for use in STED mode. Excitation wavelengths of 495 nm and 543 nm were selected from the spectrum of a white light laser by means of an acousto-optical beam splitter (AOBS). Two detectors recorded the fluorescent signals in different wavelength ranges: a PMT in the range 510-540 nm (for the FITC-dyed particle cores), and a HyD in the range 565-700 nm (for the RAS-dyed MPS protrusion). The two channels were displayed in different 8-bit color look-up tables: green (FITC-labeled core) and red (RAS-dyed protrusion). The final images were acquired by overlaying these two channels. The hetero-dimer particles with a nanoparticle cluster in one lobe were imaged using reflection mode for the nanoparticle cluster.

## 6.3 Results & Discussion

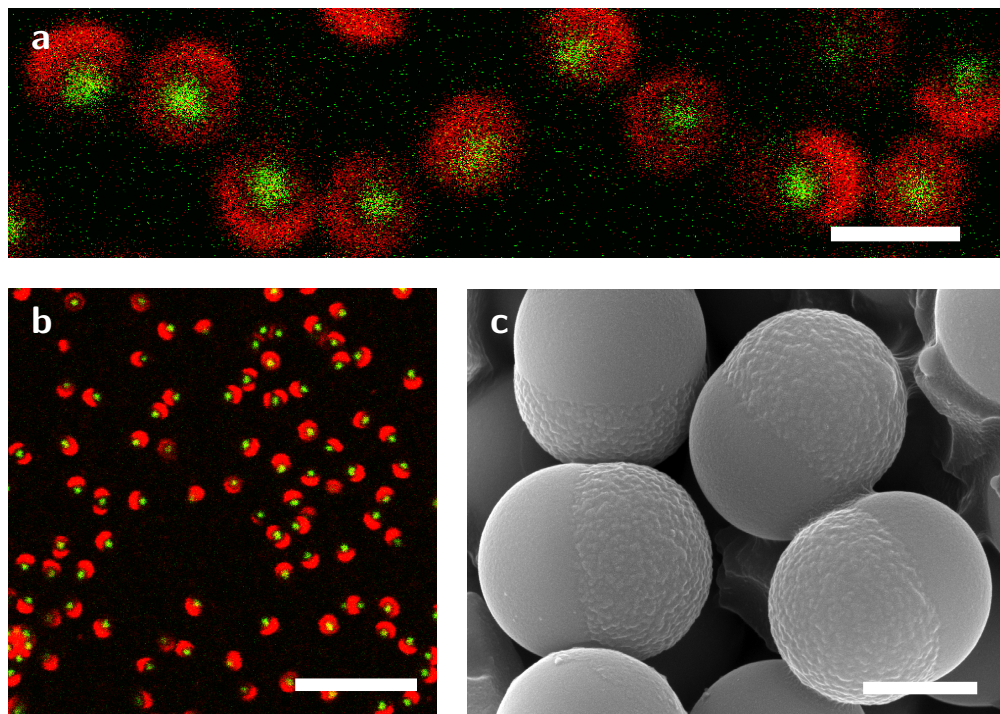


**Figure 6.1:** (a,b) Confocal microscope images and (c) SEM image of acorn-shaped silica/MPS hetero-dimers. Panel (a) is a close-up of the acorn silica/MPS particles to display the cap-like shape of the dyed MPS bulge (rhodamine labeled, displayed in red). Note that the fluorescent core (fluorescein labeled, displayed in green) of the silica particle is enveloped in a non-fluorescent shell, which is not visible. Scale bars denote 2  $\mu\text{m}$ , 10  $\mu\text{m}$  and 1  $\mu\text{m}$ , respectively.

### 6.3.1 Acorn/dumbbell-shaped silica/MPS hetero-dimers

The silica/MPS hetero-dimer particles prepared with Pluronic F108 as a surfactant possess an MPS protrusion covering half of the particle surface (Fig. 6.1). We refer to these particles as ‘acorn’ particles in view of the shape. Particles prepared with Igepal CO520 (Fig. 6.1c) or Triton X-100 as a surfactant were shaped differently: the MPS droplets formed a more spherical lobe attached to the silica surface, creating a hetero-dumbbell shape. Since the added volumes of silica particles and MPS were equal in the syntheses of both types of particles, the shape change must be a result of the different contact angle of the hydrolyzed MPS with the OTMOS-silica surface as dictated by the surfactants (cf. Fig. 6.2a,b).

Hetero-dimer particles did not form when silica particles without any surface grafting were used as template particles in the MPS nucleation/condensation synthesis route (Fig. 6.3a). Rather, rhodamine

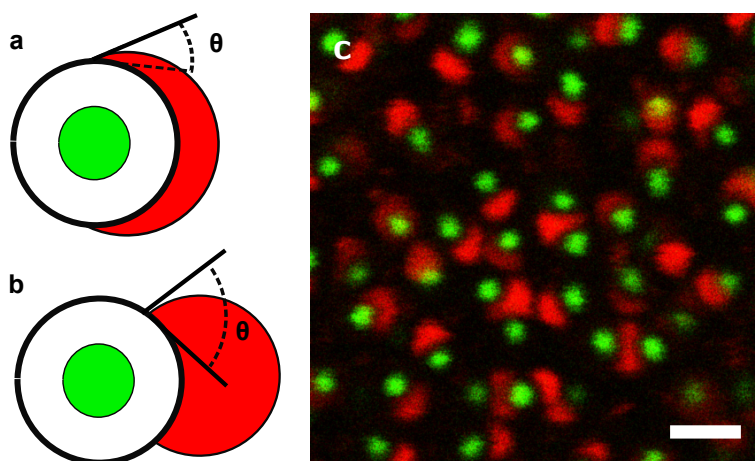


**Figure 6.2:** (a,b) Schematic drawings of the contact angles  $\theta$  of hydrolyzed MPS droplets on OTMOS-grafted silica particles for (a) F108 surfactant and (b) Igepal CO520 surfactant. (c) Confocal microscope image of dumbbell-shaped silica/MPS particles in water. Scale bar denotes 4  $\mu\text{m}$ .

aminostyrene was observed on the outside of the entire silica particle, implying that either a layer of MPS was covering the entire silica particle, or the RAS dye conjugate had adsorbed to the surface (which is somewhat unlikely in view of the hydrophobicity of RAS dye and the hydrophilicity of the surface). The fact that hydrolyzed MPS nucleates on the entire particle is not surprising, as the methoxy groups of MPS can link to the silanol groups of the silica without OTMOS-grafting. Possibly, the protruding methacryloxy groups then form a limitation for the MPS to nucleate and grow further on the surface. Moreover, Van Blaaderen and Vrij showed that organo-silica particles can be grown, but only in mixtures of silane coupling agent (APTES, in their case) and TEOS [285]. For MPS-grafted template particles, hetero-dimers formed (Fig. 6.3b) but the eccentricity of the silica sphere and the MPS bounding sphere was so small as to be nearly unnoticeable. A thin concentric shell was formed around the seed particles when Triton X-100 was used as a surfactant in the synthesis (not shown here). These experiments show that both surfactant type and surface grafting type determine the contact angle of the hydrolyzed MPS liquid with the surface and hence the final particle shape.

In this synthesis route, surfactants not only serve as a way to control the contact angle of hydrolyzed MPS with the template particles, but also as an aid to disperse the -hydrophobic- OTMOS-grafted silica template particles in water. However, some aggregates of the silica particles survived and formed irregular silica/MPS particles. In addition, occasionally two MPS droplets grew on a single silica particle, and some of the MPS droplets collided before the methacrylate groups' cross-linking step. As a rough estimate from confocal images, the sample of dumbbell-shaped particles prepared using Igepal contained  $14 \pm 1\%$  particles with two silica particles and one shared MPS droplet. The sample of acorn-shaped silica/MPS particles contained 7-12% silica particles with two MPS droplets,

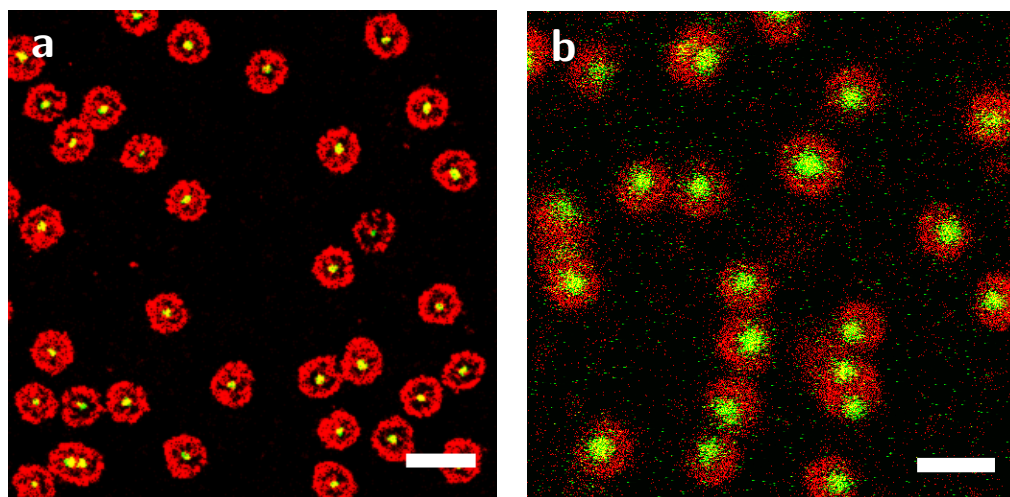


**Figure 6.3:** (a) Product of a reaction in which MPS (rhodamine-labeled, red) was condensed and grown onto silica particles (fluoresceine-labeled core, green) without a surface-grafting. (b) Product of a reaction in which MPS was condensed and grown onto silica particles previously grafted with MPS. Specifically, to 20 mL of a dispersion of 0.4 wt.% (a) non-grafted or (b) MPS-grafted silica particles in deionized water were added: 8.58 mL water and 11.42 mL of a solution of 0.35 wt.% F108 in water. After sonication of this dispersion, 40  $\mu$ L ammonia and 70  $\mu$ L MPS were added. After 30 minutes of stirring, 0.3 mL RAS dye in acetone was added. The particles in (b) were cross-linked as follows: after another 15 minutes, 60 mg AIBN was added. After 10 minutes stirring, the dispersion was heated to 70 °C overnight and washed three times with water. The scale bars represent 3  $\mu$ m and 2  $\mu$ m.

and 0.5-1.5% particles with a conjoined MPS droplet. A PVP viscosity step-gradient as described in Ch. 9 could probably be used to separate particles of different morphology.

Cross-linking of the methacryloxy groups of the MPS lobe was achieved successfully for acorn-shaped particles, but not for dumbbell-shaped hetero-dimers: most dumbbell-shaped particles lost their MPS lobes in the cross-linking step. Seeing that the MPS was not (or hardly) covalently bound to the silica surface, since the silica surface is protected by OTMOS-grafting, such detachment is not surprising. The internal stress at the silica/MPS interface caused by the cross-linking reaction results in detachment of the MPS lobe. The MPS bulge did stay attached in the case of acorn-shaped particles, where the MPS almost envelopes the silica particles forming a mechanical lock. Particles with cross-linked MPS lobes remained intact upon drying, whereas non-cross-linked hetero-dimers disintegrated (onto the sample holder, i.e. TEM grid or SEM grid) upon drying but were stable against centrifugation and washing with water. The SEM image in Fig. 6.1c shows that the MPS side on acorn-shaped silica/MPS hetero-dimers has a rough surface, which is probably caused by the internal stresses during the cross-linking step (or by the evaporation of acetone in this step) as well.

The volume of the MPS lobe on the acorn-shaped silica/MPS particles was estimated from TEM images. The protrusion is nearly spherical and comparable in size to the seed particle. In one typical image, the seed particle was  $1221 \pm 3$  nm in diameter and the protrusion was  $1205 \pm 8$  nm, with an offset of  $264 \pm 6$  nm between the centers of the sphere delineating the surfaces of the silica sphere

and the MPS protrusion. The volume of the lens-shaped intersection of two spheres of radii  $r$  and  $R$  separated at center-to-center distance  $d$  is:

$$V_{\cap} = \frac{\pi(R+r-d)^2(d^2 + 2dr - 3r^2 + 2dR + 6rR - 3R^2)}{12d} \quad (6.1)$$

This intersection can be subtracted from the volume of the sphere delineating the MPS lobe to obtain the volume of the MPS cap. With the afore-mentioned particle dimensions, the volume of the MPS 'cap' is  $0.28 \mu\text{m}^3$  or 30% of the volume of the silica particle. The volume of MPS added to the reaction mixture is higher (in fact, it equals about eight times the volume of silica in the reaction mixture), but the excess MPS forms secondary nucleation droplets visible in the supernatant after a washing step.

### 6.3.2 Self-assembly of acorn-shaped silica/MPS hetero-dimers

In CHC of low conductivity,  $C_{20}$ TES grafted acorn-shaped silica/MPS hetero-dimers acquired a long-range repulsion as a result of the low ion concentration and the concomitant large Debye layer, as observed earlier in for example OTMOS-grafted silica rods in Ref. 131. The average distance between the particles is determined by the volume fraction of particles in the solvent. For an equivalent of 30 g/L silica, the particles formed a glassy structure with average inter-particle distances of  $3.5 \pm 0.4 \mu\text{m}$  (50 counts, Fig. 6.4a). For an equivalent of 10 g/L silica, the particles formed a nearly hexagonal structure with average inter-particle distances of  $10.8 \pm 1.5 \mu\text{m}$  (20 counts, Fig. 6.4b). The structure contained too many dumbbells to fully crystallize, but the issue is not hard to solve in the future for example by the PVP viscosity step-gradient method described in CH. 9. The particles in the long-range assembly were successfully oriented with the MPS bulges to one side using a direct electric field, as described in Ch. 7.

### 6.3.3 Supraparticle/MPS dumbbell-shaped hetero-dimers

Hetero-dimers prepared from supraparticles had a dumbbell shape. The fact that the supraparticles are a suitable template for the nucleation and condensation of hydrolyzed MPS agrees with expectations based on the fact that the nanoparticles have oleic acid ligands at the surfaces. Oleic acid molecules have  $C_{18}$  chains similar to OTMOS molecules except for the presence of a double bond, and likely give the particle surface a similar water contact angle as OTMOS-silica. Fig. 6.5a,b are TEM images of two of the final particles (from the same batch), demonstrating that the supraparticles retain their shapes through the various synthesis steps. Fig. 6.5b evidences that for some supraparticles, a layer of MPS covered the entire surface. This finding raised the supposition that all hetero-dimers grown from OTMOS-grafted templates have a thin layer of MPS over the entire surface. However, the smooth side in Fig. 6.1c and the absence of a strong fluorescent signal from RAS dye leads us to believe this layer of MPS molecules is absent in the case of silica template particles. These supraparticle/MPS hetero-dimers are paramagnetic on the side of the supraparticle, since their constituent nanoparticles are paramagnetic. The hetero-dimers stick with the supraparticle side to the electrodes in an electrode cell (Fig. 6.5c), which is a 'patchy' type of interaction. The

effect might be caused by the wires' nickel content: nickel is ferromagnetic rather than magnetic, but the magnetic domains (Weiss areas) are on scale of tens of micrometers, so that paramagnetic supraparticles are attracted by it. Particles close to the wire probably move towards it due to the high field gradient (magnetophoresis).

### 6.3.4 Silica/MPS lollipop-shaped particles

The nail-shaped particles produced by temperature-regulated growth - which served as template particles for producing MPS-lollipop particles - are shown in Fig. 6.6. The smaller rods lack the flat ends which are distinctly present in most particles, having apparently lost the water/TEOS droplet before the end of the reaction. The flat ends are wider than the rod itself, hence these nail heads show up darker in the bright-field image (Fig. 6.6a) and lighter in the dark-field image (Fig. 6.6b). The average dimensions (excluding the nail's head) of the nails were: an average length of  $1554 \pm 7$  nm (p.d. 7%), an average width of  $274 \pm 16$  nm (p.d. 18%) and an average aspect ratio of  $L/D = 5.8 \pm 0.4$  (20 counts). The nail's heads had an average height (short axis) of  $0.17 \pm 0.01$   $\mu\text{m}$  (with p.d. 14%, 50 counts) and an average width (long axis) of  $0.56 \pm 0.01$   $\mu\text{m}$  (with p.d. 43%, 90 counts).

Fig. 6.7 displays CLSM images of the particles resulting from MPS hydrolysis and condensation onto dyed and OTMOS-grafted nail-shaped particles. The MPS nucleated on one end of the nail-shaped particles. In Fig. 6.7b, the FITC dye channel, the locations of the nail heads are visible. Comparison of the composite image with this channel confirmed that the MPS nucleates on the nail heads. A few particles had a small extra MPS droplet on the edge of the rod (Fig. 6.8c). Occasionally

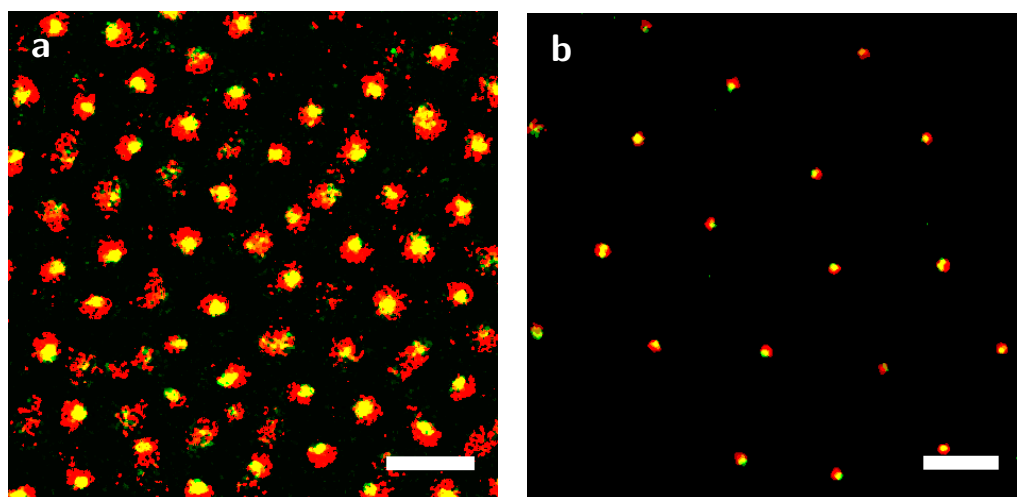


**Figure 6.4:** CLSM micrographs of acorn-shaped silica/MPS hetero-dimer particles in deionized CHC. Silica cores (fluoresceine-labeled) are shown in yellow and MPS caps (rhodamine-labeled) in red. (a) A colloidal glass with long-range interactions, formed at a particle concentration of 30 g/L silica content. (b) A colloidal crystal with long-range interactions, formed at a particle concentration of 10 g/L silica content. In both cases, particles were still fully rotating, i.e. the systems were plastic glass phases [131, 286]. Scale bars: 4  $\mu\text{m}$  and 8  $\mu\text{m}$ .

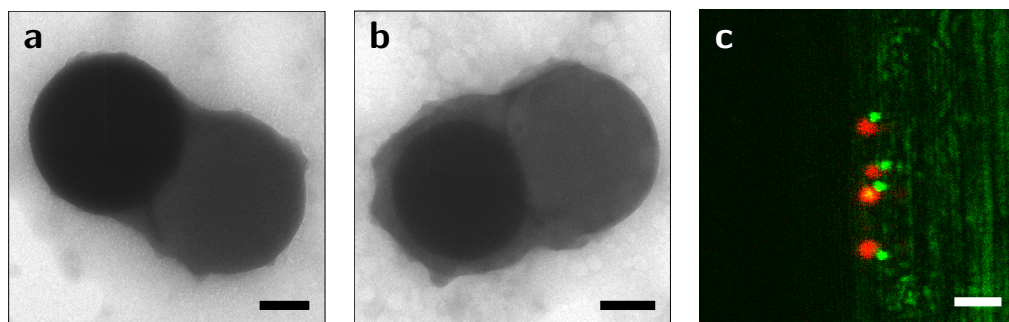


**Figure 6.5:** (a,b) TEM micrographs of two supraparticle/MPS hetero-dimers from the same batch. (c) CLSM image of these particles oriented with the supraparticle side to an electrode. The RAS-dyed MPS side is recorded in fluorescent mode (red) and the supraparticle side in reflection mode (green). The scale bars denote 200 nm, 200 nm and 2  $\mu\text{m}$ , respectively.

MPS droplets attached sideways near the end of the rod. By inspection of the FITC channel it was confirmed that those particles did not have a nail head (cf. Fig. 6.8a,b, particles on the bottom right). We conclude that MPS nucleation onto these rod-like particles is strongly influenced by the particle geometry. In particular, the presence of flat ends on the rods is a requirement to make the MPS nucleate and condense primarily on the nail heads, rather than along the edge of the rod.

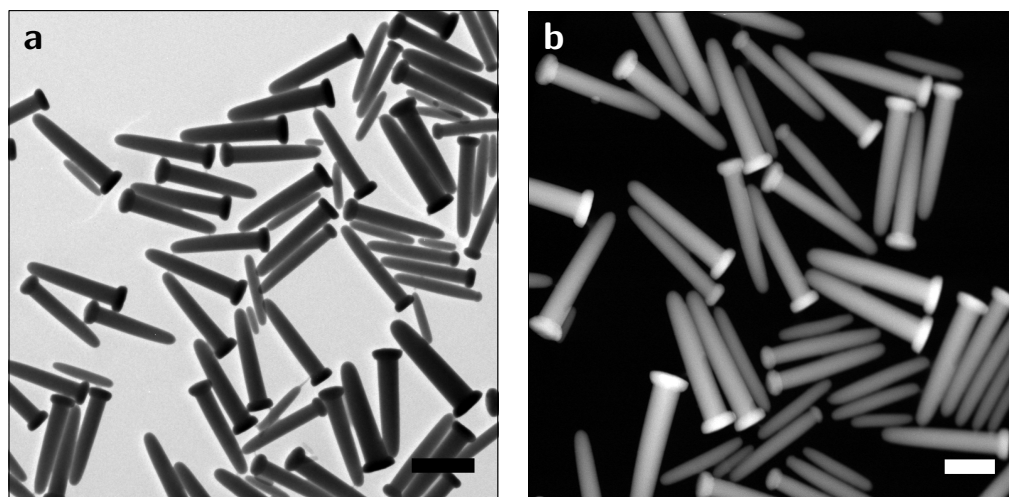


**Figure 6.6:** (a) TEM micrograph and (b) HAADF-STEM micrograph of nail-shaped particles prepared by temperature-regulated growth. Scale bars: 0.5  $\mu\text{m}$  and 1  $\mu\text{m}$ .

The preferred adsorption at the flat side of the nail is also apparent from the occasional droplets with multiple rods attached (Fig. 6.8d-f). Here, it is not immediately clear whether several lollipop particles have fused together by their MPS droplets during nucleation and growth or whether nail-

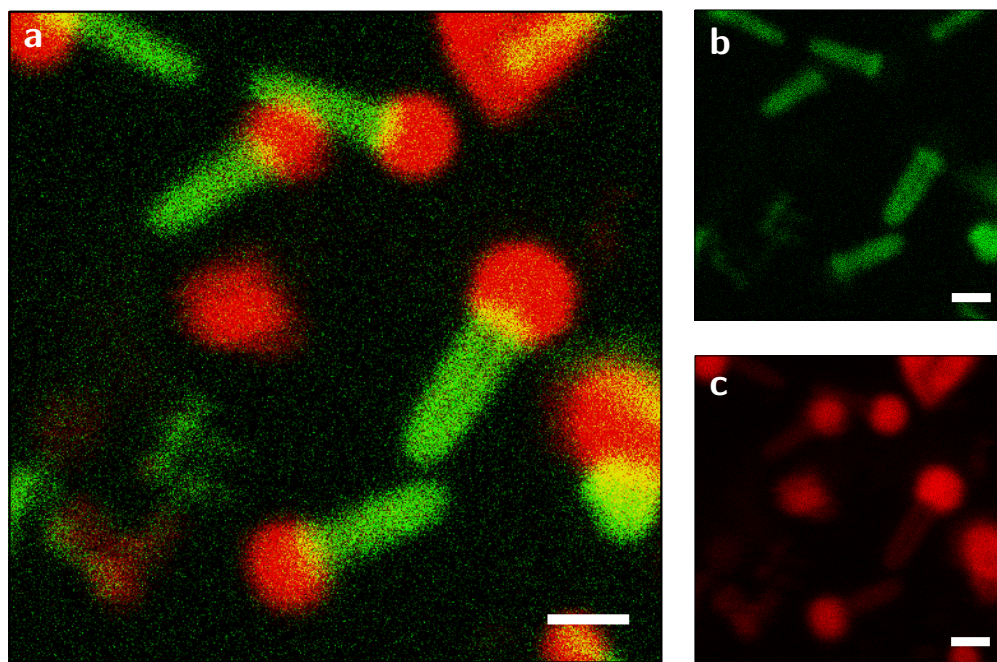


**Figure 6.7:** Confocal images of MPS-lollipop particles: (a) is an overlay of both imaging channels, (b) is the channel recording at 510-540 nm (around the emission maximum of FITC dye), and (c) is the channel recording at 565-700 nm (around the emission maximum of RAS dye, although some bleed-through from the FITC dye can be observed). The scale bars denote 1  $\mu\text{m}$ .

shaped particles attached to an existing lollipop particle. Yet, we can conclude that it is energetically favorable for the nail-shaped particles to stay attached to the droplet head-on rather than sideways.

The preferential attachment of the MPS at the nail heads also indicates that the nucleation of MPS onto the particles is most likely an equilibrium process in this particular experiment. If this were not true, one would expect a mixture of nail-shaped particles with droplets at the side and at the nail's head, since these positions are both local minima in the energy landscape. The mechanism by which the energetically favorable position is reached is difficult to determine: either the liquid droplet can move to the energetically favorable position, or the nucleation barrier is lowest at the nail head, or the molecules can condense and dissolve to explore the energy landscape (or a combination of the above). We do not think the MPS has formed a branched network at the time of nucleation onto the particles, as proposed by Wang *et al.* [276], since MPS must be a liquid rather than a gel at the time of attachment to be able to reach the energetically favored position in an equilibrium process. The ammonia concentration could be of considerable influence to yield of lollipop particles, considering that the catalyst concentration determines the rate of hydrolysis and condensation of the functional groups. Future research should look into this.

In later experiments, the MPS side was cross-linked through the methacrylate groups (Fig. 6.9). The MPS sphere stayed attached to the nail - in contrast to the MPS bulge of dumbbell-shaped

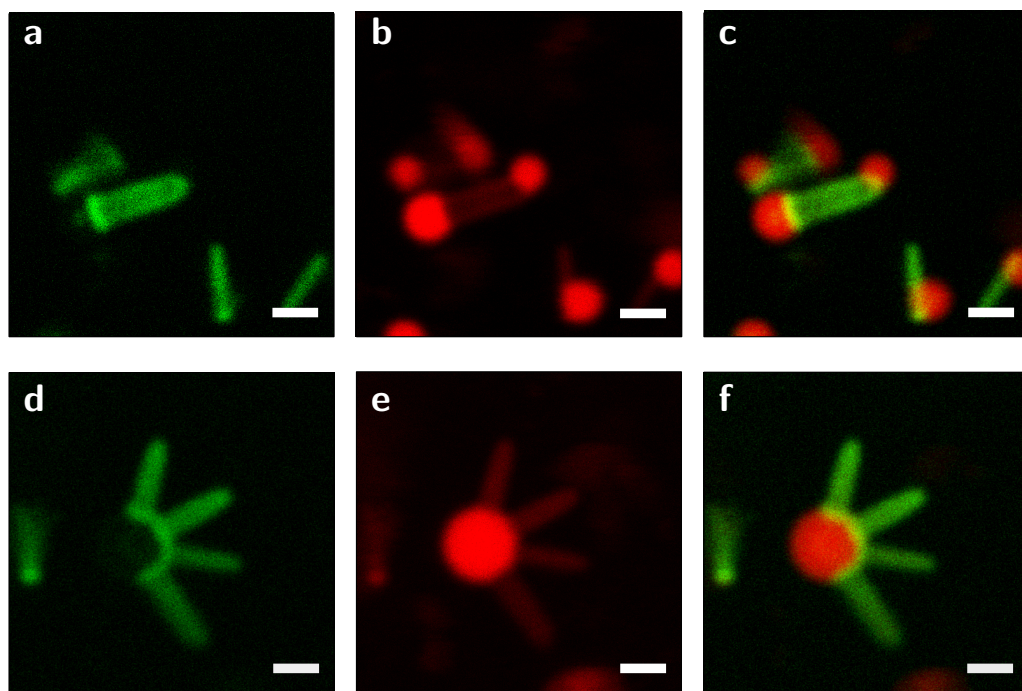


**Figure 6.8:** Confocal micrographs of the same sample as in Fig. 6.7, showing particles in the sample which had a deviating geometry. (a)-(c) Lollipops with an extra MPS droplet attached. (d)-(f) An MPS droplet with four nail-shaped particles attached to it. (a) is the channel recording at 510-540 nm (around the emission maximum of FITC dye), (b) is the channel recording at 565-700 nm (around the emission maximum of RAS dye), and (c) is an overlay of both imaging channels. Similarly, (d) and (e) are the aforementioned channels and (f) is an overlay. The scale bars denote 1  $\mu\text{m}$ .

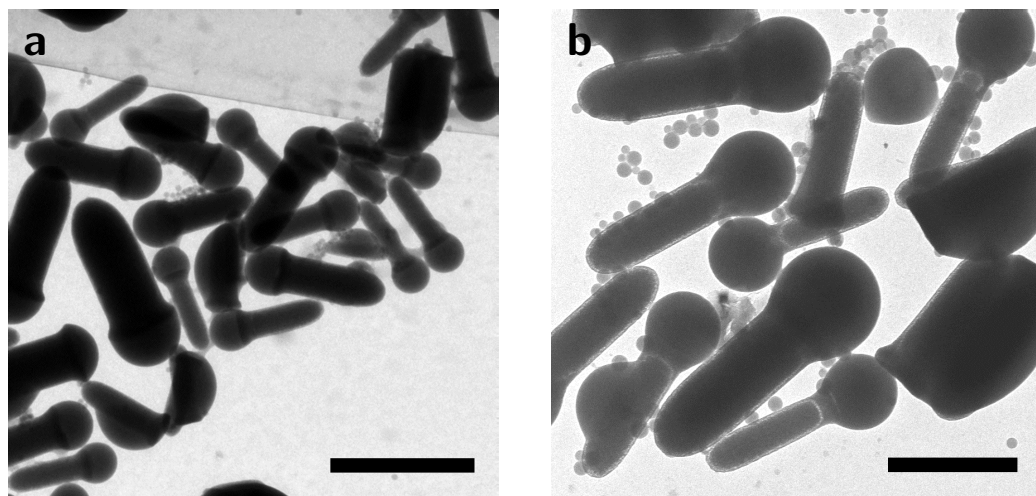


**Figure 6.9:** TEM micrographs of lollipops with cross-linked MPS lobes at two magnifications. Scale bars:  $2\ \mu\text{m}$ .

hetero-dimers - which can be explained by the larger contact area between the MPS lobe and the nail head, similar to the case of the acorn-shaped hetero-dimers. The size of the contact area is of strong influence to the stability since the nail and protrusion are not covalently bound.

Two causes for the head-on attachment of the MPS can be conjectured: the geometry of the nails (influencing the free energy of droplet attachment) or a different surface tension of the material on the edge and on the nail's head. Differences in intrinsic surface tension are not plausible for the following reason. A small amount of OTEOS was added to the silica precursor in the initial synthesis (and may have ended up selectively at the particle edge rather than the end because of the hydrophobicity of this molecule) but a similar end-on attachment was reproduced when the synthesis method for nail-shaped particles prepared without any OTEOS, see Fig. 6.9. Moreover, the entire particle was grafted with OTMOS after synthesis, which should have eliminated any differences in octadecyl-chain density at the surface. We think, therefore, that the end-on attachment of hydrolyzed MPS is dictated by the particle geometry.

If the particle geometry causes the end-on nucleation of MPS, one can still ask the question whether a nail shape is required or a bullet shape is sufficient. As a control experiment, MPS was allowed to nucleate and grow onto OTMOS-grafted (and FITC-dyed) bullet-shaped particles prepared by the route of Kuijk *et al*, with a similar aspect ratio and width ( $L/D = 6 \pm 1$ ,  $D = 0.31 \pm 0.06\ \mu\text{m}$ ) as those of the nail-shaped particles ( $L/D = 5.8 \pm 0.4$  and  $D = 0.274 \pm 0.016\ \mu\text{m}$ ). Fig. 6.10a,b display a TEM image of these bullet-shaped particles and a confocal micrograph of the resulting particles with condensed MPS on the right. The MPS droplet attached systematically to the sides of these bullet-shaped particles, despite the presence of the flat back ends. Only one rod was encountered with an MPS droplet attached to the back end. Naively, this result suggests that a nail shape is required for successful MPS nucleation and growth at the back end, perhaps as a way for the MPS

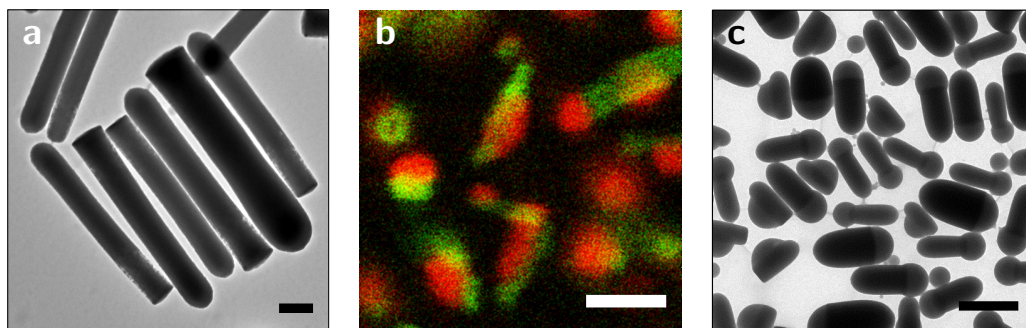


**Figure 6.10:** *Control experiments.* (a) TEM micrograph of bullet-shaped particles (aspect ratio  $6 \pm 1$ , width  $0.274 \pm 0.016 \mu\text{m}$ ) before dye labeling, OTMOS-grafting and MPS nucleation and condensation. (b) Confocal micrograph of the bullet-shaped rods after MPS nucleation and condensation. Note the end-on attached MPS droplet on the particle on the top right and the side-on attachment of all other MPS droplets. (c) TEM micrograph of bullet-shaped particles (aspect ratio  $2.1 \pm 0.4$ , width  $0.47 \pm 0.18 \mu\text{m}$ ) after MPS nucleation, condensation and polymerization through the methacrylate groups. The scale bars denote: (a) 500 nm, (b)  $2 \mu\text{m}$ , and (c)  $1 \mu\text{m}$ .

to envelope the silica particle and geometrically lock the shape. However, the absolute width of the flat end on the rod or nail may be another factor of importance, since the nail head is also wider than the nail width. In another control experiment, bullet-shaped particles with shorter aspect ratio ( $2.1 \pm 0.4$ ) but a wider absolute flat end ( $0.47 \pm 0.18 \mu\text{m}$ , compared to  $0.31 \pm 0.06 \mu\text{m}$  for the previous bullet-shaped particles) were used in the MPS nucleation routine. This particle diameter is comparable to the width of the nails' heads ( $0.56 \pm 0.01 \mu\text{m}$ ). MPS nucleated and grew onto the flat end of these bullet-shaped particles (Fig. 6.10c), proving that it is indeed possible to nucleate and grow MPS onto bullet-shaped particles when the flat end is sufficiently wide. It is also clear from Fig. 6.10c that on a fraction of particles the MPS nucleated on the sides of the particles. Possibly, the nail-shape increases the yield of lollipop-shaped particles. Further experimental and numerical or theoretical studies are required to elucidate the influence of particle shape, aspect ratio, and absolute particle size on the nucleation and growth of MPS.

## 6.4 Conclusions & Outlook

We prepared hetero-dimer particles consisting of OTMOS-grafted silica particles with an MPS protrusion. For spherical OTMOS-grafted silica particles, the resulting silica/MPS particles were acorn-shaped or dumbbell-shaped depending on the surfactant chosen for particle synthesis. The particles were stable against centrifugation and washing with deionized water. The MPS bulge was dyed with RAS dye conjugate for confocal microscopy imaging. The methacryloxy groups of the MPS of the acorn-shaped particles were cross-linked by free radical polymerization, yielding particles resilient to drying and solvent exchange with organic solvents. Dumbbell-shaped particles, on the other hand, lost the MPS bulge upon polymerization. The acorn-shaped particles were used to create plastic glasses with long-range interactions and nearly crystalline structures.

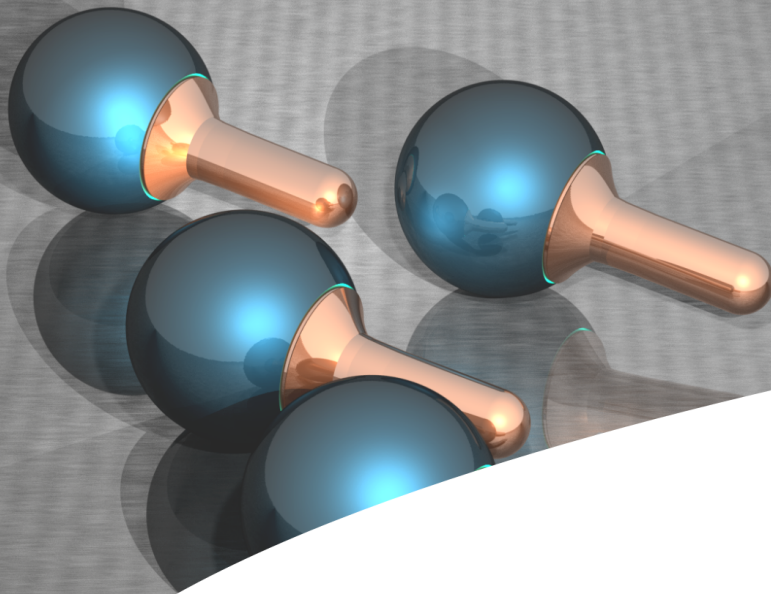
MPS nucleation and growth onto nail-shaped OTMOS-grafted silica particles resulted in lollipop-shaped silica/MPS particles, with the MPS droplet attached to the nail heads. The synthesis method was reproducible. Such an end-on attachment was not observed for OTMOS-grafted silica particles with a bullet shape of similar width and aspect ratio, except for an occasional particle in one sample of particles. Therefore, we suggest that the nail shape an important role in the adsorption process. On the other hand, MPS nucleation and growth on bullet-shaped particles of smaller aspect ratio but a width similar to the nail heads also yielded a large fraction of lollipop-shaped particles, hence particle size is also of influence. For future research, theoretical or numerical calculations should be used in addition to experiments to shed light on the influence of the nail geometry, particle width and aspect ratio on the location of MPS adsorption. Such calculations should take the curvature of the MPS droplet into account as well. The site-specific adsorption also means that the droplet is initially liquid-like and not gel-like as stated in Ref. [276], since it is able to explore the energy landscape to find the minimum adsorption energy, either as a moving droplet or as attaching and dissolving molecules.

Differences in the intrinsic surface tension on the edge and the flat end due to different PVP content, as found by Peng *et al.* [253], could be present in the nail-shaped particles as well. Experiments to determine the influence of OTMOS grafting density on MPS adsorption (by varying the reaction time of OTMOS) are currently ongoing.

The MPS-lollipop particles are interesting for future research, since several functional groups can be incorporated into the MPS droplet, either using mixtures of MPS with other silanes or by taking advantage of the methacrylate groups. For example, including amine groups could allow gold particles to attach site-specifically to the MPS bulge, which is interesting for photonic applications and for active matter. By introducing functional groups, the particles may also serve as labels or markers for materials that stick to those functional groups. Research into this direction is ongoing at the time of writing. Self-assembly studies of lollipop particles are interesting as well, however the polydispersity of the MPS droplet size adds to the typically relatively high polydispersities of the nail's width and length (~10%).

## Acknowledgements

Bo Peng is thanked as his earlier work provided the inspiration for this work. Fabian Hagemans is gratefully acknowledged for helping to clear up questions about our synthesis route when time was very limited. Figures 6.9 and 6.10c are his work. Hans Meeldijk is thanked for making the HAADF-STEM pictures of the nail-shaped particles. Bart de Nijs is thanked for providing the supraparticles for the hetero-dimer particles with a magnetic side. Jissy Jose is acknowledged for preparation of the RAS. Joost de Graaf, Giuseppe Soligno, René van Roij and Marjolein Dijkstra are sincerely thanked for providing theoretical insight into the nucleation and growth process through numerical and theoretical calculations.



# CHAPTER 7

## Electric-field-induced directional alignment of hetero-dimer colloids

In electric fields, elongated colloids align with the long axis along the field as a result of induced polarization in the colloids, inducing orientational order in the system. However, to our knowledge no examples exist in which multi-compartment colloids orient with similar sides towards the same direction in electric fields. The silica/MPS heterodimers presented in Ch. 6 are shown to orient and undergo electrophoresis with all MPS compartments directed towards the same direction. This effect was observed not only for acorn-shaped and dumbbell-shaped silica/MPS heterodimers, but also for lollipop-shaped particles. A system of lollipop-shaped silica/PMMA hetero-dimers is used to demonstrate that the effect appears for systems of various chemical compositions.

---



## 7.1 Introduction

When an electric field is applied to colloids in a dispersion, a dipole moment  $p$  is induced in the colloids. That is, charge will redistribute such that the surface effectively acquires two sides of equal but opposite net charge  $q$ . For a *permanent* point dipole, where the charges  $+q$  and  $-q$  are separated by a distance  $d$ , the dipole moment is given by:  $p = qd$ . In contrast, the *induced* dipole moment in a spherical colloid in a local electric field  $\vec{E}_{local}$  is given by [287]:

$$\vec{p} = C \frac{\pi}{2} \epsilon_m \epsilon_0 \sigma^3 \vec{E}_{local} \quad (7.1)$$

with  $\sigma$  the particle diameter,  $\epsilon_0$  and  $\epsilon_m$  the permittivity of free space and relative permittivity of the medium, and with  $C = (\epsilon_p - \epsilon_m)/(\epsilon_p + 2\epsilon_m)$  the Clausius-Mosotti factor. The quantity  $C \frac{\pi}{2} \epsilon_m \epsilon_0 \sigma^3$  is the polarizability  $\alpha$  of the particle. Notice that the local field at the position of a particle is influenced by the induced dipoles surrounding it ( $\vec{E}_{local} = \vec{E}_{applied} + \vec{E}_{dipoles}$ ). From Eqn. 7.1 follows that the dipole moment  $\vec{p}$  vanishes when the dielectric constants of the colloids and the medium are equal. Strong dipolar interactions arise when the dielectric constant of particles and medium have a large mismatch, such as for silica particles ( $\epsilon \sim 4$ ) in water ( $\epsilon = 80$ ).

For particles of non-spherical shapes, the induced dipole moment may vary along the various axes through the particles. Naively, the dipole moment is largest along the long axis for rods and ellipsoids as the largest charge separation can be achieved in this direction, and such particles have indeed been shown to align parallel to the field [131, 277]. However, for small (nanoscale) particles, there is a competition between shape anisotropy and particle volume as shown by Kwaadgras *et al.* [288]. For such nanoparticles, the polarizability tensor can be calculated with for instance the coupled dipole method [289].

The local electric field will exert a torque on the induced dipole [290]:

$$\vec{\tau} = \vec{p} \times \vec{E}_{local} \quad (7.2)$$

with  $\theta$  the angle between the dipole axis and the field axis. This torque vanishes for  $\theta=0$ ; in other words, it forces the dipole to align with the local field (where the main contribution is usually the applied field, but sometimes the field of the other dipoles must be taken into account as well). This orientation with the field is especially noticeable in rod-like particles, for example in Ref. 291.

Let us consider the interactions between dipoles in a field. For a dipole  $\vec{p}$ , the electric potential  $V_{dip}$  at position  $\vec{r}$  (and as a function of the distance  $r$  and the angle  $\theta$  with the dipole axis) is [290]:

$$V_{dipole} = \frac{1}{4\pi\epsilon_0\epsilon_m} \frac{\vec{p} \cdot \vec{r}}{|\vec{r}|^3} \quad (7.3)$$

and since  $\vec{E} = -\nabla V$ , the electric field about the dipole is:

$$\vec{E}_{dipole} = \frac{1}{4\pi\epsilon_0\epsilon_m} \frac{1}{r^3} [3(\vec{p} \cdot \hat{r})\hat{r} - \vec{p}] \quad (7.4)$$

For two spherical dipoles  $\vec{p}$  aligned with an applied field, the interaction potential  $V_{dip-dip}$  as a function

of the angle  $\theta$  (of the center-to-center distance and the direction of the applied field) is [190,287]:

$$V_{dip-dip} = -\vec{p} \cdot \vec{E}_{dipole} = \frac{1}{4\pi\epsilon_m\epsilon_0} \frac{p^2}{r^3} (1 - 3\cos^2(\theta)) \quad (7.5)$$

with  $p$  the norm of the vector in Eqn. 7.1. A corollary of this expression is that for aligned (induced) dipoles the dipolar interaction is attractive for  $\theta < 54.7^\circ$  and repulsive for  $\theta > 54.7^\circ$  [190], hence particles are expected to line up in strings, as has indeed been observed in experiments [190,292], and in fact used as a means for particle assembly, for example into 2D sheets [293].

Colloids generally not only have induced dipole (and higher order) moments that respond to an electric field, but usually also carry a net charge  $Q$ . Therefore, such colloids experience a force pulling them towards the oppositely charged electrode:

$$\vec{F} = Q\vec{E}_{local} \quad (7.6)$$

This effect is called *electrophoresis*. The electrophoretic mobility  $\mu_e$  of the particle obtained due to electrophoresis, which is affected by for example the viscosity of the solvent and drag forces due to the particle shape, is defined as:

$$\mu_e = \frac{v}{E_{local}} \quad (7.7)$$

with  $v$  the speed obtained by the particle caused by electrophoresis. The total charge  $Q$  of the particle is of course influenced by the ions in the electric double layer. The best known theory that takes these into account is the theory of Smoluchowski as proposed in his 1903 paper [169,170]:

$$\mu_e = \frac{\epsilon_m\epsilon_0\zeta}{\eta} \quad (7.8)$$

with  $\eta$  the dynamic viscosity of the medium.  $\zeta$  is the *zeta potential*; the potential at the slipping plane in the Debye layer. The Smoluchowski equation is only valid in the limit of a thin double layer, i.e.  $\sigma/\lambda_D \ll 1$ . In the limit of a large double layer, a better approximation was given by Hückel [171]:

$$\mu_e = \frac{2}{3} \frac{\epsilon_m\epsilon_0\zeta}{\eta} \quad (7.9)$$

Typically, the Smoluchowski limit is a good model when  $\sigma/\lambda_D > 10$  and the Hückel limit when  $\sigma/\lambda_D < \frac{1}{10}$ .

A different cause of motion in electric fields is related to the induced dipole moment. The phenomenon is called *dielectrophoresis* (DEP) and occurs in inhomogeneous fields (both direct or alternating). Simply put, in a non-uniform field the forces on the two sides of a dipole are unequal, causing the dipole to move. With  $\vec{F} = (\vec{p} \cdot \nabla) \vec{E}$  and Eqn. 7.1 we find, for example, that for a spherical

particle of radius  $r$  the DEP force is:

$$\vec{F}_{DEP} = 2\pi\epsilon_m r^3 Re \left( \frac{\epsilon_p - \epsilon_m}{\epsilon_p + 2\epsilon_m} \right) \nabla |E_{rms}|^2 \quad (7.10)$$

where the quantity in brackets is the Clausius-Mosotti factor and  $E_{rms}$  the root mean square value of the (alternating) electric field. One can conclude that for  $\epsilon_p > \epsilon_m$ , particles are attracted to regions of high field strength (*positive dielectrophoresis*), whereas for  $\epsilon_p < \epsilon_m$ , dielectrophoresis moves the particles towards regions of low field strength (*negative dielectrophoresis*) [290, 294]. Negative dielectrophoresis is typical for silica particles in a polar medium. The DEP force is strong enough to induce bulk crystallization in a 'dielectrophoretic bottle' [295]. The equation for the DEP force does not apply to situations where the particle size is on the order of the field gradient, such as very steep gradients. Multipolar contributions to the DEP force must then be taken into account [290]. The particles will also obtain a multipole moment, where the n-th contribution is given by [290]:

$$\vec{p}^{(n)} = \frac{4\pi\epsilon_m r^{2n+1}}{(2n-1)!!} K^{(n)} (\nabla)^{n-1} \vec{E}_{local} \quad (7.11)$$

with  $K^{(n)}$  the generalized Clausius-Mossotti factor,  $K^{(n)} = (\epsilon_p - \epsilon_m)/[n\epsilon_p + (n+1)\epsilon_m]$ .

Another interaction that can take place in direct or slowly alternating electric fields is polarization of the double layer, known as Maxwell-Wagner polarization. Polarization of the electrons within a colloid occurs on the scale of picoseconds to nanoseconds [296]. Polarization of the double layer may take longer, since the motion of ions through the double layer can be restricted by the high number of charges. For this reason, the relaxation time of the polarization of the double layer - called the Maxwell-Wagner relaxation time,  $\tau_{MW}$  - can be on the order of seconds [296]. When the electric field has a period on the order of  $\tau_{MW}$  or longer, Maxwell-Wagner relaxation must be taken into account when studying the dipole moment of a system. For a two-layer system (approximated as capacitors of volume  $V_1$  and  $V_2$ ), this relaxation time is a simple expression dependent on the bulk conductivities  $\sigma_1$  and  $\sigma_2$  of the materials 1 and 2, and their dielectric constants  $\epsilon_1$  and  $\epsilon_2$ :

$$\tau = \epsilon_0 \frac{\epsilon_1 V_2 + \epsilon_2 V_1}{\sigma_1 V_2 + \sigma_2 V_1} \quad (7.12)$$

For spherical colloids in the limit of infinitely low volume fraction, the Maxwell-Wagner time is [170, p.348]:

$$\tau_{MW} = \epsilon_0 \frac{2\epsilon_m + \epsilon_p}{2\sigma_m + \sigma_p} \quad (7.13)$$

with  $\epsilon$  denoting dielectric constants,  $\sigma$  bulk conductivities and subscripts 'm' and 'p' denoting medium and particle, respectively. An important number in relation to the Maxwell-Wagner time is the Dukhin number  $Du$ : the ratio of the surface conductivity  $\kappa_m$  to the bulk conductivity of the medium  $\sigma_m$ , for a non-conductive particle, or the excess electrical conduction tangential to a charged surface [170]:

$$Du = \frac{\kappa_m}{\sigma_m a} \quad (7.14)$$

with  $a$  the particle diameter. In the limit of ions moving only above the slipping plane in the Gouy-Chapman layer (and not below the slipping plane in the Stern layer, although there is evidence that surface conductivity in the Stern layer is common [297]) and equal ion diffusion coefficients, the Dukhin number equals [170]:

$$Du = \frac{2\lambda_D}{a} \left(1 + \frac{3m}{z^2}\right) \left[ \cosh\left(\frac{ze\zeta}{2k_B T}\right) - 1 \right] \quad (7.15)$$

with  $\lambda_D$  the Debye length,  $z$  the ion valency,  $\zeta$  the zeta potential, and  $m$  a dimensionless mobility inside the double layer:  $m = \frac{2e\eta\epsilon_m(k_B T)^2}{3\eta e^2 D}$  with  $e$  the elementary charge,  $\eta$  the viscosity of the medium, and  $D$  the diffusion coefficient of the ions in the double layer. For  $Du < 0.5$  the transport of ions through the double layer is slower than in the bulk and for  $Du > 0.5$  it is faster [298]. In the former case, the dipole induced in the double layer of the colloid is oriented perpendicular to the field direction, and in the latter with the field direction. In strong direct fields the former can lead to a rotation of the particle to align the dipole induced in the double layer with the field; this effect is called Quincke rotation.

In a broader perspective, 'dielectric dispersion' indicates the fact that polarization of a system is field frequency dependent. At frequencies in the MHz range, colloids experience no electrophoresis because of the fast field reversals, but colloids do become polarized by the field. At various frequencies in the range  $10^{10}$  to  $10^{15}$  Hz, even polar molecules in a material, ions in an ionic crystal, or electrons in atoms cannot follow the electric field (these types of polarization are called dipolar polarization, ionic polarization and electronic polarization, respectively), hence colloids do not become polarized in electric fields of such high frequencies.

In this chapter, we show that the silica/MPS hetero-dimers presented in Ch.6 can be aligned 'vectorially', that is, not only parallel to the direction of an applied electric field, but also with the MPS lobes of all particles facing the same direction. To our knowledge, this is the first instance in literature where such vectorial orientation in an electric field is achieved. The finding opens up the possibility to create long-range crystals with both long-range orientational order and directional order, and preliminary results of such a crystal are presented.

## 7.2 Experimental details

### 7.2.1 Materials

In experiments aimed at vectorial alignment of silica/MPS hetero-dimers (acorn-, dumbbell- or lollipop-shaped), silica/MPS particles were dispersed in deionized water (resistivity: 18.2 M $\Omega$ cm). In experiments aimed at vectorial alignment of particles with long-ranged repulsive potentials, C<sub>20</sub>TES-grafted acorn-shaped silica/MPS hetero-dimers were dispersed in deionized CHC (*Merck*). The CHC was deionized by adding alumina (AlO<sub>2</sub>, activated / neutral / Brockmann I, *Sigma Aldrich*). After several hours, the CHC was placed over molecular sieves (*Acros Organics*, 4Å, 10-18 mesh) for at least a day. The conductivity of the CHC was measured with a *Scientifica model 627* conductometer connected to a probe which fitted ~3.8 mL. The CHC had a conductivity of 1-2 pS/cm before

dispersing particles in it.

PMMA-lollipop particles are particles with a lollipop shape similar to the particles in Ch. 6, but with a different chemical composition. The particles were prepared by B. Peng (Utrecht University) by condensation and growth of PMMA onto MPS-grafted bullet-shaped silica particles, as described accurately in Ref. 253.

## 7.2.2 Electric field experiments with silica/MPS hetero-dimers (acorn/dumbbell/lollipop)

Electric cells were assembled from borosilicate capillaries with inner dimensions  $0.1 \times 2 \times 50$  mm (*VitroCom*, no. 5010). Wire electrodes from *Goodfellow* (diameter 0.05 mm and composition 95% Ni, 5% Al/Mn/Si) were spanned along the long sides of the inner capillary walls (see also Fig. 9.2). A *HP 33220A* 15 MHz function/arbitrary waveform generator provided sinusoidal electric fields with 5 V peak-to-peak voltage. A *Krohn-Hite 7602M* wideband amplifier was used for amplification of the signal to 2 V - 7 V (used for a slowly alternating fields, frequency 200 mHz-300 mHz) or 80 V - 100 V (used for a quickly alternating field, frequency 1 MHz). We opted for slowly alternating fields rather than a strict direct field (1) to reduce gathering of the particles near the electrodes, (2) to reduce solvent electrolysis, (3) for better imaging possibilities, since in a direct field the particle velocity becomes high due to electrophoresis.

## 7.2.3 Electric field experiments with PMMA-lollipop particles

Electric cells were prepared from borosilicate capillaries with inner dimensions  $0.1 \times 1 \times 50$  mm (*VitroCom* no.5010) as described in the previous section. To counter sticking of the particles to the capillary walls, these capillaries were treated with MPS prior to use in the following way. The capillaries were placed for 24 h in a mixture of 10 mL toluene, 1 mL butylamine and 1 mL MPS. Afterwards the capillaries were washed five times with ethanol and stored dry. The electric cells were filled with a dispersion of lollipop particles in ethanol. This dispersion was prepared from an aqueous dispersion by centrifugation, exchange of solvent, and sonication in a *Branson 2510* sonication bath. The dispersion was used directly after preparation, since ethanol dissolves the non-cross-linked PMMA grown onto the rods in the course of a day. Prolonged storage in water also reduced the described vectorial orientation in the electric field. Alternating fields of 1MHz and 2MHz were applied at voltages of 40 V-80 V. Slowly alternating fields were applied at frequencies of 300 mHz-10 Hz.

## 7.2.4 Imaging methods

### Imaging of MPS-silica hetero-dimers

Electric field experiments with silica/MPS hetero-dimers were recorded on a *Leica SP8* confocal microscope, equipped with a *Leica HCX Plan Apo STED Orange* 100x oil immersion confocal lens (NA = 1.4). Wavelengths of 495 nm and 543 nm were selected from the spectrum of a white light laser by means of an acousto-optical beam splitter (AOBS). Two detectors recorded the fluorescent

signals: a photomultiplier tube (PMT) and a hybrid detector (HyD<sup>TM</sup> from *Leica Microsystems*). The latter is a combination of a PMT and a system similar to an avalanche photodiode, which makes the HyD a more sensitive detector with a low dark noise and a large dynamic range. The PMT was used for the range 505-535 nm (fluorescein dye) and the HyD for the range 590-700 nm (rhodamine dye). The two channels were displayed using different 8-bit color look-up tables: fluorescein in green and rhodamine in red. The final images were acquired by overlaying these two channels. Imaging was typically performed at a scanning rate of 12000 Hz (resonant scanning), while using line averaging and frame averaging to increase image quality. The final recording rate was 7-10 frames per second for 512×512 or 512×256 pixels.

### Imaging of PMMA-lollipops

Electric field experiments with PMMA-lollipops were recorded on the same confocal microscope, equipped with a *Leica Plan Apo* 63x oil immersion lens (NA = 1.32). Wavelengths of 495 nm and 543 nm were again selected. Two detectors recorded in different imaging modes: a PMT was used in reflection mode and a HyD in fluorescence mode. The fluorescence channel captured photons from a wavelength range about the emission maximum of the rhodamine dye. The reflection channel was set to capture light of wavelength 495 nm. In other words, the latter channel recorded light of 495 nm scattered by the particles. Reflections were recorded in a green color look-up table and fluorescence in a red color-look-up table. The final images were acquired by overlaying the two channels. At least five images per second were needed for accurate sampling of the motion. Scanning was bidirectional and at a speed of 1400 Hz, while the images had a rectangular shape with a resolution of 1024 by 512 pixels. With these settings, the recording rate was 5.24 frames/s.

Scattering occurs due to the refractive index match mismatch between the solvent ( $n = 1.362$ ) and the particles (silica rods:  $n \sim 1.45$ , PMMA spheres:  $n \sim 1.49$ ). We were able to tune the gain of both channels such that only the spheres were visible in reflection mode, due to the larger refractive index mismatch between the PMMA spheres and solvent as compared to the silica rods and solvent. The silica rods were visible in the fluorescent channel as a result of the adsorbed RITC dye. The PMMA spheres also contained dye, but this dye leached out rather quickly in the solvents used. In combination with the strong scattering from the PMMA spheres, the fluorescent signal of the PMMA spheres was barely visible. The scattering from the silica rods was sometimes visible on top of their fluorescent signal.

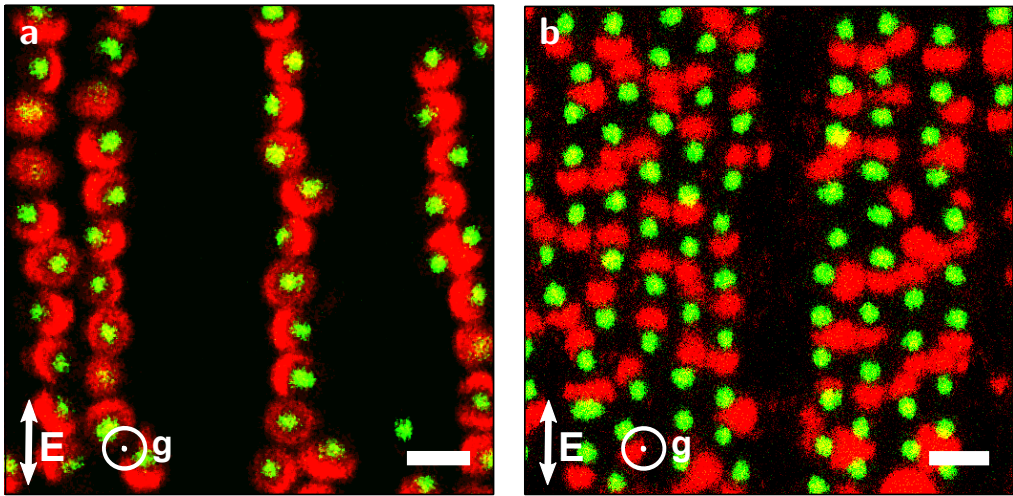


**Figure 7.1:** Confocal micrographs of (a) acorn-shaped silica/MPS particles and (b) dumbbell-shaped silica/MPS particles in an alternating field (1 MHz, 81 V,  $\approx 43$  V/mm), in deionized water. The scale bars denote 2  $\mu$ m. A gaussian filter was applied to these images to reduce noise.

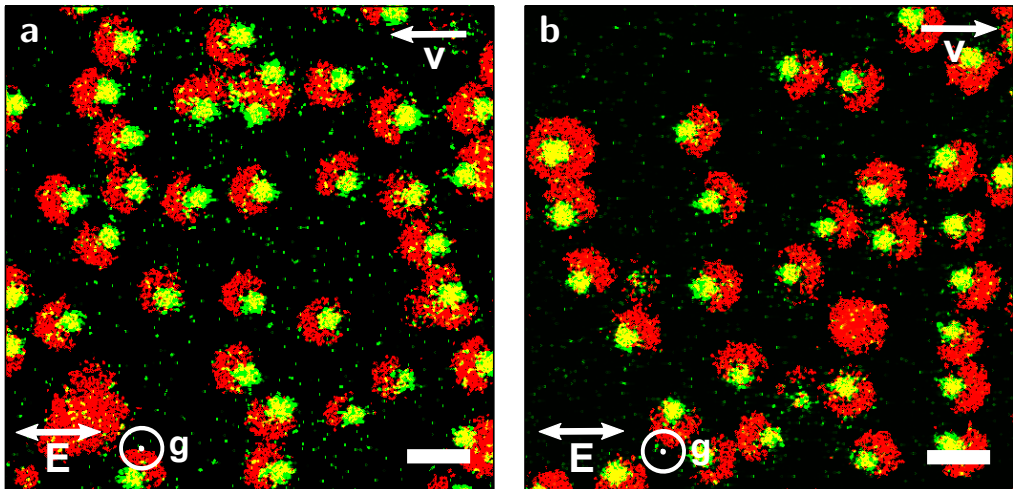


**Figure 7.2:** Confocal micrographs of acorn-shaped silica/MPS particles in a slowly alternating field (300 MHz, sinusoidal, 2 V/mm-3 V/mm) in water at two different times in the cycle of the electric field. Nearly all particles are oriented towards the same direction, and moved in the direction indicated by the top arrows. A gaussian filter was applied to these images to reduce noise.

## 7.3 Results & Discussion

### 7.3.1 Vectorial orientation of silica/MPS hetero-dimer particles

We first discuss silica/MPS hetero-dimers in *alternating* fields and in the medium water. Acorn-shaped silica/MPS particles formed strings with a preference for aligning the long axis perpendicular to the field (but with the MPS caps facing different directions), Fig. 7.1a. In contrast, dumbbell-shaped silica/MPS particles aligned with the long axis along the field under the same field frequency and strength, Fig. 7.1b. This difference in alignment of the acorn and dumbbell-shaped particles in an alternating field can be explained by the particle shape. As demonstrated in Ref. 288 - an article containing theoretical calculations of the polarizability matrix of particles ranging from spheres to dumbbells obtained with a method called the coupled dipole method - the size at which particles become aligned parallel to a field of 100 V/mm is about 2  $\mu\text{m}$  for nearly spherical particles (to which the acorn-shaped particles are closer in shape) and about 700 nm for dumbbells with a  $L/\sigma = 0.6$  (to which the dumbbell-shaped particles resemble most, although in our case the dumbbells are also heterogeneous meaning that the dielectric constant of the MPS and silica are not the same, but expectedly they are both close to that of silica,  $\epsilon \sim 4$ ). The field magnitudes used in experiments with an alternating field were on the same order of magnitude (43 V/mm) as these calculations. The acorn-shaped particles with their size below 2  $\mu\text{m}$  did not align with the field, but the dumbbell-shaped silica/MPS particles with their silica lobes of 1  $\mu\text{m}$  were large enough to align with the field, which is in broad agreement with the theory. Here, the influence of particle-particle interactions within the strings are not taken into account; possibly they can explain the observed slight preference of the acorn-shaped particles for an orientation perpendicular to the field (see Fig. 7.1a). To summarize, in such alternating fields, induced dipole moments cause string formation and the alignment of dumbbell particles with the field direction. Although they are aligned, the particles do not, however, all face towards the same direction ('vectorial' alignment).

In a direct or slowly alternating ( $< 10\text{ Hz}$ ) field, acorn-shaped particles in water oriented 'vectorially', i.e. with all MPS lobes to one side. Fig. 7.2 shows snapshots from a single movie where the electric field was alternated at a sinusoidal frequency of 300 mHz. The snapshots displayed are the last image frames before field reversal, as the particles briefly do not undergo electrophoresis (which reduces imaging quality) at this stage. The particles are nearly all directed with the MPS bulge to one side, reorienting in roughly 1.5 s after field reversal. The long axes of some particles remain at a non-zero angle with regard to the field direction, possibly due to a non-uniform charge distribution on individual parts - silica side and MPS side - of the particle, as proposed by Velegol and Feick [299, 300].

Remarkably, no such vectorial orientation was observed for (non cross-linked) dumbbell-shaped silica/MPS hetero-dimers, while the effect was clearly present for supraparticle/MPS dumbbells (Fig. 7.3a). In Fig. 7.3b, the average x- and y-component of the director through the supraparticles in a 300 mHz electric field are displayed. The sign of the x-component changes sign every  $\sim 65$  frames, meaning that the particles reoriented (turned its axis over  $180^\circ$ ) in roughly 0.7 s. At each field reversal, the y-component briefly becomes nonzero as the particles reorient.

A similar motion was observed for MPS-lollipops in water in an electric field of 200 mHz and  $2 \pm 0.5 \text{ V/mm}$  (Fig. 7.4). The particles oriented with the rod in the direction of propagation (i.e. the direction into which they underwent electrophoresis), requiring a reorientation of  $180^\circ$  to do so.

$C_{20}$ -grafted acorn-shaped silica/MPS hetero-dimer particles form long-range structures in deionized CHC. In direct electric fields of  $18 \pm 2 \text{ V/mm}$ , the particles oriented with the MPS bulge to one electrode, as displayed in Fig. 7.5. As can be seen, the structures were somewhat disturbed by the resulting motion in the field; these results should be regarded as preliminary. In AC fields of 1 MHz, no alignment parallel to the field was observed even at a field strength of  $170 \text{ V/mm}$ , which is caused by the low dielectric constant mismatch between the particles and the medium. Therefore the particles could not yet be locked in the vectorially oriented state.

It is interesting to speculate about the origin of the vectorial alignment of the silica/MPS and supraparticle/MPS hetero-dimers. Several possible causes are: charge density differences; differences in the polarizability between the silica lobe and the MPS lobe; Maxwell-Wagner relaxation; or a

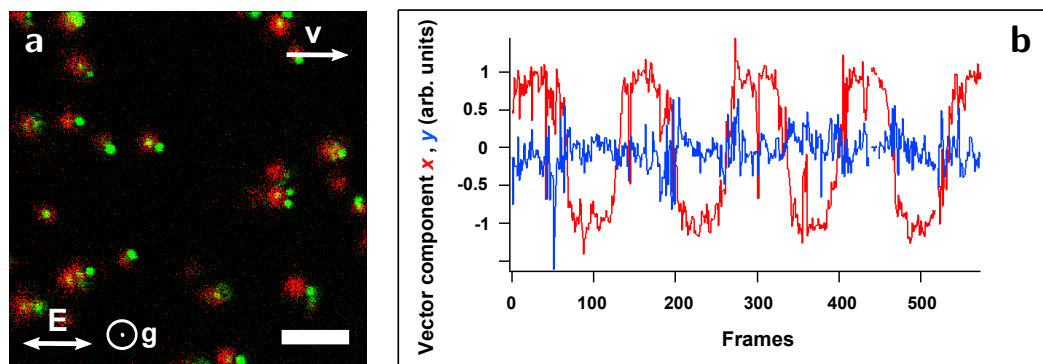


**Figure 7.3:** (a) Confocal micrographs of dumbbell-shaped supraparticle/MPS particles in a slowly alternating field (200 mHz,  $2.5 \pm 0.5 \text{ V/mm}$ ) in water. (b) For each frame in the movie of (a), a computer-generated image was made with the particles replaced by arrows (vectors) pointing from the MPS side to the supraparticle side. This graph shows the average x-component and y-component in each frame, showing that the average x-component periodically changes sign.

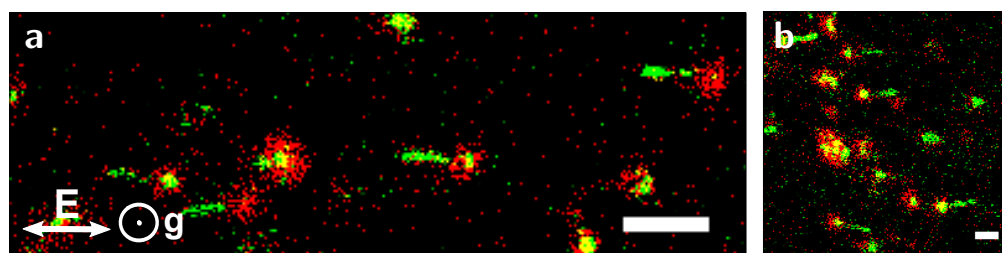


**Figure 7.4:** Confocal micrographs of lollipop-shaped silica/MPS hetero-dimers in a slowly alternating field (200 mHz,  $2 \pm 0.5 \text{ V/mm}$ ) in water, showing that the MPS-lollipops orient towards the left electrode (a) and the right electrode (b) at different times in the cycle of the slowly alternating electric field. The image quality is rather low because large pieces of secondary (MPS) nucleation could not be removed.

kinetic effect.

Charge density differences between the two sides of the silica/MPS hetero-dimers would be able to explain the described directional preference of the two sides of the hetero-dimers in electric fields (see for example Ref. 300). We measured mobilities of OTMOS-grafted silica particles and MPS droplets (with cross-linked methacrylate groups) separately using laser Doppler electrophoresis; see table 7.1. The mobilities of OTMOS-grafted silica and polymerized MPS were very similar after adsorption of surfactant and two washing steps:  $(-3.9 \pm 0.3) \times 10^{-8} \text{ m}^2/(\text{Vs})$  for OTMOS-silica and  $(-3.1 \pm 0.4) \times 10^{-8} \text{ m}^2/(\text{Vs})$  for MPS. These mobility values do not fall within each others' margins of error, but the difference is small. Although a small difference in charge density between the lobes may be enough to cause vectorial alignment, we do not feel this evidence is conclusive at this point. Secondly, the phenomenon was observed for acorn-shaped hetero-dimers both before and after cross-linking in water and with a  $\text{C}_{20}\text{TES}$  grafting in CHC. Since the surface-grafting as well as the change in solvent can greatly affect the surface charge density, it is quite surprising to observe vectorial alignment present in all these systems, if charge density differences are the main cause of the effect.

The Dukhin number for a sphere of 970 nm, a Debye layer of 100 nm (which is a reasonable assumption in a polar medium at low ionic strength) and a zeta-potential of 50 mV (or lower) is 0.11 (or lower). Thus, it is possible that polarization of the double layer is slower than polarization in the bulk, resulting in Maxwell-Wagner polarization. This scenario is not an alternative explanation for 'vectorial' alignment, but could be responsible for the observed differences regarding which face heads into the direction of propagation (for the acorn-shaped dimers and the supraparticle/MPS dimers), if the Dukhin numbers differ in the systems.

As the particles also underwent electrophoresis, a kinematic effect (e.g. differences in friction) cannot be excluded either. In at least the case of acorn-shaped hetero-dimers this seems unlikely, since the two lobes were nearly identical in size. However, although the sizes of the two lobes are similar, the roughness as is visible in the SEM images is not the same, so it could still be that the friction factors of the lobes differ significantly. It is difficult to estimate these friction factors.

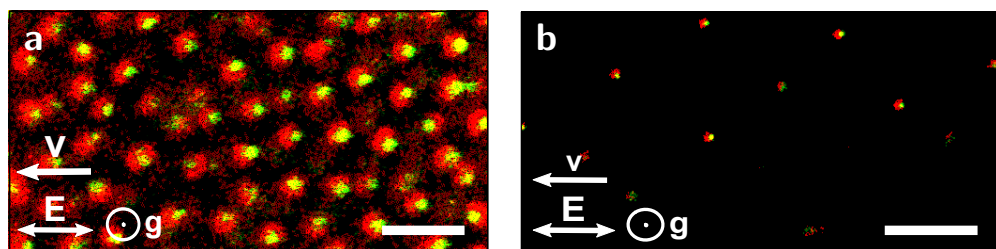


**Figure 7.5:** Confocal micrographs of acorn silica/MPS particles in a slowly alternating field (300 mHz, 18 V/mm) in deionized CHC. The silica contents are: (a) 30 g/L, (b) 10 g/L. Scale bars: 3  $\mu\text{m}$  and 5  $\mu\text{m}$ . A gaussian filter was applied to these images to reduce noise.

| Dispersion                            | Mobility   | Zeta potential          |
|---------------------------------------|--|-------------------------|
| <u>OTMOS-silica</u>                   |  |                         |
| (1) no surfactant                     | $(-5.4 \pm 0.4) \times 10^{-8} \text{m}^2/(\text{Vs})$ | $(-76 \pm 5) \text{mV}$ |
| (2) 0.005 wt.% F108                   | $(-2.3 \pm 0.3) \times 10^{-8} \text{m}^2/(\text{Vs})$ | $(-32 \pm 4) \text{mV}$ |
| (3) 0.005 wt.% F108, washed 2x        | $(-3.9 \pm 0.3) \times 10^{-8} \text{m}^2/(\text{Vs})$ | $(-55 \pm 4) \text{mV}$ |
| <u>MPS, cross-linked methacrylate</u> |  |                         |
| (4) 0.005 wt.% F108                   | $(-2.1 \pm 0.4) \times 10^{-8} \text{m}^2/(\text{Vs})$ | $(-29 \pm 6) \text{mV}$ |
| (5) 0.005 wt.% F108, washed 2x        | $(-3.1 \pm 0.4) \times 10^{-8} \text{m}^2/(\text{Vs})$ | $(-44 \pm 5) \text{mV}$ |

**Table 7.1:** Table of the electrophoretic mobilities and  $\zeta$ -potentials measured for constituent materials of acorn silica/MPS particles. All zeta-potential values were calculated from the particle mobility assuming the Smoluchowski limit since no efforts were taken to reduce the ionic strength and thus have values larger than several tens of nanometers.

### 7.3.2 Vectorial orientation of PMMA-lollipop particles

A chemically different but geometrically similar system to the MPS-lollipops was used to determine whether vectorial orientation is specific to the acorn-shaped silica/MPS particles or whether it is more general. This system consisted of silica/PMMA hetero-dimers (“PMMA lollipops”). In a direct field, PMMA-lollipop particles were successfully aligned ‘vectorially’, i.e. the lollipop particles showed a clear orientation in the field with the silica rods towards the electrode where the particle was heading to, and their PMMA spheres towards the other. Specific directional orientation was observed in both water and ethanol. Ethanol was used in an effort to reduce hydrolysis, but only partially solved the problem. Fig. 7.6 shows an overview of images taken of lollipops vectorially oriented in such a field (the solvent in these particular images was ethanol). The system is dynamic, so the images were taken in between reversals of the field direction. The figures show that almost all particles align with the field, with the silica rods to one side and the PMMA spheres towards the other side.

More specifically, in a sinusoidal electric field of frequency 400 mHz and strength 15V/mm-20V/mm, the particles followed the field by preferentially rotating the silica rods. The particles turned their silica rods towards an electrode, underwent electrophoresis towards one electrode, and turned around towards the other electrode as the field inverted. At higher frequencies, on the order of 10 Hz, displayed only Brownian motion, likely since reorienting took longer than the field period. At very high frequencies, on the order of 1 MHz, the particles were aligned with the field as a result of dipolar interaction with the field, yet the rods and PMMA spheres were oriented randomly on the field axis, and no preferential orientation of the PMMA sides and the silica rod sides towards one electrode was observed.

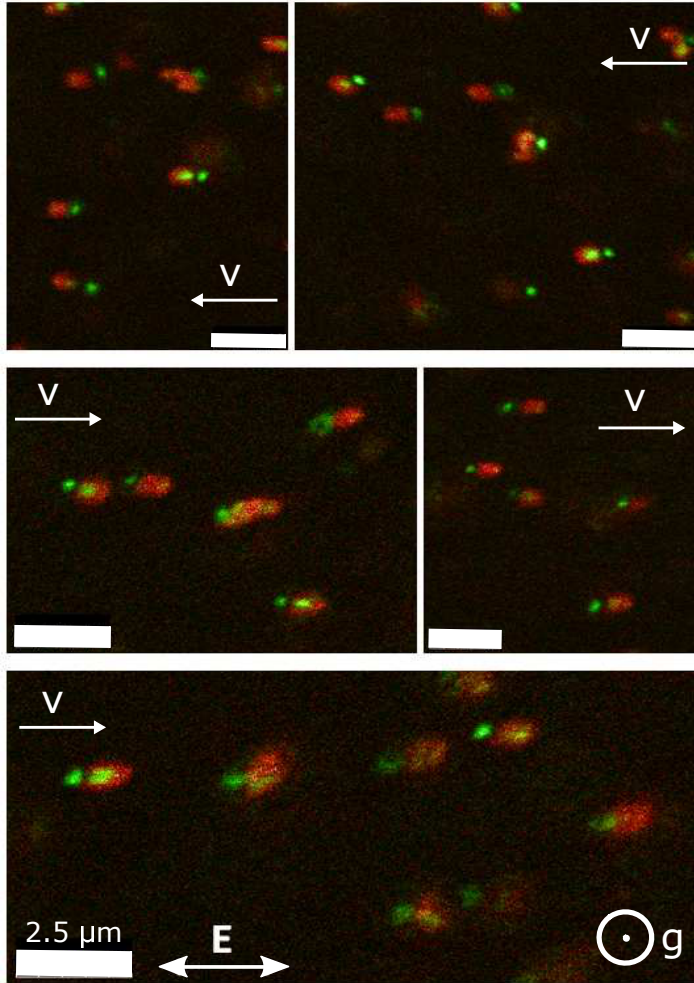


**Figure 7.6:** Several confocal microscope images of vectorially oriented lollipop particles in water in a slowly alternating electric field (frequency 300 mHz, 15 V-20 V). Scale bars denote 2.5  $\mu\text{m}$ . The direction of the electric field is indicated in the bottom panel and valid for all panels. The axis of the field is given, but that the sign of the field in each image is not known since an alternating field was used. The direction of propagation is indicated with 'v'.

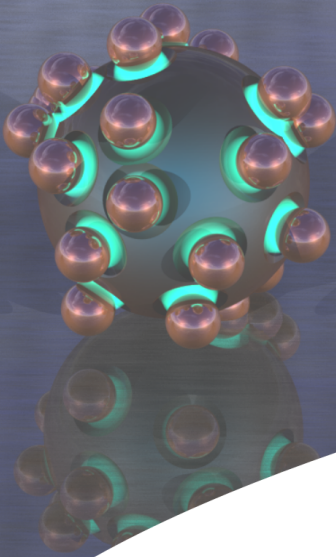
## 7.4 Conclusions & Outlook

Silica/MPS hetero-dimer particles of various shapes (acorn, dumbbell, supraparticle-dumbbell, lollipop, as discussed in Ch.6) and chemical composition (OTMOS-silica/MPS and MPS-silica/PMMA) were aligned in direct electric fields and slowly alternating fields ( $<10$  Hz). The particles showed a directional alignment, meaning that all particles headed with the same side towards the field direction which is also that of electrophoresis ("vectorial alignment"). For acorn-shaped and lollipop-shaped MPS/silica hetero-dimers, the MPS lobe oriented into the direction of propagation, while supraparticle/MPS dumbbells headed with the supraparticle lobe in front. A reasonable hypothesis is that the directional alignment is a result of a difference in zeta potential between the lobes, as also mentioned in Ref. [299, 300]. A small difference in electrophoretic mobility was detected between the OTMOS-silica particles and MPS particles (in laser Doppler electrophoresis measurements) after adding surfactant and washing twice with water. However, further investigations are required, since the mobility was considerably dependent on the surfactant concentration in the dispersion. Another explanation could be kinetic effects, since the roughness of the two lobes differ. The 'vectorial alignment' effect can be used to obtain crystals with not only spatial alignment but also directional alignment of the constituent particles. Preliminary experiments for crystals of acorn-shaped particles with long-range repulsions in CHC - presented in this chapter - were successful in this regard. Practical applications in photonic devices are also an option.

## Acknowledgements

We would like to thank to Rao Vutukuri for demonstrating the electric field cell construction. Bo Peng is thanked for providing the PMMA/silica lollipop particles and for the opportunity to collaborate on this topic.





## CHAPTER 8

# Selective depletion interactions in mixtures of rough and smooth silica spheres

The depletion interaction as induced between colloids by the addition of a polymer depletant is one of the few ways in which short-ranged attractions between particles can be induced in a controlled way through the concentration of the depletant. In this way, colloid polymer mixtures have contributed to a better understanding of the role of attractions both in equilibrium phenomena such as phase transitions, liquid surfaces and in systems falling out of equilibrium such as gelation and the glass transition. It is known that, by simple geometric effects, surface roughness decreases the strength of the depletion interaction. In this study, we demonstrate experimentally that by controlling surface roughness for charged spherical colloids it is possible to generate enough difference between the attractions between smooth particles as compared to between rough particles of similar size to induce phase separation between the former while not between the latter. Roughness was induced by coating smooth particles with smaller spherical colloids. We indicate how the interplay between gravity and the depletion interaction with a flat container wall can be used to get a simple measure of the differences in interaction strengths as a function of roughness and other parameters influencing the interactions. The results are compared to Monte Carlo simulations on the effective potentials among rough-rough, smooth-smooth and rough-smooth pairs of particles.

---



## 8.1 Introduction

In this chapter, we focus on one of the few ways in which attractions can be induced between colloidal particles in a more or less controlled way other than the temperature-induced freezing transition of a single linear alkane layer discussed in Ch. 2, namely by so-called depletion interactions. Depletion attractions are the result of an imbalance of the osmotic pressure induced by a small polymer or small colloids - the depletant - when two larger colloidal particles get closer to each other than the diameter or radius of gyration of the depletants (see Fig. 8.1 and Refs. 301–307). For relatively low concentrations of the bigger colloids and the depletion agent, the attractions are proportional to the concentration of the depletant and the overlap volumes in which the depletant cannot penetrate. As indicated schematically in Fig. 8.1 (and as has been demonstrated recently in several papers, see e.g. [45, 308]) the depletion interaction can be significantly reduced if surface roughness is introduced with a size on the order of the depletant size. These ideas are more recent extensions of the realization that geometry can be used to affect the overlap volumes [309].

Recent examples of manipulating overlap volumes are lock-and-key interactions between convex and concave particles [310], and depletion interactions between platelets [308], cylinders [45] and dumbbells [44]. Zhao and Mason prepared colloidal pentagons with surface asperities on the faces. They showed that when the depletant size exceeds the average asperity height, depletion interaction between the faces causes the pentagons to form stacks. Moreover, they explored the phase diagram of Janus platelets with one rough face. These particles formed dimers at intermediate depletant concentrations. Badaire *et al.* synthesized colloidal cylinders with rough sides and flat faces. By tuning the surface roughness, the cylinders selectively aggregated at the flat ends, forming columnar strings. This directional depletion interaction was realized when the root mean square amplitude of the roughness was larger than the diameter of the polymer. Kraft *et al.* synthesized colloidal dumbbells with one rough sphere and one smooth sphere. In this case, local roughness (on one of the particle lobes) and convex-concave aspects in the particle shape were both into play. They found that, at adequate depletant concentrations, such dumbbells form the colloidal analogue of a micelle, with the smooth sides of the dumbbells on the inside and the rough side on the outside of the micelle.

In this chapter, we focus our attention on mixtures of rough and smooth spheres of roughly the same size. This system is simpler than that presented in Ref. 44, as the particle shapes are all convex only. It is in some sense also a limiting case, as it is clear from inspecting Fig. 8.1 that depletion zones between spheres are relatively small and would be significantly increased if the surfaces were more flat (like in the experiments from Refs. 45, 273, 308) and/or had also concave parts [44, 310]. The question that we set out to answer in this chapter is whether it is possible - in mixtures of rough and smooth spheres - to induce strong enough attractions between the smooth spheres that they would phase separate or gel while the interactions between a smooth and rough particle (and thus also between two rough spheres) stay below that necessary to induce phase separation. Interestingly, the answer is yes, which is illustrated by confocal microscopy real-space measurements of mixture of rough and smooth sphere for which a depletion interaction induced by polymer resulted in the formation of a gel between the rough particles while the dynamics of the smooth particles labeled with a different dye remained still completely diffusive in between the gelled phase.

As the specifics of the interactions depend on many parameters such as the screening length in the solvent, the size of the particles with respect to that of the depletant and the roughness, and the concentration of depletant, we also demonstrate a simple experimental procedure (that was validated by simulations) to gauge the strength of the interactions. In this procedure we used a competition between depletion attractions and gravity. We determined at what depletant volume fractions the (rough and smooth) larger particles remained attracted against gravity onto a flat wall oriented perpendicularly to the direction of gravity. Roughness on the particles was controlled by aggregating a layer of smaller silica spheres of opposite charge on top of smooth silica spheres. Such a procedure is also possible for latex particles (c.f. Ref. 311), and other procedures to create rough particles are known in the literature as well [312, 313]. Using differently fluorescently labeled components allowed efficient characterization by real space confocal measurements. The effect of varying several of the many variables that influence the effective interactions was studied mostly by computer simulations in order to gauge their importance.

In this chapter, we first explain the experimental and simulation methods used. Subsequently, we describe and discuss both the effective depletion interaction potentials and how they are influenced by several variables, as obtained from the simulations and the experiments performed to gauge the interaction strength and induce the phase separation/gelation.

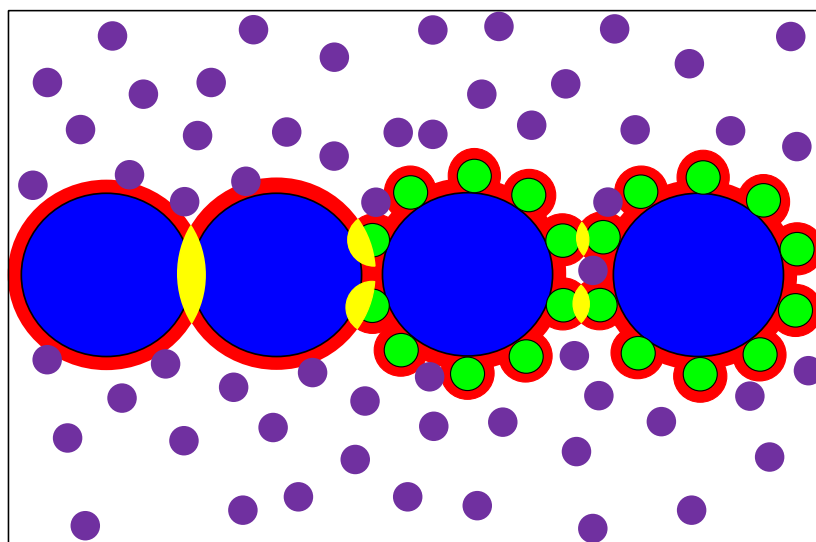


**Figure 8.1:** The depletion zones (red) and overlap volumes (yellow) for two smooth spheres; a rough and a smooth sphere; and two rough spheres. Colloids are depicted in blue, small spheres that form roughness in green, and depletant in purple.

## 8.2 Methods

### 8.2.1 Experimental methods

#### Materials and instruments

The following chemicals were used without further purification. From *Sigma Aldrich*: rhodamine B isothiocyanate (RITC, mixed isomers), eosine isothiocyanate (EITC), methacryloxypropyltrimethoxysilane (MPS,  $\geq 98\%$ ), poly(allylamine hydrochloride) (PAH,  $M_w \sim 15000$  g/mol). From *Aldrich*: cyclohexylchloride (CHC, 99%) and tetrabutylammonium chloride (TBAC). A steric stabilizer was synthesized by comb-grafting poly[12-hydroxystearic acid] (PHSA) onto a poly[methyl methacrylate] (PMMA) backbone through the method describe in reference [314]. Polystyrene (565.500 g/mole) was used as a depletant.

Transmission electron microscopy (TEM) and scanning electron microscopy (SEM) imaging were performed respectively on a *TECNAI 10* transmission electron microscope and a *XL305 FEG* from *Philips* company. Conductivity measurements were performed with a *Scientifica model 627* conductometer.

#### Colloid synthesis

Rough silica particles were synthesized via a method resembling that in Ref. [311] by C.M. van Kats. Seed colloids for the rough particles were silica spheres with an FITC-labeled core prepared by Stöber synthesis as in reference [179]. The particles had a diameter of  $1.18 \pm 0.01 \mu\text{m}$  and polydispersity 2% as measured by transmission electron microscopy (TEM). These seed colloids were given a positive charge by adsorption of PAH molecules [315–318]. In short, seed colloids were dispersed in a mixture of 20 mL water, 1.17 g NaCl and 0.06 g PAH. After stirring for at least 20 minutes, the particles were washed three times with water. Subsequently, slow sedimentation of these positively-charged seed colloids through a dispersion of small ( $130 \text{ nm} \pm 4 \text{ nm}$ ) negatively charged EITC-labeled silica particles allowed the small particles to stick to the seed colloids. A clean-up procedure by three sedimentation/redispersion steps was used to dispose of the excess small spheres. A thin ( $\sim 10 \text{ nm}$ ) Stöber silica layer was grown onto the final

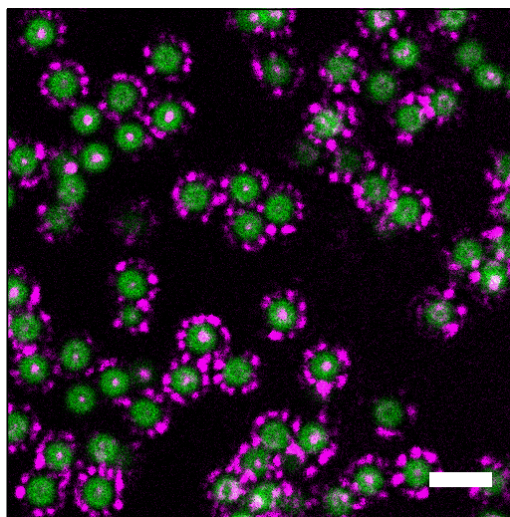


**Figure 8.2:** Confocal micrograph of rough particles in CHC. The FITC-dyed cores were recorded in fluorescence mode (green), while the small particles at the surface were recorded using scattering mode (purple).

particles using seeded growth [179]. SEM and TEM images of these particles are shown in Fig. 8.3. The surface of the final rough particles was grafted with the silane coupling agent MPS to make these colloids more hydrophobic for the intended solvent, and also to allow for a similar environment for the steric comb-graft stabilizer PHSA-PMMA to be adsorbed onto as with PMMA particles [314].

Stöber silica particles grafted with the silane coupling agent MPS were used as smooth particles. These particles had a silica core of ~300 nm which was fluorescently labeled with RITC. The particles had a diameter of  $1.24 \pm 0.01 \mu\text{m}$  (by TEM, p.d. 2%) and  $1.32 \pm 0.01 \mu\text{m}$  in ethanol (by static light scattering, SLS, [179, 319, 320]).

## Interaction strength and phase separation experiments

A stock solution of CHC ( $\epsilon = 7.6$  [270] and  $n_D^{20} = 1.46$  [271], while for silica  $n_D^{25} = 1.45$ -1.46 in most organic solvents [285]) was prepared with a stabilizer concentration of 0.6 g/L and saturated with TBAC. The salt and the stabilizer were added to the CHC before the colloids were dispersed in it. The steric stabilizer can act as an extra depletion agent, but at the concentration used both rough and smooth particles did not aggregate without adding an extra polymer depletant.

The Debye screening length  $\lambda_D$  in an electrolyte solution is given by [321]:

$$\lambda_D = \sqrt{\frac{\epsilon \epsilon_0 k_B T}{2e^2 N_A I}} \quad (8.1)$$

with  $\epsilon$  the dielectric constant of the medium,  $\epsilon_0$  the vacuum permittivity,  $k_B$  the Boltzmann constant,  $T$  the absolute temperature,  $e$  the elementary charge,  $N_A$  Avogadro's number and  $I$  the ionic strength. The added amount of TBAC was equivalent to 2 mM, yet not all TBAC was expected to dissociate. The conductivity of the solution was  $0.441 \pm 0.003 \mu\text{S}/\text{cm}$ ; with Walden's rule one arrives at a Debye length of 40 nm.

Polystyrene dispersions were prepared from this stock solution, with concentrations of 3-8 g/L (3-8 wt%). A DLS measurement (on a *ZetaSizer Nano*, *Malvern Instruments*) of a solution of 2 wt.% PS in the CHC stock solution indicated a hydrodynamic radius of gyration of the polymer of  $23 \pm 1$  nm. Additionally, stock dispersion of colloids were prepared: a stock dispersion of the smooth colloids with a concentration of 70 g/L, and a stock dispersion of the rough colloids with the same concentration. For phase separation experiments, samples with both smooth and rough particles were obtained by adding together equal volumes of the two stock dispersions. Samples with depletant were obtained by adding an equal volume of polymer stock solution to a volume of such a mixed dispersion. Capillaries were filled by dipping them into the dispersion and sealing with UV glue (Norland Optical Adhesive no. 68). After curing of the glue, capillaries were sonicated for a few seconds to liberate particles potentially sticking to the walls by depletion interaction. Afterwards, some capillaries were stored in a rotating stage [322] to approximately average out the effects of gravity. Samples were observed by confocal microscopy (Leica SP2, horizontal stage, equipped with a 63x (NA = 1.4) Leica confocal lens and type F immersion oil).

As an aside, the rough particles contained an FITC-labeled core and EITC-labeled surface roughness. The emission maxima of FITC and EITC are close together (520 nm and 540 nm in

ethanol [323]) and the emission spectra overlap. Hence, the fluorescent signals of the core and the roughness could not be detected separately. The surface roughness can, however, be imaged employing scattering. Fig. 8.2 shows rough particles imaged with a Leica SP8 confocal microscope equipped with a Leica Plan Apo 63x (NA = 1.32) lens; the FITC cores were recorded using fluorescent mode and are depicted in green, while the surface roughness was recorded in scattering mode and is depicted in purple.

For experiments to estimate the depletion interaction strength, dispersions were prepared of which 50% consisted of stock dispersion of either rough or smooth spheres in CHC, and the other 50% of polymer stock solution diluted with as much CHC stock solution as required to reach the desired polystyrene concentration in the final dispersion. Capillaries were filled with these dispersions, sealed with UV-curable glue, and left on one side for 30 minutes. The capillaries were then turned upside down and placed onto the confocal microscope. After thirty minutes equilibration time (which was enough time to have the free particles sediment to the bottom of the capillary), the dispersions were imaged by confocal microscopy. At four spots in the capillary, a confocal image was obtained from the particles remaining at the top capillary wall due to depletion attraction and the particles that had sedimented to the bottom wall. Interactive Data Language (*IDL*) tracking software by Crocker, Grier and Weeks [147, 324] was used to count the number of particles in each frame. The ratio of particles sticking to the top wall to the total number of particles was calculated for each spot. These fractions were averaged for the four spots to obtain the average fraction of particles adhering to the top wall by depletion attraction.

## 8.2.2 Numerical methods

Simulation studies were performed by M. Hermes (at Utrecht University) as described in Ref. 325. In brief, rough particles were modeled as hard spheres with diameter  $\sigma_c$  with small hard spheres of diameter  $\sigma_s$  on the colloidal surface acting as surface roughness. These particles were themselves obtained by Monte Carlo (MC) simulations of a binary mixture of oppositely charged particles in the NVT ensemble, in analogy to the experimental synthesis procedure. The colloid and polymer interactions from the experimental system were described as a pairwise colloid-colloid interaction Hamiltonian. The pair potentials between two rough particles, two smooth particles or a rough and a smooth particle were then calculated in an MC simulation. Overlap volumes were calculated by dividing a cell with two particles into subcells and summing the overlap volume of all subcells.

### 8.3 Results & Discussion

TEM and SEM images of the synthesized rough particles are shown in Fig. 8.3a-b. Based on the number of small spheres on one hemisphere, we estimate a surface coverage of 200 - 250 small particles. Fig. 8.3c displays simulated rough colloids with different surface coverages of small particles, which were obtained using a chosen value of  $\kappa\sigma_c = 10$  and varying volume fractions of small particles in the (simulated) binary mixture. These simulations indicated that a partial surface coverage of the core particle with small particles is most effective at reduction of the depletion attraction, and from Figs. 8.3a-b it is clear that the synthesized rough particles indeed satisfied that criterium.

To accomplish species-selective immobilization by depletion interaction, the size of the smooth particles was carefully chosen in the following manner. The 'size' of the rough particles was assumed to be  $\sigma_c + \sigma_s = 1.31\ \mu\text{m}$  (i.e. the size of a sphere centered on the seed colloid through the centers of the adsorbed small particles). The smooth particles were slightly smaller:  $1.24\ \mu\text{m}$ . Solely based on size, the depletion attraction among the smooth particles would be weaker than that among the rough particles due to the smaller overlap volume. However, the roughness reduces the depletion potential among the rough species.

The polymer size was chosen to be smaller than the size of the surface roughness ( $\sigma_s$ ), since simulations had pointed out that this is required for a more effective reduction of the depletion attraction: a larger polymer effectively smoothes the surface roughness. The required polymer fraction for appreciable attraction between the smooth particles will also be lower. In our case, the (hydrodynamic) radius of gyration of the polymer in this solution was  $23 \pm 1\ \text{nm}$ , which is less than half the radius of the small particles. Simultaneously, the double layer must be small compared to the surface roughness and the polymers, lest the double layer inhibit depletion attraction rather than the surface roughness. For this reason, the double layer was reduced by adding salt to the solvent. From the conductivity of a CHC stock solution (without polymer added), a Debye length of  $41\ \text{nm}$  was estimated using Walden's rule. This Debye length equals  $0.32\sigma_s$ , and is on the order of the polymer diameter, hence a moderate smoothing effect was present.

A pair potential was then also obtained by MC simulations based on the specific parameters in the experimental system, such as the diameters  $\sigma_c$ ,  $\sigma_s$  and the diameter of the smooth particles  $\sigma_{smooth}$ . The corresponding pair potentials calculated for two smooth particles, two rough particles and a rough and a smooth particle are shown in Fig. 8.3d. The smooth particles have a strong attraction of over  $15k_B T$ . The rough particles on the other hand have a weak attraction minimum on the order of  $k_B T$ , and will be able to escape from this attraction due to Brownian motion. A rough and a smooth particle have a slightly deeper attraction minimum of several  $k_B T$ , so these may be expected to stick occasionally.

In experimental dispersions in CHC without depletant, no clustering of either species was observed even after two days; we inferred that particles of both species are thermodynamically stable in this solvent. To establish the polymer concentrations at which the onset of the depletion interaction occurs, the fractions of particles sticking to the top wall of a capillary - 30 minutes after turning the capillary upside down - were measured for various polymer concentrations. When the buoyant force of the particles exceeds the depletion attraction with the wall, all particles must fall to the

bottom capillary wall after turning. On the other hand, when the depletion attraction with the wall exceeds the buoyant force, most particles are expected to remain adhered to the top capillary wall. Fig. 8.4 shows the fraction of particles adhering to the top wall as a function of polymer concentration for both smooth and rough particles. The smooth particles started to be attracted to the capillary wall at approximately 0.25 wt.% depletant, whereas the rough particles required at least 2.5 wt.% depletant. The depletion attraction between two particles of one species - or even of different species - is smaller than the depletion attraction between a particle and a capillary wall, since the flat wall has no curvature or roughness and this implies a larger overlap volume. In other words, these measurements provided a lower limit concentration of 0.25 wt.% PS needed for gelation of the smooth particles, while the lower limit concentration at which rough particles were expected to aggregate was at least 2.5 wt.%.

For a polymer concentration of 2 wt.% PS, a sample of smooth particles (70 g/L) showed large clusters after one day in the rotating stage. In a sample of rough particles (70 g/L) with a polymer concentration of 2 wt.% PS no such clustering was observed. Therefore, equal volumes of these dispersions were combined, and a glass capillary was filled with this mixed dispersion. The sample was observed five hours after preparation. This sample contained large clusters of the smooth particles but nearly all rough particles were performing Brownian motion (see Fig. 8.5).

The large clusters in Fig. 8.5a have an open, branched structure, indicating a strong depletion interaction between the smooth particles, which agrees with the deep attraction minimum ( $15k_B T$ ) found in the theoretical calculation of the pair potential. The time-averaged figure 8.5b shows that the smooth particles - trapped in clusters - had not moved, whereas the rough particles explored the space between the clusters through Brownian motion. Thus, we have found a depletant concentration for which the smooth particles spinodally demix, yet the rough particles can move freely. A few rough particles are sharply visible in the time averaged image as well, implying that those particles are trapped in the inside of the cluster. This trapping can be due to the potential minimum between rough and smooth particles, for the theoretical calculations showed a smaller minimum in the potential between rough and smooth particles, but could also simply be the result of complete caging/entrapment. In brief, surface roughness was used as a property to selectively immobilize (inhibit Brownian motion) in a mixture of two species of particles.

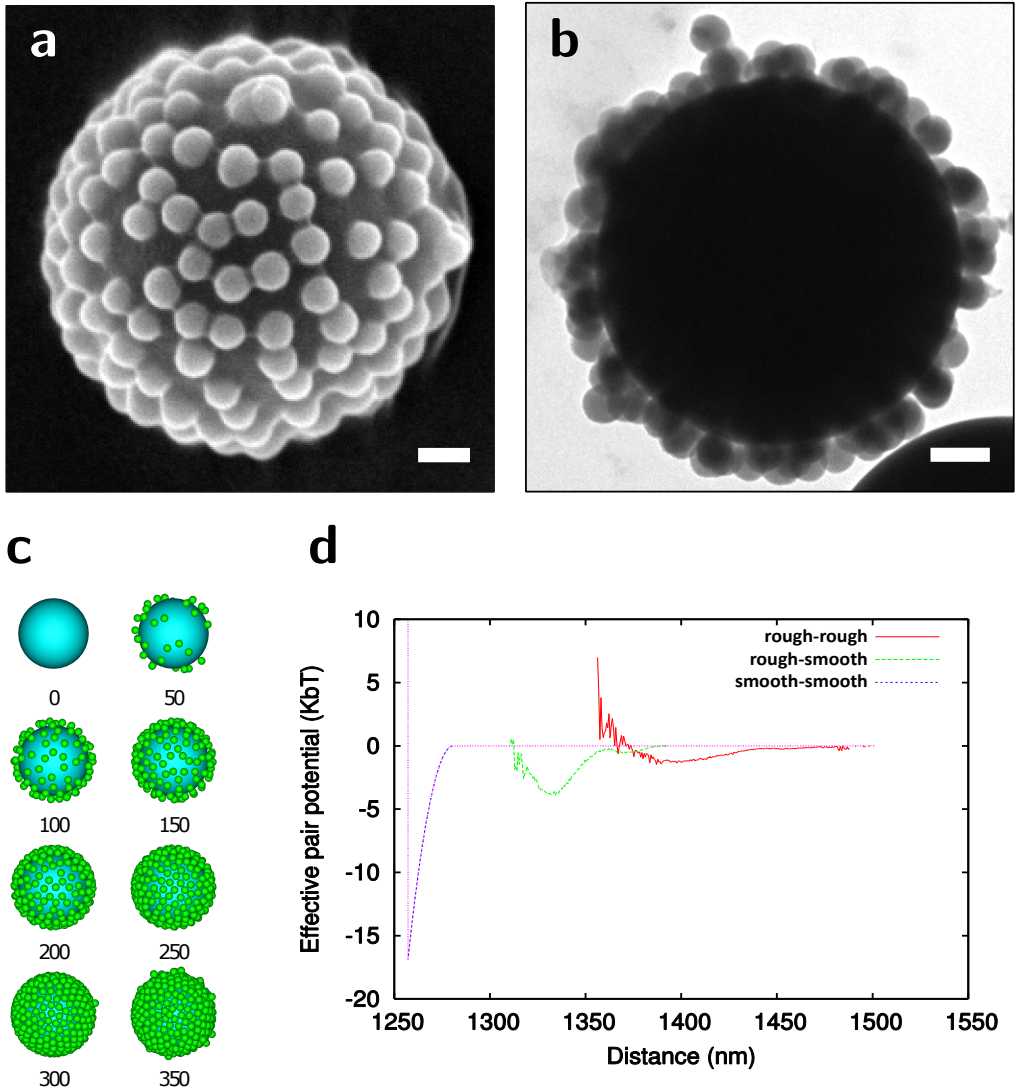


**Figure 8.3:** Micrographs of rough fluorescently labeled silica particles (core size  $\sigma = 1.18 \mu\text{m}$ , small sphere size 130 nm) imaged by (a) SEM and (b) TEM. Scale bars represent 200 nm. (c) Snapshots of simulated rough particles, obtained by varying the volume fractions of core particles and small particles in the simulated binary mixture. In these simulations, small particles were adsorbed irreversibly onto the cores using a reduced screening length of  $\sigma\kappa=10$ . (d) The effective pair potential  $\beta\phi^{eff}(r)$  as a function of center-to-center separation for the rough and smooth particles with the parameters used in the experiments:  $\sigma_c = 1175 \text{ nm}$ ,  $\sigma_{small} = 122 \text{ nm}$ ,  $\sigma_p = 23 \text{ nm}$  and  $\eta_p = 0.16$ .

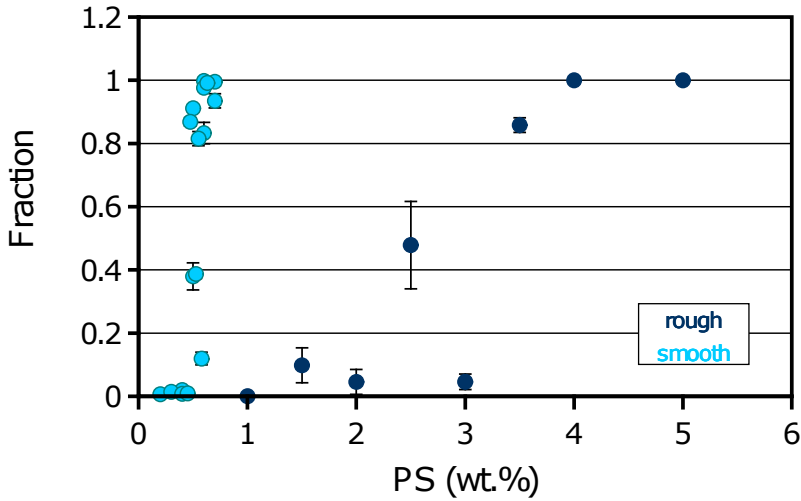


**Figure 8.4:** Graphs of the fraction of particles sticking to the top wall after turning a capillary, as a function of depletant PS concentration.

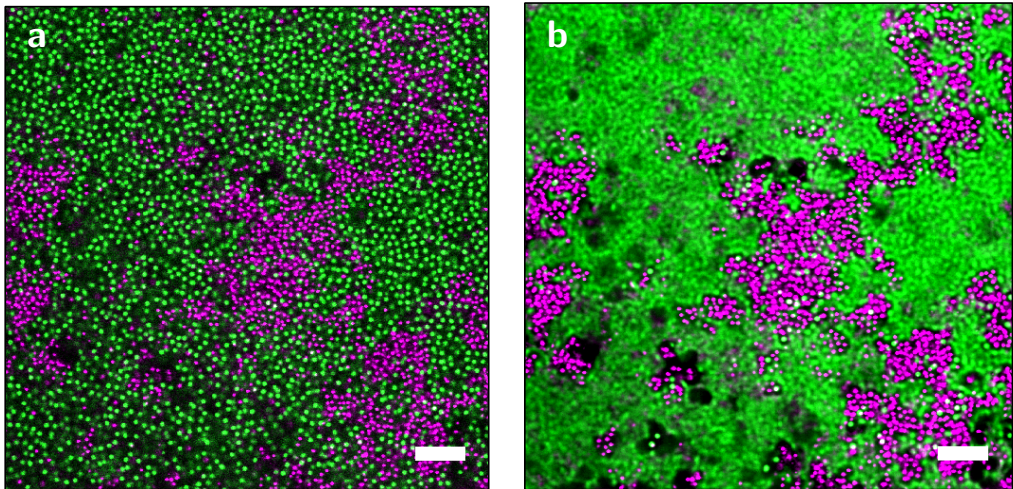


**Figure 8.5:** (a) Depletion interaction in a dispersion of smooth (purple) and rough (green) spheres. The sample contains 2wt.% PS and was imaged five hours after preparation. The smooth spheres have aggregated into a cluster while the rough spheres can move freely. (b) Time average over 60 frames of the sample with smooth and rough particles in a 2wt.% PS solution in CHC. Time between successive images was 635 ms. Rough particles are imaged in green, smooth particles in purple. Black spots are air bubbles moved to the field of view due to sonication. The scale bars denote 10  $\mu\text{m}$ .

## 8.4 Conclusions & Outlook

In conclusion, we have experimentally investigated the extent to which a polymer-induced depletion attraction can be reduced by roughness on the particle surface for similarly sized colloidal spheres. We found that it is possible to induce sufficient discrimination difference between the rough/rough and rough/smooth depletion attraction strength on the one hand, and the smooth/smooth depletion attraction strength on the other hand that the latter particles gel while the former remain completely mobile. The results were in agreement with results from MC simulations. As the depletion overlap volume for spheres is 'least' optimal and thus a kind of limiting case, this finding is of importance for inducing specificity with respect to depletion-induced attraction for other particles shapes as well. We indicated how by simulations the effective interactions can be estimated. In addition we provided a simple experimental procedure to gauge the interaction strengths by balancing depletion attractions with a flat wall against gravity. This work can be useful for other studies of patchy particles which use surface roughness and surface geometry in combination with depletion interaction as a self-assembly mechanism.

## Acknowledgements

Michiel Hermes performed all computer simulations and is sincerely thanked for his patience and help in finishing the project. Carlos van Kats synthesized the rough silica particles and is gratefully acknowledged. Daniela Kraft and Willem Kegel are thanked for sharing knowledge on depletion interaction in systems of rough and smooth particles. We thank Ahmet Demirörs for synthesis of the silica particles used as the smooth species and Johan Stiefelhagen for synthesis of the PHSA.

## 8.5 Appendix: Supplementary experimental information

### 8.5.1 Zeta potential measurements

Zeta-potential measurements were performed on a *Malvern ZetaSizer Nano* machine (Malvern Instruments). Although the Debye layer is determined by salt concentration alone, we wanted to verify whether the zeta potential was similar for rough and smooth particles. A zeta-potential measurement was performed on dilute dispersions of the smooth and the rough particles in a stock solution of CHC with salt and stabilizer. Both species of silica particles have a dye-free outer silica layer and similar (MPS) surface grafting. Differences in surface charge are thus not likely. The zeta potential was calculated from the electrophoretic mobility under assumption of the Smoluchowski limit ( $\lambda \ll R_{colloid}$ ). Figure 8.6 shows the number of counts as a function of zeta-potential. The

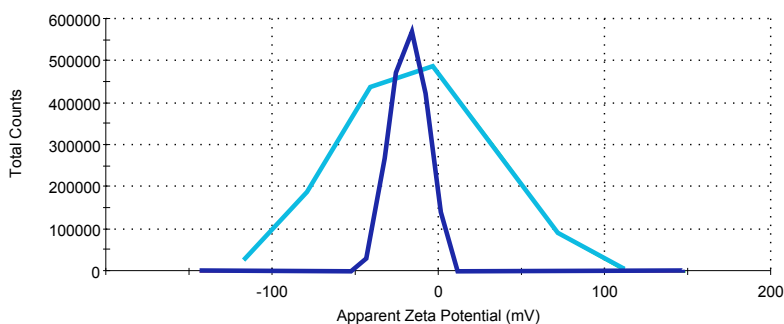
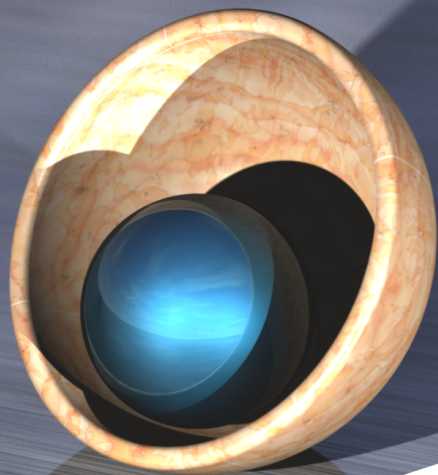


**Figure 8.6:** Zeta potentials calculated from the electrophoretic mobilities by the Smoluchowski equation for smooth particles (black line) and rough (grey line) particles in CHC saturated with TBAC and stabilized with PHSA.

measured zeta potential of the smooth particles is  $-18$  mV. The zeta potential of the rough particles is centered at approximately the same value, but it is very broad. These zeta potentials were deemed sufficiently close that the surfaces of the rough and smooth particles are similar.





## CHAPTER 9

# Electric-field-induced lock-and-key interactions between colloidal spheres and bowls

To realize new and directed self-assembly (SA) pathways, the focus in colloid science and nanoscience has shifted from spherical particles and interactions to increasingly more complex shapes and inter-particle potentials. This field is fueled by recent breakthroughs in particle synthesis, such as particles with complementary shapes that allow for specific lock-and-key interactions induced by depletants. Here, we show that electric fields form an alternative route for directing the SA of convex and concave shaped colloids, with the additional advantage that the system now becomes switchable by external conditions. Both experimental and theoretical results are presented that validate the electric-field-induced assembly mechanism and show that even irreversibly bound composites can be generated by tuning the force balance. The successful isolation of the irreversible composite particles, in combination with generalization to different materials, shows that the current mechanism provides a versatile new path not only toward complex-particle synthesis but also toward directed self-assembly.

---



## 9.1 Introduction

In the field of colloidal self-assembly, the focus in recent studies has shifted from spherical particles to anisotropic or more complex shaped particles and from spherical interaction potentials to more complex interactions. This shift in perspective is driven by newly invented synthesis routes that result in particles with more complex shapes [10, 15]. Examples include bowl-shaped particles [326], rods [13], (hollow) cubes [14], ellipsoids [327], platelets [328], colloidal molecules [63, 313], colloidal clusters [329], dumbbells [330] and polyhedral particles [273]. Combining complex particle shapes with anisotropic interactions opens many new avenues to manipulate self-assembly and materials properties. An example is the lock-and-key interaction between complementary shaped particles [62] induced by depletants [310]. Depletion-induced interactions, driven by non-adsorbing polymers or particles ('depletants'), have a range that is set by the size of the depletant, while the strength is set by the concentration of depletants [301].

Another way to induce inhomogeneous interactions is by means of external electric fields. Experimental approaches in this direction have already been described in literature [10]. For example, it is well established that electric fields can be used to influence the orientation of colloidal particles. For silica rods, the alignment of the axis in the direction of an external electric field can result in improved nm-ranged order in smectic phases [277] as well as in a transition from a plastic crystal or plastic glass to a crystal phase [131]. Such field-alignment was also used to tailor the properties of films prepared from colloidal ellipsoids [331]. In addition, an electric field can be used to alter the spatial position of the particles. As a result of the interaction of the induced polarizations, particles (spheres, rods, bowls and other anisotropic shapes) can form long chains along the direction of an external electric field [46, 277, 292]. The behavior of mixtures of polarizable colloids of different geometric shapes is less well studied, although beautiful structures in the analogous case of magnetic particles and fields are known [332]. To describe these systems, the field-induced polarization in both particle species must be taken into account as well as the interaction this induces between the particles, which can be done in a recursive manner [333]. Insight can be gained from theoretical and computational studies [334–336] and various methods have been developed in recent years to describe or predict field-induced alignment and interactions (e.g. the coupled dipole method [10, 288, 289]).

Here, we show experimentally and theoretically that electric fields can be exploited as a new route for inducing lock-and-key type of interactions between complementary (convex and concave) shaped particles (polarizable bowls and spheres). The electric field is therefore an alternative to the addition of depletants. Preliminary results in this direction were already presented in Ref. 10. A powerful advantage is that the interaction strength can now be tuned *in situ* by external control and without the need to alter the composition of the system. Moreover, we show that the force balance can be adjusted such that even irreversibly bound composites can be generated. In this way, electric fields do not only result in directed self-assembly of anisotropic particles but actually also form a means to synthesize new types of complex-shaped particles, as we will show.

## 9.2 Experimental details

### 9.2.1 Chemicals

Dimethyldiethoxysilane (DMDES, 97.0%), tetraethoxysilane (TEOS, 98.0%), 3-aminopropyltriethoxysilane (APTES, 99%), rhodamine B-isothiocyanate (RITC), polyvinylpyrrolidone (PVP,  $M_w$ : 58,000 and 40,000 g/mol), styrene, deuterium oxide ( $D_2O$ ), fluoresceine isothiocyanate (FITC) and ammonia (25 wt.%  $NH_3$ ) were purchased from *Sigma Aldrich*. Pyrromethene-567 was obtained from *Exciton*, ethanol (96%, 100%) from *Interchema*, PVP ( $M_w$ -360,000 g/mol) and 2,2-Azobis(2-methylpropionitrile) (AIBN) from *Fluka*. All chemicals were used as received. Demineralized water (resistivity 18  $M\Omega cm$ ) was used in all reactions and also for cleaning of glassware.

### 9.2.2 Particle synthesis

Bowl-shaped particles were formed from buckled, elastic microcapsules. These microcapsules were synthesized based on the method described in Ref. 337 which is a modification of the original procedure reported in Ref. 326 that uses oil-droplets as templates for shell growth. The polydimethylsiloxane (PDMS) templating oil droplets were prepared by adding 4.1% v/v of the monomer dimethyldiethoxysilane (DMDES) to an aqueous ammonia solution (700 mL, 24.4% v/v ammonia). Hereafter, the sample was mixed with a Turrax homogenizer (*IKA's Ultra-Turrax* with a *S25N 10G* dispersing element) at a speed of 11,100 rpm for 10 minutes such that the large DMDES droplets disappeared. The resulting turbid solution was poured into a 1 L flask and allowed to stand undisturbed for 2 days before start of the shell growth. For fluorescent labeling of the capsules upon shell growth, the fluorescent dye rhodamine B-isothiocyanate (RITC) was first covalently attached to the coupling agent 3-aminopropyltriethoxysilane (APTES). To this end, a mixture of 6.5 mg RITC dye, 40  $\mu L$  APTES and 1 mL anhydrous ethanol was stirred in the dark for a period of 12 hours. Subsequently, 550 mL of the as-prepared emulsion (still containing ammonia) was gently mixed with an aqueous polyvinylpyrrolidone (PVP,  $M_w = 58,000$ ) solution (volume 1375 mL, 2.9 wt% PVP) using a stirring bar. The polymer PVP was added to reduce aggregation during the coating step. Encapsulation of the oil droplets with an elastic shell was achieved by adding both the monomer tetraethoxysilane (TEOS) (8 mL) and DMDES (8 mL) simultaneously to the dispersion using a syringe pump (*KD Scientific*, 10  $\mu L/min$ ). The APTES-RITC dye solution (0.330 mL) was added after a period of about 5 hours. The sample was gently stirred for a period of 3 days after which the dispersion was dialyzed in a few hours against demineralized water. The resulting microcapsules, still containing a templating oil droplet in the core, buckled upon aging (1 up to 1.5 years), most likely because the enclosed volume is no longer preserved due to slow evaporation of the PDMS oil in time. Note that microcapsule buckling can also be induced on much shorter time-scales, and in a controlled way, via surfactant micelles [338]. For electric-field induced self-assembly studies, typically 40 mL of the particle dispersion was concentrated to  $\sim 40 \mu L$  using centrifugation at about 550 g for 25 min (*Heraeus, Labofuge Ae*). Typically, the final concentration used was on the order of 4 mg/mL (i.e.  $3 \cdot 10^9$  particles/mL).

Silica spheres with fluorescently-labeled core/shell geometry were prepared as follows. Seed particles (830 nm) were grown by reaction of TEOS in a basic solution (containing ethanol, water and ammonia) under magnetic stirring (Stöber route, [194]). A conjugate of fluoresceine isothiocyanate (FITC) and APTES was added during this growth to incorporate fluorescent dye into the silica matrix [179]. An extra layer of silica was grown around the particles by continuous addition of TEOS (Giesche seeded growth, [182]) until a final diameter of 1.4  $\mu\text{m}$  was reached (as determined by SLS). The reaction mixture was washed several times by centrifugation and removal of the supernatant with ethanol. A dispersion with a concentration of about 19 mg/mL (i.e.  $5 \cdot 10^6$  particles/mL) was prepared by washing twice with water.

Pyromethene dyed polystyrene spheres (1.5  $\mu\text{m}$  in diameter, determined by SLS) were synthesized using a two-stage dispersion polymerization method, inspired by Ref. 339. First, 25 g ethanol, 5 g styrene, 0.1 g PVP (stabilizer,  $M_w = 360,000$ ) and 0.025 g initiator (2,2-Azobis(2-methylpropionitrile), AIBN) were mixed in a 250-mL three-neck reaction flask equipped with a condenser and a gas inlet. Nitrogen gas was added at room temperature for 1 h to remove oxygen. Then, this mixture was heated to 70  $^\circ\text{C}$  in an oil bath for 1.5 h while stirring magnetically at 200 rpm. Hereafter, a mixture of 0.05 g pyromethene-567 dye, 5 g styrene and 12.5 g ethanol (pre-mixed at 70  $^\circ\text{C}$  under nitrogen) was quickly added and the reaction was allowed to continue for 24 h.

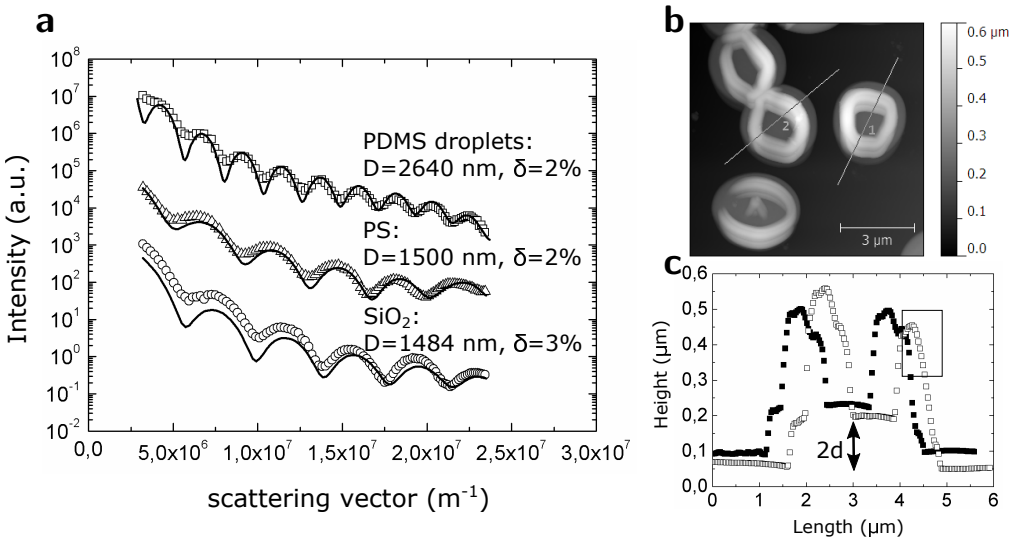


**Figure 9.1: Particle characterization.** (a) SLS experimental data (scatter) fitted by theoretical calculations with full Mie solution of the form factor (lines) for the PDMS droplets that were used to synthesize the buckled bowls and for the polystyrene (PS) and the silica (SiO<sub>2</sub>) spheres. The values for the diameters and polydispersities are obtained from the fit (described in section 5.2.3). (b) AFM image of dried bowl-particles, after removing the PDMS core by washing with ethanol. (c) Height profiles measured by scanning along lines 1 and 2 through the bowls in (b), from which we obtained a shell thickness of  $2d = 140$  nm. Note that the bowl is a collapsed shell, hence the thickness ( $2d$ ) is equal to twice the thickness of the shell before collapse ( $d$ ).

### 9.2.3 Static Light Scattering

The size and polydispersities of the PDMS oil droplets and SiO<sub>2</sub> and polystyrene spheres were determined using a home-built Static Light Scattering (SLS) apparatus with a HeNe laser as light source (632.8 nm, 10 mW). For the measurements, the particle dispersions were diluted in de-mineralized water to reach a typical concentration of 0.1% v/v of the original sample. The angular distribution of intensity of the scattered light was measured at scattering angles in the range 14° to 135° relative to the transmitted beam, with a photomultiplier detector mounted on a goniometer. The experimentally obtained data was plotted against the scattering vector  $k = 4\pi n \sin(\theta/2)/\lambda$ , where  $n$  is the solvent refractive index and  $\lambda$  the wavelength in vacuum. These scattering profiles were compared to theoretical ones calculated with the full Mie solution for the scattering factor, [340]. For this fit, the refractive index of PDMS was set to a value of  $n_D^{25}=1.394$ , corresponding to a low molecular weight silicone oil [341], for water to  $n_D^{20} = 1.333$  [261], for silica to  $n_D^{25}=1.45$  [179] and for polystyrene to  $n_D^{25}=1.58$  [342]. The positions and depths of the interference minima in the scattering curves were fitted by hand to give the size and polydispersity of the particles, respectively. The last minima in the scattering profile were used during this procedure to determine the polydispersity such that the effect of multiple scattering at low angles (the first minima) could be avoided for these micron-sized particles.

### 9.2.4 Atomic Force Microscopy (AFM)

An Atomic Force Microscope (*Digital Instrument, Nanoscope*), operating in tapping mode, was used to monitor the thickness of the microcapsules. First, any remaining PDMS oil was removed from the core of the microcapsules by transferring the shells to ethanol. Typically, about 2 mL of the original aqueous sample (straight from the reaction medium, before concentrating it) was mixed with 2 mL of ethanol after which the sample was centrifuged (2000 rpm, 10 min) and the supernatant was replaced by ethanol, followed by at least one more washing step. Hereafter, an AFM sample was prepared by applying a drop of the ethanol dispersion onto a glass cover slide and allowing the solvent to evaporate. Plateaus in the height profiles were measured and correspond to twice the thickness of the single shell due to a collapse of the particle upon drying. However, as the shells also adopted a buckled geometry in dispersion with effectively touching shell walls, the plateaus in the height profiles can be directly translated to the shell thickness of the buckled object as a whole.

### 9.2.5 Scanning Electron Microscopy (SEM)

Scanning Electron Microscopy (SEM) images were acquired using a *FEI/Philips XL30 FEG* scanning electron microscope, working at an acceleration speed of 3 kV. Samples were prepared by placing a droplet of the particle suspension on a TEM grid (G200-Cu, *Electron Microscopy Sciences*, carbon and butvar coated) and allowing the solvent to evaporate at room temperature. Subsequently, this TEM grid was placed on a SEM stub that contained a conductive, carbon sticker.

### 9.2.6 Zeta potential measurements

Zeta potentials of the particles were determined by laser Doppler micro-electrophoresis using a *Malvern Zetasizer Nano ZS*, operating at 148 V. Each sample was analyzed in triplicate, at a temperature of 20 °C.

| Sample                   | SiO <sub>2</sub> sphere<br>(% v/v) | PS sphere<br>(% v/v) | Bowls<br>(% v/v) | salt (NaCl)<br>(mM) | D <sub>2</sub> O<br>(% v/v) |
|--------------------------|------------------------------------|----------------------|------------------|---------------------|-----------------------------|
| SiO <sub>2</sub> -w4.5-1 | 51                                 | 0                    | 22               | 4.5                 | 0                           |
| SiO <sub>2</sub> -w8.3   | 38                                 | 0                    | 38               | 8.3                 | 0                           |
| SiO <sub>2</sub> -w4.5-2 | 5                                  | 0                    | 81               | 4.5                 | 0                           |
| PS-w4.5                  | 0                                  | 70                   | 16               | 4.5                 | 0                           |
| PS-d3.8                  | 0                                  | 23                   | 9                | 3.8                 | 57                          |

**Table 9.1:** Composition of the various bowl-sphere mixtures in water. The zero frequency dielectric constants ( $\epsilon_r$ ) of the materials used were taken to be 3.8 for SiO<sub>2</sub>, [343], 2.6 for polystyrene [261], 3.5 for the bowl-particles (estimated) and 80 for water [343].

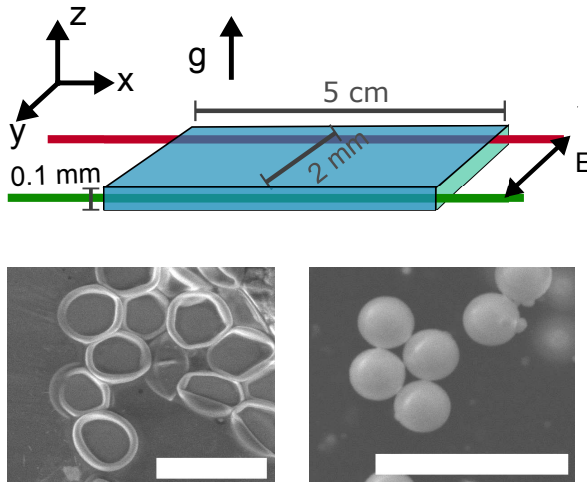


**Figure 9.2:** Schematic drawing of the experimental set-up used to create electric-field induced lock-and-key interactions. The direction of the electric field ( $E$ ), the direction of gravity ( $g$ ) and the three spatial dimensions  $x$ ,  $y$  and  $z$  (chosen along the length ( $x$ ), width ( $y$ ) and depth ( $z$ ) of the capillary) are indicated. Note that we used an alternating electric field with a frequency higher than the relaxation rate of a double layer (1 MHz). Scanning electron micrographs of bowl-like particles (left) and silica spheres (right) are shown in the inset. The scale bars denote 5  $\mu\text{m}$ .

### 9.2.7 Preparation of dispersions and sample cells

Mixtures of spheres (silica or polystyrene) and bowls were prepared both in water and in D<sub>2</sub>O, see Table 9.1. These mixtures were obtained by combining the stock dispersions (section 9.2.2) and adding a small amount of a 33 mM NaCl stock solution and optionally D<sub>2</sub>O. The sample names reflect the sample composition: SiO<sub>2</sub> for silica spheres, PS for polystyrene spheres, 'w' for pure water as a solvent, 'd' for D<sub>2</sub>O added as a solvent, and the number indicates the salt concentration in

mM. Samples were homogenized using a vortex mixer (*IKA minishaker MS2*) at 2500 rpm for a few seconds, after which the sample cells (see below) were filled.

Sample cells for electric field induced self-assembly were constructed from borosilicate glass capillaries (*VitroCom* no.5012, 0.2 × 2 × 50 mm) mounted on a glass cover slide (*Thermo Scientific*) using Scotch tape. Two electrode wires (T2 thermocouple alloy wire, *Goodfellow*, diameter = 0.05 mm) were spanned along the inside (long axis) of the capillaries such that they were spaced 2 mm apart, see Fig. 9.2. Filled capillaries were sealed using either candle wax or UV glue (*Norland Optical Adhesive* no. 68).

### 9.2.8 Confocal microscopy

Electric-field-induced SA of mixtures of bowls and spheres in electric sample cells were imaged using a *Leica SP2* inverted confocal microscope fitted with a *Plan Apo 63x* (NA = 1.4) *Leica* confocal oil immersion objective. Each sample cell was placed on the sample stage with the capillary facing downwards, and the objective placed against the capillary with a drop of Leica type F immersion oil. The excitation laser lines used were 488 nm (blue) for the FITC-labeled silica spheres and the pyromethene dyed polystyrene spheres and 543 nm (green) for the RITC-labeled bowls. These laser lines were selected by acousto-optical filters (AOTFs) from the lines of an ArKr laser and a GreNe laser. The fluorescent signals were collected by photomultiplier tube (PMT) detectors in the ranges 500 nm-535 nm (for the emission signal of FITC and pyromethene dye) and 555 nm-620 nm (for the emission signal of RITC dye) in sequential scanning mode between lines, and at a scanning speed of 800 Hz. The pinhole size was 114.6 μm (Airy disk). Typical images had a resolution of 512 × 512 pixels and a typical pixel size of 40 nm-100 nm.

A *HP 33220A* 15 MHz function/arbitrary waveform generator provided sinusoidal electric fields (1 MHz, with typically a 5V peak-to-peak voltage). A *Krohn-Hite 7602M* wideband amplifier was used for amplification of the signal to 25V - 40V.

### 9.2.9 Viscosity step-gradient centrifugation

After SA in an electric field, the different particle species (bowls, spheres and composite particles) were separated by viscosity step-gradient centrifugation. To this end, capillaries were opened by scraping off the wax, and the bowl/sphere mixtures were recollected from the capillary using a strong air flow.

Viscosity gradients were built as in Ref. 274 from aqueous polyvinylpyrrolidone (PVP,  $M_w = 40,000$ ) solutions of various concentrations: 5.8, 8.8, 11.8, 14.8, 18.7, 22.8, 27.0 % w/w. Centrifuge tubes (*Ultra-Clear Tubes, Beckman-Coulter*, 1.5 mL) were filled with consecutive layers (275 μL) of PVP solution, starting from the highest concentration. The sample to be separated (about 40 μL, originating from 6 electric sample cells) was premixed with 120 μL of 5.8 % w/w PVP solution and placed on top of the step-gradient. The tube was centrifuged for 25 minutes at 82 g (*Hettich Rotina* centrifuge) after which the separate bands were collected by piercing the wall of the tube using a syringe.

## 9.3 Results & Discussion

### 9.3.1 Electric-field-induced lock-and-key interactions

In this chapter we introduce a novel route, based on electric fields rather than depletants, to induce site-specific lock-and-key interactions between colloids. To this end, aqueous mixtures of shape-complementary particles (bowls and spheres) were prepared, with a few millimolars of NaCl. The exact composition of the various samples is given in Table 9.1. The bowl-shaped particles were made by buckling of hollow, elastic microcapsules [338]. Scanning Electron Microscopy images of both particle species are shown in Fig. 9.2. We note that the elastic bowls collapsed upon drying, but have a well-defined bowl-shape as can be inferred from the confocal images. The bowl-shaped particles had a diameter of  $2.6\ \mu\text{m}$  and a shell thickness of  $140\ \text{nm}$ , as determined by Static Light Scattering (SLS) and Atomic Force Microscopy (AFM), respectively (Fig. 9.1). The  $1.48\ \mu\text{m}$  diameter of the silica particles (SLS, Fig. 9.1) was chosen such that these spheres fitted inside the bowl-shaped cavity. A homogeneous, alternating electric field ( $-1\ \text{MHz}$ , typically  $10\text{-}20\ \text{V/mm}$ ) was applied in a sample cell as shown in Fig. 9.2. Due to the high frequency of this alternating electric field, which is much higher than the relaxation rate of a double layer, the dominant polarization contribution stems from the particles rather than from ionic double layers [10]. As reported in literature [292], spheres line up in such a field to form strings since the induced polarizations prefer a head-to-toe arrangement, like dipoles. Bowl-shaped particles attain an orientation with the symmetry axis perpendicular to the field and form strings in which the individual particles face alternating directions [10]. Incidentally, bowls at high volume fractions even started to stack in the direction perpendicular to the field (see Fig. 9.3a).

In mixtures of bowls and silica spheres dispersed in water and exposed to an electric field, strings were found to consist of both species combined. The applied field strength was low enough to allow for some particle displacements, resulting in spheres that were captured by the bowls. The majority of the bowls was typically filled with a sphere after about 30 minutes, as depicted in Fig. 9.3b. This image was taken of sample  $\text{SiO}_2\text{-w}4.5\text{-}1$  (see Table 9.1). The sample name reflects the sample composition:  $\text{SiO}_2$  for silica spheres, PS for polystyrene spheres (used later), 'w' for pure water as a solvent, 'd' for  $\text{D}_2\text{O}$  added as a solvent (used later), and the number indicates the salt concentration in millimolars (mM). Directly after the electric field was switched off completely, the captured silica spheres were released and the individual particles performed Brownian motion again. This directly also highlights the additional advantage of the current study as the lock-and-key interactions are now switchable by external conditions, which for depletion interactions can be realized only when temperature tunable polymers are used. This is in contrast to the conventional method based on depletants, where the interaction can only be tuned by changing the sample composition (i.e. depletant concentration). Typically, when gradually reducing the electric field, filled bowls were initially aligned in strings ( $\sim 20\ \text{V/mm}$ ), the strings of filled bowls then broke up ( $\sim 10\ \text{V/mm}$ ) after which composites disassembled and bowls were no longer aligned ( $\sim 5\ \text{V}$ ). Interestingly, a small fraction of composite particles remained, despite the fact that no salt was added, a point we will come back to later.

Also note that the method can be generalized to other materials, provided that the zero frequency

dielectric constant mismatch between colloids and solvents is sufficiently large for appreciable dipolar interactions to occur. We demonstrated this by using polystyrene spheres (1.5  $\mu\text{m}$  in diameter) instead of silica spheres (see Fig. 9.4). The composition of this sample (PS-w4.5) is given in Table 9.1.

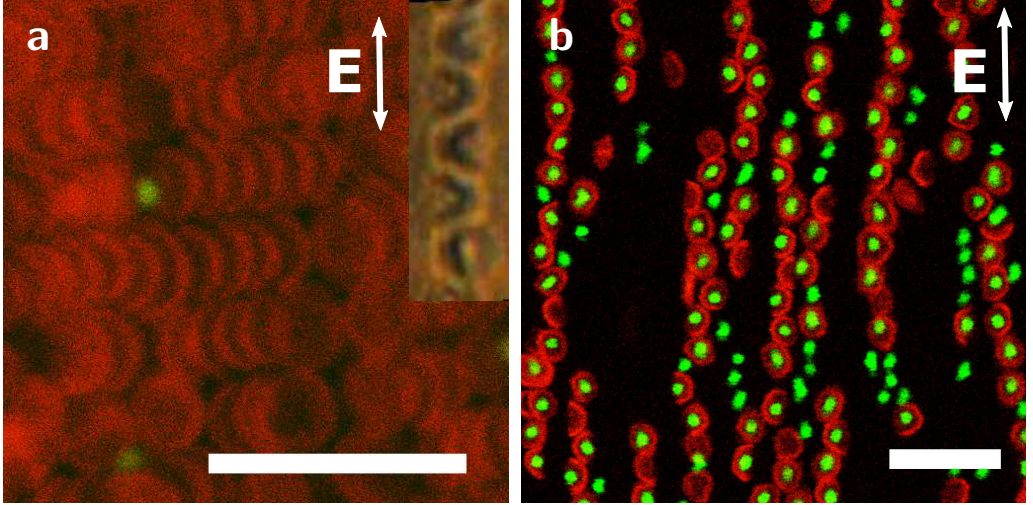


**Figure 9.3: Electric field-induced self-assembly.** (a) Confocal micrograph of a sample region with a high concentration of bowls (RITC dyed, red). Bowls form chains in a direction perpendicular to the electric field (19.1 V/mm, 30 mM NaCl). Note the alternating orientation of the bowls in a string. Inset: optical micrograph of a chain. (b) Confocal micrograph of bowls and spheres self-assembled in an electric field. Bowls (2.6  $\mu\text{m}$  diameter, 140 nm shell thickness, see Fig. 9.1) were dyed with RITC (red) and fluorescent core-shell silica spheres (1.5  $\mu\text{m}$  diameter) were FITC dyed (green). The aqueous sample contained a salt (NaCl) concentration of 4.5 mM and the electric field strength was 12.5 V/mm. The scale bars denote 10  $\mu\text{m}$ .

### 9.3.2 Self-assembly mechanism

To gain more insights into the above described electric-field-induced lock-and-key interactions, the interactions between polarizable colloidal particles subject to an external electric field were investigated through theoretical calculations. Consider an electric field  $\mathbf{E} = |\mathbf{E}|\hat{\mathbf{e}}$ , where  $\hat{\mathbf{e}}$  denotes the direction of the field. We consider the field-induced dipolar interaction between a sphere ( $\epsilon_{\text{sphere}} = 3.5$ ,  $D_{\text{sphere}} = 1.48 \mu\text{m}$ ) and one, three and five aligned bowls. Approximating the induced dipole density inside the particles as homogeneous, the dipolar interaction between two particles  $i$  and  $j$  with volumes  $V_i$  and  $V_j$  is given by

$$U_{ij}^{\text{dip}}(\mathbf{r}_{ij}, \hat{\mathbf{e}}) = \frac{1}{V_i V_j} \int_{V_i} \int_{V_j} d\mathbf{r}_1 d\mathbf{r}_2 \times \quad (9.1)$$

$$u(\mathbf{r}_{ij} + \mathbf{r}_1 - \mathbf{r}_2, \hat{\mathbf{e}}),$$

where  $\mathbf{r}_{ij}$  denotes the distance between the respective centers of the particles, and  $\epsilon_0$  and  $\epsilon_W$  the dielectric constants of vacuum and the solvent, in this case either water or  $\text{D}_2\text{O}$ . The dipole-dipole

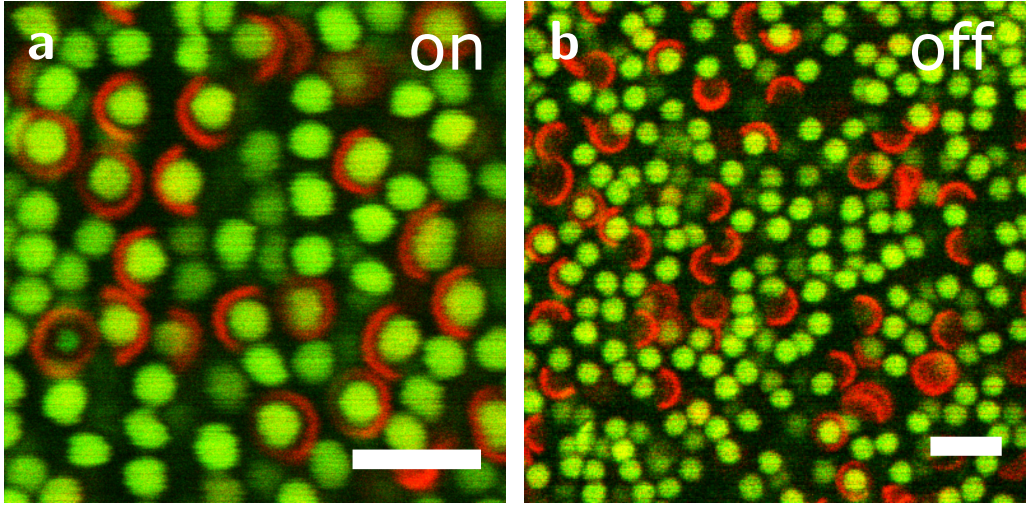


**Figure 9.4: Generalizing electric-field induced lock-and-key interactions to polystyrene spheres.** Confocal micrographs of polystyrene spheres (1.5  $\mu\text{m}$  diameter, pyromethene dyed, green) and bowls (2.6  $\mu\text{m}$  diameter, 140 nm shell thickness, RITC dyed, red) in an electric field of 17.5 V/mm (a), applied for about 1h, after which the field was switched off (b). Salt (NaCl) concentration in the aqueous sample was 4.5 mM.

interaction is given by

$$u(\mathbf{r}, \hat{\mathbf{e}}) = \frac{p_i p_j}{4\pi\epsilon_W\epsilon_0} \frac{1 - 3(\hat{\mathbf{e}} \cdot \mathbf{r}/|\mathbf{r}|)^2}{|\mathbf{r}|^3}. \quad (9.2)$$

Using the Clausius Mossotti equation, we estimate the dipole moments  $p_i$  and  $p_j$  of the point dipoles in both kinds of particles as

$$\mathbf{p}_i = 3\epsilon_W\epsilon_0 V_i \frac{\epsilon_W - \epsilon_i}{\epsilon_W + 2\epsilon_i} \mathbf{E}. \quad (9.3)$$

On the basis of Eq. 9.1 - Eq. 9.3, the field-induced dipolar interaction was estimated of a single sphere and one, three and five aligned bowls as a function of the position of the sphere with respect to the (string of) bowls. The interaction energy landscape is presented in Fig. 9.5a. For one bowl, a location on the outside of the bowl (along the field direction) has the deepest potential well and is therefore favorable for the spheres. For a chain of three or five bowls, a location inside the centrally located bowls becomes preferred. Note that the energy minimum is deepest for centrally located bowls in the chain. This theoretical prediction implies that longer chains are required for successful electric-field-induced SA. To validate this theoretical result, experiments were performed with a partially density-matched dispersion, such that the particles were more homogeneously spread throughout the volume of the sample cell, resulting in shorter chains. To this end, polystyrene spheres were used in combination with the bowls, and were density-matched in the solvent  $\text{D}_2\text{O}$  (sample PS-d3.8, table 9.1). Representative confocal micrographs are shown in Fig. 9.5b-g. Experimentally,

the shortest observed chains consisted of three particles in the backbone. Within this geometry, only one out of the six monitored chains contained a bowl with a captured sphere. This is in strong contrast to significantly larger chains, consisting of at least seven particles in the backbone. Here, the 5 studied chains all contained at least one composite particle. This scenario was also confirmed while recording a time series. During the experimentally considered time-scale, a backbone of three particles was stable in the sense that it was not observed to collapse into a backbone of two particles with one particle filled. However, a sphere was captured by an approaching bowl that was part of a backbone consisting of initially four particles. Despite the limited statistics of these observations, these experimental findings are consistent with the theoretical calculations on the field-induced interactions, which indicated that the self-assembly process requires sufficiently long chains to induce lock-and-key interactions (i.e. at least three-four particles in the backbone) for the cases studied here.

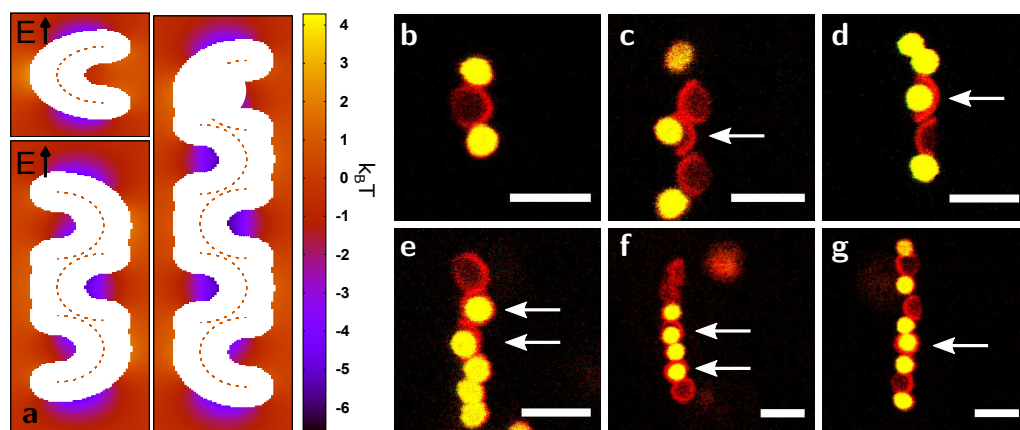


**Figure 9.5: Chain length dependence of the potential energy minimum, affecting the chain configuration.** (a) Theoretical result for the interaction potential created between short chains of bowls and a sphere in an electric field (20 V/mm). The color look-up table indicating the potential in  $k_B T$  is located to the right. It is apparent that already very short chains consisting of only three particles create a deep minimum inside the central bowl. (b-g) Confocal micrographs of strings of increasing chain length, composed of bowls and spheres. The backbone consisted of 3 (b), 4 (c), 5 (d), 6 (e), 7 (f) and 9 (g) particles, and filled bowls are indicated by the arrows. Bowls (2.6  $\mu\text{m}$  diameter, 140 nm shell thickness) were dyed with RITC (red) and polystyrene spheres (1.5  $\mu\text{m}$  diameter) were dyed with pyromethene throughout (yellow). The sample was prepared in (57% v/v)  $\text{D}_2\text{O}$  with a salt (NaCl) concentration of 3.8 mM. The electric field strength was 15 V/mm. The scale bars denote 5  $\mu\text{m}$ .

### 9.3.3 Irreversibly bound composite particles

Although the induced dipolar interactions described by Eqs. 9.1-9.3 describe the capturing probability of spheres in terms of the energy landscape of Fig. 9.5a on the micrometer length scale, it cannot account for the irreversible binding between bowls and spheres that is also observed. The theoretical analysis was therefore extended to also account for van der Waals attractions due to the

dielectric constant mismatch between particles and solvent, and for screened-Coulomb repulsions that originate from the electrostatic repulsion between the like-charged particle surfaces and double layer overlap. Here, the experimental zeta potentials were used to match the charge density on the surface to that of a particle near a planar surface. While the dipolar interaction plays a dominating role for distances between the particles larger than  $\sim 10$  nanometers, once the surfaces of two particles approach each other closely (in the range of several nanometers) they are quickly outgrown by van der Waals attractions and Coulomb repulsions of the surface charges.

In Fig. 9.6a we show the van der Waals and Coulombic potential separately as well as combined, as a function of the surface-to-surface distance ( $\Delta x$ ) of a bowl and a sphere on the symmetry axis of the bowl, for  $\rho_S = 30$  mM, revealing a picture that is consistent with well-known DLVO theory: a deep primary minimum at  $\Delta x \leq 1$  nm and a much more shallow secondary minimum at  $\Delta x \approx 10$  nm, separated by a barrier of  $400 kT$ . For these parameters, one does not expect irreversible binding since the barrier would prevent any approach below the 1 nm distance. In Fig. 9.6b the sum of van der Waals and screened Coulomb interactions is plotted in the same regime, but now for a variety of salt concentrations. The barrier increases with lowering  $\rho_S$ , as expected, and decreases at higher  $\rho_S$  to essentially vanish at  $\rho_S = 100$  mM. We could thus expect irreversible binding in the primary minimum at high enough salt concentrations.

It was experimentally found that in the case of a surplus of bowls, a small fraction of composite particles remained irreversibly bound after switching off the electric field (Fig. 9.6c-d, taken of sample SiO<sub>2</sub>-w4.5-2). This fraction did not significantly increase upon addition of salt (NaCl, maximum concentration investigated 30 mM). In the case of a surplus of spheres, however, adding salt was found to shift the SA from reversible to irreversible binding. In absence of salt, the majority of the composite particles was reversibly bound, similar to the behavior for an excess of bowls. However, at a salt concentration of 4.5 mM (sample SiO<sub>2</sub>-w4.5-1) or 8.3 mM (sample SiO<sub>2</sub>-w8.3) (Fig. 9.6e-f), most composite particles were irreversibly bound. Unfortunately, the strong dependency on the salt concentration with respect to the mixing ratio of bowls and spheres could not be clarified from theory, perhaps because many body interactions were not taken into account. An alternative, and simpler, explanation could be that the sphere dispersion itself already contained some (more) salt, lowering the threshold concentration required for irreversible binding. However, the ability to tune the reversible and irreversible behavior directly points to an important additional feature of our methodology: one can now also use this new self-assembly method for synthesis of colloids of complex shapes and mixed composition.

### 9.3.4 Isolating composite particles

The irreversible binding of spheres inside bowls allowed us to harvest the composite particles from the mixture of spheres, bowls and composite colloids in sample SiO<sub>2</sub>-w8.3 (see Table 9.1). The composite colloids were initially formed in 1h in an electric field of 20 V/mm (see Fig. 9.6f). A viscosity step-gradient [274] was used to separate the three types of particle species over three distinct bands (Fig. 9.7a). After recollecting the bands, confocal microscopy confirmed that each band contained a different type of particle. The top band contained only bowls, followed by the

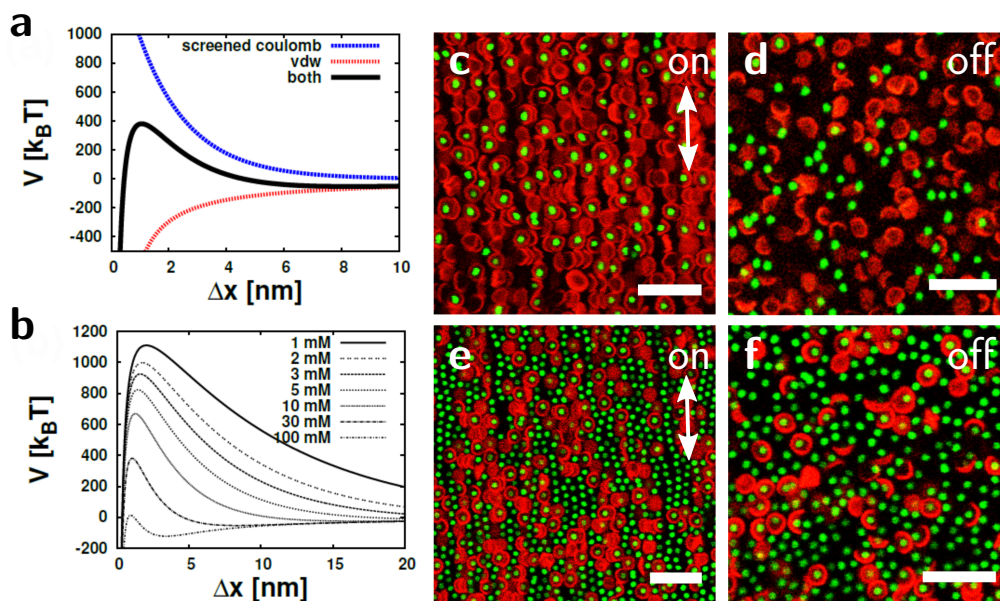


**Figure 9.6: Van der Waals attractions allow for the creation of irreversible 'sphere-in-bowl' composite particles.** (a-b) Theoretical calculations of the potential between a bowl and a sphere that is moving into the bowl along the bowl's symmetry axis (i.e. is being captured). Panel (a) displays the screened-Coulomb repulsion and van der Waals attraction between the bowl and the sphere as a function of the surface-to-surface distance  $\Delta x$ . A deep potential well exists near  $\Delta x = 0$ , so a sphere which overcomes the potential barrier will be irreversibly bound to the shell. Panel (b) displays the total potential for various salt concentrations. Salt can help to reduce the energy barrier. Experimentally we observed irreversible binding for salt concentrations as low as 5 mM. (c-d) Reversible lock-and-key interactions between bowls and spheres were observed when the number of bowls exceeded the number of spheres. The aqueous sample contained a salt (NaCl) concentration of 4.5 mM and the electric field (12.5 V/mm) was applied for a period of ~5.5h (c) after which it was switched off (d). (e-f) Irreversibly bound composite particles of spheres in bowls were observed when the number of spheres exceeded the number of bowls. The salt (NaCl) concentration in the aqueous medium was 8.2 mM. The electric field (20 V/mm) was applied for 1h (e) after which it was switched off (f). Bowls (2.6  $\mu\text{m}$  diameter, 140 nm shell thickness) were dyed with RITC (red) and fluorescent core-shell silica spheres (1.5  $\mu\text{m}$  diameter) were FITC dyed (green). The scale bars denote  $10 \mu\text{m}$ .

middle band that contained the composite particles and the lower band contained single spheres (Fig. 9.7b-f). This separation was performed about an hour after self-assembly, further proving the long-term stability of the composite particles.

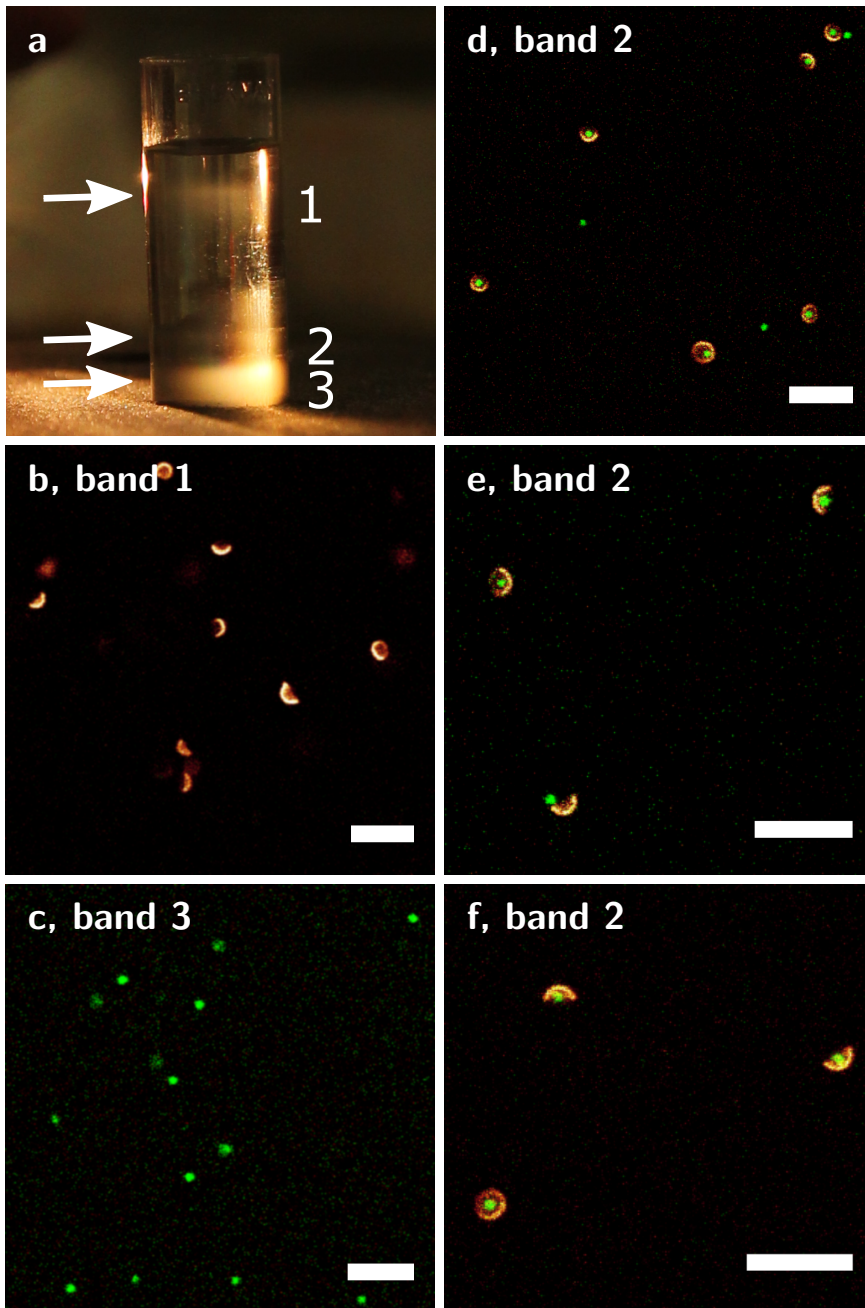


**Figure 9.7: Collecting composite particles using a step-wise viscosity gradient combined with centrifugation.** (a) Separation of bowls (band 1), composite particles (band 2) and spheres (band 3) in a PVP viscosity step-gradient. (b-f) Confocal micrographs of the bowls in band 1 (b), spheres in band 3 (c) and composite particles in band 2 (d-f). Bowls (2.6  $\mu\text{m}$  diameter, 140 nm shell thickness) were dyed with RITC (red) and silica spheres (1.5  $\mu\text{m}$  diameter) were FITC dyed (green). The scale bars denote 10  $\mu\text{m}$ .

## 9.4 Summary & Outlook

In summary, we have shown that external electric fields can be used in a novel route to induce lock-and-key interactions between a binary system of convex and concave particles. The additional advantage, with respect to depletion interactions, is that these interactions are reversible and can be controlled on millisecond timescales. In this way, we have prepared reversibly bound composite particles consisting of shape-complementary bowls and spheres. These experiments can be extended to many different materials, and as a proof of principle we already used both silica and polystyrene spheres. Through calculations of the relevant inter-particle interactions (using the materials parameters studied in this paper, i.e. dielectric constants  $\epsilon_{water} = 80$ ,  $\epsilon_{sphere} = \epsilon_{bowl} = 3.5$ , and diameters  $D_{sphere} = 1.48 \mu\text{m}$ ,  $D_{bowl,inner} = 2.60 \mu\text{m}$ ,  $D_{bowl,outer} = 2.88 \mu\text{m}$ ), we have shown that in an electric field, a potential minimum exists for the spheres inside the bowls, provided the backbone of the chain of colloids contains at least three particles. The force balance of the bowls and spheres was also tuned (by adding salt and by varying the ratio of the number of convex and concave particles), such that the majority of composite particles remained irreversibly bound even after the field was turned off. These composite particles could be purified from the single components by simply using a viscosity step-gradient combined with centrifugation. Although the scale of the current experiment was small, there are no fundamental obstacles to scaling it up. We thereby have shown that this mechanism does not only provide a new route for self-assembly, but also for synthesis of complex-shaped colloids.

Our method can be further extended and generalized in the sense that one does not need to rely on van der Waals attractions. This could be achieved by coating one of the two components of our convex and concave particles with two different layers of polyelectrolytes: the first layer of opposite charge, the second layer of the same charge as the charge of the other component. Bringing the particles together with electric fields will now also expose the lower layer of oppositely charged polyelectrolyte to the other component. The particles are then bound by electrostatic interactions instead of van der Waals interactions. This method, already used in Ref. 292, will therefore make our attachment strategy more easily controllable. Finally we would like to stress that this SA method can also be extended to particles with flat facets (hence flat-flat combinations). Although the concave-convex combination in this study is probably most efficient, making a spherical shape flat [273] will still reduce the electric field strength required for SA when compared to sphere-sphere or sphere-flat combinations of particles.

## Acknowledgements

All experimental work described in this chapter was carried out jointly with Nina Elbers (equal contributions), and she is gratefully acknowledged for this fruitful and pleasurable collaboration. We sincerely thank Thomas Troppenz for his hard work on all theory in this chapter. Esther Vermolen and Bo Peng are acknowledged for providing the silica spheres and polystyrene spheres, respectively.





# Summary

Colloids are particles with a size on the scale of microns in at least one dimension (but which are built up by molecules and atoms, which in turn are built up of fundamental particles such as electrons and protons). Colloids undergo Brownian motion when dispersed in a medium, and this allows the colloids to explore the energy landscape of the system and find a potential minimum in it, which can even lead to the formation of ordered structures. This 'spontaneous' ordering is called *self-assembly* (SA). Spherical colloids of sufficient monodispersity sedimenting in gravity will assemble into close-packed lattices called hexagonal close-packing (HCP) and face-centered cubic (FCC) packing. Since the latter two crystal structures have nearly equal free energies [344, 345], in practice spherical particles often assemble in a random combination of FCC and HCP, a structure called random hexagonal close-packing (RHCP). FCC and HCP lattices and other structures with full rotational and positional order are known as 'crystals' in the field of soft matter physics. *Anisotropic* colloids such as rods, cubes and polyhedral particles can also form 'liquid crystals' (e.g. nematic, smectic or cholesteric phases), that is, crystal structures which do not possess full positional and/or full rotational order.

The central theme of this thesis is the synthesis of model colloids with anisotropic interactions - often called 'patchy' colloids, a subclass of 'complex colloids' - as well as the search for pathways to let such patchy colloids self-assemble. Patchy particles can be used to obtain new structures through self-assembly. Methods to build non-close-packed structures from isotropic colloids do exist (e.g. using binary crystals), and also anisotropic colloids can give rise to interesting crystal structures. An advantage of patchy colloids is that additional features such as a varying surface charge or hydrophobicity throughout the system can be introduced.

In Chapters 2 and 3, we investigate properties of silica grafted with linear alkane chains, since this material is used in later chapters to prepare patchy colloids. **Chapter 2** focusses on the surface-freezing transition observed in silica surfaces grafted with  $C_{18}$  chains with temperature decrease and the resulting gelation transition that n-octadecyl-alkane-grafted colloids undergo in certain solvents. We confirmed experimentally that a gelation transition exists not only for octadecanol-grafted colloids but also for colloids grafted with octadecyltrimethoxysilane (OTMOS). We also study the freezing transition by exploiting the concomitant change in contact angle of an alkane solvent and an n-octadecyl-alkane-grafted surface. The capillary rise of an alkane in a surface-grafted capillary changes abruptly around the freezing transition temperature. This study yields more accurate insight into the freezing transition temperature than studies of the gelation of colloids by microscopic or light scattering techniques, since the latter can have time, size and volume fraction dependencies. We

---

find that, on OTMOS-grafted borosilicate capillaries, the onset of the freezing transition increases from 20°C to 30°C as the alkane solvent chain length increases from 14 to 18 carbon atoms. This provides an opportunity for future research to create patchy particles with different surface freezing temperatures on the patches and on the rest of the surface. To the contrary, for hexadecane ( $C_{16}H_{34}$ ) as a solvent, the freezing transition occurred at a higher temperature for  $C_{18}$ -grafted capillaries than for  $C_{16}$ -grafted or  $C_{20}$ -grafted surfaces, indicating an 'ideal' chain length mismatch between grafting agent and solvent.

In **Chapter 3** we studied the properties of n-octadecyl-alkane-grafted silica surfaces in the low-polar solvent cyclohexyl chloride (CHC). By thermogravimetric analysis (TGA), we found that OTMOS-grafted silica particles had a slightly higher packing density of  $C_{18}$  chains at the surface than octadecanol-grafted silica particles. This finding is in line with the notion that OTMOS molecules could form branched networks at the surface and hence have a higher packing density (although not necessarily a higher surface-grafting density). The surface charges of OTMOS-grafted and octadecanol-grafted silica particles in CHC were examined in two ways. Firstly, 2D radial distribution functions were measured by confining particles electrostatically between two surface-grafted coverslips. Yukawa potentials were fitted to the pair potentials obtained from these RDFs, and the fitted contact potentials corresponded to charges of  $109e$  and  $630e$  respectively. In addition, the RDFs were compared to simulated RDFs of Yukawa disks with the fitted contact potential and Debye length. The RDFs obtained by simulations agreed well with the experimental RDFs, indicating that no anomalous attractions were present in the system. Secondly, capillary micro-electrophoresis was used to directly measure the electrophoretic mobility (which can be converted to particle charges using the theory of Carrique and coworkers [177]). For octadecanol-grafted silica particles a charge of  $600e$  was found by capillary micro-electrophoresis. For OTMOS-grafted particles, the theory of Carrique and coworkers did not have a solution for the experimentally found mobility and suitable values of  $\kappa R$ , presumably since the mobility is high,  $-6000 \mu\text{m}^2\text{V/s}$  compared to  $-3000 \mu\text{m}^2\text{V/s}$  for octadecanol-grafted silica. All in all, a higher charge was found for OTMOS-grafted particles in CHC compared to octadecanol-grafted particles in CHC with both techniques, RDF fitting and electrophoresis. Most likely, the non-condensed silanol groups on the branched OTMOS molecules (versus the monofunctional octadecanol molecules) causes this higher charge of OTMOS-grafted particles compared to octadecanol-grafted particles.

In Chapters 4 and 5, we present a colloidal 'patchy' model system of silica particles with titania protrusions. The focus of **Chapter 4** is on the synthesis of this model system. The particles are prepared by surface-grafting a dried colloidal crystal of silica particles. After redispersion of the particles by sonication, the colloids have a 'patterned' surface. We grew hemispherical titania protrusions onto these patterned colloids by adding titania precursor to the dispersion. The amorphous mesoporous protrusions were successfully infiltrated with an RITC-APTES (dye-silane) conjugate, which covalently links a fluorescent dye to the titania surface but not to the OTMOS-grafted silica surface. In this way, the particles became suitable for confocal microscopy, where the core particle and the protrusions were made distinguishable by having different dyes incorporated. The titania protrusions were also annealed at temperatures up to 1100°C, and were found to remain intact if (and only if)

---

previously infiltrated with APTES. For sintering temperatures between 500°C and 900°C (for 2-5 h sintering time) the resulting crystalline titania protrusions were identified as the titania polymorph anatase by means of selected area electron diffraction (SAED). Protrusions sintered at 1100°C for 2 h became monocrystalline and faceted.

In **Chapter 5**, we analyzed confocal microscopy to obtain distributions of the number of protrusions per patchy particle for the particles in Ch. 4. In the ideal case, each particle has twelve protrusions, since the colloids were surface-grafted while packed in an RHCP colloidal crystal during synthesis. However, in practice the average number of protrusions per particle was below twelve. This effect is caused not only by defects in the crystal, but more importantly by the fact that a patch is formed solely when two particles' surfaces are in closer proximity than roughly the size of the grafting agent. Kinetic factors also play a role; the probability that a grafting molecule diffuses into a crevice becomes smaller with the crevice's dimensions. The patch number distributions obtained by tracking 3D images of the particles obtained by confocal tomography were in agreement with the simulations for a bond length of  $1.1\sigma_{core}$ - $1.21.1\sigma_{core}$ , which is a reasonable choice since the centers of the protrusions reside at  $1\sigma_{core}$ . The experimental results were compared to simulations of the number of patches per particle expected for a given size polydispersity (p.d.) of the particles' cores and maximum separation  $d$  between the surfaces (representing the grafting agent size and kinetic factors). The median number of patches per particle decreased with size polydispersity of the core particles (for polydispersities up to 5%) and with decreasing  $d$ . The median number of patches per particle (for  $d = 0.001\sigma$ ) diminished from the ideal twelve to six patches per particle already for a p.d. of 1%. We predict that in order to prepare patchy colloids with twelve protrusions per particle, it is necessary to use core particles of p.d. 0.5% or lower. The experimental patch number distributions were in qualitative agreement with the calculated distributions. The variation in number of patches per particle implies that it is difficult to form crystalline structures with these patchy particles. However, patchy silica particles with titania protrusions formed open gel networks in low-polar media CHC and DCE. Based on zeta potential measurements of OTMOS-silica particles and dyed titania particles, as well as confocal images of mixtures of the same constituents, we also concluded that the gels in DCE are most likely formed through attractive (solvophobic and/or van der Waals) patch-patch interactions.

In **Chapters 6** and 7, we introduced a new system of lollipop-shaped hetero-dimer particles with a silica stem and a sphere of 3-methacryloxypropyltrimethoxysilane (MPS), and demonstrated their self-assembly in an electric field. To synthesize these lollipop-shaped particles, we first prepared nail-shaped silica particles based on a recipe for silica rods in combination with regulation of the growth temperature. Then, MPS was nucleated and grown onto the back of these nail-shaped particles. The MPS was dyed for confocal microscopy by allowing it to absorb (rhodamine isothiocyanate)-aminostyrene (RAS) in acetone. The MPS protrusion was subsequently cross-linked through the methacrylate groups by introducing an initiator, making the particles resistant to solvent exchange and drying. MPS nucleation and growth on bullet-shaped particles was only successful for bullets of a width comparable to the nail heads of the nail-shaped particles. We conjecture that the nail shape stimulates nucleation of MPS at the flat end of the silica particle, but the influence of absolute

width and aspect ratio should be further investigated via experimental and theoretical or numerical studies. A similar synthesis route with spherical silica particles as templates yielded acorn-shaped and dumbbell-shaped hetero-dimer particles. Only acorn-shaped hetero-dimers were successfully polymerized, most likely since there is no covalent binding of the MPS to the silica core in this synthesis routine, hence the MPS must sufficiently envelope the silica core particle for the hetero-dimer not to break up under the internal stresses during polymerization, which is not the case for dumbbell-shaped hetero-dimers. We showed that acorn-shaped particles can form crystals with long-range repulsions in the low-polar solvent CHC (after an OTMOS-grafting step which covers the MPS side and replenishes the silica side with  $C_{18}$  chains). These lollipop-shaped hetero-dimers are interesting for future research, since various functional groups can be incorporated into the protrusion.

In **Chapter 7**, we showed that the nail-shaped silica/MPS hetero-dimers presented in Ch. 6 - that when subjected to an electric field - aligned with the silica sides towards the same electrode and towards the direction of electrophoresis (which we called 'vectorial alignment'). Vectorial alignment of the constituents of a crystal is also possible: preliminary experiments for hexagonally ordered acorn-shaped particles with long-range repulsions in CHC were successful in this regard.

In **Chapter 8**, we investigated an interaction which is often used in self-assembly of patchy (and non-patchy) colloids, namely depletion interaction. Rather than using patchy or hetero-dimer particles, we focussed on spherical particles with a surface roughness comprised of small silica particles. Previous MC simulations of pair potentials and overlap volumes between two rough particles had shown that the best reduction of the attractive depletion potential is reached when the surface roughness layer is incomplete, as is the case for our experimental system. The simulations had also shown that a polymer concentration regime exists for which the smooth particles have a potential minimum of several  $k_B T$  but for which two rough particles (or a rough and a smooth particle) do not have an appreciable potential minimum. We were thus interested in whether it is possible to selectively immobilize rough particles in a mixture of rough and smooth particles of the same effective size. Rough particles were prepared by applying a positively charged PAH layer on the core particles and by electrostatically linking small (negatively charged) silica particles to the core particle for roughness. The particles were dispersed in CHC with polystyrene (PS) as a depletant. We demonstrated experimentally that the depletion interaction between a rough particle and a wall is reduced compared to the depletion attraction between a smooth particle (of the same size) and a wall in the following way: we filled a capillary with particles and polymer depletant, allowed the particle to sediment towards one wall, and counted (the ratio of) the number of particles sticking to the top wall after turning it upside down. These experiments provided approximate limits (taking into account that the capillary wall is a flat surface) for the polymer concentration needed to induce selective clustering. We then demonstrated experimentally that in a mixture of rough and smooth particles of equal size, it is possible to selectively cluster the rough particles via depletion attractions.

In **Chapter 9**, we have shown that external electric fields can be used as a novel route to induce lock-and-key interactions between shape-complementary bowls and spheres. In this way, reversibly bound composite particles of bowls and (silica or polystyrene) spheres were prepared. Calculations of the relevant inter-particle interactions - using the materials parameters studied experimentally -

---

showed that for the spheres a potential minimum exists inside the bowls in an electric field, provided the backbone of the chain in which the bowl resides is three particles or longer. The potential energy well was deepest for bowls located at the center of the chain. The force balance of the bowls and spheres was also experimentally tuned (by adding salt and by varying the ratio of the number of bowls and spheres), such that the majority of composite particles remained irreversibly bound even after the field was turned off. These composite particles were purified from the single components by simply using viscosity step-gradient centrifugation. The latter points at an important additional advantage of this self-assembly method: the possibility to create novel complex colloids.



# Samenvatting voor een breed publiek

Het onderzoek beschreven in dit proefschrift behoort tot het natuurkundige gebied *zachte materie*. Dit gebied behandelt materie die makkelijk verstoord of vervormd wordt door temperatuurfluctuaties. Het gaat bijvoorbeeld om vloeistoffen, emulsies, suspensies, dispersies, gelen en schuimen. Hoewel het woord *zachte materie* niet zo bekend is buiten de natuurkunde, gaat het dus over zaken die we veel tegenkomen in het dagelijks leven, bijvoorbeeld in de vorm van verf, tandpasta, melk, bloed, shampoo, scheerschuim, enzovoorts.

De hoofdrolspelers in dit proefschrift zijn colloïden. Colloïden zijn deeltjes die afmetingen hebben van enkele nanometers tot enkele micrometers in ten minste één van de drie ruimtelijke dimensies (een nanometer is een miljardste van een meter en een micrometer is een miljoenste van meter). Het zijn dus geen fundamentele deeltjes (zoals elektronen, protonen, muonen, etcetera), want ze zijn zelf opgebouwd uit moleculen en atomen, die op hun beurt weer uit fundamentele deeltjes bestaan. Colloïden hebben ruwweg een grootte van een honderdste maal de breedte van een menselijke haar. De deeltjes zijn door die afmetingen ook waarneembaar met microscopische technieken. Vaak gaat het daarbij om optische technieken zoals een 'gewone' microscoop of een confocale laser fluorescentiemicroscoop, maar men gebruikt ook elektronenmicroscopen (zie Fig. 9.8). Het woord 'colloïde' is afkomstig van het Griekse woord  $\kappa\omicron\lambda\lambda\alpha$ , dat door de vroege colloïden-onderzoeker Thomas Graham werd gebruikt, omdat hij meende dat de capaciteit om door een membraan heen te gaan met de lijm-achtige aard van zijn testmaterialen van doen had.

Colloïden kunnen bestaan uit allerlei materialen, bijvoorbeeld glas (silica), goud, latex (poly methylmethacrylaat) of 'piepschuim' (polystyreen). Colloïden hebben de interessante eigenschap dat, wanneer ze in een medium worden gedispergeerd, de moleculen van het medium in staat zijn de deeltjes door middel van bostingen heen en weer te bewegen; dit heet Brownse beweging. Onder invloed van die bewegingen kunnen colloïden soms ordenen in 'kristallen'; zo heten systemen die opgebouwd zijn uit een repeterende eenheid. Zulk collectief gedrag wordt zelforganisatie genoemd, en is voordelig omdat de deeltjes dan meer rotatie- en/of translatie vrijheid hebben (hogere entropie). Anisotrope (dat wil zeggen: niet-sferische) colloïden kunnen naast kristallen ook 'vloeibare kristallen'

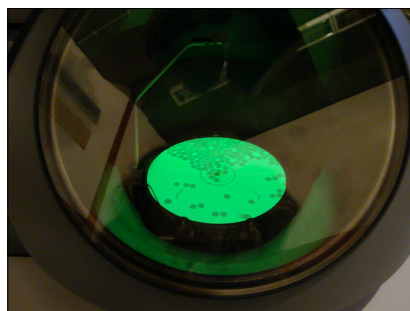


**Figure 9.8:** Bolvormige silica colloïden zichtbaar gemaakt met een elektronenmicroscoop.

vormen; dit zijn geordende systemen met een positionele en rotationele ordening in een of meer dimensies (maar geen volledige kristallijne ordening). Deeltjes groter dan enkele micrometers vallen in de categorie "granulaire materie", en er zijn weer andere theorieën en technieken nodig om hun collectieve gedrag te beschrijven.

Het centrale thema van dit proefschrift is om colloïden te maken met niet-uniforme oppervlakte eigenschappen, alsmede om wegen te zoeken om deze deeltjes op nieuwe manieren te zelf-assembleren. Dergelijke colloïden staan bekend als 'patchy' colloïden, en hebben als voordeel ten opzichte van uniforme en anisotrope colloïden dat er ook interessante verschillen in oppervlakte-eigenschappen in de systemen aangebracht kunnen worden, bijvoorbeeld verschillen in hydrophobiciteit, in lading en in dielektrische of magnetische eigenschappen.

In Hoofdstukken 2 en 3 onderzoeken we eigenschappen van silica-oppervlakken die bewerkt zijn met alkaanstaarten (moleculen met 18 koolstofatomen). Dit type oppervlak wordt namelijk verderop in het proefschrift gebruikt voor het maken van patchy colloïden. In **Hoofdstuk 2** richten we onze aandacht op het uit de literatuur bekende fenomeen 'oppervlaktebevrozing'. Meer in het bijzonder bedoelen we hier dat silica-oppervlakken behandeld met octadecanol ( $C_{18}$  alcohol) een transitie in oppervlaktespanning ondergaan voor het medium hexadecaan wanneer de temperatuur van het systeem beneden een bepaalde overgangstemperatuur wordt gebracht. Dit is een gevolg van het feit dat hexadecaan-moleculen de beharingslaag kunnen infiltreren en opvullen tot een kristallijne laag is gevormd. Het is tevens bekend dat silica-colloïden met zo'n beharing in hexadecaan een gelatie-overgang hebben: ze vormen een gel beneden een bepaalde temperatuur en een dispersie bij die overgangstemperatuur [105, 106]. In het hoofdstuk tonen we aan dat niet alleen octadecyl alcohol gemodificeerde silica colloïden in hexadecaan zo'n overgang vertonen, maar ook octadecyltrimethoxysilane (OTMOS) behaarde silica colloïden. Daarenboven bestuderen we de verandering in oppervlaktespanning als functie van de temperatuur op de volgende manier. Silica capillairen (buisjes met een binnendiameter van 0.2 mm) worden behandeld met alkaanstaarten en recht op in een alkaan-medium geplaatst; de stijghoogte hangt af van de oppervlaktespanning/contacthoek van het medium met het oppervlak bij een bepaalde temperatuur. Rond de overgangstemperatuur neemt men dus een snelle stijging van het medium in de capillairen waar. Het voordeel van een dergelijke meetmethode t.o.v. het bestuderen van deeltjesdispersies en -gelen is dat de mogelijke invloeden van deeltjesgrootte, volumefractie, en gel-veroudering worden geëlimineerd. We vonden dat bij OTMOS-behaarde capillairen en hexadecaan als medium, de bevrozingsovergang een geleidelijke overgang is over een tiental graden. Ook neemt de starttemperatuur van de overgang (in de richting van het smelten van de oppervlaktelaag) toe van  $20^{\circ}\text{C}$  naar  $30^{\circ}\text{C}$  voor een alkaanmedium van 14 tot 18 koolstofatomen (tetradecane tot octadecane). Omgekeerd werd ook het silica-oppervlak met verschillende lengtes van de alkaanstaarten (16, 18 en 20 koolstofatomen) behandeld. Voor een hexadecaan medium, was de overgangstemperatuur het hoogst bij de  $C_{18}$  behaarde capillairen, wat doet vermoeden dat er een 'optimaal' verschil in koolstofketenlengte tussen de beharing en het medium bestaat, waarbij de overgangstemperatuur het hoogst is (d.w.z. waarbij oppervlaktebevrozing het eenvoudigst optreedt). Wij denken dat er een temperatuur-'venster' bestaat waardoor het mogelijk is om patchy colloïden met alkaanstaarten van verschillende lengte te beharen, zodanig dat de deeltjes

---

aan elkaar plakken op de patches (via deze overgang) terwijl de rest van het deeltjes nog sterisch gestabiliseerd is in de hexadecaan. Daartoe moet eerst de vorming van grote aggregaten van deeltjes in de hexadecaan worden voorkomen.

In **Hoofdstuk 3** bestudeerden we de eigenschappen van octadecanol- en OTMOS-gefunctionaliseerde silica deeltjes, met name in het laag-polaire medium (d.w.z. een medium dat niet veel ionen kan bevatten) cyclohexyl chloride (CHC). Door middel van thermogravimetrische analyse (TGA) vonden we dan OTMOS-gefunctionaliseerde deeltjes een iets hogere pakingsgraad van alkaanstaarten heeft, wat het gevolg moet zijn van het feit dat OTMOS drie functionele groepen heeft: de OTMOS-moleculen kunnen netwerken vormen op het oppervlak. De lading van de deeltjes in CHC werd op twee manieren bepaald. Ten eerste door de bewegingen van de deeltjes over lange tijd te volgen. Daaruit werd de gemiddelde kans berekend om op een bepaalde afstand van een willekeurig deeltje een ander deeltje te vinden; deze kansverdeling heet een paarcorrelatiefunctie. Uit deze kansverdelingen kan een experimentele interactiepotentiaal worden gevonden. Vervolgens werd een theoretische potentiaal (Yukawa potentiaal) aan deze experimentele functie gefit, en werden hieruit waarden voor de deeltjeslading berekend. Ten tweede werd de bewegingssnelheid van de deeltjes in een elektrisch veld gemeten; dit heet micro-elektroforese. Hoewel de ladingen berekend met beide technieken verschillen doordat de theorie erachter verschilt (Yukawa potentialen gaan uit van de gelineariseerde versie van de Poisson-Boltzmann vergelijking), werd steeds een veel hogere lading voor de OTMOS-gefunctionaliseerde deeltjes dan voor de octadecanol-gefunctionaliseerde deeltjes gevonden. Dit is waarschijnlijk het gevolg van het feit dat OTMOS-moleculen drie functionele groepen hebben; de niet-gecondenseerde groepen kunnen lading dragen.

In hoofdstukken 4 en 5 presenteren we 'patchy' colloïden bestaande uit een sferische silica kern met half-sferische titania uitstulpingen. In **Hoofdstuk 4** wordt de synthese van deze deeltjes besproken. De colloïden worden gemaakt door sferische silica-deeltjes te laten kristalliseren, daarna het kristal als geheel te met moleculen te bewerken, en vervolgens het kristal weer kapot te maken zodat er weer individuele deeltjes ontstaan. Deze individuele deeltjes hebben dan een patroon van onbewerkte cirkels op hun oppervlak, want de plaatsen waar de deeltjes elkaar (bijna) raakten in het kristal bleven onbewerkt. Op de onbewerkte plekken groeiden we vervolgens titania. Dit titania is interessant, omdat we het konden infiltreren met een fluorescente stof (gekoppeld aan een molecuul dat deze 'verf' aan het oppervlak bint). Zodoende konden de uitstulpingen ook zichtbaar worden gemaakt in een confocale microscoop. De titania uitstulpingen konden middels een hitte-behandeling naar een (op atomair niveau) kristallijne toestand worden gebracht. De infiltratie met het koppel-molecuul was hierbij cruciaal om de vorm van de uitstulpingen te behouden. In **Hoofdstuk 5** bekeken we of het aantal uitstulpingen op de patchy colloïden ook voldeed aan het verwachte aantal. Idealiter zouden deze deeltjes twaalf uitstulpingen hebben, gezien hun omgeving in het kristal tijdens de deeltjessynthese. Echter, in de praktijk is het aantal uitstulpingen veel minder, wat veroorzaakt wordt door de polydispersiteit (variatie in deeltjesgrootte) van de silicadeeltjes. Wanneer twee colloïden in het kristal elkaar niet raken, kan het functionalisatiemolecuul ertussen kruipen tijdens de synthese. Door middel van simulaties bepaalden we het aantal verwachte 'patches', gegeven een bepaalde polydispersiteit van de deeltjes en een vastgestelde maximale afstand  $d$  tussen de deeltjesoppervlakken. Het gemiddelde

aantal patches nam natuurlijk af voor hogere polydispersiteit en kleinere  $d$ . Experimenteel werden distributies van de aantallen patches per deeltjes bepaald aan de hand van confocale microscopie opnames. Deze experimentele verdelingen van aantallen patches per deeltjes kwamen goed overeen met de voorspelde waarden bij de betreffende deeltjespolydispersiteiten. We concludeerden ook dat, om het aantal patches per deeltje dicht bij de ideale twaalf te brengen, de polydispersiteit van de kerndeeltjes lager dan 0.5% moet zijn.

In **Hoofdstukken 6** en **7** introduceerden we een nieuw systeem van lolly-vormige deeltjes met een silica steeltje en een 'kop' van 3-methacryloxypropyltrimethoxysilaan (MPS), waarna we de zelforganisatie van de deeltjes in een elektrisch veld aantoonde. Deze lolly-vormige hetero-dimeer deeltjes werden gemaakt door eerst spijkervormige silica deeltjes te maken; dat is mogelijk door bij de synthese van silica staafjes de goeitemperatuur te variëren. De spijkerdeeltjes werden bewerkt met het eerder genoemde OTMOS. Tot slot lieten we MPS nucleëren op deze spijkerdeeltjes, wat interessant genoeg enkel op de platte kant van de spijkerdeeltjes gebeurde. De vorm van de spijkerdeeltjes draagt mogelijk bij aan succesvolle nucleatie op de platte kant, hoewel de absolute breedte van de deeltjes ook van invloed kan zijn. Verder experimentele en theoretische studies moeten de invloeden van deeltjesvorm en -grootte onderzoeken. De MPS uitstulpingen konden een fluorescente stof opnemen voor confocale microscopie, en kon bestendig gemaakt worden tegen verwisseling van medium. Via een zelfde synthese-route was het mogelijk om halter-vormige deeltjes te maken. We hebben getoond dat deze deeltjes na een OTMOS-functionaliseringsproces in CHC kristallen kunnen vormen met enkele micrometers afstand tussen de deeltjes. In **Hoofdstuk 7** beschrijven we dat de hiervoor genoemde deeltjes (lolly- en halter-vormig) in een elektrisch veld uitrichten met de silica zijde naar een elektrode en in de bewegingsrichting. Dit is mogelijk het gevolg van een verschil in lading tussen de twee delen van de hetero-dimeer deeltjes, alhoewel zo'n ladingsverschil niet duidelijk bleek uit metingen. Een andere mogelijke oorzaak is een verschil in fractie tussen de twee delen, die een verschillende ruwheid hebben. Dit uitrichten bleek ook mogelijk te zijn in het genoemde kristal met lange afstanden tussen de deeltjes.

In **Hoofdstuk 8** bestudeerden we "depletie-interactie". Dit is een aantrekkingskracht tussen colloïden veroorzaakt door de aanwezigheid van grote moleculen (of kleine colloïden); omdat de moleculen niet meer tussen de colloïden passen zodra deze elkaar dicht naderen ontstaat er een netto druk die de deeltjes naar elkaar toe drijft. Deze interactie wordt vaak gebruikt voor zelf-assemblage. Wij gebruikten een modelsysteem van 'ruwe colloïden': grote silica colloïden met kleine silica deeltjes op het oppervlak. Deze deeltjes werden geredispergeerd in CHC met polystyreen moleculen als depletie middel. We toonden aan dat de ruwheid de depletie-interactie sterk reduceert door de colloïden op de wand van een capillair te laten sedimenteren en het capillair daarna om te keren; de verhouding van het aantal deeltjes dat aan de wand bleef plakken was veel kleiner in het geval van ruwe colloïden. Ruwe colloïden werden ook via computersimulaties bestudeerd. Via zogeheten Monte Carlo simulaties werden deeltjes vergelijkbaar met die gebruikt in de experimenten gemodelleerd. Vervolgens werden paar potentialen en overlapvolumes berekend - belangrijke parameters die de depletie interactie beschrijven. Hieruit bleek dat de beste reductie van de depletiekracht wordt verkregen bij een incomplete laag kleine deeltjes die de ruwheid vormen. Ook wordt de invloed van de ruwheid

---

kleiner naarmate de moleculen die de depletie verzorgen de maat van de oppervlakteruwheid van de ruwe colloïden benaderen. De simulaties lieten duidelijk zien dat er een polymeer-concentraties-regime bestaat waarvoor gladde deeltjes een aanzienlijke depletie attractie ondervinden, terwijl de ruwe deeltjes elkaar nauwelijks aantrekken. Zo zou het mogelijk zijn om in een mengsel van ruwe en gladde deeltjes van gelijke grootte, de gladde deeltjes selectief clusters vormen. Experimenteel lukte het met die gegevens om daadwerkelijk een mengsel van ruwe en gladde deeltjes te maken en de juiste polymeergrootte te secteren, waardoor we gladde deeltjes in een mengsel selectief konden immobiliseren.

In **Hoofdstuk 9** gebruikten we elektrische velden als innovatieve manier om “lock-and-key” (pen-gat) verbindingen tussen complementaire colloïden tot stand te brengen. We toonden aan dat bolvormige colloïden in een elektrisch veld worden ingevangen door komvormige colloïden. Op deze manier vormden we composietdeeltjes van silica of polystyreen bollen in kom-vormige organo-silica . De deeltjes waren bovendien reversibel gebonden, d.w.z. de beide typen deeltjes bewogen weer vrijelijk na het uitzetten van het elektrische veld. Theoretische berekeningen werden uitgevoerd om het ‘energielandschap’ - dat zijn de invloeden van polarisaties, De berekeningen lieten zien dat het invangen van bollen energetisch gunstig wordt (in natuurkundige termen: er ontstaat een minimum in het energielandschap) als de komvormige colloïden een keten vormen van drie of meer deeltjes. Zulke ketens van komvormige deeltjes vormen spontaan onder invloed van het elektrische veld als gevolg van de polarisaties die zij krijgen, zoals tevens middels berekeningen werd aangetoond. Het minimum in de potentiële energie, gesitueerd binnen in de komvormige deeltjes, was bovendien dieper voor langere ketens van colloïden en voor komvormige colloïden dichtbij het midden van de ketens. De omkeerbaarheid van het invang-mechanisme kon beïnvloed worden door toevoeging van zout en het wisselen van de verhouding bollen en komvormige deeltjes (hetgeen de zoutconcentratie ook verandert). Zodoende was het mogelijk de composietdeeltjes ook na het uitzetten van het veld te behouden. Deze deeltjes werden uit het mengsel (van bollen, kommen en composietdeeltjes) geïsoleerd door middel van centrifugatie in een viscositeitsgradient. Dit laatste toont dat onze nieuwe zelfassemblagemethode een extra voordeel heeft: de mogelijkheid om een nieuwe type complexe colloïden te genereren.



# References

- [1] T. Graham, "Liquid Diffusion Applied to Analysis," *Philosophical Transactions of the Royal Society of London*, vol. 151, pp. 183–224, June 1861.
  - [2] S. Iqbal and Y. Mido, *Physical Chemistry*. Discovery Publishing House, 2005.
  - [3] D. Abbott, B. Davis, N. Phillips, and K. Eshraghian, "Simple derivation of the thermal noise formula using window-limited Fourier transforms and other conundrums," *IEEE Transactions on Education*, vol. 39, pp. 1–13, February 1996.
  - [4] L. T. Sarasohn, *The Natural Philosophy of Margaret Cavendish: Reason and Fancy During the Scientific Revolution*. JHU Press, 2010.
  - [5] A. Einstein, "On the movement of small particles suspended in stationary liquids required by the molecular-kinetic theory of heat," *Annalen der Physik*, vol. 17, p. 16, May 1905.
  - [6] R. Home, B. McKellar, and A. Jamieson, "World year of physics - William Sutherland at the University of Melbourne." Essay, 2005.
  - [7] C. W. W. Ostwald and E. Hatschek, *A handbook of colloid-chemistry: the recognition of colloids, the theory of colloids, and their general physico-chemical properties*. P. Blakiston's son & co., 1910.
  - [8] S. Stanislaw, A. J. V., G. R. G., H. Michael, H. Kazuyuki, J. R. G., K. Przemyslaw, M. Ingrid, M. Werner, P. Stanisaw, and S. R. F. T., "Terminology of polymers and polymerization processes in dispersed systems (iupac recommendations 2011)," 2011.
  - [9] J. Alemán, A. V. Chadwick, J. He, M. Hess, K. Horie, R. G. Jones, P. Kratochvíl, I. Meisel, I. Mita, G. Moad, S. Penczek, and R. F. T. Stepto, "Definitions of terms relating to the structure and processing of sols, gels, networks and inorganic-organic hybrid materials (IUPAC Recommendations 2007)," *Pure Applied Chemistry*, vol. 79, pp. 1801–1829, October 2007.
  - [10] A. van Blaaderen, M. Dijkstra, R. van Roij, A. Imhof, M. Kamp, B. Kwaadgras, T. Vissers, and B. Liu, "Manipulating the self assembly of colloids in electric fields," *The European Physical Journal Special Topics*, vol. 222, pp. 2895–2909, November 2013.
  - [11] T. Vissers, A. van Blaaderen, and A. Imhof, "Band Formation in Mixtures of Oppositely Charged Colloids Driven by an ac Electric Field," *Physical Review Letters*, vol. 106, p. 228303, June 2011.
  - [12] S.-M. Yang, S.-H. Kim, J.-M. Lim, and G.-R. Yi, "Synthesis and assembly of structured colloidal particles," *Journal of Materials Chemistry*, vol. 18, no. 19, pp. 2177–2190, 2008.
  - [13] A. Kuijk, A. van Blaaderen, and A. Imhof, "Synthesis of Monodisperse, Rodlike Silica Colloids with Tunable Aspect Ratio," *Journal of the American Chemical Society*, vol. 133, pp. 2346–2349, January 2011.
  - [14] L. Rossi, S. Sacanna, W. T. M. Irvine, P. M. Chaikin, D. J. Pine, and A. P. Philipse, "Cubic crystals from cubic colloids," *Soft Matter*, vol. 7, pp. 4139–4142, April 2011.
  - [15] S. C. Glotzer and M. J. Solomon, "Anisotropy of building blocks and their assembly into complex structures," *Nature Materials*, vol. 6, pp. 557–562, August 2007.
  - [16] A. B. Pawar and I. Kretschmar, "Fabrication, Assembly, and Application of Patchy Particles," *Macromolecular Rapid Communications*, vol. 31, pp. 150–168, January 2010.
  - [17] A. Walther and A. H. E. Müller, "Janus Particles: Synthesis, Self-Assembly, Physical Properties, and Applications," *Chemical Reviews*, vol. 113, pp. 5194–5261, July 2013.
  - [18] A. Walther and A. H. E. Müller, "Janus particles," *Soft Matter*, vol. 4, pp. 663–668, February 2008.
  - [19] A. Kumar, B. J. Park, F. Tu, and D. Lee, "Amphiphilic janus particles at fluid interfaces," *Soft Matter*, vol. 9, pp. 6604–6617, April 2013.
  - [20] A. Perro, S. Reculosa, S. Ravaine, E. Bourgeat-Lami, and E. Duguet, "Design and synthesis of Janus micro- and nanoparticles," *Journal of Materials Chemistry*, vol. 15, pp. 3745–3760, July 2005.
  - [21] K. J. Lee, J. Yoon, and J. Lahann, "Recent advances with anisotropic particles," *Current Opinion in Colloid & Interface Science*, vol. 16, pp. 195–202, June 2011.
-

- [22] J. Du and R. K. O'Reilly, "Anisotropic particles with patchy, multicompartiment and Janus architectures: preparation and application," *Chemical Society Reviews*, vol. 40, pp. 2402–2416, March 2011.
- [23] J. Hu, S. Zhou, Y. Sun, X. Fang, and L. Wu, "Fabrication, properties and applications of Janus particles," *Chemical Society Reviews*, vol. 41, pp. 4356–4378, November 2012.
- [24] Q. Chen, J. Yan, J. Zhang, S. C. Bae, and S. Granick, "Janus and Multiblock Colloidal Particles," *Langmuir*, vol. 28, pp. 13555–13561, September 2012.
- [25] E. W. Edwards, D. Wang, and H. Mhwald, "Hierarchical Organization of Colloidal Particles: From Colloidal Crystallization to Supraparticle Chemistry," *Macromolecular Chemistry and Physics*, vol. 208, pp. 439–445, March 2007.
- [26] C. Casagrande, P. Fabre, E. Raphael, and M. Veyssié, "'Janus Beads': Realization and Behaviour at Water/Oil Interfaces," *EPL (Europhysics Letters)*, vol. 9, p. 251, June 1989.
- [27] P.-G. de Gennes, "Soft Matter (Nobel Lecture)," *Angewandte Chemie International Edition*, vol. 31, pp. 842–845, July 1992.
- [28] N. Sheridon, "Us patent no. 4,126,854 A: Twisting ball panel display," 1978.
- [29] L. Hong, S. Jiang, and S. Granick, "Simple Method to Produce Janus Colloidal Particles in Large Quantity," *Langmuir*, vol. 22, pp. 9495–9499, November 2006.
- [30] S. Jiang, M. J. Schultz, Q. Chen, J. S. Moore, and S. Granick, "Solvent-Free Synthesis of Janus Colloidal Particles," *Langmuir*, vol. 24, pp. 10073–10077, September 2008.
- [31] A. Perro, F. Meunier, V. Schmitt, and S. Ravaine, "Production of large quantities of Janus nanoparticles using wax-in-water emulsions," *Colloids and Surfaces A: Physicochemical and Engineering Aspects*, vol. 332, pp. 57 – 62, January 2009.
- [32] H. Takei and N. Shimizu, "Gradient Sensitive Microscopic Probes Prepared by Gold Evaporation and Chemisorption on Latex Spheres," *Langmuir*, vol. 13, pp. 1865–1868, April 1997.
- [33] O. Cayre, V. N. Paunov, and O. D. Velev, "Fabrication of asymmetrically coated colloid particles by microcontact printing techniques," *Journal of Materials Chemistry*, vol. 13, no. 10, pp. 2445–2450, 2003.
- [34] R. K. Shah, J.-W. Kim, and D. A. Weitz, "Janus Supraparticles by Induced Phase Separation of Nanoparticles in Droplets," *Advanced Materials*, vol. 21, pp. 1949–1953, May 2009.
- [35] K. P. Yuet, D. K. Hwang, R. Haghgoie, and P. S. Doyle, "Multifunctional Superparamagnetic Janus Particles," *Langmuir*, vol. 26, pp. 4281–4287, March 2010.
- [36] S. Yang, F. Guo, B. Kiraly, X. Mao, M. Lu, K. W. Leong, and T. J. Huang, "Microfluidic synthesis of multifunctional Janus particles for biomedical applications," *Lab on a Chip*, vol. 12, pp. 2097–2102, June 2012.
- [37] S. Hwang, K.-H. Roh, D. W. Lim, G. Wang, C. Uher, and J. Lahann, "Anisotropic hybrid particles based on electrohydrodynamic co-jetting of nanoparticle suspensions," *Physical Chemistry Chemical Physics*, vol. 12, pp. 11894–11899, September 2010.
- [38] T. Ondarçuhu, P. Fabre, E. Raphaël, and M. Veyssié, "Specific properties of amphiphilic particles at fluid interfaces," *Journal of Physics France*, vol. 51, pp. 1527–1536, July 1990.
- [39] S. Jiang and S. Granick, "Controlling the Geometry (Janus Balance) of Amphiphilic Colloidal Particles," *Langmuir*, vol. 24, pp. 2438–2445, March 2008.
- [40] B. Liu, C. Zhang, J. Liu, X. Qu, and Z. Yang, "Janus non-spherical colloids by asymmetric wet-etching," *Chemical Communications*, pp. 3871–3873, January 2009.
- [41] A. B. Pawar and I. Kretzschmar, "Patchy Particles by Glancing Angle Deposition," *Langmuir*, vol. 24, pp. 355–358, January 2008.
- [42] Z. He and I. Kretzschmar, "Template-Assisted GLAD: Approach to Single and Multipatch Patchy Particles with Controlled Patch Shape," *Langmuir*, vol. 29, pp. 15755–15761, December 2013.
- [43] Q. Chen, S. C. Bae, and S. Granick, "Directed self-assembly of a colloidal kagome lattice," *Nature*, vol. 469, pp. 381–384, January 2011.
- [44] D. J. Kraft, R. Ni, F. Smalenburg, M. Hermes, K. Yoon, D. A. Weitz, A. van Blaaderen, J. Groenewold, M. Dijkstra, and W. K. Kegel, "Surface roughness directed self-assembly of patchy particles into colloidal micelles," *Proceedings of the National Academy of Sciences*, vol. 109, pp. 10787–10792, July 2012.
- [45] S. Badaire, C. Cottin-Bizonne, and A. D. Stroock, "Experimental Investigation of Selective Colloidal Interactions Controlled by Shape, Surface Roughness, and Steric Layers," *Langmuir*, vol. 24, pp. 11451–11463, September 2008.
- [46] D. Nagao, M. Sugimoto, A. Okada, H. Ishii, M. Konno, A. Imhof, and A. van Blaaderen, "Directed Orientation of Asymmetric Composite Dumbbells by Electric Field Induced Assembly," *Langmuir*, vol. 28, pp. 6546–6550, April 2012.
- [47] J.-W. Kim, R. J. Larsen, and D. A. Weitz, "Synthesis of Nonspherical Colloidal Particles with Anisotropic Properties," *Journal of the American Chemical Society*, vol. 128, pp. 14374–14377, November 2006.

- [48] B. G. P. van Ravensteijn, M. Kamp, A. van Blaaderen, and W. K. Kegel, "General Route toward Chemically Anisotropic Colloids," *Chemistry of Materials*, vol. 25, pp. 4348–4353, November 2013.
- [49] S. Sacanna, L. Rossi, and D. J. Pine, "Magnetic Click Colloidal Assembly," *Journal of the American Chemical Society*, vol. 134, pp. 6112–6115, April 2012.
- [50] J. He, B. Yu, M. J. Hourwitz, Y. Liu, M. T. Perez, J. Yang, and Z. Nie, "Wet-Chemical Synthesis of Amphiphilic Rodlike Silica Particles and their Molecular Mimetic Assembly in Selective Solvents," *Angewandte Chemie International Edition*, vol. 51, pp. 3628–3633, April 2012.
- [51] K. Chaudhary, Q. Chen, J. J. Juárez, S. Granick, and J. A. Lewis, "Janus Colloidal Matchsticks," *Journal of the American Chemical Society*, vol. 134, pp. 12901–12903, August 2012.
- [52] J. Yan, K. Chaudhary, S. Chul Bae, J. A. Lewis, and S. Granick, "Colloidal ribbons and rings from Janus magnetic rods," *Nature Communications*, vol. 4, p. 1516, February 2013.
- [53] A. A. Shah, B. Schultz, K. L. Kohlstedt, S. C. Glotzer, and M. J. Solomon, "Synthesis, Assembly, and Image Analysis of Spheroidal Patchy Particles," *Langmuir*, vol. 29, pp. 4688–4696, April 2013.
- [54] C. Tang, C. Zhang, Y. Sun, F. Liang, Q. Wang, J. Li, X. Qu, and Z. Yang, "Janus Anisotropic Hybrid Particles with Tunable Size from Patchy Composite Spheres," *Macromolecules*, vol. 46, pp. 188–193, January 2013.
- [55] Q. Chen, S. C. Bae, and S. Granick, "Staged Self-Assembly of Colloidal Metastructures," *Journal of the American Chemical Society*, vol. 134, pp. 11080–11083, July 2012.
- [56] Q. Chen, E. Diesel, J. K. Whitmer, S. C. Bae, E. Luijten, and S. Granick, "Triblock Colloids for Directed Self-Assembly," *Journal of the American Chemical Society*, vol. 133, pp. 7725–7727, May 2011.
- [57] G. Zhang, D. Wang, and H. Möhwald, "Decoration of Microspheres with Gold Nanodots Giving Colloidal Spheres Valences," *Angewandte Chemie International Edition*, vol. 44, pp. 7767–7770, December 2005.
- [58] A. F. Demirors, J. C. P. Stiefelhagen, T. Vissers, F. Smalenburg, M. Dijkstra, A. Imhof, and A. van Blaaderen, "Long-Ranged Oppositely Charged Interactions for Designing New Types of Colloidal Clusters," *Physical Review X*, accepted.
- [59] Y.-S. Cho, G.-R. Yi, S.-H. Kim, M. T. Elsesser, D. R. Breed, and S.-M. Yang, "Homogeneous and heterogeneous binary colloidal clusters formed by evaporation-induced self-assembly inside droplets," *Journal of Colloid and Interface Science*, vol. 318, pp. 124 – 133, February 2008.
- [60] Y.-S. Cho, G.-R. Yi, S.-H. Kim, S.-J. Jeon, M. T. Elsesser, H. K. Yu, S.-M. Yang, and D. J. Pine, "Particles with Coordinated Patches or Windows from Oil-in-Water Emulsions," *Chemistry of Materials*, vol. 19, pp. 3183–3193, June 2007.
- [61] Y. Wang, Y. Wang, D. R. Breed, V. N. Manoharan, L. Feng, A. D. Hollingsworth, M. Weck, and D. J. Pine, "Colloids with valence and specific directional bonding," *Nature*, vol. 491, pp. 51–55, November 2012.
- [62] S. Sacanna, M. Korpics, K. Rodriguez, L. Coln-Melndez, S.-H. Kim, D. J. Pine, and G.-R. Yi, "Shaping colloids for self-assembly," *Nature Communications*, vol. 4, p. 1688, April 2013.
- [63] D. J. Kraft, W. S. Vlug, C. M. van Kats, A. van Blaaderen, A. Imhof, and W. K. Kegel, "Self-Assembly of Colloids with Liquid Protrusions," *Journal of the American Chemical Society*, vol. 131, pp. 1182–1186, January 2009.
- [64] D. J. Kraft, J. Groenewold, and W. K. Kegel, "Colloidal molecules with well-controlled bond angles," *Soft Matter*, vol. 5, pp. 3823–3826, July 2009.
- [65] C. E. Snyder, A. M. Yake, J. D. Feick, and D. Velegol, "Nanoscale Functionalization and Site-Specific Assembly of Colloids by Particle Lithography," *Langmuir*, vol. 21, pp. 4813–4815, May 2005.
- [66] T. T. Chastek, S. D. Hudson, and V. A. Hackley, "Preparation and Characterization of Patchy Particles," *Langmuir*, vol. 24, pp. 13897–13903, December 2008.
- [67] L. Wang, L. Xia, G. Li, S. Ravaine, and X. S. Zhao, "Patterning the Surface of Colloidal Microspheres and Fabrication of Nonspherical Particles," *Angewandte Chemie International Edition*, vol. 47, pp. 4725–4728, June 2008.
- [68] G. Braun, I. Pavel, A. R. Morrill, D. S. Seferos, G. C. Bazan, N. O. Reich, and M. Moskovits, "Chemically Patterned Microspheres for Controlled Nanoparticle Assembly in the Construction of SERS Hot Spots," *Journal of the American Chemical Society*, vol. 129, pp. 7760–7761, June 2007.
- [69] K. Kamalasanan, S. Jhunjhunwala, J. Wu, A. Swanson, D. Gao, and S. R. Little, "Patchy, Anisotropic Microspheres with Soft Protein Islets," *Angewandte Chemie International Edition*, vol. 50, pp. 8706–8708, September 2011.
- [70] K. Maeda, H. Onoe, M. Takinoue, and S. Takeuchi, "Controlled Synthesis of 3D Multi-Compartmental Particles with Centrifuge-Based Microdroplet Formation from a Multi-Barrelled Capillary," *Advanced Materials*, vol. 24, pp. 1340–1346, February 2012.
- [71] J. M. Crowley, N. K. Sheridon, and L. Romano, "Dipole moments of gyron balls," *Journal of Electrostatics*, vol. 55, pp. 247 – 259, July 2002. [jce:titleSelected Papers from the 2000 IEJ-ESA Joint Symposiumjce:title](#).

- [72] A. Synytska, R. Khanum, L. Ionov, C. Cherif, and C. Bellmann, "Water-Repellent Textile via Decorating Fibers with Amphiphilic Janus Particles," *ACS Applied Materials & Interfaces*, vol. 3, pp. 1216–1220, April 2011.
- [73] J. N. Anker, C. J. Behrend, H. Huang, and R. Kopelman, "Magnetically-modulated optical nanoprobes (MagMOONs) and systems," *Journal of Magnetism and Magnetic Materials*, vol. 293, pp. 655–662, May 2005. [jce:titlejProceedings of the Fifth International Conference on Scientific and Clinical Applications of Magnetic Carriers;/ce:titlej.](#)
- [74] Y. Gao and Y. Yu, "How Half-Coated Janus Particles Enter Cells," *Journal of the American Chemical Society*, vol. 135, pp. 19091–19094, December 2013.
- [75] S. Hwang and J. Lahann, "Differentially Degradable Janus Particles for Controlled Release Applications," *Macromolecular Rapid Communications*, vol. 33, pp. 1178–1183, July 2012.
- [76] X. Yong, E. J. Crabb, N. M. Moellers, and A. C. Balazs, "Self-Healing Vesicles Deposit Lipid-Coated Janus Particles into Nanoscopic Trenches," *Langmuir*, vol. 29, pp. 16066–16074, December 2013.
- [77] B. J. Park, T. Brugarolas, and D. Lee, "Janus particles at an oil-water interface," *Soft Matter*, vol. 7, pp. 6413–6417, June 2011.
- [78] Q. Chen, J. K. Whitmer, S. Jiang, S. C. Bae, E. Luijten, and S. Granick, "Supracolloidal Reaction Kinetics of Janus Spheres," *Science*, vol. 331, pp. 199–202, January 2011.
- [79] S. M. Anthony, M. Kim, and S. Granick, "Single-Particle Tracking of Janus Colloids in Close Proximity," *Langmuir*, vol. 24, pp. 6557–6561, June 2008.
- [80] S. Gangwal, O. J. Cayre, M. Z. Bazant, and O. D. Velev, "Induced-Charge Electrophoresis of Metallo-dielectric Particles," *Physical Review Letters*, vol. 100, p. 058302, February 2008.
- [81] M. Z. Bazant and T. M. Squires, "Induced-charge electrokinetic phenomena," *Current Opinion in Colloid & Interface Science*, vol. 15, pp. 203 – 213, June 2010.
- [82] A. M. Boymelgreen and T. Miloh, "Induced-charge electrophoresis of uncharged dielectric spherical Janus particles," *Electrophoresis*, vol. 33, no. 5, pp. 870–879, 2012.
- [83] A. M. Boymelgreen, G. Yossifon, S. Park, and T. Miloh, "Spinning Janus doublets driven in uniform AC electric fields," *Physical Review E*, vol. 89, pp. 011003–011008, January 2013.
- [84] A. J. Logsdail and R. L. Johnston, "Predicting the Optical Properties of Core-Shell and Janus Segregated Au-M Nanoparticles ( $M = \text{Ag}, \text{Pd}$ )," *The Journal of Physical Chemistry C*, vol. 116, pp. 23616–23628, November 2012.
- [85] K. I. Hadjiivanov and D. G. Klissurski, "Surface chemistry of titania (anatase) and titania-supported catalysts," *Chemical Society Reviews*, vol. 25, pp. 61–69, January 1996.
- [86] D. A. Wilson, B. de Nijs, A. van Blaaderen, R. J. M. Nolte, and J. C. M. van Hest, "Fuel concentration dependent movement of supramolecular catalytic nanomotors," *Nanoscale*, vol. 5, pp. 1315–1318, February 2013.
- [87] J. Palacci, S. Sacanna, A. P. Steinberg, D. J. Pine, and P. M. Chaikin, "Living Crystals of Light-Activated Colloidal Surfers," *Science*, vol. 339, pp. 936–940, February 2013.
- [88] D. Fusco and P. Charbonneau, "Crystallization of asymmetric patchy models for globular proteins in solution," *Physical Review E*, vol. 88, p. 012721, July 2013.
- [89] D. Fusco, J. J. Headd, A. De Simone, J. Wang, and P. Charbonneau, "Characterizing protein crystal contacts and their role in crystallization: rubredoxin as a case study," *Soft Matter*, vol. 10, pp. 290–302, November 2014.
- [90] J. P. K. Doye, A. A. Louis, I.-C. Lin, L. R. Allen, E. G. Noya, A. W. Wilber, H. C. Kok, and R. Lyus, "Controlling crystallization and its absence: proteins, colloids and patchy models," *Physical Chemistry Chemical Physics*, vol. 9, pp. 2197–2205, January 2007.
- [91] E. Mani, E. Sanz, S. Roy, M. Dijkstra, J. Groenewold, and W. K. Kegel, "Sheet-like assemblies of spherical particles with point-symmetrical patches," *The Journal of Chemical Physics*, vol. 136, pp. 144706–a.f., April 2012.
- [92] R. Mezzenga and P. Fischer, "The self-assembly, aggregation and phase transitions of food protein systems in one, two and three dimensions," *Reports on Progress in Physics*, vol. 76, p. 046601, March 2013.
- [93] B. Ruzicka, E. Zaccarelli, L. Zulian, R. Angelini, M. Sztucki, A. Moussad, T. Narayanan, and F. Sciortino, "Observation of empty liquids and equilibrium gels in a colloidal clay," *Nature Materials*, vol. 10, pp. 56–60, January 2011.
- [94] W. K. Kegel and H. N. W. Lekkerkerker, "Colloidal gels: Clay goes patchy," *Nature Materials*, vol. 10, pp. 5–6, January 2011.
- [95] K. P. Velikov, C. G. Christova, R. P. A. Dullens, and A. van Blaaderen, "Layer-by-Layer Growth of Binary Colloidal Crystals," *Science*, vol. 296, pp. 106–109, April 2002.
- [96] F. Romano and F. Sciortino, "Colloidal self-assembly: Patchy from the bottom up," *Nat. Mater.*, vol. 10, pp. 171–173, March 2011.
- [97] F. Romano and F. Sciortino, "Two dimensional assembly of triblock Janus particles into crystal phases in the two bond per patch limit," *Soft Matter*, vol. 7, pp. 5799–5804, June 2011.

- [98] F. Romano and F. Sciortino, "Patterning symmetry in the rational design of colloidal crystals," *Nat. Commun.*, vol. 3, p. 975, July 2012.
- [99] E. Bianchi, R. Blaak, and C. N. Likos, "Patchy colloids: state of the art and perspectives," *Physical Chemistry Chemical Physics*, vol. 13, pp. 6397–6410, April 2011.
- [100] F. Sciortino and E. Zaccarelli, "Reversible gels of patchy particles," *Current Opinion in Solid State and Materials Science*, vol. 15, pp. 246–253, December 2011.
- [101] A. Giacometti, "Self-assembly mechanism in colloids: perspectives from statistical physics," *Cent. Eur. J. Phys.*, vol. 10, pp. 540–551, March 2012.
- [102] F. A. Escobedo, "Engineering entropy in soft matter: the bad, the ugly and the good," *Soft Matter*, vol. 10, pp. 8388–8400, November 2014.
- [103] N. Pan, "Exploring the significance of structural hierarchy in material systems - A review," *App. Phys. Rev.*, vol. 1, p. 021302, June 2014.
- [104] J. W. Jansen, *Attractive interactions in sterically stabilized silica dispersions: phase separation and particle interactions*. PhD thesis, Universiteit Utrecht, 1986.
- [105] S. Roke, J. Buitenhuis, J. C. van Miltenburg, M. Bonn, and A. van Blaaderen, "Interface-solvent effects during colloidal phase transitions," *Journal of Physics: Condensed Matter*, vol. 17, pp. S3609–S3618, October 2005.
- [106] S. Roke, O. Berg, J. Buitenhuis, A. van Blaaderen, and M. Bonn, "Surface molecular view of colloidal gelation," *Proceedings of the National Academy of Sciences*, vol. 103, pp. 13310–13314, September 2006.
- [107] M. E. Montgomery and M. J. Wirth, "Spectroscopic Study of the Molecular Basis of Wetting of a C18 Surface by Long-Chain n-Alcohols," *Analytical Chemistry*, vol. 66, pp. 680–684, March 1994.
- [108] J. Jansen, C. De Kruif, and A. Vrij, "Phase separation of sterically stabilized colloids as a function of temperature," *Chemical Physics Letters*, vol. 107, pp. 450–453, June 1984.
- [109] P. Rouw, A. Vrij, and C. De Kruif, "Adhesive hard-sphere colloidal dispersions III. stickiness in n-dodecane and benzene," *Colloids and Surfaces*, vol. 31, pp. 299–309, September 1988.
- [110] F. Riedo, M. Czencz, O. Liardon, and E. s. Kováts, "Chemically modified silicon dioxide surfaces. wetting properties of compact n-alkyl-dimethylsiloxy layers, and their mixed surface crystals. the Question of Wetting of Molecularly Rough and of Swollen Surfaces," *Helvetica Chimica*, vol. 61, pp. 1912–1941, July 1978.
- [111] B. M. Ocko, X. Z. Wu, E. B. Sirota, S. K. Sinha, O. Gang, and M. Deutsch, "Surface freezing in chain molecules: Normal alkanes," *Physical Review E*, vol. 55, pp. 3164–3182, March 1997.
- [112] A. P. R. Eberle, N. J. Wagner, B. Akgun, and S. K. Satija, "Temperature-Dependent Nanostructure of an End-Tethered Octadecane Brush in Tetradecane and Nanoparticle Phase Behavior," *Langmuir*, vol. 26, pp. 3003–3007, January 2010.
- [113] A. Y. Fadeev and T. J. McCarthy, "Trialkylsilane Monolayers Covalently Attached to Silicon Surfaces: Wettability Studies Indicating that Molecular Topography Contributes to Contact Angle Hysteresis," *Langmuir*, vol. 15, pp. 3759–3766, April 1999.
- [114] T. Chau, "A review of techniques for measurement of contact angles and their applicability on mineral surfaces," *Minerals Engineering*, vol. 22, pp. 213–219, February 2009.
- [115] E. I. Franses, O. A. Basaran, and C.-H. Chang, "Techniques to measure dynamic surface tension," *Current Opinion in Colloid & Interface Science*, vol. 1, pp. 296–303, April 1996.
- [116] J. Spelt, *Applied Surface Thermodynamics*. CRC Press, 1996.
- [117] J. Jansen, C. de Kruif, and A. Vrij, "Attractions in sterically stabilized silica dispersions: I. Theory of phase separation," *Journal of Colloid and Interface Science*, vol. 114, pp. 471–480, December 1986.
- [118] H. Verduin and J. K. Dhont, "Phase Diagram of a Model Adhesive Hard-Sphere Dispersion," *Journal of Colloid and Interface Science*, vol. 172, pp. 425–437, June 1995.
- [119] A. K. Van Helden, J. W. Jansen, and A. Vrij, "Preparation and characterization of spherical monodisperse silica dispersions in nonaqueous solvents," *Journal of Colloid and Interface Science*, vol. 81, pp. 354–368, June 1981.
- [120] D. L. J. Vossen, M. J. A. de Dood, T. van Dillen, T. Zijlstra, E. van der Drift, A. Polman, and A. van Blaaderen, "Novel Method for Solution Growth of Thin Silica Films from Tetraethoxysilane," *Advanced Materials*, vol. 12, pp. 1434–1437, October 2000.
- [121] U. Domanska, J. Lachwa, P. Morawski, and S. K. Malanowski, "Phase Equilibria and Volumetric Properties in Binary Mixtures Containing Branched Chain Ethers (Methyl 1,1-Dimethylethyl Ether or Ethyl 1,1-Dimethylethyl Ether or Methyl 1,1-Dimethylpropyl Ether or Ethyl 1,1-Dimethylpropyl Ether)," *Journal of Chemical and Engineering Data*, vol. 44, pp. 974–984, August 1999.
- [122] H. Tanaka, Y. Yamaki, and M. Kato, "Solubility of carbon dioxide in pentadecane, hexadecane, and pentadecane + hexadecane," *Journal of Chemical and Engineering Data*, vol. 38, pp. 386–388, July 1993.

## References

---

- [123] V. Sharma and S. Maken, "Excess molar volume of binary mixtures containing nitrotoluene at 308.15 K," *Indian Journal of Chemistry Section A*, vol. 31, pp. 791–722, February 1992.
- [124] A. Matilla, G. Tardajos, and E. Aicart, "Thermodynamic mixing properties of (chlorobenzene+an alkane)," *The Journal of Chemical Thermodynamics*, vol. 25, pp. 201–207, February 1993.
- [125] M. I. Aralaguppi, T. M. Aminabhavi, R. H. Balundgi, and S. S. Joshi, "Thermodynamic interactions in mixtures of bromoform with hydrocarbons," *The Journal of Physical Chemistry*, vol. 95, pp. 5299–5308, June 1991.
- [126] Z. Aizenshtat, *The Analysis of Alkanes and Cycloalkanes*, pp. 289–349. John Wiley & Sons, Ltd, 2006.
- [127] A.-F. A. Asfour, M. H. Siddique, and T. D. Vavanellos, "Density-Composition Data for Eight Binary Systems Containing Toluene or Ethylbenzene and CB-C,6 n-Alkanes at 293.15, 298.15, 308.15, and 313.15 K," *Journal of Chemical Engineering Data*, vol. 35, pp. 192–198, April 1990.
- [128] J. J. Jasper and E. V. Kring, "The Isobaric Surface Tensions and Thermodynamic Properties of the Surfaces of a Series of n-Alkanes, C5 to C18, 1-alkenes, C6 to C16, and of n-Decylcyclopentane, n-Decylcyclohexane and n-Decylbenzene," *The Journal of Physical Chemistry*, vol. 59, pp. 1019–1021, October 1955.
- [129] D. Caudwell, J. Trusler, V. Vesovic, and W. Wakeham, "The Viscosity and Density of n-Dodecane and n-Octadecane at Pressures up to 200MPa and Temperatures up to 473 K," *International Journal of Thermophysics*, vol. 25, pp. 1339–1352, September 2004.
- [130] N. A. M. Verhaegh and A. v. Blaaderen, "Dispersions of Rhodamine-Labeled Silica Spheres: Synthesis, Characterization, and Fluorescence Confocal Scanning Laser Microscopy," *Langmuir*, vol. 10, pp. 1427–1438, May 1994.
- [131] B. Liu, T. H. Besseling, M. Hermes, A. F. Demirörs, A. Imhof, and A. van Blaaderen, "Switching plastic crystals of colloidal rods with electric fields," *Nature Communications*, vol. 5, p. 3092, January 2014.
- [132] S. H. Behrens and D. G. Grier, "Pair interaction of charged colloidal spheres near a charged wall," *Physical Review E*, vol. 64, p. 050401, October 2001.
- [133] A.-P. Hynninen and M. Dijkstra, "Phase diagram of hard-core repulsive Yukawa particles with a density-dependent truncation: a simple model for charged colloids," *Journal of Physics: Condensed Matter*, vol. 15, pp. S3557–S3567, December 2003.
- [134] M. F. Hsu, E. R. Dufresne, and D. A. Weitz, "Charge Stabilization in Nonpolar Solvents," *Langmuir*, vol. 21, pp. 4881–4887, April 2005.
- [135] J. C. Crocker and D. G. Grier, "Microscopic measurement of the pair interaction potential of charge-stabilized colloid," *Physical Review Letters*, vol. 73, pp. 352–355, July 1994.
- [136] M. D. Carbajal-Tinoco, F. Castro-Román, and J. L. Arauz-Lara, "Static properties of confined colloidal suspensions," *Physical Review E*, vol. 53, pp. 3745–3749, April 1996.
- [137] J. K. Percus and G. J. Yevick, "Analysis of Classical Statistical Mechanics by Means of Collective Coordinates," *Physical Review*, vol. 110, pp. 1–13, April 1958.
- [138] M. S. Wertheim, "Exact Solution of the Percus-Yevick Integral Equation for Hard Spheres," *Physical Review Letters*, vol. 10, pp. 321–323, April 1963.
- [139] M. Heinen, P. Holmqvist, A. J. Banchio, and G. Ngele, "Pair structure of the hard-sphere Yukawa fluid: An improved analytic method versus simulations, Rogers-Young scheme, and experiment," *The Journal of Chemical Physics*, vol. 134, pp. 044532–a.f., January 2011.
- [140] P. S. Mohanty, D. Paloli, J. J. Crassous, E. Zaccarelli, and P. Schurtenberger, "Effective interactions between soft-repulsive colloids: Experiments, theory, and simulations," *The Journal of Chemical Physics*, vol. 140, pp. 094901–a.f., March 2014.
- [141] L. Verlet, "On the theory of classical fluids IV," *Physica*, vol. 31, pp. 959 – 966, June 1965.
- [142] E. M. Chan, "Two-dimensional Born-Green-Yvon and other integral equations," *Journal of Physics C: Solid State Physics*, vol. 10, p. 3477, September 1977.
- [143] G. M. Kepler and S. Fraden, "Attractive potential between confined colloids at low ionic strength," *Physical Review Letters*, vol. 73, pp. 356–359, July 1994.
- [144] C. P. Royall, M. E. Leunissen, and A. van Blaaderen, "A new colloidal model system to study long-range interactions quantitatively in real space," *Journal of Physics: Condensed Matter*, vol. 15, pp. S3581–S3596, December 2003.
- [145] C. R. Iacovella, R. E. Rogers, S. C. Glotzer, and M. J. Solomon, "Pair interaction potentials of colloids by extrapolation of confocal microscopy measurements of collective suspension structure," *The Journal of Chemical Physics*, vol. 133, pp. 164903–164938, October 2010.
- [146] C. P. Royall, A. A. Louis, and H. Tanaka, "Measuring colloidal interactions with confocal microscopy," *The Journal of Chemical Physics*, vol. 127, p. 044507, July 2007.
- [147] J. C. Crocker and D. G. Grier, "Methods of Digital Video Microscopy for Colloidal Studies," *Journal of Colloid and Interface Science*, vol. 179, pp. 298 – 310, April 1996.

- 
- [148] D. G. Grier and Y. Han, "Anomalous interactions in confined charge-stabilized colloid," *Journal of Physics: Condensed Matter*, vol. 16, p. S4145, April 2004.
- [149] C. P. Royall, M. E. Leunissen, A.-P. Hynninen, M. Dijkstra, and A. van Blaaderen, "Re-entrant melting and freezing in a model system of charged colloids," *The Journal of Chemical Physics*, vol. 124, pp. 244706–1–244706–8, June 2006.
- [150] W. Mulder, "Reply to 'Comment on 'On the Theory of Electrostatic Interactions in Suspensions of Charged Colloids'' by Willem H. Mulder," *Soil Science Society of America Journal*, vol. 74, p. 1846, September 2010.
- [151] N. Ise and I. S. Sogami, "Comment on 'On the Theory of Electrostatic Interactions in Suspensions of Charged Colloids' by Willem H. Mulder," *Soil Science Society of America Journal*, vol. 74, pp. 1844–1845, September 2010/9.
- [152] W. H. Mulder, "On the theory of electrostatic interactions in suspensions of charged colloids," *Soil Science Society of America Journal*, vol. 74, pp. 1–4, January 2010.
- [153] A. R. Denton, "Phase separation in charge-stabilized colloidal suspensions: Influence of nonlinear screening," *Physical Review E*, vol. 73, p. 041407, April 2006.
- [154] B. V. R. Tata and S. S. Jena, "Ordering, dynamics and phase transitions in charged colloids," *Solid State Communications*, vol. 139, pp. 562–580, September 2006.
- [155] P. Attard, "Recent advances in the electric double layer in colloid science," *Current Opinion in Colloid & Interface Science*, vol. 6, pp. 366–371, August 2001.
- [156] L. Belloni, "Review Article: Colloidal Interactions," *Journal of Physics: Condensed Matter*, vol. 12, p. R549R587, November 2000.
- [157] O. Spalla, "Long-range attraction between surfaces: existence and amplitude?," *Current Opinion in Colloid & Interface Science*, vol. 5, pp. 5–12, March 2000.
- [158] J.-P. Hansen and H. Löwen, "Effective Interactions Between Electrical Double Layers," *Annual Review of Physical Chemistry*, vol. 51, pp. 209–242, October 2000.
- [159] H. Helmholtz, "Ueber einige Gesetze der Vertheilung elektrischer Ströme in körperlichen Leitern mit Anwendung auf die thierisch-elektrischen Versuche," *Annalen der Physik*, vol. 165, no. 6, pp. 211–233, 1853.
- [160] G. Gouy, "Sur la constitution de la charge lectrique a la surface d'un lectrolyte," *Journal of Physics*, vol. 9, no. 1, p. 457, 1910.
- [161] D. L. Chapman, "LI. A contribution to the theory of electrocapillarity," *Philosophical Magazine Series 6*, vol. 25, pp. 475–481, April 1913.
- [162] O. Stern, "Zur Theorie der elektrolytischen doppelschicht," *Zeitschrift für Elektrochemie und angewandte physikalische Chemie*, vol. 30, pp. 508–516, November 1924.
- [163] D. C. Grahame, "The Electrical Double Layer and the Theory of Electrocapillarity," *Chemica Reviews*, vol. 41, pp. 441–501, December 1947.
- [164] F. D. Morgan, E. R. Williams, and T. R. Madden, "Streaming potential properties of westerly granite with applications," *Journal of Geophysical Research*, vol. 94, no. B9, pp. 12449–12461, 1989.
- [165] D. A. Haydon, "A Study of the Relation Between Electrokinetic Potential and Surface Charge Density," *Proceedings of the Royal Society of London A: Mathematical, Physical and Engineering Sciences*, vol. 258, pp. 319–328, October 1960.
- [166] P. Ducheyne, C. S. Kim, and S. R. Pollack, "The effect of phase differences on the time-dependent variation of the zeta potential of hydroxyapatite," *Journal of Biomedical Materials Research*, vol. 26, pp. 147–168, February 1992.
- [167] M. Kaszuba, J. Corbett, F. M. Watson, and A. Jones, "High-concentration zeta potential measurements using light-scattering techniques," *Philosophical Transactions of the Royal Society of London A: Mathematical, Physical and Engineering Sciences*, vol. 368, pp. 4439–4451, August 2010.
- [168] J. D. Clogston and K. Patri, Anil, "Zeta potential measurement," in *Methods in Molecular Biology* (S. E. McNeil, ed.), vol. 697, pp. 63–70, Humana Press, 2011.
- [169] M. von Smoluchowski, "Sur les phnomnes arodynamiques et les effets thermiques qui les accompagnent [ut supra].," *Bulletin of the International Academy of Sciences of Cracovie*, vol. 184, no. Classe des sciences math. et naturelles., p. 143182, 1903.
- [170] A. Delgado, F. Gonzalez-Caballero, R. Hunter, L. Koopal, and J. Lyklema, "Measurement and interpretation of electrokinetic phenomena," *Journal of Colloid and Interface Science*, vol. 309, pp. 194–224, My 2007.
- [171] E. Hückel *Physik Zeitung*, vol. 25, p. 204, 1924.
- [172] R. J. Hunter, "Chapter 3 - The Calculation of Zeta Potential," in *Zeta Potential in Colloid Science* (R. J. HUNTER, ed.), pp. 59–124, Academic Press, 1981.
- [173] S. Levine and G. H. Neale, "The prediction of electrokinetic phenomena within multiparticle systems. I. Electrophoresis and electroosmosis," *Journal of Colloid and Interface Science*, vol. 47, pp. 520–529, May 1974.
-

- [174] M. W. Kozak and E. Davis, "Electrokinetics of concentrated suspensions and porous media: 1. Thin electrical double layers," *Journal of Colloid and Interface Science*, vol. 127, pp. 497–510, February 1989.
- [175] M. W. Kozak and E. Davis, "Electrokinetics of concentrated suspensions and porous media: 2. Moderately thick electrical double layers," *Journal of Colloid and Interface Science*, vol. 129, pp. 166–174, April 1989.
- [176] H. Ohshima, "Sedimentation Potential in a Concentrated Suspension of Spherical Colloidal Particles," *Journal of Colloid and Interface Science*, vol. 208, pp. 295–301, December 1998.
- [177] F. Carrique, F. Arroyo, and A. Delgado, "Electrokinetics of Concentrated Suspensions of Spherical Colloidal Particles with Surface Conductance, Arbitrary Zeta Potential, and Double-Layer Thickness in Static Electric Fields," *Journal of Colloid and Interface Science*, vol. 252, pp. 126–137, August 2002.
- [178] F. Arriagada and K. Osseo-Asare, "Synthesis of Nanosize Silica in a Nonionic Water-in-Oil Microemulsion: Effects of the Water/Surfactant Molar Ratio and Ammonia Concentration," *Journal of Colloid and Interface Science*, vol. 211, pp. 210–220, Mar.March 1999.
- [179] A. van Blaaderen and A. Vrij, "Synthesis and characterization of colloidal dispersions of fluorescent, monodisperse silica spheres," *Langmuir*, vol. 8, pp. 2921–2931, December 1992.
- [180] J. P. Hoogenboom, *Colloidal Epitaxy. A Real-Space Analysis*. PhD thesis, Utrecht University, 2002.
- [181] J. P. Hoogenboom, A. K. van Langen-Suurling, J. Romijn, and A. van Blaaderen, "Epitaxial growth of a colloidal hard-sphere hcp crystal and the effects of epitaxial mismatch on crystal structure," *Physical Review E*, vol. 69, p. 051602, May 2004.
- [182] H. Giesche, "Synthesis of monodispersed silica powders II. Controlled growth reaction and continuous production process," *Journal of the European Ceramic Society*, vol. 14, pp. 205 – 214, March 1994.
- [183] S. Rodríguez, C. Lafuente, P. Cea, F. M. Royo, and J. S. Urieta, "Densities and Viscosities of Binary Mixtures of Some Cyclic Ethers + Chlorocyclohexane at 298.15 and 313.15 K," *Journal of Chemical & Engineering Data*, vol. 42, pp. 1285–1289, November 1997.
- [184] J. C. Crocker and D. G. Grier, "When Like Charges Attract: The Effects of Geometrical Confinement on Long-Range Colloidal Interactions," *Physical Review Letters*, vol. 77, pp. 1897–1900, August 1996.
- [185] M. N. van der Linden, J. C. P. Stiefelhagen, G. Heessels-Gürboga, J. E. S. van der Hoeven, N. A. Elbers, M. Dijkstra, and A. van Blaaderen, "Charging of Poly(methyl methacrylate) (PMMA) Colloids in Cyclohexyl Bromide: Locking, Size Dependence, and Particle Mixtures," *Langmuir*, vol. 31, pp. 65–75, January 2015.
- [186] T. Vissers, A. Imhof, F. Carrique, A. V. Delgado, and A. van Blaaderen, "Electrophoresis of concentrated colloidal dispersions in low-polar solvents," *Journal of Colloid and Interface Science*, vol. 361, pp. 443–455, September 2011.
- [187] L. Zhuravlev, "The surface chemistry of amorphous silica. Zhuravlev model," *Colloids and Surfaces A: Physicochemical and Engineering Aspects*, vol. 173, pp. 1 – 38, November 2000.
- [188] M. Castellano, E. Marsano, A. Turturro, L. Conzatti, and G. Busca, "Dependence of surface properties of silylated silica on the length of silane arms," *Adsorption*, vol. 18, pp. 307–320, November 2012.
- [189] H. Míguez, F. Mesezuer, C. López, A. Blanco, J. S. Moya, J. Requena, A. Mifsud, and V. Fornés, "Control of the Photonic Crystal Properties of fcc-Packed Submicrometer SiO<sub>2</sub> Spheres by Sintering," *Advanced Materials*, vol. 10, pp. 480–483, April 1998.
- [190] M. Leunissen, *Manipulating colloids with charges & electric fields*. PhD thesis, Utrecht University, 2007.
- [191] H. Mohan and P. N. Moorthy, "Formation of radical cations of polyiodomethanes: a pulse radiolysis study," *Journal of the Chemical Society, Perkin Transactions 2*, vol. -, pp. 277–282, February 1990.
- [192] Y. C. Wu and P. A. Berezansky, "Low Electrolytic Conductivity Standards," *Journal of Research of the National Institute of Standards and Technology*, vol. 100, p. 521, September-October 1995.
- [193] M. N. van der Linden, *Long-range repulsive charged colloids in and out of equilibrium*. PhD thesis, Utrecht University, 2013.
- [194] W. Stöber, A. Fink, and E. Bohn, "Controlled growth of monodisperse silica spheres in the micron size range," *Journal of Colloid and Interface Science*, vol. 26, pp. 62–69, January 1968.
- [195] A. M. Buckley and M. Greenblatt, "The Sol-Gel Preparation of Silica Gels," *Journal of Chemical Education*, vol. 71, p. 599, July 1994.
- [196] A. P. Philipse and A. Vrij, "Polydispersity probed by light scattering of secondary particles in controlled growth experiments of silica spheres," *The Journal of Chemical Physics*, vol. 87, pp. 5634–5643, October 1987.
- [197] G. Bogush, M. Tracy, and C. Zukoski IV, "Preparation of monodisperse silica particles: Control of size and mass fraction," *Journal of Non-Crystalline Solids*, vol. 104, pp. 95 – 106, August 1988.
- [198] H. E. Bergna and W. O. Roberts, eds., *Colloidal Silica: Fundamentals and Applications*. CRC Press, 2006.
- [199] H. Ohshima, *Electrical Phenomena at Interfaces and Biointerfaces: Fundamentals and Applications in Nano-, Bio-, and Environmental Sciences*. John Wiley & Sons, 2012.

- [200] J. H. Masliyah and S. Bhattacharjee, *Electrokinetic and Colloid Transport Phenomena*. John Wiley & Sons, 2006.
- [201] R. J. Hunter, *Foundations of Colloid Science*. Oxford, 2002.
- [202] G. Fritz, V. Schädler, N. Willenbacher, and N. J. Wagner, "Electrosteric Stabilization of Colloidal Dispersions," *Langmuir*, vol. 18, pp. 6381–6390, August 2002.
- [203] G. S. Roberts, R. Sanchez, R. Kemp, T. Wood, and P. Bartlett, "Electrostatic Charging of Nonpolar Colloids by Reverse Micelles," *Langmuir*, vol. 24, pp. 6530–6541, July 2008.
- [204] C. E. Espinosa, Q. Guo, V. Singh, and S. H. Behrens, "Particle Charging and Charge Screening in Nonpolar Dispersions with Nonionic Surfactants," *Langmuir*, vol. 26, pp. 16941–16948, November 2010.
- [205] S. Poovarodom and J. C. Berg, "Effect of particle and surfactant acid-base properties on charging of colloids in apolar media," *Journal of Colloid and Interface Science*, vol. 346, pp. 370 – 377, June 2010.
- [206] L. H. Allen and E. Matijevic, "Stability of colloidal silica: I. Effect of simple electrolytes," *Journal of Colloid and Interface Science*, vol. 31, pp. 287–296, November 1969.
- [207] K. Higashitani, M. Kondo, and S. Hatade, "Effect of particle size on coagulation rate of ultrafine colloidal particles," *Journal of Colloid and Interface Science*, vol. 142, pp. 204–213, March 1991.
- [208] J. Depasse and A. Watillon, "The stability of amorphous colloidal silica," *Journal of Colloid and Interface Science*, vol. 33, pp. 430–438, July 1970.
- [209] M. Kobayashi, F. Juillerat, P. Galletto, P. Bowen, and M. Borkovec, "Aggregation and Charging of Colloidal Silica particles: Effect of Particle Size," *Langmuir*, vol. 21, pp. 5761–5769, May 2005.
- [210] M. Kobayashi, M. Skarba, P. Galletto, D. Cakara, and M. Borkovec, "Effects of heat treatment on the aggregation and charging of stöber-type silica," *Journal of Colloid and Interface Science*, vol. 292, pp. 139–147, December 2005.
- [211] T. Seki and T. Ikariya, "In situ diffuse reflectance infrared fourier transform spectroscopy of MCM-41 mesoporous silica: mechanistic consideration on the chemical fixation of CO<sub>2</sub> with N,N-dimethylethylenediamine to 1,3-dimethyl-2-imidazolidinone," *Physical Chemistry Chemical Physics*, vol. 11, pp. 10073–10079, November 2009.
- [212] N. Boon and R. van Roij, "Charge reversal of moisturous porous silica colloids by take-up of protons," *Journal of Colloid and Interface Science*, vol. 385, pp. 66–72, November 2012.
- [213] A. Walcarius, C. Despas, and J. Bessière, "Molecular sieving with amorphous monodisperse silica beads," *Microporous and Mesoporous Materials*, vol. 23, pp. 309–313, September 1998.
- [214] L. C. Sander, K. A. Lippa, and S. A. Wise, "Order and disorder in alkyl stationary phases," *Analytical and Bioanalytical Chemistry*, vol. 382, pp. 646–668, April 2005.
- [215] Y. Hirata, M. Novotny, T. Tsuda, and D. Ishii, "Packed microcapillary columns with different selectivities for liquid chromatography," *Analytical Chemistry*, vol. 51, pp. 1807–1809, September 1979.
- [216] M. Hennion, C. Picard, and M. Caude, "Influence of the number and length of alkyl chains on the chromatographic properties of hydrocarbonaceous bonded phases," *Journal of Chromatography A*, vol. 166, pp. 21–35, December 1978.
- [217] T. G. Waddell, D. E. Leyden, and M. T. DeBello, "The nature of organosilane to silica-surface bonding," *Journal of the American Chemical Society*, vol. 103, pp. 5303–5307, September 1981.
- [218] D. A. Hanaor and C. C. Sorrell, "Review of the anatase to rutile phase transformation," *Journal of Materials Science*, vol. 46, pp. 855–874, February 2011.
- [219] A. Di Paola, M. Bellardita, and L. Palmisano, "Brookite, the Least Known TiO<sub>2</sub> Photocatalyst," *Catalysts*, vol. 3, pp. 36–73, January 2013.
- [220] Y. Hu, H.-L. Tsai, and C.-L. Huang, "Effect of brookite phase on the anatase-rutile transition in titania nanoparticles," *Journal of the European Ceramic Society*, vol. 23, pp. 691–696, April 2003.
- [221] A. Pottier, C. Chanéac, E. Tronc, L. Mazerolles, and J.-P. Jolivet, "Synthesis of brookite TiO<sub>2</sub> nanoparticles by thermolysis of TiCl<sub>4</sub> in strongly acidic aqueous media," *Journal of Materials Chemistry*, vol. 11, pp. 1116–1121, March 2001.
- [222] S. Bakardjieva, V. Stengl, L. Szatmary, J. Subrt, J. Lukac, N. Murafa, D. Niznansky, K. Cizek, J. Jirkovsky, and N. Petrova, "Transformation of brookite-type TiO<sub>2</sub> nanocrystals to rutile: correlation between microstructure and photoactivity," *Journal of Materials Chemistry*, vol. 16, pp. 1709–1716, March 2006.
- [223] A. Asthana, T. Shokuhfar, Q. Gao, P. Heiden, C. Friedrich, and R. Yassar, "A Real Time Observation of Phase Transition of Anatase TiO<sub>2</sub> Nanotubes into Rutile Particles by in situ Joule Heating Inside Transmission Electron Microscope," *Microscopy and Microanalysis*, vol. 16, pp. 1360–1361, July 2010.
- [224] A. F. Demirörs, A. van Blaaderen, and A. Imhof, "Synthesis of Eccentric Titania-Silica Core-Shell and Composite Particles," *Chemistry of Materials*, vol. 21, pp. 979–984, February 2009.
- [225] A. F. Demirörs, A. van Blaaderen, and A. Imhof, "A General Method to Coat Colloidal Particles with Titania," *Langmuir*, vol. 26, pp. 9297–9303, June 2010.

## References

---

- [226] S.-D. Mo and W. Ching, "Electronic and optical properties of three phases of titanium dioxide: rutile, anatase, and brookite," *Physical Review B*, vol. 51, p. 13023, May 1995.
- [227] W. Hu, L. Li, G. Li, C. Tang, and L. Sun, "High-quality brookite TiO<sub>2</sub> flowers: Synthesis, characterization, and dielectric performance," *Crystal Growth and Design*, vol. 9, pp. 3676–3682, August 2009.
- [228] H. Tang, K. Prasad, R. Sanjinès, P. E. Schmid, and F. Lévy, "Electrical and optical properties of TiO<sub>2</sub> anatase thin films," *Journal of Applied Physics*, vol. 75, pp. 2042–2047, February 1994.
- [229] S. Valencia, J. M. Marín, and G. Restrepo, "Study of the Bandgap of Synthesized Titanium Dioxide Nanoparticles Using the Sol-Gel Method and a Hydrothermal Treatment.," *Open Materials Science Journal*, vol. 4, pp. 9–14, January 2010.
- [230] B. Prasai, B. Cai, M. K. Underwood, J. P. Lewis, and D. Drabold, "Properties of amorphous and crystalline titanium dioxide from first principles," *Journal of Materials Science*, vol. 47, pp. 7515–7521, November 2012.
- [231] J. G. Gibbs, S. Kothari, D. Saintillan, and Y.-P. Zhao, "Geometrically Designing the Kinematic Behavior of Catalytic Nanomotors," *Nano Letters*, vol. 11, pp. 2543–2550, May 2011.
- [232] T. Van Le, E. E. Ross, T. R. C. Velarde, M. A. Legg, and M. J. Wirth, "Sintered Silica Colloidal Crystals with Fully Hydroxylated Surfaces," *Langmuir*, vol. 23, pp. 8554–8559, July 2007.
- [233] F. Meseguer, "Colloidal crystals as photonic crystals," *Colloids and Surfaces A: Physicochemical and Engineering Aspects*, vol. 270-271, pp. 1 – 7, December 2005. *Liquids and MesoScience*.
- [234] R. L. W. Popma, *Sintering characteristics of nano-ceramic coatings*. PhD thesis, Rijksuniversiteit Groningen, 2002.
- [235] W. Widiyastuti, S. Y. Lee, F. Iskandar, and K. Okuyama, "Sintering behavior of spherical aggregated nanoparticles prepared by spraying colloidal precursor in a heated flow," *Advanced Powder Technology*, vol. 20, pp. 318 – 326, July 2009.
- [236] S. Wong, V. Kitaev, and G. A. Ozin, "Colloidal Crystal films: Advances in Universality and Perfection," *Journal of the American Chemical Society*, vol. 125, pp. 15589–15598, December 2003.
- [237] B. Hatton, L. Mishchenko, S. Davis, K. H. Sandhage, and J. Aizenberg, "Assembly of large-area, highly ordered, crack-free inverse opal films," *Proceedings of the National Academy of Sciences*, vol. 107, pp. 10354–10359, June 2010.
- [238] A. P. Philipse, "Solid opaline packings of colloidal silica spheres," *Journal of Materials Science Letters*, vol. 8, pp. 1371–1373, December 1989.
- [239] T. Okubo, M. Nozawa, and A. Tsuchida, "Kinetic aspects in the drying dissipative crack patterns of colloidal crystals," *Colloid and Polymer Science*, vol. 285, pp. 827–832, April 2007.
- [240] N. V. Dziomkina and G. J. Vancso, "Colloidal crystal assembly on topologically patterned templates," *Soft Matter*, vol. 1, pp. 265–279, September 2005.
- [241] T. Okubo, S. Okuda, and H. Kimura, "Dissipative structures formed in the course of drying the colloidal crystals of silica spheres on a cover glass," *Colloid and Polymer Science*, vol. 280, pp. 454–460, May 2002.
- [242] W. Man and W. B. Russel, "Direct Measurements of Critical Stresses and Cracking in Thin Films of Colloid Dispersions," *Physical Review Letters*, vol. 100, p. 198302, May 2008.
- [243] M. S. Tirumkudulu and W. B. Russel, "Cracking in Drying Latex Films," *Langmuir*, vol. 21, pp. 4938–4948, May 2005.
- [244] E. R. Dufresne, D. J. Stark, N. A. Greenblatt, J. X. Cheng, J. W. Hutchinson, L. Mahadevan, and D. A. Weitz, "Dynamics of Fracture in Drying Suspensions," *Langmuir*, vol. 22, pp. 7144–7147, August 2006.
- [245] F. García Santamaría, *Photonic Crystals Based on Silica Microspheres*. PhD thesis, Universidad Autónoma de Madrid, 2003.
- [246] A. V. Petukhov, J. H. J. Thijssen, A. Imhof, A. van Blaaderen, P. I. Dolbnya, A. Snigirev, I. Snigireva, and M. Drakopoulos, "3d structure and dis-(order) in photonic crystals by microradian synchrotron X-ray diffraction," *ESRF Newsletter*, vol. 38, pp. 19–20, December 2003.
- [247] J. H. J. Thijssen, A. V. Petukhov, D. C. 't Hart, A. Imhof, C. H. M. van der Werf, R. E. I. Schropp, and A. van Blaaderen, "Characterization of Photonic Colloidal Single Crystals by Microradian X-ray Diffraction," *Advanced Materials*, vol. 18, pp. 1662–1666, July 2006.
- [248] A. V. Petukhov, J. H. J. Thijssen, D. C. 't Hart, A. Imhof, A. van Blaaderen, I. P. Dolbnya, A. Snigirev, A. Moussaïd, and I. Snigireva, "Microradian X-ray diffraction in colloidal photonic crystals," *Journal of Applied Crystallography*, vol. 39, pp. 137–144, April 2006.
- [249] J. F. Mooney, A. J. Hunt, J. R. McIntosh, C. A. Liberko, D. Walba, and C. Rogers, "Patterning of functional antibodies and other proteins by photolithography of silane monolayers," *Proceedings of the National Academy of Sciences of the United States of America*, vol. 93, no. 22, pp. 12287–12291, 1996.

- [250] B. M. Vogel, D. M. DeLongchamp, C. M. Mahoney, L. A. Lucas, D. A. Fischer, and E. K. Lin, "Interfacial modification of silica surfaces through  $\gamma$ -isocyanatopropyl triethoxy silane-amine coupling reactions," *Applied Surface Science*, vol. 254, pp. 1789 – 1796, January 2008.
- [251] J. A. C. Veerman and D. Frenkel, "Phase diagram of a system of hard spherocylinders by computer simulation," *Physical Review A*, vol. 41, pp. 3237–3244, March 1990.
- [252] P. Bolhuis and D. Frenkel, "Tracing the phase boundaries of hard spherocylinders," *The Journal of Chemical Physics*, vol. 106, pp. 666–687, January 1997.
- [253] B. Peng, G. Soligno, M. Kamp, B. de Nijs, J. de Graaf, M. Dijkstra, R. van Roij, A. van Blaaderen, and A. Imhof, "Site-specific growth of polymers on silica rods," *Soft Matter*, vol. 10, pp. 9644–9650, December 2014.
- [254] C. Bae, J. Moon, H. Shin, J. Kim, and M. M. Sung, "Fabrication of Monodisperse Asymmetric Colloidal Clusters by Using Contact Area Lithography (CAL)," *J. Am. Chem. Soc.*, vol. 129, pp. 14232–14239, October 2007.
- [255] J. J. Bozzola and L. D. Russell, *Electron Microscopy: Principles and Techniques for Biologists*. Jones & Bartlett Learning, 1999.
- [256] B. de Nijs, *Towards Crystals of Crystals of Nanocrystals: a Self-assembly Study*. PhD thesis, Utrecht University, 2014.
- [257] T. Durrani and D. Bisset, "The Radon transform and its properties," *Geophysics*, vol. 49, pp. 1180–1187, August 1984.
- [258] M. Radermacher, "Three-dimensional reconstruction from random projections: orientational alignment via Radon transforms," *Ultramicroscopy*, vol. 53, pp. 121 – 136, February 1994.
- [259] F. Natterer, *The Mathematics of Computerized Tomography*. Vieweg+Teubner Verlag, 1986.
- [260] T. H. Besseling, J. Jose, and A. van Blaaderen, "Methods to calibrate and scale axial distances in confocal microscopy as a function of refractive index," *Journal of Microscopy*, vol. 257, pp. 142–150, February 2015.
- [261] *Handbook of Chemistry & Physics*. CRC Press, 65th ed. ISBN 0-8493-0465-2.
- [262] A. Kuijk, D. V. Byelov, A. V. Petukhov, A. van Blaaderen, and A. Imhof, "Phase behavior of colloidal silica rods," *Faraday Discussions*, vol. 159, pp. 181–199, June 2012.
- [263] C. Brinker, "Hydrolysis and condensation of silicates: Effects on structure," *Journal of Non-Crystalline Solids*, vol. 100, pp. 31 – 50, March 1988. Glasses and Glass Ceramics from Gels.
- [264] M. T. Harris, R. R. Brunson, and C. H. Byers, "The base-catalyzed hydrolysis and condensation reactions of dilute and concentrated {TEOS} solutions," *Journal of Non-Crystalline Solids*, vol. 121, pp. 397 – 403, May 1990. Proceedings of the Fifth International Workshop on Glasses and Ceramics from Gels.
- [265] G. Bogush and C. Zukoski IV, "Studies of the kinetics of the precipitation of uniform silica particles through the hydrolysis and condensation of silicon alkoxides," *Journal of Colloid and Interface Science*, vol. 142, pp. 1 – 18, March 1991.
- [266] A. F. Demirörs, *Anisotropic Colloids: Synthesis and Phase Behavior of Eccentric, Dimer and String-like Colloids*. PhD thesis, Utrecht University, 2010.
- [267] *Powder Diffraction Data*. Joint Committee on Powder Diffraction Standards Associateship at the National Bureau of Standards, 1976.
- [268] S. Pronk and D. Frenkel, "Point Defects in Hard-Sphere Crystals," *The Journal of Physical Chemistry B*, vol. 105, pp. 6722–6727, July 2001.
- [269] N. Geerts, S. Jahn, and E. Eiser, "Direct observation of size fractionation during colloidal crystallization," *Journal of Physics: Condensed Matter*, vol. 22, p. 104111, December 2010.
- [270] J. W. Williams, "The dieconstant constants of binary mixtures. X. The electric moments of simple derivatives of cyclohexane an of dioxan," *Journal of the Americal Chemical Society*, vol. 52, pp. 1831–1837, May 1930.
- [271] R. W. Crowe and C. P. Smyth, "The Dielectric and Polymorphic Behavior of Cyclohexanol, Cyclohexanone, Chloro-cyclohexane and Cyclohexane1,2," *Journal of the Americal Chemical Society*, vol. 73, pp. 5406–5411, November 1951.
- [272] F. Corradini, A. Marchetti, M. Tagliazucchi, and L. Tassi, "Static dielectric constants of 1,2-dichloroethane + 2-methoxyethanol + 1,2-dimethoxyethane ternary liquid mixtures from -10 to 80°C," *Fluid Phase Equilibria*, vol. 124, pp. 209–220, September 1996.
- [273] H. R. Vutukuri, A. Imhof, and A. van Blaaderen, "Fabrication of Polyhedral Particles from Spherical Colloids and Their Self-Assembly into Rotator Phases," *Angewandte Chemie International Edition*, vol. 53, pp. 13830–13834, November 2014.
- [274] P. Qiu and C. Mao, "Viscosity Gradient as a Novel Mechanism for the Centrifugation-Based Separation of Nanoparticles," *Advanced Materials*, vol. 23, pp. 4880–4885, November 2011.

- [275] M. N. van der Linden, A. van Blaaderen, and M. Dijkstra, "Effect of size polydispersity on the crystal-fluid and crystal-glass transition in hard-core repulsive Yukawa systems," *The Journal of Chemical Physics*, vol. 138, pp. 114903–1–114903–10, March 2013.
- [276] Y. Wang, Y. Wang, X. Zheng, G.-R. Yi, S. Sacanna, D. J. Pine, and M. Weck, "Three-Dimensional Lock and Key Colloids," *Journal of the American Chemical Society*, vol. 136, pp. 6866–6869, May 2014.
- [277] A. Kuijk, A. Imhof, M. H. W. Verkuijlen, T. H. Besseling, E. R. H. van Eck, and A. van Blaaderen, "Colloidal Silica Rods: Material Properties and Fluorescent Labeling," *Particle & Particle Systems Characterization*, vol. 31, pp. 706–713, June 2014.
- [278] J. de Graaf, M. Dijkstra, and R. van Roij, "Adsorption trajectories and free-energy separatrices for colloidal particles in contact with a liquid-liquid interface," *The Journal of Chemical Physics*, vol. 132, p. 164902, April 2010.
- [279] J. de Graaf, M. Dijkstra, and R. van Roij, "Triangular tessellation scheme for the adsorption free energy at the liquid-liquid interface: Towards nonconvex patterned colloids," *Physical Review E*, vol. 80, p. 051405, November 2009.
- [280] G. Soligno, M. Dijkstra, and R. van Roij, "The equilibrium shape of fluid-fluid interfaces: Derivation and a new numerical method for Young's and Young-Laplace equations," *The Journal of Chemical Physics*, vol. 141, p. 244702, December 2014.
- [281] G. Bosma, C. Pathmanoharan, E. H. de Hoog, W. K. Kegel, A. van Blaaderen, and H. N. Lekkerkerker, "Preparation of Monodisperse, Fluorescent PMMA-Latex Colloids by Dispersion Polymerization," *Journal of Colloid and Interface Science*, vol. 245, pp. 292–300, January 2002.
- [282] M. I. Bodnarchuk, M. V. Kovalenko, H. Groiss, R. Resel, M. Reissner, G. Hesser, R. T. Lechner, W. Steiner, F. Schöffler, and W. Heiss, "Exchange-Coupled Bimagnetic Wüstite/Metal Ferrite Core/Shell Nanocrystals: Size, Shape, and Compositional Control," *Small*, vol. 5, pp. 2247–2252, October 2009.
- [283] B. de Nijs, S. Dussi, F. Smalenburg, J. D. Meeldijk, D. J. Groenendijk, L. Filion, A. Imhof, A. van Blaaderen, and M. Dijkstra, "Entropy-driven formation of large icosahedral colloidal clusters by spherical confinement," *Nature Materials*, vol. 14, pp. 56–60, January 2015.
- [284] P. Datskos and J. Sharma, "Synthesis of Segmented Silica Rods by Regulation of the Growth Temperature," *Angewandte Chemie International Edition*, vol. 53, pp. 451–454, January 2014.
- [285] A. van Blaaderen and A. Vrij, "Synthesis and Characterization of Monodisperse Colloidal Organo-silica Spheres," *Journal of Colloid and Interface Science*, vol. 156, pp. 1–18, March 1993.
- [286] T. Besseling, *Self-assembly of colloidal spheres and rods in external fields*. PhD thesis, Utrecht University, 2014.
- [287] J. Jackson, *Classical Electrodynamics*. John Wiley and Sons, Inc., 3rd ed., 1999.
- [288] B. W. Kwaadgras, M. Dijkstra, and R. van Roij, "Communication: Bulkiness versus anisotropy: The optimal shape of polarizable brownian nanoparticles for alignment in electric fields," *The Journal of Chemical Physics*, vol. 136, pp. 131102–1–131102–4, April 2012.
- [289] B. W. Kwaadgras, M. Verdult, M. Dijkstra, and R. van Roij, "Polarizability and alignment of dielectric nanoparticles in an external electric field: Bowls, dumbbells, and cuboids," *The Journal of Chemical Physics*, vol. 135, pp. 134105–1–134105–4, October 2011.
- [290] T. Jones, "Basic theory of dielectrophoresis and electrorotation," *Engineering in Medicine and Biology Magazine, IEEE*, vol. 22, pp. 33–42, Nov.-Dec. 2003.
- [291] A. Kuijk, T. Troppenz, L. Filion, A. Imhof, R. van Roij, M. Dijkstra, and A. van Blaaderen, "Effect of external electric fields on the phase behavior of colloidal silica rods," *Soft Matter*, vol. 10, pp. 6249–6255, June 2014.
- [292] H. R. Vutukuri, A. F. Demirörs, B. Peng, P. D. J. van Oostrum, A. Imhof, and A. van Blaaderen, "Colloidal Analogues of Charged and Uncharged Polymer Chains with Tunable Stiffness," *Angewandte Chemie International Edition*, vol. 51, pp. 11249–11253, November 2012.
- [293] M. E. Leunissen, H. R. Vutukuri, and A. van Blaaderen, "Directing Colloidal Self-Assembly with Biaxial Electric Fields," *Advanced Materials*, vol. 21, pp. 3116–3120, April 2009.
- [294] A. Kuijk, *Fluorescent Colloidal Silica Rods: Synthesis and Phase Behavior*. PhD thesis, Utrecht University, 2012.
- [295] M. E. Leunissen and A. van Blaaderen, "Concentrating colloids with electric field gradients. II. Phase transitions and crystal buckling of long-ranged repulsive charged spheres in an electric bottle," *The Journal of Chemical Physics*, vol. 128, pp. 164509–1–164509–4, April 2008.
- [296] O. Martinsen, S. Grimnes, and H. Schwan, *Encyclopedia of Surface and Colloid Science*. Marcel Dekker, Inc, 2002.
- [297] A. Crespy, A. Bolève, and A. Revil, "Influence of the Dukhin and Reynolds numbers on the apparent zeta potential of granular porous media," *Journal of Colloid and Interface Science*, vol. 305, pp. 188 – 194, January 2007.
- [298] T. Vissers, *Oppositely charged colloids out of equilibrium*. PhD thesis, Utrecht University, 2010.

- [299] J. D. Feick and D. Velegol, "Measurements of Charge Nonuniformity on Polystyrene Latex Particles," *Langmuir*, vol. 18, pp. 3454–3458, February 2002.
- [300] D. Velegol and J. D. Feick, "Evaluating Randomness of Charge Distribution on Colloidal Particles Using Stationary Electrophoresis Angles," *Langmuir*, vol. 19, pp. 4592–4596, May 2003.
- [301] S. Asakura and F. Oosawa, "Interaction between particles suspended in solutions of macromolecules," *Journal of Polymer Science*, vol. 33, pp. 183–192, December 1958.
- [302] P. Jenkins and M. Snowden, "Depletion flocculation in colloidal dispersions," *Advances in Colloid and Interface Science*, vol. 68, pp. 57 – 96, November 1996.
- [303] H. N. W. Lekkerkerker, W. C.-K. Poon, P. N. Pusey, A. Stroobants, and P. B. Warren, "Phase Behaviour of Colloid + Polymer Mixtures," *Europhysics Letters*, vol. 20, p. 559, November 1992.
- [304] R. Tuinier, J. Rieger, and C. G. de Kruif, "Depletion-induced phase separation in colloid-polymer mixtures," *Advances in Colloid and Interface Science*, vol. 103, no. 1, pp. 1 – 31, 2003.
- [305] R. Lekkerkerker H.N.W., Tuinier, *Colloids and the Depletion Interaction*. Lecture Notes in Physics, Springer Netherlands, 2011.
- [306] E. A. G. Jamie, R. P. A. Dullens, and D. G. A. L. Aarts, "Tuning the demixing of colloid-polymer systems through the dispersing solvent," *Journal of Physics: Condensed Matter*, vol. 23, p. 194115, April 2011.
- [307] W. C. K. Poon, S. U. Egelhaaf, J. Stellbrink, J. Allgaier, A. B. Schofield, and P. N. Pusey, "Beyond simple depletion: phase behaviour of colloid-star polymer mixtures," *Philosophical Transactions of the Royal Society of London A: Mathematical, Physical and Engineering Sciences*, vol. 359, pp. 897–907, May 2001.
- [308] K. Zhao and T. G. Mason, "Directing Colloidal Self-Assembly through Roughness-Controlled Depletion Attractions," *Physical Review Letters*, vol. 99, p. 268301, December 2007.
- [309] A. D. Dinsmore and A. G. Yodh, "Entropic Confinement of Colloidal Spheres in Corners on Silicon Substrates," *Langmuir*, vol. 15, pp. 314–316, January 1999.
- [310] S. Sacanna, W. T. M. Irvine, P. M. Chaikin, and D. J. Pine, "Lock and key colloids," *Nature*, vol. 464, pp. 575–578, March 2010.
- [311] S. Harley, D. W. Thompson, and B. Vincent, "The adsorption of small particles onto larger particles of opposite charge: Direct electron microscope studies," *Colloids and Surfaces*, vol. 62, pp. 163 – 176, January 1992.
- [312] R. P. A. Dullens, E. M. Claesson, and W. K. Kegel, "Preparation and Properties of Cross-Linked Fluorescent Poly(methyl methacrylate) Latex Colloids," *Langmuir*, vol. 20, pp. 658–664, December 2004.
- [313] B. Peng, F. Smallenburg, A. Imhof, M. Dijkstra, and A. van Blaaderen, "Colloidal Clusters by Using Emulsions and Dumbbell-Shaped Particles: Experiments and Simulations," *Angewandte Chemie International Edition*, vol. 52, pp. 6709–6712, June 2013.
- [314] M. T. Elsesser and A. D. Hollingsworth, "Revisiting the Synthesis of a Well-Known Comb-Graft Copolymer Stabilizer and Its Application to the Dispersion Polymerization of Poly(methyl methacrylate) in Organic Media," *Langmuir*, vol. 26, pp. 17989–17996, December 2010.
- [315] G. Decher, "Fuzzy Nanoassemblies: Toward Layered Polymeric Multicomposites," *Science*, vol. 277, pp. 1232–1237, August 1997.
- [316] Y. Lvov, G. Decher, and H. Moehwald, "Assembly, structural characterization, and thermal behavior of layer-by-layer deposited ultrathin films of poly(vinyl sulfate) and poly(allylamine)," *Langmuir*, vol. 9, pp. 481–486, February 1993.
- [317] G. Decher and J. Schlenoff, *Multilayer thin films: Sequential Assembly of Nanocomposite Materials*. Wiley-VCH Verlag GmbH & Co, 2012.
- [318] J. Schmitt, G. Decher, W. J. Dressick, S. L. Brandow, R. E. Geer, R. Shashidhar, and J. M. Calvert, "Metal nanoparticle/polymer superlattice films: Fabrication and control of layer structure," *Advanced Materials*, vol. 9, pp. 61–65, January 1997.
- [319] A. van Helden and A. Vrij, "Static light scattering of concentrated silica dispersions in apolar solvents," *Journal of Colloid and Interface Science*, vol. 78, pp. 312 – 329, December 1980.
- [320] D. Lehner, G. Kellner, H. Schnablegger, and O. Glatter, "Static Light Scattering on Dense Colloidal Systems: New Instrumentation and Experimental Results," *Journal of Colloid and Interface Science*, vol. 201, pp. 34 – 47, May 1998.
- [321] W. Russel, D. Saville, and W. R. Schowalter, *Colloidal Dispersions*. Cambridge University Press, 1989.
- [322] D. El Masri, T. Vissers, S. Badaire, J. C. P. Stiefelhagen, H. R. Vutukuri, P. Helfferich, T. H. Zhang, W. K. Kegel, A. Imhof, and A. van Blaaderen, "A qualitative confocal microscopy study on a range of colloidal processes by simulating microgravity conditions through slow rotations," *Soft Matter*, vol. 8, pp. 6979–6990, May 2012.
- [323] P. Meallier, S. Guittouneau, C. Emmelin, and T. Konstantinova, "Photochemistry of fluorescein and eosin derivatives," *Dyes and Pigments*, vol. 40, pp. 95 – 98, January 1999.
- [324] J. Crocker, D. Grier, and E. Weeks, "[http://www.physics.emory.edu/faculty/weeks//idl/.](http://www.physics.emory.edu/faculty/weeks//idl/)"

## References

---

- [325] M. Hermes, *Hard Spheres out of Equilibrium*. PhD thesis, Utrecht University, 2010.
- [326] C. I. Zoldesi and A. Imhof, "Synthesis of monodisperse colloidal spheres, capsules, and microballoons by emulsion templating," *Advanced Materials*, vol. 17, pp. 924–928, April 2005.
- [327] A. Mohraz and M. J. Solomon, "Direct visualization of colloidal rod assembly by confocal microscopy," *Langmuir*, vol. 21, pp. 5298–5306, June 2005.
- [328] J. E. G. J. Wijnhoven, "Seeded growth of monodisperse gibbsite platelets to adjustable sizes," *Journal of Colloid and Interface Science*, vol. 292, pp. 403–409, December 2005.
- [329] V. N. Manoharan, M. T. Elsesser, and D. J. Pine, "Dense packing and symmetry in small clusters of microspheres," *Science*, vol. 301, pp. 483–487, July 2003.
- [330] B. Peng, H. R. Vutukuri, A. van Blaaderen, and A. Imhof, "Synthesis of fluorescent monodisperse non-spherical dumbbell-like model colloids," *Journal of Materials Chemistry*, vol. 22, pp. 21893–21900, October 2012.
- [331] M. Mittal and E. M. Furst, "Electric Field-Directed Convective Assembly of Ellipsoidal Colloidal Particles to Create Optically and Mechanically Anisotropic Thin Films," *Advanced Functional Materials*, vol. 19, pp. 3271–3278, October 2009.
- [332] R. M. Erb, H. S. Son, B. Samanta, V. M. Rotello, and B. B. Yellen, "Magnetic assembly of colloidal superstructures with multipole symmetry," *Nature*, vol. 457, pp. 999–1002, February 2009.
- [333] H. Ma, W. Wen, W. Y. Tam, and P. Sheng, "Dielectric electrorheological fluids: Theory and experiment," *Advances in Physics*, vol. 52, pp. 343–383, June 2003.
- [334] A.-P. Hynninen and M. Dijkstra, "Phase Diagram of Dipolar Hard and Soft Spheres: Manipulation of Colloidal Crystal Structures by an External Field," *Physical Review Letters*, vol. 94, pp. 138303–1–138303–4, April 2005.
- [335] A.-P. Hynninen and M. Dijkstra, "Phase behavior of dipolar hard and soft spheres," *Physical Review E*, vol. 72, pp. 051402–1–051402–10, November 2005.
- [336] X. Zhang, Z. Zhang, and S. C. Glotzer, "Simulation Study of Dipole-Induced Self-Assembly of Nanocubes," *Journal of Physical Chemistry C*, vol. 111, pp. 4132–4137, March 2007.
- [337] N. A. Elbers, J. Jose, A. Imhof, and A. van Blaaderen, "Bulk Scale Synthesis of Monodisperse PDMS Droplets above 3  $\mu\text{m}$  and Their Encapsulation by Elastic Shells," *Chemistry of Materials*, vol. 27, pp. 1709–1719, March 2015.
- [338] J. Jose, M. Kamp, A. van Blaaderen, and A. Imhof, "Unloading and Reloading Colloidal Microcapsules with Apolar Solutions by Controlled and Reversible Buckling," *Langmuir*, vol. 30, pp. 2385–2393, March 2014.
- [339] J.-S. Song, F. Tronc, and M. A. Winnik, "Two-Stage Dispersion Polymerization toward Monodisperse, Controlled Micrometer-Sized Copolymer Particles," *Journal of the American Chemical Society*, vol. 126, pp. 6562–6563, June 2004.
- [340] D. R. Bohren, C. F. & Huffman, *Absorption and Scattering of Light by Small Particles*. Wiley, 2008.
- [341] A. L. Smith, *The Analytical Chemistry of Silicones*, vol. 112. Wiley-Interscience, 1991.
- [342] C. Smart and E. Willis, "Determination of refractive indices of polystyrene latices by light scattering," *Journal of Colloid and Interface Science*, vol. 25, pp. 577–583, December 1967.
- [343] J. Depasse, "Silica Hydrosols: Influence of the Refractive Index of the Electrolyte Solution on the Turbidity and on the Interparticle Interactions," *Journal of Colloid and Interface Science*, vol. 188, pp. 229–231, April 1997.
- [344] D. Frenkel and A. J. C. Ladd, "New Monte Carlo method to compute the free energy of arbitrary solids. Application to the fcc and hcp phases of hard spheres," *The Journal of Chemical Physics*, vol. 81, pp. 3188–3193, October 1984.
- [345] P. G. Bolhuis, D. Frenkel, S.-C. Mau, and D. A. Huse, "Entropy difference between crystal phases," *Nature*, vol. 388, pp. 235–236, July 1997.





# Dankwoord

Het is al vaak gezegd: promoveren doe je niet alleen. Je hebt mensen nodig om van te leren, om samen na te denken, en mensen die je helpen ontspannen. Ik ben heel dankbaar voor alle steun (van wetenschappelijk en niet-wetenschappelijk karakter) die ik heb gekregen van zoveel verschillende kanten.

Allereerst wil ik mijn promotor Alfons van Blaaderen van harte bedanken, voor de mooie kans om in de groep te komen werken en voor de prettige onderzoeksomgeving die je creëert. Ik ben erg blij geweest met de vele ideeën, het feilloos vaststellen van wat aan een observatie interessant en belangrijk is, en de deur die altijd open stond. Verder waardeer ik de grote vrijheid die ik kreeg om ook nieuwe wegen in te slaan. Arnout Imhof, mijn co-promotor, wil ik bedanken voor alle inzet. Je nauwkeurigheid heeft bovendien veel kromme zinnen en onlogische sprongen in dit proefschrift voorkomen.

I would like to thank all my colleagues at the Soft Condensed Matter group for the wonderful time I had, having always felt very much at home at SCM. I would like to thank everyone personally, which probably won't fit here, but I'll try anyway. My roommates Nina Elbers, Bing Liu, Thijs Besseling and Somil Gupta: thank you for the nice atmosphere in our room upstairs. Nina, wij hebben vaak onze successen gevierd en de minder succesvolle gedeeld; dat heeft me heel vaak weer verder geholpen. Ik ben ook zo blij dat we nog een mooi samenwerkingsproject hebben opgezet (h.9). Daar heb ik van genoten, dankjewel! Anjan Gantapara, thank you for your friendship, and also for teaching me little bits about computer simulations. Thijs, wat in dit proefschrift staat over particle tracking heb ik van jou geleerd. Dank voor het belangeloos delen van codes en kennis. Fabian Hagemans, de laatste maanden - toen ik al druk aan 't schrijven was - werkten we nog veel samen aan experimenten voor h. 6. 't Was natuurlijk heel fijn voor mij dat niet alleen te hoeven doen. Dankjewel dat je zo snel nog zoveel opgehelderd hebt. Jissy Jose, you were my closest predecessor in terms of starting a PhD project. Thank you for the collaboration on colloidal bowl-shaped colloids, and also for sharing your experiences on completing a PhD project and job hunting. Johan Stiefelhagen, ik heb veel van je geleerd, bedankt! Rao Vutukuri, you always had suitable answers to my research insecurities; it helped a lot. Bo Peng, thanks for being so open to collaborate, which I genuinely enjoyed. Helene, thanks for all the moral support. Marjolein van der Linden, jij hebt

---

heel veel bijgedragen aan dit proefschrift (hfdst. 3 en 5), zelfs nog vanuit Parijs. Bedankt! Michiel Hermes, wat fijn dat je wilde samenwerken zoals beschreven in hfdst. 8. Het ging allemaal te langzaam, dus dank voor je geduld. Wessel Vlug, bedankt voor de gezelligheid in het lab (vooral als we lange  $g(r)$  metingen moesten doen) en het delen van je kennis over silica. Patrick Baesjou, Krassimir Velikov en Marcel di Vece, bedankt voor jullie oprechte interesse en voor alle gesprekken over werken aan de universiteit en in het bedrijfsleven. Laura Filion and Teun Vissers, you were always interested in how I was doing with my research and outside of it. Thank you! Peter Helfferich, dankzij jouw geduld durfde ik steeds met mijn grote/kleine computerproblemen langs te komen; heel belangrijk voor een PhD student! Marion Wijburg, Thea Pozzi, en Marjoke Hoenderdos: van organisatorische tot administratieve zaken, jullie staan altijd voor iedereen klaar. Dat helpt enorm bij het werk. Dank daarvoor! Thomas Troppenz (ITF), thanks for collaborating with Nina and me on the 'caps-project'. I also enjoyed our conversations and hunting for cake! Zdenek, thanks for sharing your ideas on (simulations of) patchy particles, even though we did not end up collaborating as we hoped. Merel Lefferts, fijn dat je mijn master-student was. Dankzij jouw hulp zijn er veel vragen uit hfdst. 4 helder geworden. René van Roij en Marjolein Dijkstra, jullie interesse in onze experimenten is zeer waardevol. Bedankt daarvoor. Judith Wijnhoven, geweldig hoe jij je inzet om het lab op rolletjes te laten lopen. Ook bedankt voor het advies en de gezelligheid bij het werk. Bart, hier natuurlijk bedankt voor alle hulp van wetenschappelijke aard. Actually, all group members of SCM&B have helped me in some way or another through these years. So Henriëtte Bakker, Simone Dussi, John Edison, Anke Kuijk, Ernest van der Wee, Wiebke Albrecht, Da Wang, Vasileios Prymidis, Srivatsan Mohan, Jessi van der Hoeven, Ran Ni, Weikai Qi, Bas Kwaadgras, Murphy Lee, Douglas Ashton, Nick Tasios, Marijn van Huis, Matthew Dennison, Kristina Milikovic, Harini Pattabiraman Stéphane Badaire, Djamel al Masri, Ahmet Demirörs, Mattieu Marechal, Dannis 't Hart, Esther Vermolen, Peter van Oostrum, Frank Smallenburg, Carlos van Kats, Tian-Song Deng, Guido Avvisati, Berend van der Meer, Pepijn Moerman, Tonnishtha Dasgupta, Yang Liu, Gülsen Heessels-Gürboga, Dave van den Heuvel and everyone I may have missed: a heartfelt thank you!

I also want to thank the people in the FCC group (Van 't Hoff laboratory) for their kindness and willingness to collaborate. In particular, I want to thank Willem Kegel and Bas van Ravensteijn for inviting me to collaborate on chemically anisotropic dumbbells. Furthermore, I thank Anke Leferink op Reinink, Janne-Mieke Meijer, Sonja Castillo, Susanne van Berkum, Chris Evers, Joost Wolters, Julius de Folter, Andrei Petoukhov and Dima Byelov for the nice contact, and the first four people for generously sharing 'promotietips' with me. The people of CMI are thanked for the nice atmosphere at the first floor, also since I was the first 'intruder' from downstairs. Special thanks to Francesca Pietra, Relinde van Dijk-Moes, Ingmar Swart, Joren Eilers, and Mark Boneschanscher for the nice contact. As a member of SCM, I also

---

benefitted from the fruitful contact we have with the Institute for Theoretical Physics. René van Roij, Simone Belli, Jos Zwanikken, Niels Boon, Thomas Troppenz and all others: thank you! Hans Meeldijk en Chris Schneidenberg, jullie inzet voor de elektronen-microscopen faciliteit is fenomenaal. Jullie zijn goud waard (liefst in gold-targets)! Isja de Feijter en Ilja Voets van het ICMS (TU Eindhoven): bedankt voor het vertrouwen en de samenwerking, dat we hopelijk nog zullen publiceren. Ik voelde me erg welkom in Eindhoven. I'd like to say a big *thank you* to my colleagues at the Melville and Cavendish labs (all mixed: Setu, Felix, Jade, Daniel, Richard, Will, Hamid, Alex, Steve, Matt, Alex, Anna, Lee, Vlad, Yang, Marie-Elena, Claire, Rohit, Alan, Yago, Giuliana, Tijmen, Jan, Magdalena, Dominique, Ji, Guolei, Yuchao, Aniello, Cindy, Helen, Rebecca, Silvia, Chi, Xiaohe, Enass, Bruno, Silvia, Giulia, Olimpia and everyone else, and of course dr. Oren A. Scherman and prof. Jeremy Baumberg) for welcoming me so kindly, making these hectic last months a really pleasurable experience for me.

Ik heb ook geluk met fantastische vrienden. Suzanne van der Veer, Remko van Hierden, Lidewij van Dijck, Jeroen van Oort, Anouk Stigter, Bart van Vliet, Marten Verhoog, Emile Bosman, Naomi van Wijck, Peter Bouwman, Sara Veldhoen, Paul Wiggers, Anja Schaapman: dankjulliewel voor alle leuke feestjes, spelavonden, kerstavonden en zomaar-avonden. De snowboarders (en Frederieke en Veerle!) natuurlijk ook bedankt voor de fantastische wintersportvakanties! Kirsty van Nierop, we hebben elkaar o.a. door onze drukke agenda's niet genoeg gezien, maar dat halen we gewoon weer in :-)

Leny en Jos, bij jullie ben ik altijd welkom, bijvoorbeeld om van jullie heerlijke kookkunsten te genieten of om een spelletje Kolonisten te verliezen. Bedankt! Ook Maaïke, Erwin en Tessa bedankt voor jullie interesse en alle gezelligheid. Lieve Opa en Oma Kamp, lieve Opa en Oma van der Meulen: dan toch eindelijk klaar met die 'studie', bedankt voor de fijne tijd die we samen beleefd hebben. Ronald, je bent de beste broer/collega-onderzoeker die er is. Bedankt dat je altijd geïnteresseerd bent in wat ik beleef (en me ook nog eens uit allerlei computer 'situations' hebt gered, zoals die keer van die laptop en dat glas wijn...). Jan en Atje / Pap en Mam, op jullie kan ik altijd rekenen. Ik heb geluk met jullie! Bedankt voor alle fijne weekenden, de mooie reizen die we hebben gemaakt, en alle praktische hulp waardoor ik dan nét weer mijn agenda rond kon krijgen. En last but not least... lieve Bart, dankjewel!

– Marlous, mei 2015



# About the Author



Marlou Kamp was born in Ermelo (The Netherlands) on the 22<sup>nd</sup> of May, 1986. She finished secondary school at Atheneum level at College Groevenbeek in 2004. After completing the first year of studies at University College Utrecht in 2005, she started the 'twin' bachelor program *Physics & Astronomy* and *Mathematics* with a minor in *History and Philosophy of Science*. Part of these studies were completed at the University of California in Berkeley (USA). The bachelor's thesis was titled *Polydispersity-induced effects on long-range order in silica crystals* and was carried out at the Soft Condensed Matter group in Utrecht under supervision of drs. Johan Stiefelhagen and dr. Arnout Imhof. After graduating in 2008 (cum laude), she started the Master's program 'Nanomaterials: Chemistry & Physics'. For the Master's research, Marlou investigated stack formation in hemispherical colloidal caps under supervision of dr. Arnout Imhof and prof. dr. Alfons van Blaaderen. Attaining her diploma in 2010 (cum laude), she started a PhD project in the same group, focussing on synthesis pathways towards directional colloidal interactions and self-assembly of these 'patchy particles'. The most important results of that research are reported in this thesis. Currently, she is working as a researcher at Cambridge University in the group of dr. Oren A. Scherman (Melville Laboratory), in a collaborative project with the Nanophotonics group of prof. Jeremy Baumberg (Cavendish Laboratory).

---



# List of Publications

This thesis is partly based on the following publications:

- M. Kamp, I. de Feijter, I. Voets, A. Imhof and A. van Blaaderen, *Silica particles with fluorescently-labeled and crystalline titania protrusions*, in preparation – Chapter 4
- B. Peng, G. Soligno, M. Kamp, B. de Nijs, J. de Graaf, M. Dijkstra, R.H.H.G. van Roij, A. van Blaaderen and A. Imhof, *Site-specific growth of polymers on silica rods*, *Soft matter* 10 : 48, pp. 9644-9650 (2014) - Chapter 6
- M. Kamp *et al.*, *Lollipop-shaped silica/MPS hetero-dimer particles prepared by site-specific nucleation and growth of a silane coupling agent on silica rods and nails*, in preparation – Chapters 6 and 7
- M. Kamp, M. Hermes, C.M. van Kats, D.J. Kraft, W.K. Kegel, M. Dijkstra, and A. van Blaaderen, *Selective depletion interactions in mixtures of rough and smooth silica spheres*, to be submitted – Chapter 8
- M. Kamp / N.A. Elbers / T. Troppenz, A. Imhof, M. Dijkstra, R.H.H.G. van Roij and A. van Blaaderen, *Electric-field induced lock-and-key interactions between colloidal spheres and bowls*, to be submitted – Chapter 9

Other publications by the author:

- A. van Blaaderen, M. Dijkstra, R.H.H.G. van Roij, A. Imhof, M. Kamp, B.W. Kwaadgras, T. Vissers and B. Liu, *Manipulating the self assembly of colloids in electric fields*, *The European Physical Journal Special Topics* 222 : 11, pp. 2895-2909 (2013).
  - J. Jose, M. Kamp, A. van Blaaderen and A. Imhof, *Unloading and reloading colloidal microcapsules with apolar solutions by controlled and reversible buckling*, *Langmuir* 30:9, pp. 2385-2393 (2014).
-

- B.G.P. van Ravensteijn, M. Kamp, A. van Blaaderen and W.K. Kegel, *General route toward chemically anisotropic colloids*, Chemistry of Materials 25 : 21, pp. 4348-4353 (2013).